STRUCTURAL ANALYSIS WITH NON-SYMMETRIC CROSS SECTIONS

by

Edward J. Sippel

A dissertation submitted in partial fulfillment of
the requirements for the degree of

Doctor of Philosophy

(Civil and Environmental Engineering)

at the

UNIVERSITY OF WISCONSIN–MADISON

2022

Date of final oral examination: 07/25/2022

The dissertation is approved by the following members of the Final Oral Committee:
Hannah B. Blum, Assistant Professor, Civil and Environmental Engineering
Pavana Prabhakar, Associate Professor, Civil and Environmental Engineering
Wendy C. Crone, Professor, Engineering Physics
Ronald D. Ziemian, Professor, Civil & Environmental Engineering (Bucknell University)

THESIS AUTHORSHIP ATTRIBUTION

This dissertation contains material published or submitted for publication, based on the work presented in this dissertation, for which I am the main author or co-author.

Journal Papers

Edward J. Sippel, Ronald D. Ziemian, and Hannah B. Blum, "Structural analysis using line elements to model members with non-symmetric cross sections." *Thin-Walled Structures*, 169 (2021): 108407. https://doi.org/10.1016/j.tws.2021.108407

Edward J. Sippel, and Hannah B. Blum, "Structural analysis of steel structures with non-symmetric members." *Engineering Structures*, 245 (2021): 112739. https://doi.org/10.1016/j.engstruct.2021.112739

Edward J. Sippel, Ronald D. Ziemian, and Hannah B. Blum, "Experimental verification of eccentrically loaded steel joist analysis with non-symmetric sections." Submitted to *Journal of Structural Engineering*, (2022).

Max E. Laracuente, Edward J. Sippel, and Hannah B. Blum, "Experimental evaluation of hot-rolled unequal-leg stainless-steel angle columns." Submitted to *Journal of Constructional Steel Research*, (2022).

Edward J. Sippel, Ronald D. Ziemian, and Hannah B. Blum, "Importance of Flexural-Torsional Buckling for Double Angle Joist and Joist Girder Chords Design." Submitted to *Journal of Constructional Steel Research*, (2022).

Peer-Reviewed Conference Papers

Edward J. Sippel, and Hannah B. Blum, "Virtual Reality Field Trip of a Steel Building Under Construction," in *Proceedings of the 2022 ASEE Annual Conference*, 2022, p. 1-21.

Conference Papers

Edward J. Sippel, Ronald D. Ziemian, and Hannah B. Blum, “Analysis of non-symmetric cross-sections relative to the provisions of AISC 360-10", in *Proceedings of the 2020 SSRC Annual Stability Conference*, Atlanta, GA: SSRC, 2020, pp. 1-28.

Edward J. Sippel, and Hannah B. Blum, “System analysis of nonsymmetric cold-formed steel cross sections members,” in *Proceedings of the 2020 CFSRC Colloquium*, 2020, 1–8. [Online] Available: http://jhir.library.jhu.edu/handle/1774.2/63157

Edward J. Sippel, Ronald D. Ziemian, and Hannah B. Blum, “Experimental verification of eccentrically loaded steel joists with non-symmetric sections," in *Proceedings of the 2021 SSRC Annual Stability Conference*, Louisville, KY: SSRC, 2021, pp. 1-28.

Edward J. Sippel, Ronald D. Ziemian, and Hannah B. Blum, “Buckling behavior of open-web steel joists and joist girders," in *Proceedings of the 2022 SSRC Annual Stability Conference*, Denver, CO: SSRC, 2022, pp. 1-20.

Max E. Laracuente, Edward J. Sippel, and Hannah B. Blum, “Stability considerations of unequal-leg angle stainless steel columns," in *Proceedings of the 2022 SSRC Annual Stability Conference*, Denver, CO: SSRC, 2022, pp. 1-20.

Research Reports

Committee on Specifications for the Design of Cold-Formed Steel Structural Members, *Tutorials for MASTAN 2 and Related Validation*. American Iron and Steel Institute, 2021. [Online] Available: https://scholarsmine.mst.edu/ccfss-aisi-spec/227

Edward J. Sippel, Ronald D. Ziemian, and Hannah B. Blum, *Flexural-Torsional Buckling of Double Angle Joist and Joist Girder Chords*. University of Wisconsin-Madison. Madison, WI. Expected Fall 2022.

ACKNOWLEDGMENTS

I would like to extend my sincere thanks to my advisor, Assistant Professor Hannah Blum, for her guidance and support throughout my candidature. The various opportunities she provided have aided me in reaching my goals. I would also like to thank Professor Ronald Ziemian for his insight through this work. Thanks to them as well as Associate Professor Pavana Prabhakar and Professor Wendy Crone for serving on my defense committee.

I would like to thank Max Laracuente for his collaboration on the stainless steel component of this research and Jacob Zeuske for his assistance with the experimental components of my thesis. I'd also like to acknowledge by fellow group mates Hyeyoung Koh and Yu Xia for their assistance. Lastly, I would be remiss in not mentioning the various industry professionals that provided their expertise across this project.

I am also grateful for the various financial assistance that was provided for my work. From the University of Wisconsin-Madison grants to the AISI small research grant and material donations from New Millenium Building Systems, SJI, AISC, and Stainless Structurals, the research would have not be possible without your support.

Lastly, I would like to thank my family and friends for their support.

LIST OF TABLES

LIST OF FIGURES

ABSTRACT

A study of structural members with non-symmetric cross sections was completed to provide additional insight into the impact of non-symmetric behavior. There are known differences in the fundamental mechanical response of non-symmetric versus double symmetric sections; however, these are not consistently applied throughout the structural design process. This study discusses the relevance of non-symmetric behavior when completing structural analysis as well as when calculating design capacities.

The structural analysis investigation implemented numerical evaluations complemented with an experimental validation. Six three-dimensional non-symmetric cross section benchmark examples, three based on individual members and three considering systems, were evaluated using typical engineering practice methods assuming doubly symmetric behavior as well as more complex methods incorporating non-symmetric behavior. Doubly symmetric based analyses were found to consistently miss part of the response, which could be captured by line elements including non-symmetric behavior, especially the appropriate torsional response. These variations led to significant issues in stability, which would limit the accuracy of more complex analysis procedures. The experimental evaluation of an open-web steel joist compared to a non-symmetric line element model indicated that it was possible to predict the behavior of a complex system. Results highlighted the opportunity to improve member-to-member connections considering the more complex non-symmetric behavior.

The design capacity investigation focused on compression in carbon steel equal-leg double angle joist chords and stainless steel unequal-leg single angles, particularly the importance of flexural-torsional buckling. Utilizing existing research, finite element modeling procedures were validated for both series. Subsequent parametric studies indicated that flexural-torsional buckling was not as critical as indicated by current AISC design provisions. Double angle cross sections exhibited increased torsional stiffness due to the transfer of torsion between the individual chord angles, which emphasized the individual angle twisting behavior. The equivalence of a single angle failing in flexural-torsional buckling and local buckling, applicable to carbon and stainless steel, highlighted the possibility of applying the same reduction twice when considering flexural-torsional buckling directly. The buckling capacity of carbon steel equal-leg double angle joist chords and stainless steel unequal-leg single angles were found to be adequately predicted by only evaluating flexural buckling with local buckling reductions.

1.1 Motivation

Non-symmetric cross sections are utilized in a variety of different structural applications. While various behaviors are known to be attributed to non-symmetric cross sections, how this information is accounted for in the structural analysis process varies. Some information is implemented during the analysis phase, while other details are considered during the design phase. As the use of computational tools grows, it becomes increasingly important to understand the intent and limitations behind what structural engineers are implementing in practice.

Starting with structural analysis, current requirements detailed in the American Institute of Steel Construction (AISC) Specification for Structural Steel Buildings [1] have been developed with a two-dimensional focus. According to the AISC Specification, a structural analysis including members with non-symmetric cross sections only requires the consideration of (1) flexural, shear, axial, and all other component deformations that contribute to the displacement of the structure and (2) second-order (geometric nonlinear) behavior including P-δ (member) and P-Δ (system) effects. The consideration of three-dimensional analysis effects such as torsion, warping, and second-order twisting effects are left to the discretion of the engineer. Although these effects are mentioned in the advanced analysis method, the use of this design approach is limited to specific applications that exclude non-symmetric cross sections. Limited benchmarks are available for such three-dimensional analysis [2], [3] and provide limited guidance on the effects of including or excluding non-symmetric cross-section behaviors.

Following existing requirements, the analysis of structural members has typically been completed using a 12-DOF line element that assumes a doubly symmetric response, irregardless of the actual cross-section geometry, which provides limited means to approximate the non-symmetric response. Recent work by researchers, such as Rinchen, Hancock, and Rasmussen [4] and Liu, Ziemian, Chen, and Chan [5], [6], has lead to the development of new line elements that are capable of directly modeling non-symmetric effects. The implementation of the work by Liu, Ziemian, Chen, and Chan [5], [6] into the structural analysis algorithms within MASTAN2 [7] has provided the opportunity to complete meaningful evaluations on the behavior of non-symmetric cross sections in structural systems as well as to further validate this new line element.

In addition to completing the appropriate structural analysis, the design of non-symmetric cross sections have additional challenges to consider. Focusing on compression with non-symmetric sections, the compression capacity is determined as a function of the flexural and torsional buckling behavior that is influenced by the non-coincident shear center and centroid in addition to any local buckling considerations. The current AISC Specification [1] requires that non-symmetric carbon steel sections account for the full interaction of flexural and torsional buckling except single angles. Based on the inelastic behavior of carbon steel, Galambos [8] determined that the design of single angles could conservatively be calculated based on the flexural buckling capacity with local buckling considerations, while neglecting flexural-torsional buckling. This work also considered double angles and tee-sections, but determined that flexural-torsional buckling should be considered as it represented a significant reduction in capacity in some applications. However, the current design practice for open-web steel joists allows double angles to be designed considering only flexural buckling with local buckling reductions [9]. The historical performance of steel joists has shown this procedure to be adequate and more recent work by Simpson Gumpertz & Heger [10] found that the inclusion of flexural-torsional buckling for double angles was overly conservative. In both the design requirements and the more recent research, no reasoning based on the mechanical behavior was provided as to why flexural-torsional buckling could be excluded from the design process.

In recent years, an increased interest in structural stainless steel lead to design recommendations becoming available in AISC's Design Guide 27 [11], which included a limited selection of non-symmetric sections. Angles in compression were limited to compact, equal-leg geometries due to limited testing, but followed similar design provisions as indicated in the Structural Steel Specification. Recently, an official Specification for Structural Stainless Steel Buildings [12] has been released with updated provisions that still had the limited scope of compact, equal-leg angle. While unequal-leg angles exist and are used in practice, additional research is needed to verify the expected behavior and if the same provisions apply or if modifications are needed. Another major change was the removal of the flexual-torsional buckling exception, which results in a significant reduction in capacity for short compression members. As a result, practicing engineers can encounter challenging situations where previously adequately designed elements are now under-designed per code with no reason provided as to why.

1.2 Scope and Objectives

The aim of this study is to provide additional understanding of the behavior of members with non-symmetric cross sections. Similar to how structural members are commonly analyzed for structural performance and then evaluated for strength, this research starts with an investigation into the analytical behavior of non-symmetric cross sections and concludes with an investigation into the design capacity in compression of single and double angles, a subset of non-symmetric cross sections.

The research into the analytical behavior of non-symmetric cross sections is focused on identifying significant variations that occur when evaluating members using conventional methods compared to more detailed approaches. To achieve this objective, a series of six benchmark examples were investigated that focused on various non-symmetric behaviors. The investigation utilized a series of finite element models including a shell element model, a doubly symmetric line element model, and a non-symmetric line element model. As multiple structural analysis programs were implemented in the comparison, a preliminary baseline evaluation was completed to verify consistent results for known doubly symmetric examples that covered the required minimum structural behavior per design requirements. As a control for internal programming variations, two models were evaluated for both line element alternatives to ensure the results represented typical behavior. The subsequent benchmark examples were selected from literature, where possible, to highlight different non-symmetric behaviors. The first three examples focused on the response of individual members, while the later three introduced structural systems to include the effects of member to member interactions. Based on the results, a discussion on the practical implications of current analysis requirements for non-symmetric sections was presented.

In addition to the theoretical validation of the updated MASTAN2 line element in the above work, an experimental verification of the non-symmetric behavior captured by the line element was completed. The experimental validation of the novel line element utilized a 20-foot open-web steel joist subjected to an eccentric hanging load. Two steel joists were connected by metal decking and diagonal cross-bracing to create a laterally stable system that could be subjected to three levels of uniform top chord loading combined with an eccentric hanging load. The measured deformations and strains were compared to the results of analytical models, which aligned with typical design practices. The investigation focused on the displacement and internal stress distribution of the loaded joist bottom chord. This investigation also considered the effects of various modeling assumptions and how it would impact the structural analysis results to provide insight to engineers on what issues exist when evaluating the behavior of the angle chords.

The investigation into the design capacity of non-symmetric cross sections focused on the behavior of concentric compression for two applications, equal-leg carbon steel double angles and unequal-leg stainless steel single angles. Each topic included an investigation of the theoretical behavior, model validation against experimental results from others, and a parametric study. The design implications of the results are discussed.

The double angle study was limited to carbon steel joist and joist girder chord applications. Following SJI's recommendations, the investigated chords were equal-leg double angles with a 1-inch gap between the vertical legs connected by 7/8-inch solid rod spacer. A theoretical buckling investigation was used to identify cross section sizes and associated lengths where flexural-torsional buckling was expected to control. Using this information, one joist and two joist girders were modeled to verify the influence of flexural-torsional buckling considering member continuity and joint stiffness. These advanced shell finite element models were validated using existing experimental results [13], [14]. The full joist structure model results were verified using simplified chord segment models, which was supplemented with investigation into the observed critical behavior. A discussion of the importance of global flexural-torsional buckling is provided.

The unequal-leg stainless steel angle study builds upon the experimental work being led by Master's student Max Laracuente [15]. That work encompasses tension coupon testing, residual stress measurements, imperfection measurements, and full-scale compression tests. Experimental work incorporated hot rolled and laser welded, dual-certified 304/304L L3″x2″x1/4″ sections, one of the most popular sizes per the distributor. This experimental data was used to validate a finite element model depicting the buckling behavior of unequal-leg stainless steel angles. A parametric study implementing this modeling procedure was completed for twelve compact cross sections with a slenderness ratio varying from 5 to 200. A discussion of the results in context of existing provisions and relevant theory is included.

1.3 Dissertation Layout

This dissertation is a synthesis of five sections, each summarizing one aspect of the overall project. The first four sections are journal papers that have either been published, as in the case of Chapter 2 and 3, or in the process of being submitted, Chapter 4 and 5. The fifth section summarizes the renaming work that will be implemented into a future publication. The following is a brief summary of the content provided in each chapter of this dissertation. It should be noted that there is no overall literature review chapter as relevant information is presented within each individual chapter.

Chapter 2 contains details on the numerical evaluation of individual members with non-symmetric cross sections to compare different analysis methods and a brief introduction into systems. This includes description of the modeling techniques considered, verification of those methods, modeling convergence, and four examples considering an angle subjected to torsion, a lipped channel buckling axial load and moments, Z-section bending, and an I-beam portal frame.

Chapter 3 contains details on the extension of this numerical evaluation of members with non-symmetric cross sections to consider systems of members. This section discusses a lipped channel portal frame and a roof system considering two different roof purlin cross-section geometries.

Chapter 4 contains details on an experimental validation on the use of a non-symmetric line element to determine the response of non-symmetric sections in an open-web steel joist. This section includes details of the experimental set-up, instrumentation, and results before presenting details of the analytical model and computation results, which includes variations based on common design assumptions.

Chapter 5 contains details on a numerical evaluation of buckling in double equal-leg angle joist and joist girder chords. This section discusses theoretical buckling behavior, full joist modeling, chord segment modeling, and further investigation into the cause of the observed behavior. The results are discussed in relation to the existing design provisions.

Chapter 6 contains details on the finite element modeling of stainless steel unequal-leg angles including calibration and validation to experimental results. A parametric study was utilized to evaluate a series of compact angles and compared to existing design provisions.

Chapter 7 contains a summary of the project, conclusions, and recommendations for future work.

2 STRUCTURAL ANALYSIS USING LINE ELEMENTS TO MODEL MEMBERS WITH NON-SYMMETRIC CROSS SECTIONS

Sippel, Edward J., Ziemian, Ronald D., and Blum, Hannah B. "Structural analysis using line elements to model members with non-symmetric cross sections." *Thin-Walled Structures*, 169 (2021): 108407. https://doi.org/10.1016/j.tws.2021.108407

Abstract

This study investigated the response of non-symmetric cross sections using line finite element models that were created with conventional elements that assumed a doubly symmetric response and sophisticated elements that included additional non-symmetric behavior. These models were compared to shell element models and experimental results when available. It was found that in many cases the doubly symmetric analyses missed physical responses that the non-symmetric analyses could capture. It was observed that twisting and second-order effects due to twisting played a significant factor in the final response. Furthermore, consideration of non-symmetric behavior was required to calculate some responses accurately.

2.1 Introduction

Current standards around the world provide minimum requirements for the design of steel structures. Each standard further indicates to some degree that their design provisions are a function of the analysis method being employed. For example, Eurocode 3 [16] states that the analysis needs to be appropriate for the relevant limit states considered and must be consistent with the relevant design assumptions. The Australian Standard for Steel Structures, AS 4100 [17], follows a comparable format that has the requirement that a structure should be analyzed in its entirety by default, but such an analysis can often be simplified depending on the design procedure being employed. The American Institute of Steel Construction's (AISC) Specification for Structural Steel Buildings [1] provides similar requirements on modeling structural behavior, but differs in that most requirements emphasize a two-dimensional analysis.

AISC's requirements for the structural analysis are implied within the code's general provisions for the design of structural stability. Of relevance to this paper are the following effects that must be considered: (1) flexural, shear, axial, and all other component deformations that contribute to the displacement of the structure; and (2) second-order (geometric nonlinear) behavior including P-δ (member) and P-Δ (system) effects. With a mindset towards design by two-dimensional analyses, there are no specific requirements related to the inclusion of torsion and/or second-order twisting effects. Although the Specification's appendix on design by advanced analysis does require such effects be considered, the use of this design approach is often limited to unusual and/or complex design problems. Further complicating this option are the requirements that the analysis model must be three-dimensional and also include the direct modeling of initial member imperfections.

In general, routine design relies on the discretion of the engineer on when to include twisting effects within the analysis. A structure comprised of members with doubly symmetric sections, such as standard I-beams and HSS (hollow structural sections), will tend to have negligible twisting effects if the members are loaded in a single plane and do not have any eccentricity out of that plane. If either of these conditions is not met, such doubly symmetric sections will begin to twist and this can lead to significantly different results as discussed by Ziemian *et al.* [2]. Of course, the routine use of non-symmetric sections, such as channels, angles, and tees, further complicates this issue. These cross sections have a centroid and shear center that are not coincidental, which means an applied load may result in a net torsional moment to the member and can cause the cross section to begin to move out-of-plane, even when the load is centered on the section. As a result, structures with eccentricities due to the location of applied loading and/or the cross section geometries will often exhibit three-dimensional behavior that could impact stability behavior, and which may be missed by the use of two-dimensional analysis or an over-simplified three-dimensional analysis.

The engineer's decision on what structural behavior to model is often further limited by the abilities of the structural analysis software available to them. Many structural analysis programs utilize a line (frame) element that assumes a doubly symmetric cross section with six degrees of freedom per element end, regardless of the actual shape being employed. With concern for torsion of non-symmetric shapes, some of these programs provide an element offset feature to approximate the potential impact of an eccentricity due to the misalignment of the shear center and centroid. Recent work by researchers, such as Rinchen *et al.* [4] and Liu *et al.* [5], [6], has resulted in new line element formulations that remove the doubly symmetric assumption - and the use of any related approximations - and instead, directly account for the twisting effect associated with members with non-symmetric (singly symmetric, point symmetric, and asymmetric) sections. The work by Liu *et al.* has been implemented into the structural analysis algorithms within MASTAN2 [7], along with additional tools to readily model these sections, and in part, provides a basis for this paper.

The primary objective of this paper is to report on a study that compared results determined from analyses using different modeling approaches of structural systems with members comprised of non-symmetric sections. Solutions of a shell element model, a doubly symmetric line element model, and a non-symmetric line element model are presented. In addition to providing much needed benchmark examples, the results are discussed as to whether or not twist should be included in the evaluation of non-symmetric sections.

2.2 Structural Analysis Programs Employed

Many different options and methods are available to engineers to complete their structural analysis. A common approach for practicing engineers is to use a commercially available structural analysis program that implements a conventional line element that assumes a doubly symmetric cross section without warping, such as using SAP2000 [18] or RFEM [19]. One method engineers can currently use to avoid making the doubly symmetric behavior assumption would be to use finite element analysis based on shell or solid elements. However, a simple structural system modeled this way would become unwieldy quite quickly. A desirable alternative would be to employ a robust line element program that has accurate facilities for members with symmetric and non-symmetric cross sections, such as MASTAN2 [7] and Abaqus [20].

2.2.1 Minimum Analysis Requirements

With this study focused on the behavior of members with non-symmetric sections evaluated by analyses with varying assumptions, each of the analysis methods employed were first assessed in their ability to model minimum behavioral requirements needed in design. This behavior was identified as the two-dimensional flexural and axial deformation, including the related P-δ and P-Δ second-order effects. Although many tabulated examples exist for these conditions, such validations were confirmed using the examples provided in the commentary to the AISC Specification [1] and are shown in Figure 2.1. These programs were further validated in their three-dimensional structural analysis capabilities, including torsion and second-order effects that include twist. This process was completed using another benchmark provided in the AISC Commentary, which is shown in Figure 2.2. With an initial lateral imperfection in the I-beam, the applied vertical loading and axial force produces out-of-plane deflections that include twist. It is further noted that this AISC

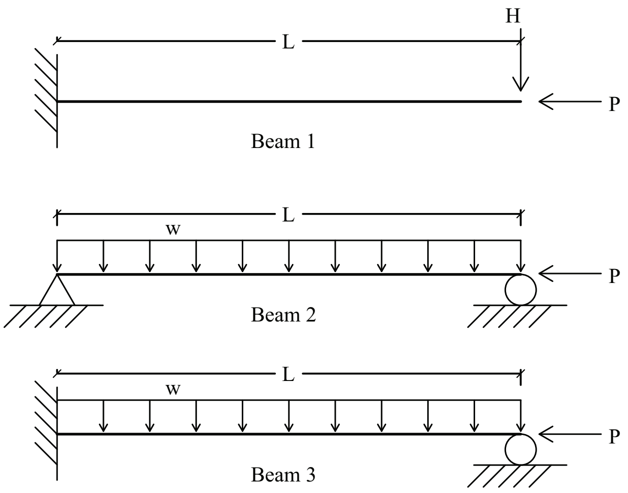

Standard Properties: W360x72 (W14x48) [Strong axis bending]
E = 200 GPa (29,000 ksi)
L = 8.53 m (28 ft)
H = 4.45 kN (1 kip)
w = 2.92 kN/m (0.2 kip/ft)
P varies

Figure 2.1: Verification problems for minimum response in two-dimensional structural analysis per [1]

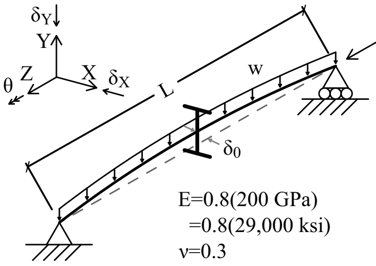

E=0.8(200 GPa)
=0.8(29,000 ksi)
ν=0.3

W460x97 (W18x65)
L = 6.1 m (20 ft)
δ0 = L/1000 sine wave
imperfection

Case 1: w = 58.4 kN/m (4 k/ft)
P = 0 kN (0 kips)
Case 2: w = 29.2 kN/m (2 k/ft)
P = 556 kN (125 kips)

Figure 2.2: Verification problem for minimum response in three-dimensional structural analysis per [1]

verification example includes design capacity checks, and as a result the structural analysis includes AISC's reduction to the modulus of elasticity (0.8E).

2.2.2 Computational Models

The main focus of this study was to compare analysis results and not a program specific algorithm. Table 2.1 provides abbreviations of the analysis models employed. SAP2000 and RFEM were used to represent an analysis in which members are assumed to have a doubly symmetric cross section with nonuniform torsion (warping) neglected. The default line (frame) element within each program, that utilize 6 degrees of freedom per element end, were used, and any additional options that allow for approximations of nonuniform torsion were not used, unless specifically mentioned below. The analysis of non-symmetric cross sections was completed with the use of MASTAN2 and Abaqus. Within MASTAN2, the

Table 2.1: Analysis results labels

Program	Analysis Element	Label
SAP2000	**D**oubly **S**ymmetric line element without warping	DS-1
RFEM	**D**oubly **S**ymmetric line element without warping	DS-2
RFEM Module [1]	**D**oubly **S**ymmetric line element with **W**arping	DS-W
MASTAN2	**N**on-**S**ymmetric line element with **W**arping	NSW-1
Abaqus	**N**on-**S**ymmetric line element with **W**arping	NSW-2
Abaqus	Shell element	Shell

[1] This module was used while evaluating the channel buckling in Section 2.3.2.

analysis models were completed with its 14 degree of freedom default line element, which permits the modeling of both symmetric and non-symmetric sections. Of the multiple line element options available in Abaqus, the B31OS line element [21] was utilized. Similar to MASTAN2, this element is a two node, three-dimensional open section element that includes warping effects. A key difference from MASTAN2 relevant to this study is that Abaqus employs integration within each load increment to obtain the element stiffness matrices.

The results of these line element models were compared with Abaqus shell element analysis results. A shell element model was chosen over a solid element because a shell element could accurately model members with a cross-section width to thickness ratio of 3 or larger [22]. The S4R shell element, which has a 4 node linear formulation with reduced integration, hour-glass control, and a general formulation that includes both thick and thin shell behavior [21], was employed.

Loading was applied as distributed loads on elements and discrete point loads on nodes in these models. For the purpose of mesh verification, the line element models were meshed from 2 elements to 64 elements with steps of a factor of 2 along the length of the member.

The shell element models were defined by the center line dimensions of the cross section. The I-beam members consisted of three planes of elements attached together to form the complete section. Modeling consideration was given to defining the cross-section profile with and without overlap at the flange to web intersections as shown in Figure 2.3a and b, respectively. Based on preliminary results, the overlapped profile was adopted because it best matched the thin-wall modeling techniques used within the line element models. The overlapped area also approximated the effect of fillets within rolled sections. Given that the results of the two-dimensional verification problems shown in Figure 2.1 are independent of modeling the end warping condition as free or fixed, the nodes at the end of the members were rigidly tied together as one. Although this provided a warping fixed condition, it allowed the end support to be defined by one reference node. When the end of the member

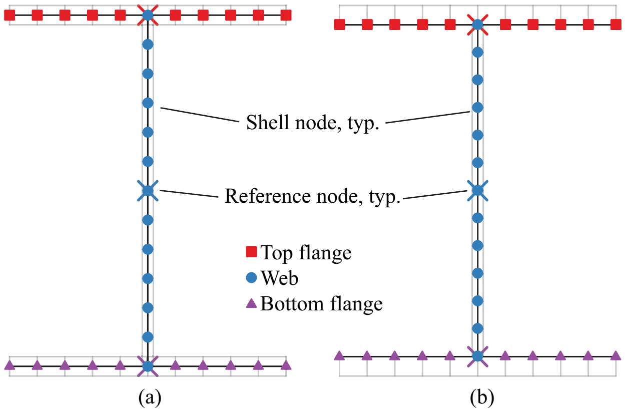

Figure 2.3: Shell model offsets in I-beam. (a) Overlapped web and flange alternative (b) No overlap alternative. Each node region represents a separate tie group.

needed to be modeled as warping free, per the beam in Figure 2.2, three rigid ties were assigned to the web and flanges separately as illustrated in Figure 2.3. An additional link was then defined to connect the translation of the two flange reference nodes to the reference node of the web, both of which are represented by an 'X' in the figure. This single node at the middle of the web then interacted with the whole cross section and also allows for boundary conditions and point loads to be easily defined. Distributed loading was applied as a series of point loads at all nodes on the neutral axis of the member based on the tributary length of the elements. For the purpose of mesh verification, the shell model was consistently subdivided into approximately square elements along the full length of the member. The resulting shell element mesh varied from 2 elements across the top flange using a seed value of 101.6 mm (4 inches) up to 128 elements with a seed value of 0.79 mm (1/32 inch). While the use of the extremely dense mesh would be impractical in most design applications, it ensured accurate results needed for these benchmark studies.

2.2.3 Model Verification

The verification analysis indicated that all of the structural analysis programs employed in this study were able to calculate the expected solutions to the example problems. Results for Beam 3 in Figure 2.1 are provided in Table 2.2, with additional results and discussion provided in [23]. Although the programs produced results that are slightly different than the “exact" solution based on the closed form solutions provided in [24], such solutions do not include the effects of the axial displacement and shear deformations. The results for the example in Figure 2.2 are summarized in Table 2.3. In this case, there are significant differences between the doubly symmetric analyses and the more sophisticated analyses. These differences are attributed to the program’s abilities or inabilities to model nonuniform

Table 2.2: Analysis results of Beam 3: a propped cantilever

Program	Exact [24]	DS-1	DS-2	NSW-1	NSW-2	Shell
P [kN (kip)]	Vertical Displacement at Midspan, Δ , [mm (in)]					
0	2.01	2.13	2.16	2.13	2.06	2.16
(0)	(0.079)	(0.084)	(0.085)	(0.084)	(0.081)	(0.085)
1334	2.26	2.44	2.44	2.44	2.34	2.44
(300)	(0.089)	(0.096)	(0.096)	(0.096)	(0.092)	(0.096)
2669	2.62	2.82	2.82	2.82	2.67	2.82
(600)	(0.103)	(0.111)	(0.111)	(0.111)	(0.105)	(0.111)
4003	3.07	3.35	3.38	3.35	3.18	3.35
(900)	(0.121)	(0.132)	(0.133)	(0.132)	(0.125)	(0.132)
5338	3.76	4.19	4.19	4.17	3.86	4.14
(1200)	(0.148)	(0.165)	(0.165)	(0.164)	(0.152)	(0.163)
P [kN (kip)]	Support Moment, M, [kN-mm (kip-in)]					
0	58.5	58.3	58	58.3	58.5	58.3
(0)	(235)	(234)	(233)	(234)	(235)	(234)
1334	64	64	63.8	64	63.8	64
(300)	(257)	(257)	(256)	(257)	(256)	(257)
2669	70.7	71.5	71.2	71.5	70.7	71.5
(600)	(284)	(287)	(286)	(287)	(284)	(287)
4003	80.2	81.7	81.5	81.7	80.2	81.7
(900)	(322)	(328)	(327)	(328)	(322)	(328)
5338	93.4	96.9	96.6	96.9	93.9	96.6
(1200)	(375)	(389)	(388)	(389)	(377)	(388)

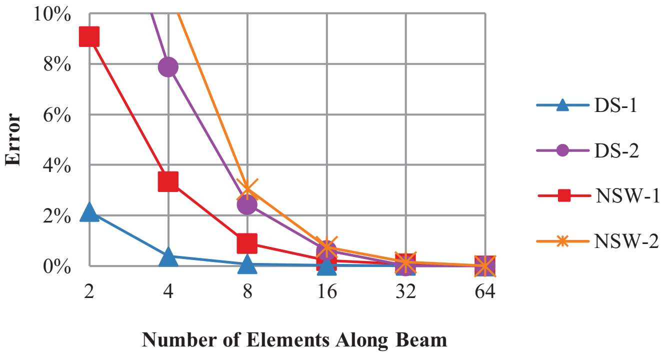

Figure 2.4: Deflection convergence for Beam 3 with P=5338 kN (1200 kip)

torsion. For programs that more accurately model twist, their results match well with the values presented in the commentary to the AISC Specification [1].

The convergence study on mesh refinement varied across structural analysis programs as well as with the applied loads. When a small axial load was applied in the Beam 3 example from Figure 2.1, the analysis displayed little nonlinearity and converged rapidly with minimal mesh refinement. On the other hand, and as shown in Figure 2.4, it was observed that at a large axial loading, which equaled 48% of the elastic in-plane buckling load, produced significant nonlinear behavior that required a finer mesh size to produce an accurate solution. For the line element models, it was found that the analyses were

Table 2.3: Three-dimensional structural analysis verification results

Program	Without Warping			Including Warping			
	AISC [1]	DS-1	DS-2	AISC [1]	NSW-1	NSW-2	Shell
	Case 1						
M_{ux}	594	594	594	598	595	597	597
[N-m (k-ft)]	(2386)	(2386)	(2386)	(2399)	(2389)	(2398)	(2398)
M_{uy}	64.3	64.3	64.3	13.9	18.2	14.2	15.7
[N-m (k-ft)]	(258)	(258)	(258)	(55.8)	(73)	(57)	(63)
δ_y	17.6	17.6	17.6	15	15	15.8	15.6
[mm (in)]	(0.694)	(0.694)	(0.692)	(0.589)	(0.589)	(0.624)	(0.615)
δ_x	24.6	24.6	24.6	5.44	5.41	5.59	6.3
[mm (in)]	(0.967)	(0.968)	(0.967)	(0.214)	(0.213)	(0.22)	(0.248)
θ (rad)	0.1078	0.1079	0.1079	0.0233	0.0231	0.0238	0.0265
	Case 2						
M_{ux}	308	308	307	308	308	308	308
[N-m (k-ft)]	(1235)	(1235)	(1234)	(1237)	(1235)	(1237)	(1237)
M_{uy}	47.8	48.1	47.6	34.9	35.9	35.6	36.9
[N-m (k-ft)]	(192)	(193)	(191)	(140)	(144)	(143)	(148)
δ_y	8.69	8.69	8.64	8.08	8.03	8.56	8.48
[mm (in)]	(0.342)	(0.342)	(0.34)	(0.318)	(0.316)	(0.337)	(0.334)
δ_x	21.2	21.2	20.9	15.6	14.9	16.1	16.7
[mm (in)]	(0.833)	(0.835)	(0.823)	(0.616)	(0.588)	(0.632)	(0.656)
θ (rad)	0.0471	0.0472	0.0467	0.0266	0.0242	0.0275	0.0297

exhibiting less than a 1% change to the solution when using a mesh size of at least 32 elements per member corresponding with 267 mm (10.5 in) segments. The shell element model was excluded from this figure because the minimum meshing condition, required to keep the elements approximately square, of 84 elements along the length of the beam was acceptable, especially given that only in-plane behavior was considered.

Although the mesh convergence of the line element models did not change substantially when introducing twisting effects, the convergence of the shell element model changed significantly. The twisting effects introduced variations in the stress across the flanges that required a significantly greater number of elements to minimize error. The three-dimensional example significantly increased convergence requirements, with the largest variation observed in Case 2 as shown in Figure 2.5. The strong axis moment and vertical deflection were found to have errors that quickly decreased, but the amount of twist and lateral displacement of the cross section required significantly more elements to converge. Mesh refinement for the shell element model was based on the moment equilibrium convergence, which was often controlled by the reference nodes of any rigid tie included. With less than 1% error to the 128-element solution, the study proceeded based on the 32-element result shown in Figure 2.5. This corresponded to using a minimum of 16 elements across a flange width for most of the non-symmetric sections considered in this study.

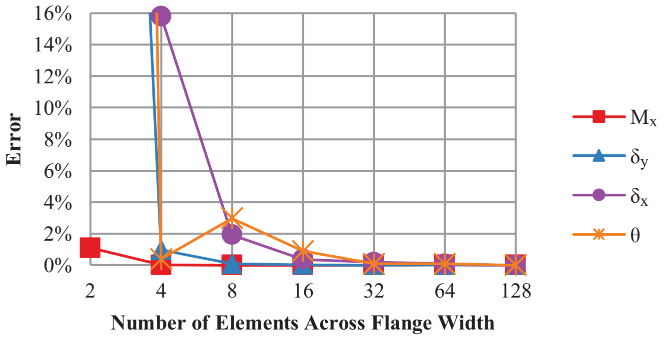

Figure 2.5: Shell model convergence in Case 2 of the three-dimensional analysis example

2.3 Member Modeling

Liu *et al.* [5], [6] showed that the new line element implemented in MASTAN2 was capable of modeling non-symmetric behavior excluded in doubly symmetric structural analyses. Their work included the lateral torsional buckling and deflection of simply supported monosymmetric I-beams, the deflection of cantilevered channels, and the buckling of angles under compression. Rather than repeating those previous models to obtain a baseline comparison, three new single member examples were considered for this study: an angle subjected to torsion, channel buckling, and Z-section bending. While the examples and discussion thus far have focused on hot-rolled steel sections, the main interest in this study is non-symmetric sections with compact, linear elastic behavior. As a result, priority was given to existing examples of any material over novel alternatives with hot-rolled steel sections. Each example was selected based on the presence of a distinct behavior observed in non-symmetric members.

2.3.1 Pure Torsion on an Angle

A single member subjected to equal and opposite end torques is one of the simplest twisting problems that can be solved. The twisting of a noncircular section introduces warping as the cross section will not remain planar. In the absence of a end warping restraint, the warping results in helical deformations across the section. For example, an I-beam section would shorten as the member twists about the concentric shear center and centroid to avoid developing a net tension [25]. This twisting response is further complicated in a non-symmetric section as the location of the shear center moves laterally as depicted in Figure 2.6 for an equal-leg angle. The helical strains from twisting of the equal-leg angle induce an axial and weak axis bending response based on equilibrium requirements, which was experimentally verified by Gregory [26]. Attard [27] found a similar relationship for non-doubly symmetric sections using nonlinear torsion theory. The movement of the shear center of a singly symmetric section is given by,

$$V = \beta_1/2(1 - \cos\theta) \tag{2.1}$$

$$W = \beta_1/2(\theta - \sin\theta) \tag{2.2}$$

where V is the displacement parallel to the plane of symmetry, W is the displacement perpendicular to the plane of symmetry, β_1 is the Wagner coefficient, and θ is the total twist of the section. The Wagner coefficient is defined as,

$$\beta_1 = \frac{1}{I_w} \int_A (v^3 + vw^2) dA - 2v_s \tag{2.3}$$

where (v, w) are the coordinates with reference to the principal axes, I_w is the weak axis moment of inertia, and v_s is the coordinate of the shear center. Eq. 2.1 and Eq. 2.2 are slightly different from the ones presented by Gregory and by Attard as the definition of β_1 was updated to match MASTAN2 and CUFSM [28].

Based on the experiment by Gregory [26], this example considered a 177.8 mm long, equal-leg brass angle subjected to pure torsion, with the cross section shown in Figure 2.7. Material properties used were a modulus of elasticity of 89,660 MPa and a Poisson's ratio of 0.44 [27]. The cantilevered angle was subjected to a 100° rotation. The ends of the angle were free to warp so that the member was in pure torsion.

The line element models were meshed with 64 elements measuring 2.78 mm. A vertical rigid link was included between the end node and shear center to track its position.

The shell element model was meshed with 30 elements per leg using a seed size of 0.487 mm. The warping free, cantilever support was achieved by restraining torsion and both transverse shears for all end nodes. To provide the axial and moment support, the nodes at the heel and tips of the angle were longitudinally restrained. The end rotation was specified using a reference point at the centroid tied to the same three nodes.

The resulting shear center displacements are shown in Figure 2.8 in addition to the solution provided in Eq. 2.1 and Eq. 2.2 utilizing a thin-walled approximation, $\beta_1 = \sqrt{2}(14.61 \text{ mm})$. The two very distinct displacement patterns were expected. The solutions from DS-1 and DS-2 are accurately displaying the doubly symmetric assumption that the section would rotate about the centroid, which is assumed to be the shear center. As a result, the plot is showing the circular path around the centroid with the first movement in the W-direction. While this response is completely different from the non-symmetric

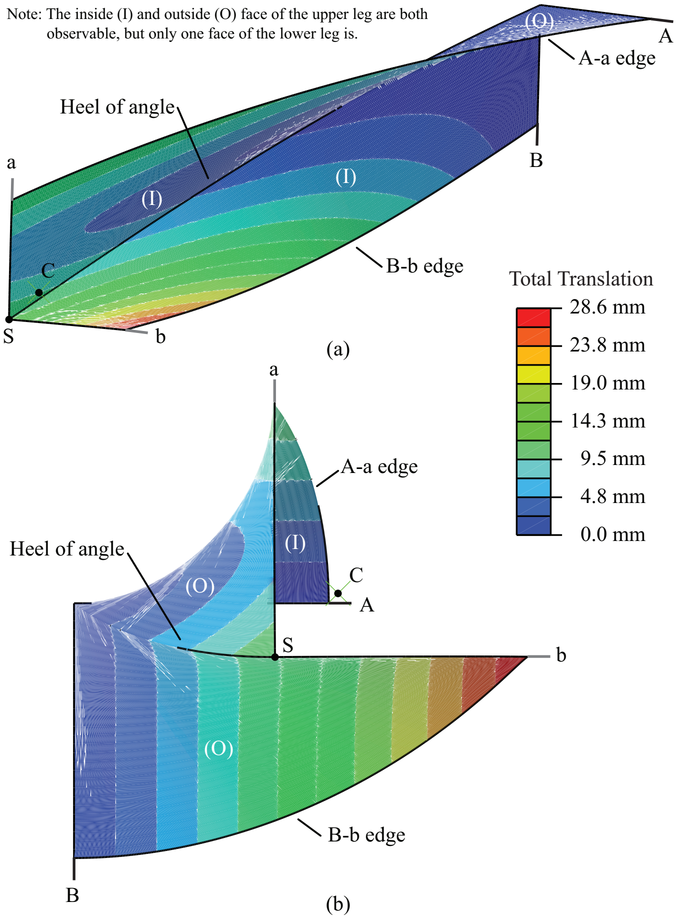
Note: The inside (I) and outside (O) face of the upper leg are both observable, but only one face of the lower leg is.

To aid in perspective, the angle has been rotated so that legs are vertical and horizontal at the start and end position. Deflections are a 1:1 scale relative to the angle.

Figure 2.6: Overall response of angle subjected to 90° twist. (a) Three-dimensional overview (b) Profile view of twisting response

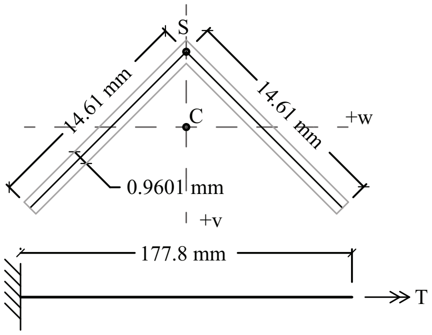

Figure 2.7: Equal-leg angle subjected to pure torsion

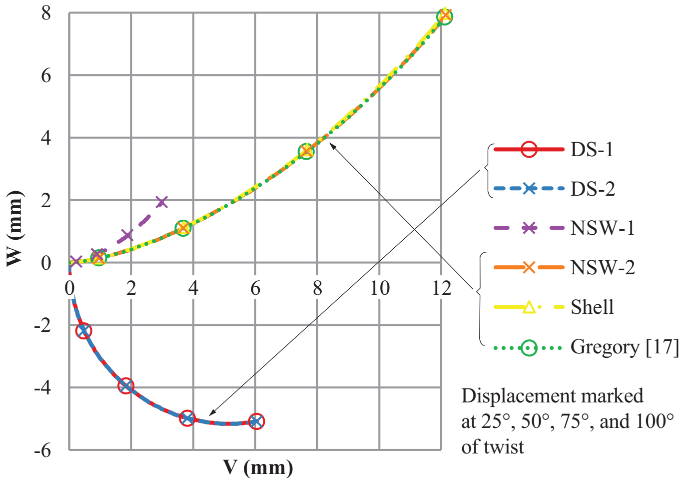

Figure 2.8: Shear center displacement of an equal-leg angle subjected to pure torsion

behavior in the *W*-direction, the *V*-direction displacement corresponds to approximately 50% of the non-symmetric result for the equal-leg angle.

The more sophisticated analyses captured the different center of rotation and resulting cycloid-shaped deformation presented in the benchmark solution from Gregory. The NSW-2 and shell element analyses captured the complex axial equilibrium condition. As a result, the NSW-2 displacements exhibited less than 0.8% error, whereas the shell element model errors were 0.5% in the *V*-direction and 3% in the *W*-direction. Though the results from NSW-1 exhibited the correct general behaviors, the deformation was observed at 25% of the expected response. Investigation into the discrepancy between NSW-1 and NSW-2 identified the helical strain term as an important factor. If the NSW-2 analysis was altered by replacing the integration of the stiffness matrix in each step with a stiffness matrix defined once at the start of analysis, which alters how the helical strain component effects the cross section, the displacement of the shear center would be zero. This alternative analysis captured the appropriate center of rotation while missing any additional bending effects that cause translation of the shear center. The proper evaluation of twisting in elements with non-symmetric sections requires interaction with axial and bending effects that are excluded in simpler models. Lastly, it is noted that this evaluation is for an unrealistic maximum twist for common structural systems. At a more realistic extreme twist of 10°, the nonlinear shear center displacement would only be 0.16 mm representing a fraction of the displacements depicted in Figure 2.8.

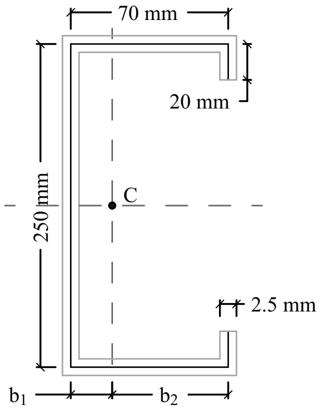

Force at first yield
$P = 370.9$ kN
$M_s = 27.74$ kN-m
$M_w = 4.748$ kN-m

Figure 2.9: Lipped channel dimensions

2.3.2 Stability of a Lipped Channel

The second example was selected to investigate non-symmetric member stability. A lipped channel was subjected to a series of different loading combinations at different lengths to consider a range of global buckling responses. The different loading combinations included variations to address non-symmetric loading conditions as well. The full buckling response of this thin-walled section includes local and distortional effects in addition to the flexural and torsional responses associated with global buckling. These complex buckling modes can be identified using CUFSM [28] under various loading conditions. However, typical line elements are not capable of including the local and distortional buckling response. The global buckling behavior, considering only flexural, torsional, and combined effects, can be calculated using the solution presented by Cheng *et al.* [29] for a lipped channel.

Figure 2.9 shows the dimensions of the lipped channel. The channel was modeled with a modulus of elasticity equal to 203 GPa, a Poisson's ratio of 0.3, and a yield stress of 345 MPa. The channel was evaluated as a simply supported member with no end warping restraint for two different lengths, 3 m and 12 m, subjected to eight different loading combinations. The loading combinations, listed in Table 2.4, are a fraction of the load necessary for first yield of the channel due to uniform compression (P), a strong axis moment (M_s), and a weak axis moment causing compression at the lips on the channel (M_w).

Since the expected line element solution will only include global behavior, the reference solution for this comparison was based on the approach provided by Cheng *et al.* To ensure the accuracy of this reference solution, the critical load factor for each scenario was calculated using both CUFSM and Cheng's approach with results summarized in Table 2.4. The two methods obtained nearly identical results for the 12 m examples where global buckling dominated behavior. As expected, the results of the 3 m examples exhibited some variation due to the influence of local and distortional buckling effects captured by CUFSM.

Table 2.4: Lipped channel buckling factors

Case		1	2	3	4	5	6	7	8
Method	L (m)	P	M_s	M_w	$0.5P+ 0.5M_s$	$0.5P+ 0.5M_w$	$0.5P+ 0.25M_s+ 0.25M_w$	$0.5M_s+ 0.5M_w$	$0.5M_s- 0.5 \cdot b_2/b_1 \cdot M_w$
CUFSM	N/A[1]	0.303	1.400	2.085	0.587	0.917	0.721	1.800	0.592
CUFSM	3	0.411	0.663	1.633	0.530	0.727	0.632	1.089	1.988
CUFSM	12	0.027	0.062	0.228	0.044	0.054	0.050	0.109	0.179
Cheng	3	0.431	0.670	1.676	0.538	0.731	0.640	1.101	2.284
Cheng	12	0.027	0.062	0.228	0.044	0.054	0.050	0.109	0.180

[1] Length varies as this row provides the critical local or distortional buckling value.

Table 2.5: Lipped channel buckling with L = 3m. Error versus Cheng's solution [29]

Program/Case	1	2	3	4	5	6	7	8
DS-1	-2.9%	-54.3%	N/A	-48.0%	11.9%	-30.1%	-66.5%	-80.1%
DS-W	-0.9%	-1.2%	7157%	-1.2%	16.7%	7.9%	46.2%	-66.6%
NSW-1	0.0%	0.0%	0.1%	0.0%	1.0%	0.2%	0.0%	0.0%
NSW-2	-0.2%	-0.1%	-12.7%	-0.2%	17.6%	4.8%	21.5%	-41.9%
Shell	-30.9%	-1.1%	-6.7%	-1.4%	-1.4%	-1.5%	-2.0%	-75.5%

The consistency of the results for both lengths validated the use of Cheng's approach as the benchmark.

The lipped channel was evaluated for all scenarios within each structural analysis program. A simply supported member was subdivided into 64 line elements with the ends restrained for torsion and free to warp. The members were loaded at both ends with equal and opposite magnitudes. The solutions for NSW-1 and NSW-2 were obtained from an eigenvalue buckling analysis. An eigenvalue buckling analysis, DS-W, was also completed with a doubly symmetric cross section, which required the inclusion of some nonuniform torsion to include moments. Since not all structural analysis programs can complete an eigenvalue buckling analysis including moments, the results of DS-1 were found by incrementally increasing the applied load. For this method to capture buckling, the model was altered with an initial lateral imperfection of L/2000. Failure was defined in a stable post buckling condition when the incremental displacement was found to be at least 1000 times the initial displacement rate. In an unstable condition, failure was defined at the maximum applied load when the model failed to converge after exhibiting an eigenvalue corresponding to negative stiffness or growing displacements near midspan.

The shell element model was meshed with a seed size of 2.5 mm resulting in 172 elements around the perimeter of the channel. The requirement that the end of the channel was free to warp necessitated that the end of the member could not be tied together. As a result, the load was applied directly to the shell elements as distributed edge loads for the linear buckling analyses.

Table 2.6: Lipped channel buckling with L = 12m. Error versus Cheng's solution [29]

Program/Case	1	2	3	4	5	6	7	8
DS-1	-3.4%	-28.7%	N/A	-16.1%	-2.5%	-7.6%	-4.8%	-38.1%
DS-W	0.0%	-0.4%	3447%	-0.2%	0.0%	1.0%	29.8%	-52.9%
NSW-1	0.0%	0.0%	0.1%	0.0%	0.0%	0.0%	0.0%	0.0%
NSW-2	0.0%	0.0%	-40.3%	0.0%	0.0%	0.6%	14.1%	-31.2%
Shell	-0.1%	-0.5%	-4.7%	-0.3%	-0.1%	-0.2%	-1.1%	1.0%

The results summarized in Table 2.5 and Table 2.6 indicate that it was not possible to capture all buckling responses when using doubly symmetric analysis, even considering nonuniform torsion. Results from both DS-W and DS-1 were reasonably accurate for situations controlled by flexural buckling. DS-W captured some torsional effects, but DS-1 consistently underestimated capacity in these situations. The missing weak axis moment result for DS-1 was not surprising as the initial imperfection was aligned with the resulting deformation. Repeating the buckling evaluation with a modified vertical initial imperfection might have caused an instability to develop. However, this result was left to highlight the challenges with this analysis type. Neither analysis was able to identify buckling modes that included non-symmetric behavior.

The more sophisticated methods were better able to calculate the buckling behavior. The analysis from NSW-1 agreed very well with the anticipated solutions. The NSW-2 line elements performed better than the doubly symmetric results, but discrepancies were still found in the presence of weak axis moment. These errors were attributed largely to the limitations of the analysis type used. The use of a linear buckling analysis excluded the recalculation of the stiffness matrix. Similar to the torsion example, this alteration reduced the ability of this line element to capture the nonlinear behavior of the non-symmetric section. A nonlinear buckling analysis, akin to the one completed with DS-1, could have possibly addressed these issues but was not completed.

The shell element modeling accurately captured the global features as well as local and distortional buckling. However, as this study used a global buckling baseline only, this led to the large errors in Table 2.5. It should be noted that the shell results agreed with the local and distortional buckling limits identified by CUFSM, which were provided in Table 2.4. Significantly smaller errors of -2.0% and -5.4% were observed for Case 1 and Case 8, respectively, between the shell model results and CUFSM.

The above results provided some evidence for the importance of non-symmetric section properties; however, it was difficult to identify the range of importance. In an attempt to isolate this effect in buckling, a comparison of the non-symmetric buckling capacity from the method in Cheng *et al.* [29] and the analytical equation for the interaction of moment and axial force for buckling about the perpendicular axis was completed for both the strong

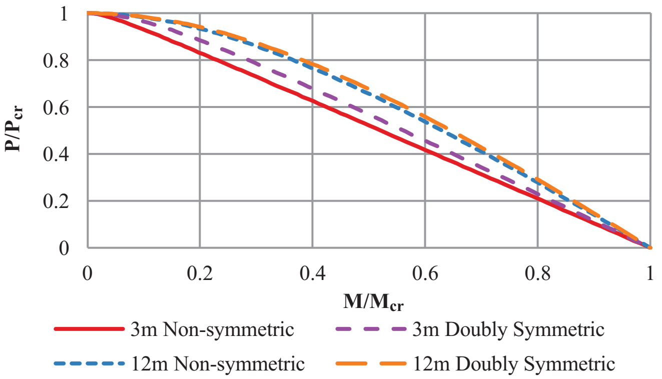

Figure 2.10: Buckling behavior with axial and strong axis moment loading

and weak axis [30]. The critical buckling load in the presence of a strong axis moment, P_{crs}, is given by,

$$P_{crs} = \frac{P_t + P_s}{2} - \sqrt{\frac{(P_t - P_s)^2}{4} - P_t P_s + \frac{M_j^2 A}{I_w + I_s}} \tag{2.4}$$

where,

$$P_t = \frac{GJ + \pi^2 E C_w / L^2}{(I_w + I_s)/A} \tag{2.5}$$

$$P_s = \frac{\pi^2 E I_s}{L^2} \tag{2.6}$$

where E is the modulus of elasticity, G is the shear modulus, J is the torsional constant, C_w is the warping constant, L is the length of the member, A is the cross-sectional area, I_w is the weak axis moment of inertia, I_s is the strong axis moment of inertia, and M_j is the moment applied. To calculate the critical buckling load in the presence of a weak axis moment, P_{crw}, the references to the strong and weak axes in Eq. 2.4-2.6 need to just be inverted.

Using these relationships, it was possible to produce the axial-moment buckling interaction for all combinations of loading about the strong axis, Figure 2.10, and the weak axis, Figure 2.11. The plots have been normalized to the critical buckling load to accommodate multiple lengths. While the critical buckling load for compression and strong axis moment were not affected by the non-symmetric versus doubly symmetric assumption, the weak axis moment buckling behavior was changed. Ignoring the effects of non-symmetric properties causes the critical buckling load, $M_{w,cr}$, to increase from $1.676 M_w$ to $14.64 M_w$ for the 3 m length and from $0.228 M_w$ to $1.361 M_w$ for the 12 m length. As shown in both figures, the inclusion of non-symmetric properties changed the stability behavior over the

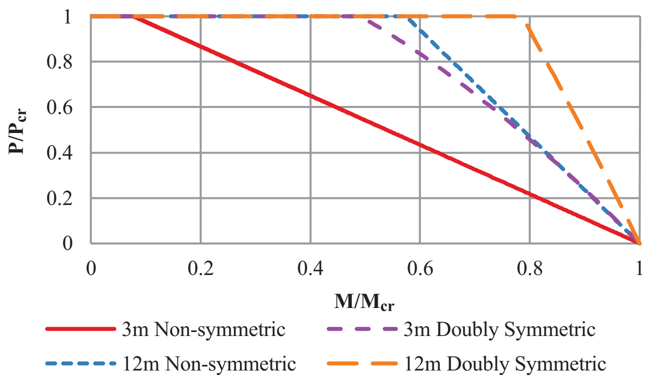

Figure 2.11: Buckling behavior with axial and weak axis moment loading

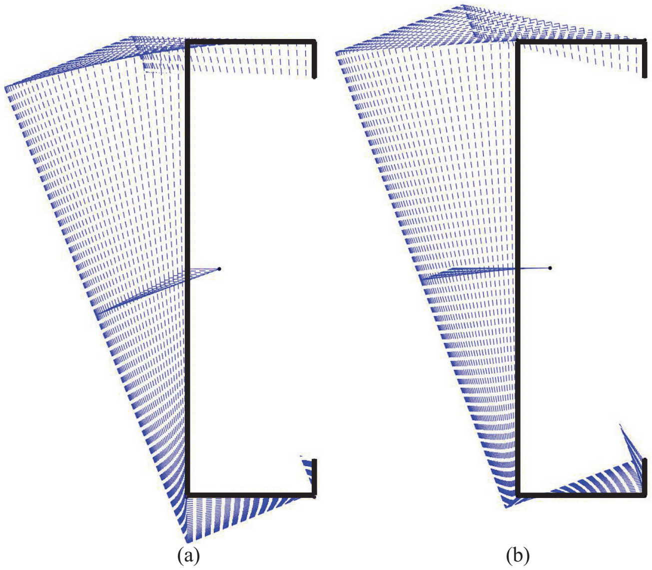

Figure 2.12: End view of the buckled shape of a lipped channel under combined axial force and strong axis moment based on Case 4. Scale factor ×100 (a) Non-symmetric response. (b) Doubly symmetric response

entire ratio of applied loads. A doubly symmetric buckling response was overestimating the non-symmetric response by up to 5.5% which decreased as the beam length increased. This different response was also visible in the buckled geometry as the non-symmetric model was observed to have greater twist and a more lateral movement than the doubly symmetric model as illustrated in Figure 2.12. In contrast, the weak axis moment response was quite different based on the underlying behavior as seen in Figure 2.11. Once a large enough weak axis moment was applied, a combined response controls over the axial effects alone. The exclusion of the non-symmetric properties delayed this interaction while also increasing the allowable applied moment.

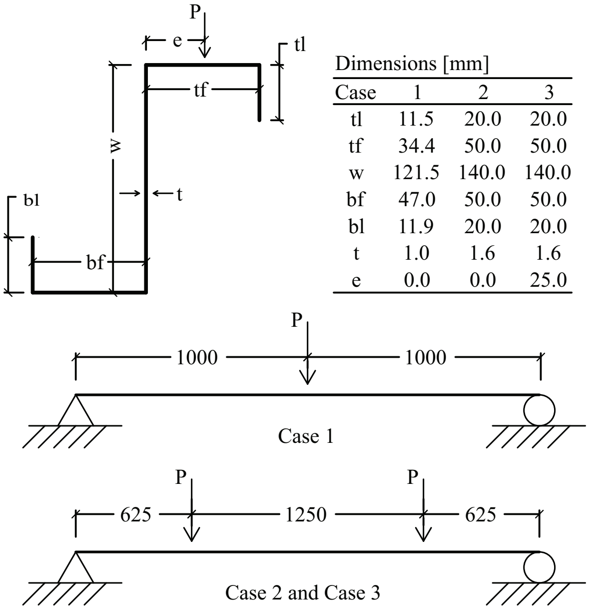

Dimensions [mm]

Case	1	2	3
tl	11.5	20.0	20.0
tf	34.4	50.0	50.0
w	121.5	140.0	140.0
bf	47.0	50.0	50.0
bl	11.9	20.0	20.0
t	1.0	1.6	1.6
e	0.0	0.0	25.0

Figure 2.13: Z-section dimensions and loading configuration

2.3.3 Simply Supported Z-Section

Members with non-symmetric sections subjected to bending will exhibit displacements in the plane of the applied load as well as the perpendicular direction whenever the load does not align with the principal axes of the section. In the deformed position, any applied transverse loading will introduce torsion along the length of the member. This combined bending response was the driving motivation behind the series of simply supported Z-section beams. Moore [31] provided references to two previous sets of experimental results comprising three tests of an unrestrained Z-section member as well as a nonlinear beam theory evaluation of those tests. Figure 2.13 shows the geometry and loading configuration for the members considered. The first case was a 2 m, unequal flange Z-section subjected to a single point load at midspan. The other two experiments subjected a 2.5 m, equal flange Z-section to equal point loads at the quarter points on the top flange at either the web or middle of the flange. The ends of the beams were assumed to be fixed for torsion, but free to warp. The modulus of elasticity was set to 203 GPa (29,500 ksi) and the Poisson's ratio to 0.3 based on typical AISI values for all models [32].

The shell element model was constructed as shown in Figure 2.14. A rigid tie was defined over the height of the web to distribute any incidental axial reactions. This web tie and all remaining end nodes were restrained for translation in the vertical and lateral directions as well as torsional rotations. At the point load locations, another rigid tie was defined to connect the web and top flange of the Z-section to distribute the applied load. The member was meshed with a seed size of 1 mm in all directions.

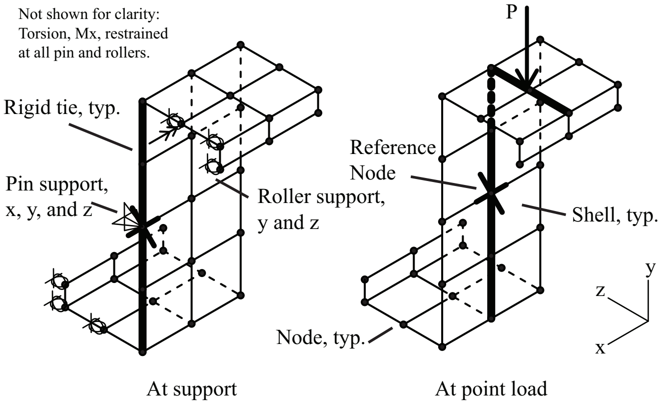

Figure 2.14: Typical shell modeling at support and at point load

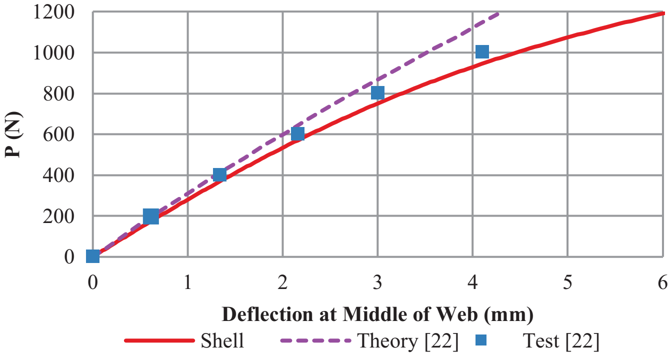

Figure 2.15: Vertical deflection at the middle of web at midspan of Case 1

The original examples were provided with limited information on the support details and the material properties. Based on this limitation and the good agreement between the shell element models and anticipated behavior in the previous sections, the values from [31] were used as guidance for validation of the overall behavior of the shell element model, which would then be defined as the benchmark. The shell element analysis was exhibiting similar nonlinear deformations compared to the experimental results and Moore's reference theory as shown in Figure 2.15 where the shell model results were consistently larger. The greatest discrepancies occurred in Case 3 with the eccentrically applied loading. Nevertheless, the shell element analysis captured the reduced stiffness and increasing vertical deflection of the example as shown in Figure 2.16. Other minor discrepancies existed; however, without additional details of the original experimental set-up it was determined that the shell element analysis as completed was an acceptable benchmark.

The line element analysis was completed with an initially straight member meshed into 64 elements. To simulate the shell element loading condition, the line element models were analyzed with either a point load and equivalent initial torsional moment applied to the

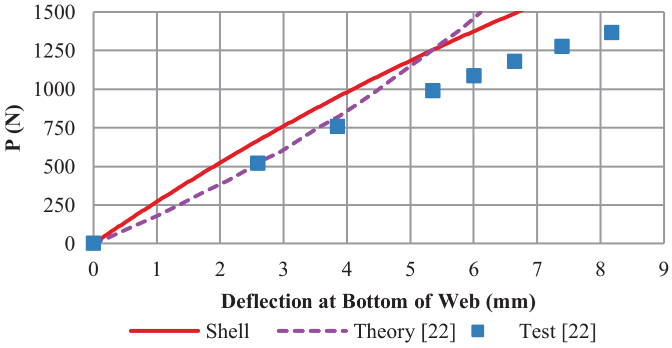

Figure 2.16: Vertical deflection at the middle of web at midspan of Case 3

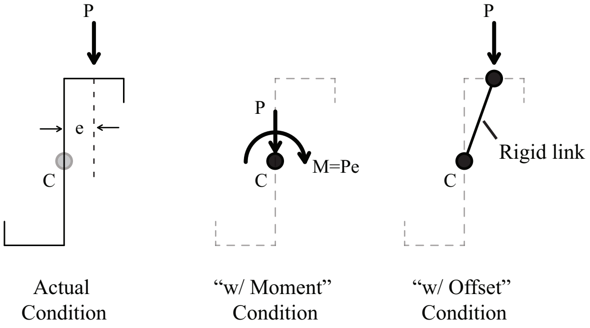

Figure 2.17: Loading applied to channel in line element models

centroid, 'w/ Moment', or a point load applied at the end of a rigid link connecting the beam model and the point where the load was actually located, 'w/ Offset', as depicted in Figure 2.17. The vertical deflections from Case 2 using both loading methods are shown in Figure 2.18. For clarity, only one set of results is shown for DS-1 and DS-2 and another set for NSW-1 and NSW-2 since the results were visually similar as confirmed by Table 2.7. The evaluations 'w/ Moment' excluded additional second-order effects due to the twisting of the cross section that were captured in the evaluations 'w/ Offset'. Making use of the rigid link instead of the discrete moment in NSW-1 and NSW-2 reduced the calculated maximum displacement errors from 25% to 5%. Looking at Case 2 where the second-order evaluation introduced torsion, the sophisticated line elements from NSW-1 and NSW-2 where able to capture the expected displacements with 1.0% error. In the presence of an initial torsion, Case 3, the methods still were able to perform well with errors of 3.3% and 1.2% for NSW-1 and NSW-2, respectively. In contrast, the doubly symmetric analyses predicted significantly larger than expected deformations. While reasonable solutions could be seen at low load levels, the displacements rapidly increased, to more than 3.5 times the expected answer in some instances.

Despite the large deflections, the individual deformations from doubly symmetric anal-

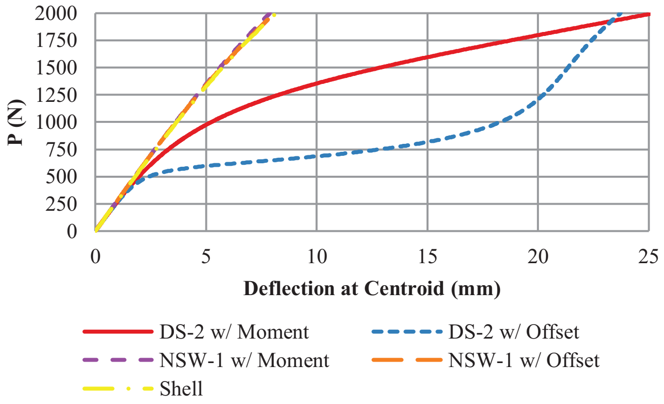

Figure 2.18: Vertical deflection of the centroid at midspan of Case 2

Table 2.7: Error in vertical deflection of the centroid at midspan of Case 2

Program	DS-1 w/ Moment	DS-2 w/ Moment	NSW-1 w/ Offset	NSW-2 w/ Offset	Shell
P (N)	Error				Reference (mm)
500	8.87%	9.13%	-1.01%	-0.50%	1.800
1000	42.1%	42.4%	-0.97%	-0.54%	3.679
1500	124%	124%	-0.86%	-0.70%	5.745
2000	184%	209%	-0.61%	-1.01%	8.164

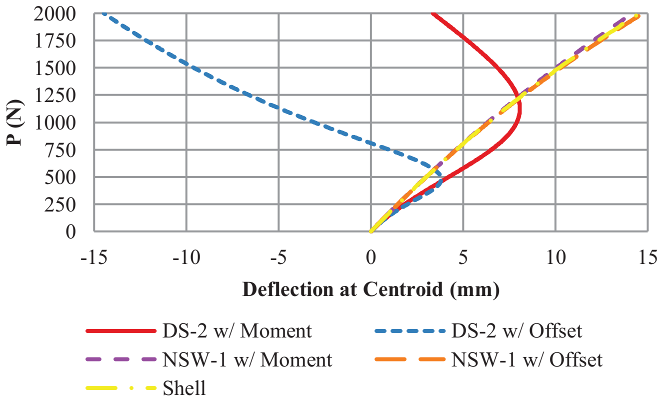

Figure 2.19: Lateral displacement of centroid at midspan from Case 3

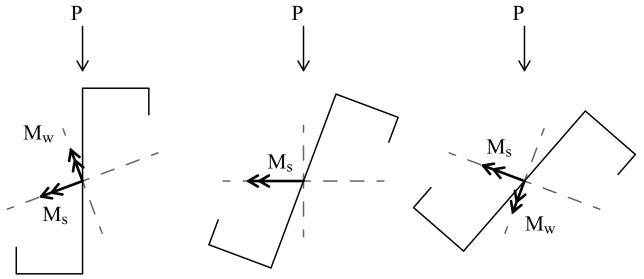

Figure 2.20: Principal moments considering member twist

yses were not always conservative. For example consider Case 3, the lateral displacement started in the anticipated direction in a conservative manner as shown in Figure 2.19. However as the loading increased, the lateral deformation of the beam could be observed to suddenly reverse. In these instances, the additional rotation of the cross section caused the local beam displacement to change from downwards and to the right to downwards only and eventually started moving back to the left due to the redistribution of the principal axis moments (as depicted in Figure 2.20). This type of behavior would not have been able to occur until a much higher loading if the total rotation was more accurately captured. Lastly, the unequal flange Z-section of Case 1 provided another interesting situation. While the centroid would continually move downward, the combination of rotation and translation indicated that the middle of the web would stop moving downwards around a load of 560 N and begin moving upwards. Without proper consideration of what led to this response, this displacement could cause a concern. For instance, if an engineer was concerned about a pipe or other element passing through the web of a member and taking unintended loading, this calculated deflection could result in a hole being incorrectly located or sized.

2.4 System Modeling

The proper evaluation of structural systems relies not only on the accurate evaluation of an individual member but also the interaction of various components. The analysis procedure needs to account for compatibility while distributing loading according to the stiffness of each member. This member to member interaction is complicated by the behavior of non-symmetric sections shown above. Therefore, this study considered that behavior by investigating a series of portal frames with non-symmetric sections.

The portal frames utilized for this study were based on the frames originally used by El-Zanaty *et al.* [33] since the authors were not able to identify any experimental testing of non-tapered mono-symmetric I-beams in a system. Rosson [34] and Ziemian and McGuire [35] have used frames based on El-Zanaty's initial work to validate various inelastic analysis results. While this investigation is limited to an elastic analysis, these frames exhibited preferable behavior including minimal force redistribution and minimal buckling effects due to the compactness of the cross sections.

Figure 2.21 depicts the modified portal frame which has equal length beam and columns with a given L/r ratio. The beam and column bottom flange, t_b, was varied among 12 mm, 18 mm, and 24 mm to introduce non-symmetry to the cross section. Similar to the analysis completed by Ziemian and McGuire [35], the columns were oriented in weak axis bending with the variable flange in the positive z-direction while the beam was oriented in strong

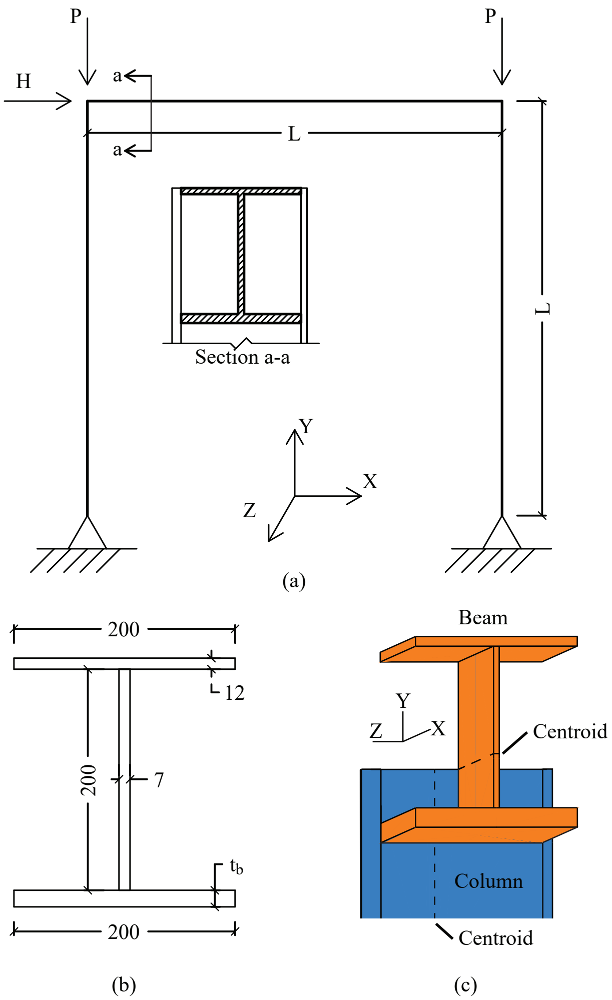

Figure 2.21: Modified portal frame for mono-symmetric system. (a) Elevation view with section (b) Mono-symmetric cross section (c) Three-dimensional view of joint alignment

axis bending with the variable flange down. The beam and columns were modeled with the beam flange aligned with the column web as shown in Figure 2.21c which causes an eccentricity between the beam and column centroids when t_b was greater than 12 mm. This combination of geometry and the strong and weak axis bending caused the frame to exhibit out-of-plane movements without an initial imperfection when subjected to the lateral loading, H. The ends of all members were treated as fixed for warping. The top of each column was supported with a roller in the out-of-plane direction. The bottom supports were treated as simple pins and pins with y-axis moment restrained.

The portal frames were first loaded with the axial load, P, and then subjected to the lateral load, H. The loading varied according to Table 2.8 where $P_y = F_y A$ using a thin-walled approximated area for A. The frame was modeled with the modulus of elasticity as 0.8(200) GPa, the Poisson's ratio as 0.3, and the yield stress as 345 MPa. The modulus

Table 2.8: Portal frame loading schedule

Case	1		2	
L/r	P	H	P	H
40	0 kN	240 kN	$0.4P_y$	120 kN
60	0 kN	160 kN	$0.2P_y$	80 kN
120	0 kN	80 kN		

of elasticity was reduced inline with requirements of the AISC Specification [1], which accounts for some residual stress and partial yielding, to encourage amplified deformations. No other stiffness modifications were incorporated into the model.

2.4.1 Frame Model Construction

The line elements models were created with three straight, full length members meshed into 50 elements.To accommodate the offset highlighted in Figure 2.21c, a single horizontal rigid link connected the end nodes of the beam and column without the use of member offsets. Additional nodes were defined in the NSW-2 model at relevant centroid locations which were then rigidly tied to the origin of the cross section.

The shell element model was constructed of three identical I-beam members which were modeled in accordance with the method in Section 2.2.2. The end of each beam was similarly fixed for warping using a rigid tie at the centroid. In addition to the benefits noted earlier, this rigid tie allowed for a rigid joint at the corner of the portal frame as well as equal member lengths between the shell and line element models. This modeling approach replaced the realistic column-beam joint behavior with a rigid connection that allowed for a better comparison to the rigid connection line element models. The I-beam model was meshed with 100 elements across the flange using a seed mesh size of 2 mm.

2.4.2 Frame Results

The overall frame stability was dominated by in-plane behavior which was controlled by the weak axis buckling of the column. The controlling buckling mode of the column was technically a combined flexural-torsional failure but could reasonably be approximated by just the weak axis flexural buckling mode with less than a 1% error. As a result, the evaluation of these frames by all analysis methods found similar dominant behavior for lateral deformations, in-plane shear reactions, and vertical reactions as shown in Figure 2.22.

All structural analysis methods employed captured some out-of-plane behavior due to the offset between the beam and column centroids. However, the response observed in

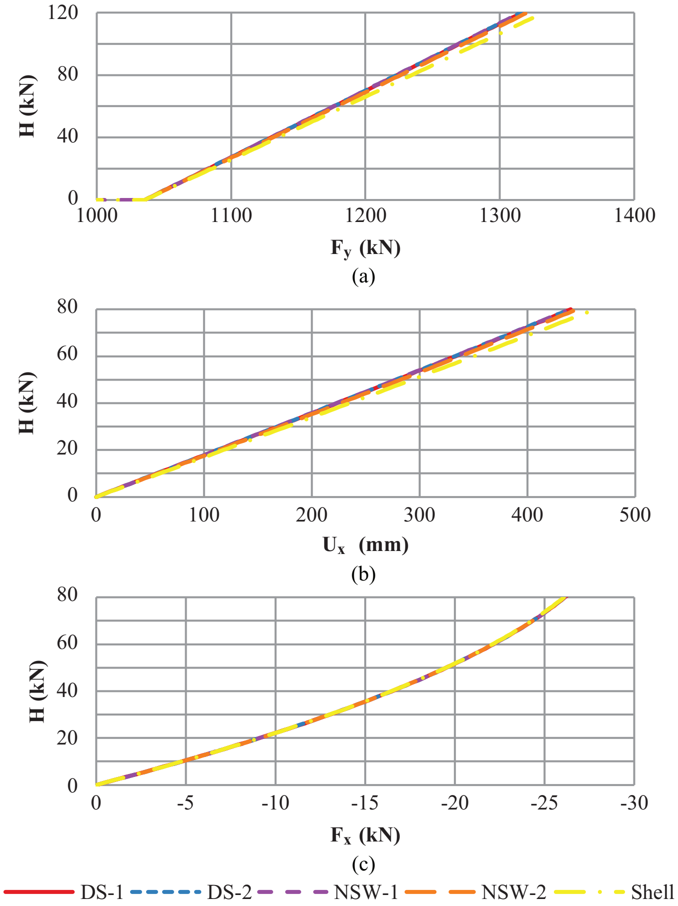

Figure 2.22: Consistent in-plane behavior of portal frame. (a) F_y at the right column base for Case 2 with torsion released, $L/r = 40$, and $t_b = 18$ mm; (b) U_x at the top of the right column for Case 2 with torsion fixed, $L/r = 60$, and $t_b = 18$ mm; (c) F_x at the right column base for Case 1 with torsion fixed, $L/r = 120$, and $t_b = 24$ mm

the doubly symmetric analyses were not consistent with the more sophisticated analyses. For example, the z-direction displacement at the middle of the columns was observed to vary considerably. As shown in Figure 2.23, the left column exhibited similar displacement patterns while underestimating the magnitude in the doubly symmetric analyses. The right column displayed more complex displacement, depicted in Figure 2.24, that was completely missed in the doubly symmetric results. The non-symmetric line elements were better able to capture this displacement; however, as the twist of the column increased as shown in Figure 2.25, a greater variation was observed with the results from NSW-1.

The column twisting varied significantly with reduced deflections observed in the doubly symmetric analysis as shown in Figure 2.26. Despite the more sophisticated methods including the additional stiffness from warping, the twist of the column was increased in these methods due to the consideration of other non-symmetric effects including the longer moment arm for the lateral load. The column twist variations still existed when the base

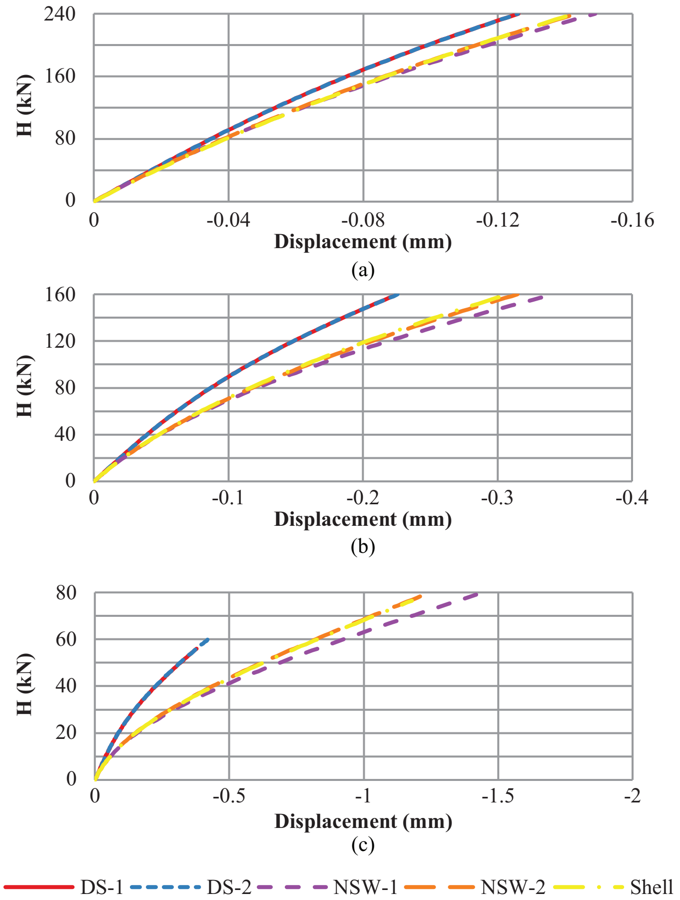

Figure 2.23: Z-displacement at midheight of left column centroid under Loading Case 1 with torsion released, $t_b = 18$mm, and L/r = (a) 40 (b) 60 and (c) 120

torsion was restrained. Akin to the response in Figure 2.26, the more sophisticated methods captured larger torsion reactions with similar agreement. The doubly symmetric analyses captured a reduced torsion reaction with the additional discrepancy that the reaction was in the opposite direction. The torsional restraint was also noted to affect the reaction at the top of the columns. The lateral supports were initially found to be consistent while the base was free to twist, but the torsion restraint caused a significant reduction in the lateral reaction observed in the doubly symmetric analyses compared to the other methods.

2.5 Discussion

Many common structures that engineers encounter can often be evaluated with two-dimensional structural analysis. This simplified approach captures the necessary behavior to meet the requirements of the design standard whether it be Eurocode 3, AS4100, AISC 360, or another. When the structure becomes more complex, for example with either out-of-

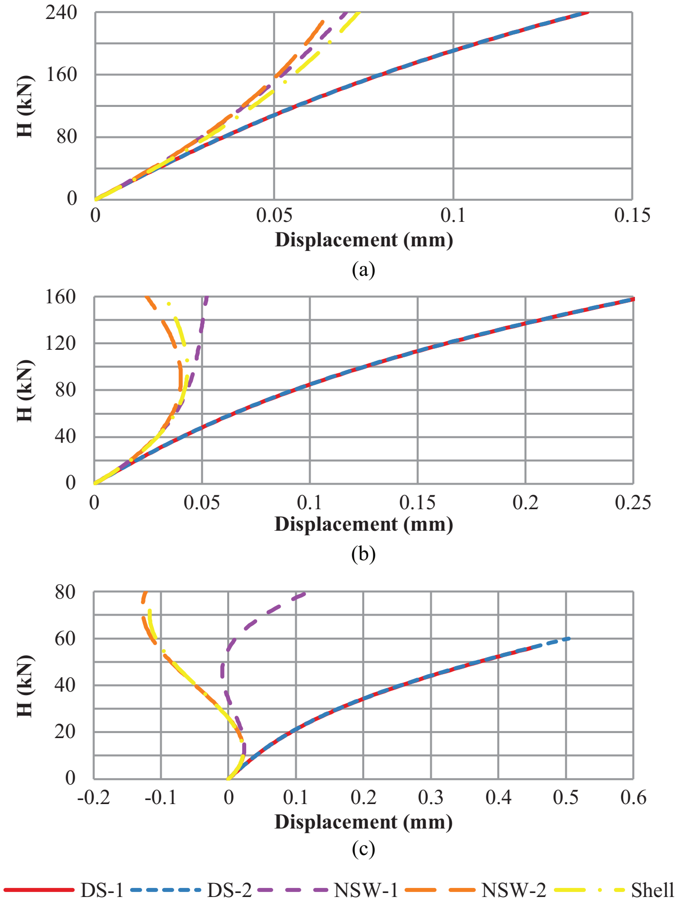

Figure 2.24: Z-displacement at midheight of right column centroid under Loading Case 1 with torsion released, t_b = 18mm, and L/r = (a) 40 (b) 60 and (c) 120

plane loading or the use of non-symmetric sections, the engineer needs to critically consider what improvements to the analysis are required. The emphasis of two-dimensional behavior in the AISC Specification places the onus of these decisions on the engineer. If an engineer determines that an acceptable analysis includes P-δ and P-Δ as the only second-order effects, they could conclude that the first-order and second-order results are identical in the absence of axial loading. Using Case 2 from Section 2.3.3 as an example, the analysis would consist of a beam subjected to bi-axial bending from the 2000 N load. The engineer would determine first-order deflections of 7.1 mm downwards and 11.4 mm to the right. While this solution is reasonably close to the detailed shell element result, it poorly represents the complete equilibrium condition by ignoring any effect of twisting. Following similar logic, an engineer could conclude that the deflection of the beam in Case 3 from Section 2.3.3 would be equal to that of Case 2 plus a superimposed twist due to torsion from the initial eccentricity. Both examples would be underestimating the expected translation as well as missing a component of the actual torsional loading.

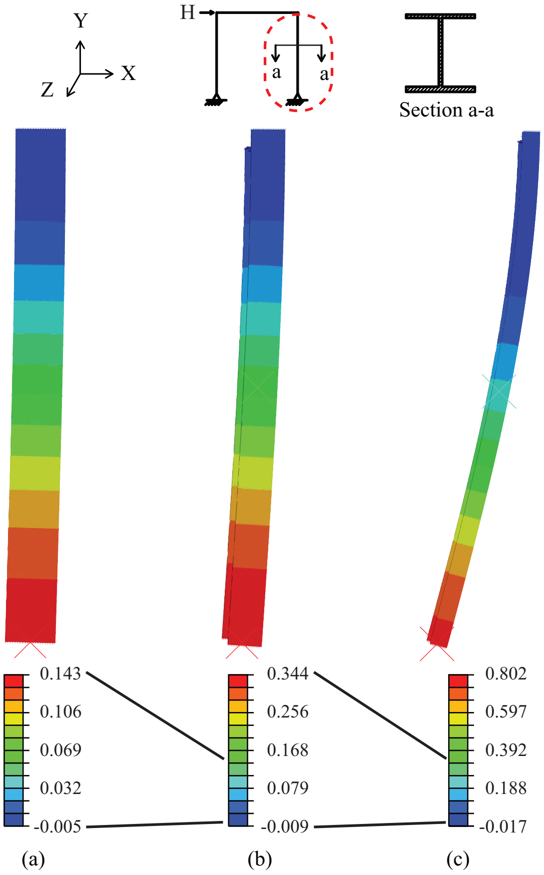

Figure 2.25: Twist about y-axis over length of right column under Loading Case 1 at H = 80 kN with torsion released, t_b = 18mm, and L/r = (a) 40 (b) 60 and (c) 120

If an engineer does include torsion and second-order effects that consider twist, the structural analysis better captures three-dimensional equilibrium but introduces the need to consider whether or not to include nonuniform torsion (warping) in the analysis. Currently, the engineer may be in need of guidance for determining how such effects would alter their design. Consider again Case 2 from Section 2.3.3, a second-order analysis with a conventional line element without warping effects would result in deflections of 25.3 mm downwards and 16.5 mm to the right. Not only is this a large increase from the first-order result, 256% and 45% respectively, these deflections overestimate the expected displacements of 8.2 mm downwards and 12.5 mm to the right by a significant amount due to overestimating the rotation. The inclusion of warping effects would stiffen the twisting response to more accurately predict the rotation. While the Case 2 example indicated a completely conservative response, other interactions indicated that part of the final analysis could be nonconservative. The excessive rotation could cause a large enough reorientation of the principal axes as illustrated in Figure 2.20 to exhibit an increased vertical stiffness

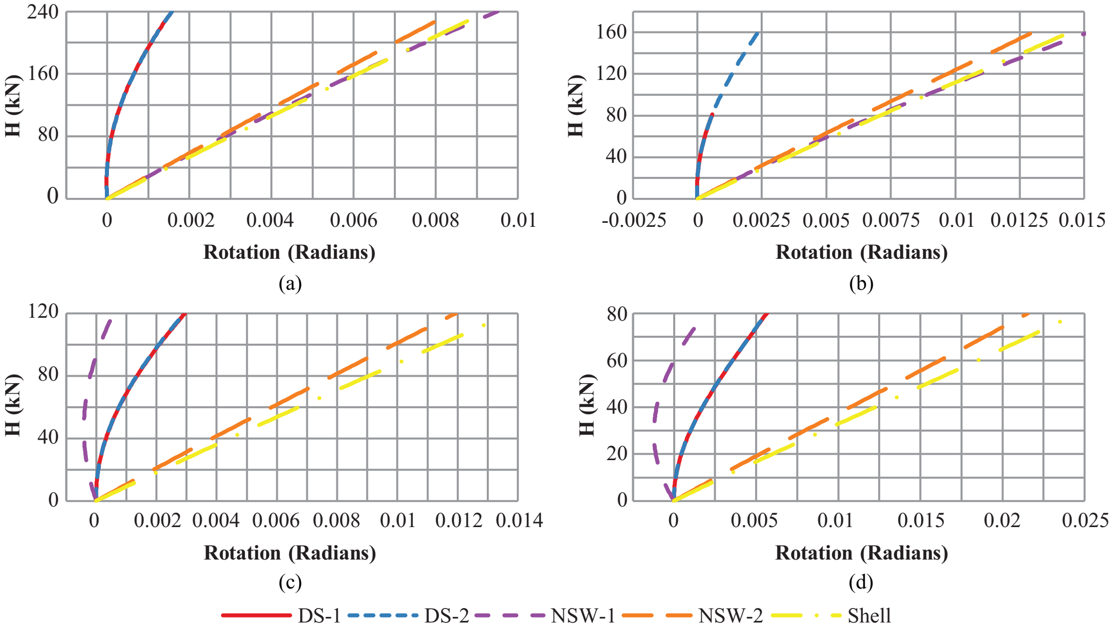

Figure 2.26: Twist at base of left column with t_b = 24 mm with torsion released with Loading Case 1 for L/r = (a) 40 and (b) 60 and Loading Case 2 for L/r = (c) 40 and (d) 60

and change the direction of lateral deflections. Although the examples of this behavior required a significant rotation to occur in this study, a different cross section with more closely aligned geometric and principal orientations would exhibit this response at smaller rotations. While this behavior could be possible in all analyses, a realistic consideration of twisting stiffness, by including warping or a modified torsional constant [36], would prevent premature activation of this behavior.

While the discussion thus far has focused on critical issues present in any structure, an engineer would also need to consider what non-symmetric behavior to include in their analysis. Throughout this paper, multiple examples have been shown where an assumption of doubly symmetric behavior is unable to capture the actual response of non-symmetric sections. In some applications, part of the response could be simulated in doubly symmetric analyses through careful manipulation such as including rigid offsets to capture the torsion from a load being applied offset from the shear center. However, this manipulation can become quite challenging as unintended force transfers can occur when multiple loading directions are considered. Even in cases where doubly symmetric behavior appears to represent the extreme response as demonstrated in the axial-strong axis moment buckling in Section 2.3.2, the complex three-dimensional interaction of non-symmetric sections causes problems when looking at slightly more interesting examples like combined axial force and strong axis moment. The inability to directly account for effects related to the shear center and appropriate twisting stiffness makes it difficult to predict the actual behavior of non-symmetric sections as observed in the large variations in the weak axis moment buckling of the lipped channel and the deflection of the Z-section. This challenge only increases as the complexity of the system grows. Even with an understanding of the underlying principals, it is difficult to predict the outcome of interacting behaviors, such as those shown in Figure 2.24. While it might be possible to verify if neglecting the increased moment arm due to the shear center position causes a similar effect as excluding warping and that the column moves in the appropriate direction at the start of the doubly symmetric analysis, it is difficult to know if such an analysis will miss the interaction of deformations that reverse the out-of-plane bending response of the column.

2.6 Conclusions

By presenting results for a range of benchmark problems, comparisons are made with finite element analysis programs that use various formulations to model members with non-symmetric cross sections. Initially, all of analysis programs employed in this study were shown to be capable of accurately solving problems with doubly symmetric sections in accordance with the minimum two-dimensional structural analysis requirements described in the commentary to the AISC Specification. Finite element models were then created for a series of problems that would exhibit significant differences in results when the behavior of non-symmetric sections are not properly accounted for. An evaluation of these problems highlighted the importance of accurately modeling twist for members not only with non-symmetric sections but also for members with symmetric sections. Major differences in displacements and internal moments were observed for problems in which nonuniform (warping) torsion, noncoincidence of centroid and shear center, and/or second-order twisting effects are significant. Although a few differences could be attributed to a single modeling feature, most differences could not be easily predicted. As a consequence, it is recommended that additional guidance be developed and provided to the engineer as to when such effects should be included in the structural analysis.

3 STRUCTURAL ANALYSIS OF STEEL STRUCTURES WITH NON-SYMMETRIC MEMBERS

Sippel, Edward J. and Blum, Hannah B. “Structural analysis of steel structures with non-symmetric members.” *Engineering Structures*, 245 (2021): 112739.
https://doi.org/10.1016/j.engstruct.2021.112739

Abstract

Cold-formed steel components exist in a variety of structural systems including wall, floor, and roofing systems. A common feature of these cross sections is that they are often open and singly symmetric or point symmetric. While design requirements for these cross-sections account for the relevant effects resulting from their lack of symmetry, structural analysis programs do not always consider these effects. Engineers will use structural analysis programs to calculate the appropriate load sharing among members in the structural system. Accounting for the appropriate stiffness of each member and the related deformations is a vital component to determining the final distribution of bending moment, forces, and displacements. Many common structural analysis programs treat all sections as doubly symmetric without warping. Removing this assumption causes non-symmetric cross sections to exhibit nonplanar displacements and complicates the stability limits. The analysis of two structural systems composed of non-symmetric members was completed with varying member modeling assumptions utilizing multiple finite element software programs. A single channel portal frame was investigated that was subjected to simulated gravity load and wind loading with varying bracing support. Additionally, a roofing system with Z-section or channel purlins and channel bracing was investigated. The finite element analysis results were compared among the various modeling assumptions and existing experiments where available. It was observed that good agreement between the doubly symmetric and the more complex analyses was obtained in some instances, particularly when the members were loaded to low levels and highly constrained. However when loading is closer to the elastic limits and members can more freely move out-of-plane, the inclusion of non-symmetric section properties becomes a critical factor in determining an accurate response for both internal forces and displacements. The variations between these different analysis methods were found to be difficult to predict due to the cumulative effect of the competing mechanical behaviors that could result in either conservative or unconservative responses when ignoring non-symmetric behavior.

3.1 Introduction

Thin-walled cold-formed steel sections are often not doubly symmetric which results in complex structural behavior that cannot be fully defined by the base behavior introduced in a Mechanics of Materials course. The AISI Specification [32] identifies some of the complex behavior through the required design capacity provisions. These provisions include accounting for warping and the associated additional normal stresses, the effects of a nonconcentric shear center and centroid for a column buckling under axial load, and Wagner coefficients when defining the lateral torsional buckling capacity of a beam in bending. Other behaviors such as local and distortional buckling effects are also covered.

In contrast, the requirements for an elastic structural analysis for demand and serviceability detailed in the AISI Specification [32] do not cover the same scope of behaviors. The requirements related to behavior are primarily focused on a two-dimensional evaluation of cold-formed steel structures. The minimum required behavior includes (1) flexural, shear, and axial member deformations as well as effects of connection deformations with (2) second-order effects highlighting the inclusion of P-δ (member) and P-Δ (system) effects. The consideration of twist, warping, or non-symmetric section properties is left to the discretion of the engineer. In the design phase, the impact of twist including warping effects and second-order twist effects is highlighted in a user note and commentary for the Direct Strength Method which indicates that ignoring these effects may underestimate elastic buckling capacities. Ziemian et al. [2] showed how the twisting of doubly symmetric sections can result in significantly different displacements and internal forces when ignoring warping effects. This response is amplified in non-symmetric sections as they are often either not loaded in alignment with a single principal axis or not loaded through the shear center which introduces an initial out-of-plane deformation including twist.

In addition to engineering judgement for determining which modeling assumptions to utilize, an engineer is often limited by the abilities of the structural analysis software available to them. Many structural analysis programs utilize a line (beam) element that assumes a doubly symmetric cross section with six degrees of freedom per end of the element [1], [37] which results in linear torsion and the exclusion of warping effects [32]. Non-doubly symmetric cross sections employed in these programs commonly assume the member to behave as a doubly symmetric section in the principal orientation. Any specific non-symmetric section behavior is left to the user to attempt to model with some direction from design guides, help forums, and experience. Recent work by various researchers [4], [6], [38]–[40] has resulted in new line element formulations that remove the doubly symmetric assumption and related approximations and instead, directly account for the twisting effect associated with members with non-symmetric (singly symmetric, point symmetric, and asymmetric) sections. The work by Liu *et al.* [40] has been implemented into the structural analysis algorithms within MASTAN2 [7], along with additional tools to readily model these sections, and in part, provides a basis for this paper.

Another important facet of the evaluation of structures is the connection behavior. Recent work has sought new ways to capture this response as even a simple rigid connection with thin-walled members provide challenging interactions at connection due to warping effects [41]. Shayan and Rasmussen [42] modeled connection behavior in doubly symmetric I-beams using line elements by adding springs to the fixed connection to simulate warping effects. Sapountzakis and Dikaros [43] modeled connection behavior directly using line elements by introducing a number of additional degrees of freedom to capture distortion. Hansen and Jönsson [44] isolated the connection behavior by using a hybrid modeling approach with shell elements to create the connection which was then transitioned to a less demanding line element for the remainder of the span. In non-symmetric sections, Hancock [45] and Rinchen *et al.* [46] noted the connection behavior was complicated further due to all internal forces not acting at a single concentric location which complicated the bimoment.

The primary objective of this paper is to report on a study that compared results determined from analyses using different modeling approaches of structural systems with members comprised of non-symmetric sections. Solutions of a shell element model, a doubly symmetric line element model, and a non-symmetric line element model are presented. This paper builds on the previous evaluation of single members including an angle, channel, and Z-section and a simple I-beam portal frame presented in Sippel *et al.* [47]. The systems presented in this paper include a single channel portal frame with connection discontinuities and a roof system containing discretely braced cold-formed Z-section or channel purlins.

3.2 Structural Analysis Methodology

Many different options and methods are available to engineers to complete their structural analysis. A common approach for practicing engineers is to use a commercially available structural analysis program that implements a conventional line element that assumes a doubly symmetric cross section. If the engineer wants to avoid this assumption, an alternative would be to utilize finite element models created with shell or solid elements. However, even a small structure modeled this way would become unwieldy quite quickly. A preferable alternative would be to implement a line element evaluation that can readily account

Table 3.1: Analysis results labels

Program	Analysis Element	Label
SAP2000	**D**oubly **S**ymmetric line element without warping	DS-1
RFEM	**D**oubly **S**ymmetric line element without warping	DS-2
MASTAN2	**N**on-**S**ymmetric line element with **W**arping	NSW-1
Abaqus	**N**on-**S**ymmetric line element with **W**arping	NSW-2
Abaqus	Shell element	Shell

for both symmetric and non-symmetric section within existing modeling procedures.

The main focus of this study was to compare the analysis results of a structural system and not a program specific algorithm. Table 3.1 provides abbreviations of the analysis models employed based on the underlying model behavior. SAP2000 [18] and RFEM [19] were used represent an analysis in which members are assumed to have a doubly symmetric cross section and ignore warping effects. The default line (beam) element within each program, that utilize 12 degrees of freedom per element, were used. The use of both programs allowed for cross validation of the results as there are possible variations in the underlying formulations. The analysis of non-symmetric cross sections was completed with the use of MASTAN2 [7] and Abaqus [20]. Within MASTAN2, the analysis models were completed with the default line element which permits the modeling of symmetric and non-symmetric section with its 14 degree of freedom line element. Of the multiple line elements in Abaqus, the B31OS line element [21] was utilized. Similar to MASTAN2, this element is a two node, three-dimensional open section element that includes warping effects. It differs from MASTAN2 in that integration is employed within each load increment to obtain the element stiffness matrices. Similar to the doubly symmetric analyzes, the use of both non-symmetric programs allowed for cross validation of a line element response while also allowing for verification of the results from the novel MASTAN2 approach. These line element models were also compared with SR4 shell element models that were created in Abaqus.

With this study focused on the system behavior of non-symmetric sections, each of the structural analysis programs was first assessed for the ability to model minimum behavioral requirements. The verification started with two-dimensional, geometrically nonlinear analysis identified through the commentary in the AISC Specification for Steel Building [1] as AISC and AISI have similar base analysis requirements. It was noted that all of the structural analysis methods considered are capable of capturing consistent flexural, shear, and axial member deformations with consideration of P-δ and P-Δ effects with a summary provided in [47]. The next level of validation evaluated the three-dimensional analysis with twisting effects based on the advanced analysis example presented in the commentary of the AISC Specification. Each set of analysis results were in agreement with the reference solutions, which provided different results based on whether nonuniform torsion (warping) was included in the evaluation. Ignoring the effects of warping is often considered conservative for the analysis of hot-rolled steel sections as discussed in Ziemian *et al.* [2] due to the softer twisting response. The exclusion of warping will cause increase initial rotations; however, it becomes difficult to predict the overall response as the increased rotation can cause unexpected changes to the expected load path [47]. After establishing a baseline behavior, a study of individual non-symmetric members was completed as discussed in [47]. Three example problems were introduced that identified specific non-symmetric section responses. The more sophisticated analyses were able to capture behaviors that were missed by the doubly symmetric evaluations. These behaviors included the translation of a non-symmetric section due to twist, buckling interactions with shear center offsets, and bi-axial bending responses. In these individual members, a primary factor driving the observed differences could often be noted; however, in a slightly more complex system, such as a mono-symmetric I-beam portal frame, the combined interactions quickly made it difficult to assign a cause to variations in displacement and moment reactions.

The comparison of the structural systems in this study was primarily focused on the forces and displacements determined using each analysis method. This comparison also included consideration of stability while observing the same details. This investigation into stability was limited to behaviors captured by line elements, a primary component of this study. As a result, scenarios where local and distortional effects controlled the behavior were not evaluated with the various analysis methods.

3.3 Portal Frame

3.3.1 Portal Frame Description

The first example was of an experimental series of single bay, single channel portal frames tested by Baigent and Hancock [48]. The channel portal frames allowed for an investigation into the deformation of channels under combined loading. The combined loading response was of interest as previous investigations with lipped channels indicated that combined interactions required non-symmetric modeling to accurately capture the complete behavior [47].

The typical portal frame is described in [48] with more detailed information provided in [49]. Figure 3.1 shows the left-hand side of the frame geometry which would be mirrored about the centerline to obtain the full frame. The frame was subjected to three loading

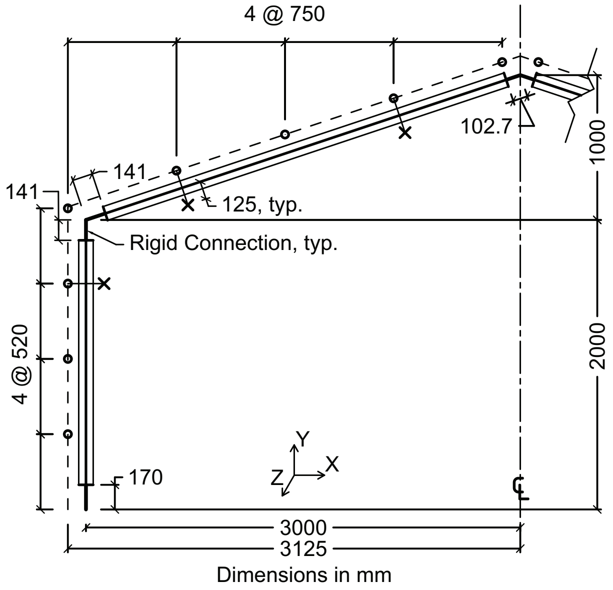

Figure 3.1: Single channel portal frame geometry. Dimensions shown are symmetric

combinations illustrated in Figure 3.2 representing vertical only loading (Case 1), transverse wind loading (Case 2), and longitudinal wind loading (Case 3) with one of two lateral support conditions. The first condition provided support at the external lateral bracing locations only, while the second condition provided support at the external and internal lateral bracing locations. The external lateral support was applied at the locations marked by a • in Figure 3.1 to simulate purlins and girts. The addition of the interior supports at the locations marked with an 'x' simulated fly-bracing by introducing a torsional restraint to the channels due the second lateral support. The loading shown in Figure 3.2 was applied at the same location as the external lateral support using suspended lead weights. The frame was constructed with lipped channels as the main members and custom bracket connections with the cross-section dimensions shown in Figure 3.3 [49]. The modulus of elasticity was taken as 203 GPa with a Poisson's ratio of 0.3.

3.3.2 Portal Frame Modeling Details

As part of their investigation, Baigent and Hancock [48] presented good agreement between the experiments and their models. As such, the models built in this study were constructed to best replicate major modeling features which primarily focused on the connections at the eave and apex. Baigent and Hancock treated the connection brackets as rigid links due to the significantly thicker and larger sections used which was similarly used in this study. The connection brackets were only bolted to the channel web which was modeled as a fixed connection allowing for the transfer of moments and forces with the warping

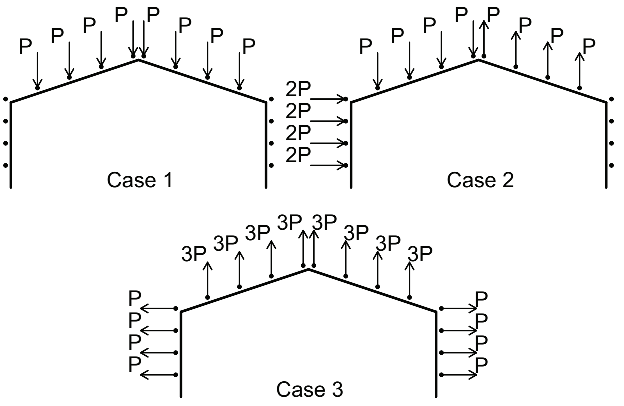

Figure 3.2: Three loading scenarios applied to portal frame

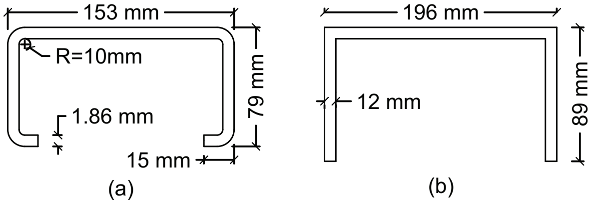

Figure 3.3: Cross-sectional dimensions of (a) lipped channel and (b) bracket

unrestrainted in the connection or channel. Lastly, the original model accounted for the connection behavior at the middle of the channel web which was implemented in the various models.

Following the geometry indicated in Figure 3.1, the channel portal frame models were created with the channel members between rigid connections. The channel members were assumed to extend between the center of the bolt group on each end. The base of each column was modeled as a hinge only free to rotate about the z-axis. In the physical experiment, brackets were attached to the flanges of the main channels and connection brackets to allow for the attachment of lateral supports and to apply the vertical loading. As a result, the support nodes were centered on the flange of the channel, 125 mm from the strong axis of the section. This node was then pinned in the z-direction.

The line element models were readily created based on the above features. The necessary offsets were obtained using rigid links. Each model was meshed uniformly between critical dimensions with a reference size of 50 mm based on the mesh study completed as part of an earlier phase in this study [47].

The shell element models were created to replicate the same modeling assumptions as the line element models. The fixed but free to warp connection constraint at the ends of channels was created by a rigid tie along the web of the channel. The rigid tie on the web was extended along the length of the member as illustrated in Figure 3.4 to ensure

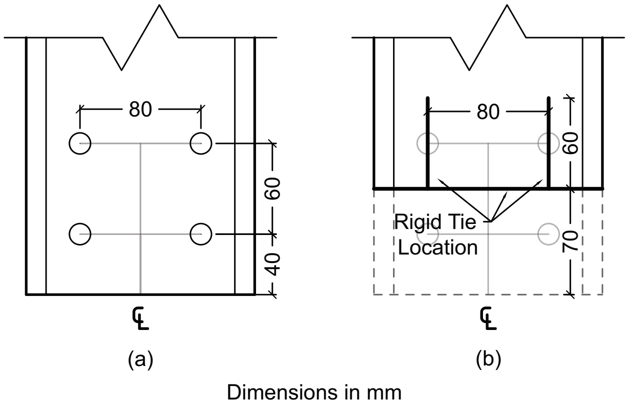

Figure 3.4: Dimensions of channel (a) end bolted connection and (b) rigid tie model

weak axis moment connection. The 60 mm extension of the rigid ties were aligned with the bolt position to approximate the internal cover plate at the eave and apex. The rigid tie at the web was readily integrated into a rigid assembly that included the supports at the column base and eave connections. Due to modeling constraints and the need to include two lateral supports at the apex connection, a shell element model of the apex was included as a deformable body. To approximate rigid deformation in this connection, this larger channel bracket was defined with a modulus of elasticity 10 times the standard value and a full depth stiffener at the lateral support locations. The remaining lateral supports and loading offsets were obtained using a 12 mm thick tab directly attached to the flat of the channel flange with the increased modulus of elasticity. The shell element model was meshed with a seed size of 2 mm.

The loading was applied to all models as point loads on the appropriate nodes. This study was completed using an undeformed model because no initial imperfections was noted in the prior model evaluation [48] and the offset of the applied loading would introduce out-of-plane effects without additional imperfections. This decision was reinforced by the two sets of experimental results available for Case 1 with lateral supports exhibiting similar elastic responses prior to local failure of the channels with different imperfections. Since the actual failure mode of frames was local buckling in the channel members, no stability analysis was considered for this frame as the limiting behavior would not be captured by the line element analyses.

This study considered the same loading procedure as the physical experiment with a preload step and then the full load incrementally applied. The initial preload was included as it applied loading to the frame in a slightly different distribution compared to the full load increments while still being a significant fraction of the total vertical load applied. The undeformed model was initially loaded with 175 N in the vertical direction and 10 N in

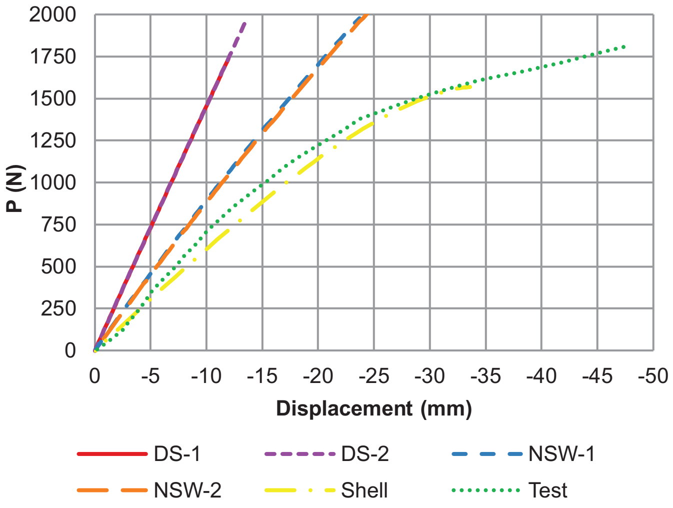

Figure 3.5: Vertical displacement at midspan of left rafter for Load Case 1 with external lateral support

the horizontal direction at each node corresponding to the loading directions shown in Figure 3.2. After this initial step, the loading was increased at each node corresponding to the loading distribution indicated in Figure 3.2.

3.3.3 Portal Frame Results

The available experimental data in [49] provided the in-plane deformation for most of the test configurations. As shown in Figure 3.5, the shell analysis model was capable of reasonably modeling the main behavior of the frames while most line element models were stiffer. In this example where the frame is only laterally supported, the non-symmetric line element analyses captured a softer displacement response compared to the doubly symmetric evaluation. This different response between the doubly symmetric and non-symmetric evaluations could be observed in other load cases as well as shown for Case 3 for the lateral displacement, Figure 3.6, and the vertical displacement, Figure 3.7, of the rafter. The variation between the methods decreased as the channel members where more restrained with the addition of the internal lateral support. Similar results from Case 1 are highlighted in Table 3.2 which summarizes some results with absolute error to the shell model results provided in parentheses after the numeric value. Another significant change to the system shown in Table 3.2 was the out-of-plane behavior. With only the external restraint, the non-symmetric analyses displayed 60% larger out-of-place displacement than the doubly symmetric behavior in Case 1. However once the internal restraint was added, minimal variation was observed in the different line element methods.

The non-symmetric section structural analysis procedures were reviewed since the

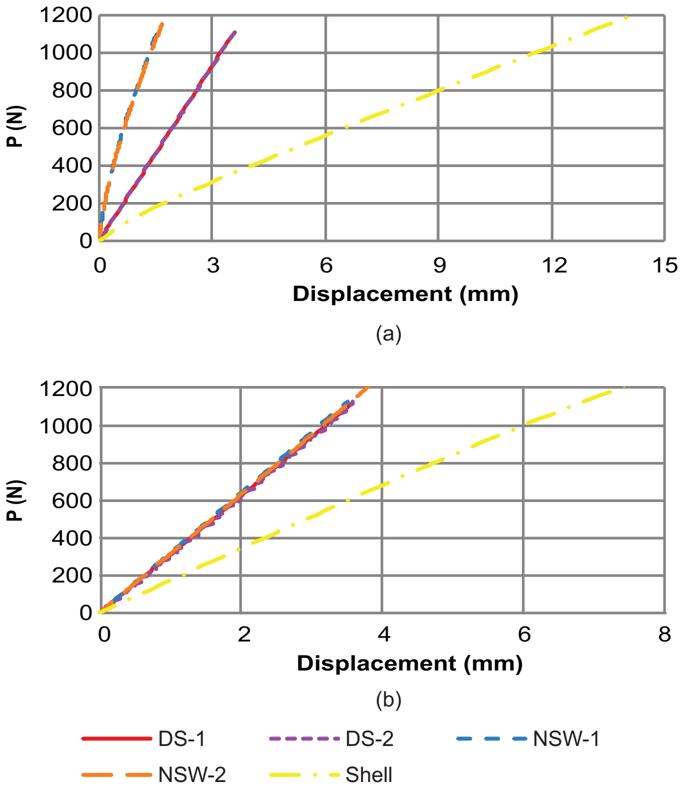

Figure 3.6: Lateral displacement at midspan of left rafter for Load Case 3 with (a) external lateral support and (b) internal and external lateral support

Table 3.2: Analysis results for single channel portal frames at P=500 N

Load Case 1 with Exterior Lateral Supports

Results		DS-1	DS-2	NSW-1	NSW-2	Shell	Test
Ux-2	(mm)	-1.83 (41.9%)	-1.82 (42.2%)	-2.01 (36.2%)	-2.04 (35.2%)	-3.15	-2.78
Uy-3	(mm)	-3.45 (58.6%)	-3.44 (58.8%)	-5.53 (33.7%)	-5.63 (32.5%)	-8.34	-7.29
My-1	(N-m)	27.2 (172%)	27.2 (172%)	-33.9 (9.8%)	-34.7 (7.7%)	-37.6	-
Uz-3	(mm)	-1.88 (77.9%)	-1.88 (77.9%)	-5.43 (36.3%)	-5.43 (36.3%)	-8.52	-

Load Case 1 with Exterior and Interior Lateral Supports

Results		DS-1	DS-2	NSW-1	NSW-2	Shell	Test
Ux-2	(mm)	-1.78 (45.2%)	-1.80 (44.6%)	-1.79 (44.9%)	-1.82 (44.0%)	-3.25	-2.61
Uy-3	(mm)	-3.45 (46.1%)	-3.40 (46.9%)	-3.50 (45.3%)	-3.58 (44.1%)	-6.40	-4.66
My-1	(N-m)	27.1 (171%)	27.1 (171%)	-39.7 (4.2%)	-40.2 (5.5%)	-38.1	-
Uz-3	(mm)	-0.02 (98.7%)	-0.03 (98.1%)	-0.09 (94.3%)	-0.09 (94.3%)	-1.59	-

Load Case 2 with Exterior Lateral Supports

Results		DS-1	DS-2	NSW-1	NSW-2	Shells	Test
Uy-3	(mm)	-3.75 (54.8%)	-3.72 (55.2%)	-4.11 (50.5%)	-4.12 (50.4%)	-8.30	-8.14
Fy-4	(N)	-251 (1.2%)	-251 (1.2%)	-252 (1.6%)	-249 (0.4%)	-248	-

Position Number: 1 = Left Column Base Connection, 2 = Left Eave, 3 = Midspan of Left Rafter, & 4 = Right Column Base Connection

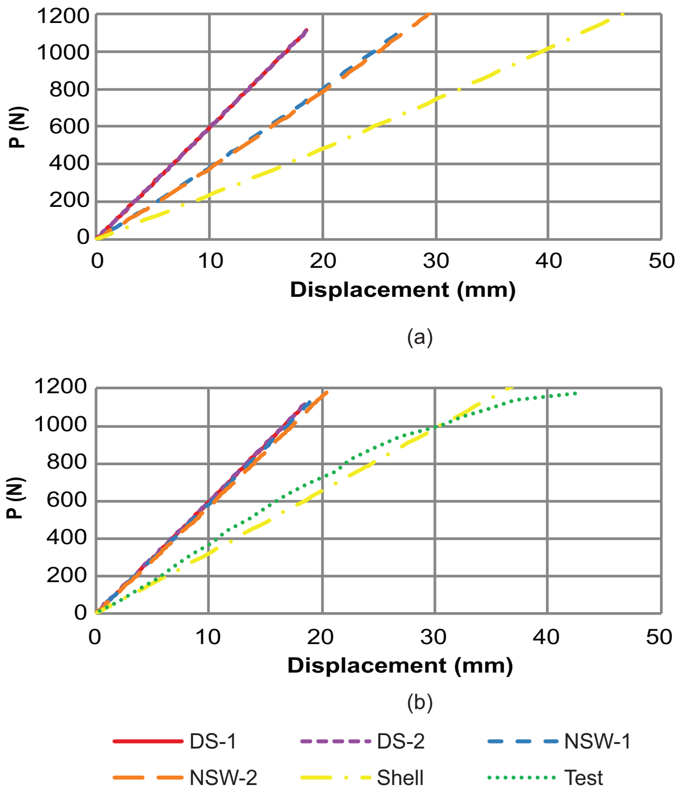

(a)

(b)

Figure 3.7: Vertical displacement at midspan of left rafter for Load Case 3 with (a) external lateral support and (b) internal and external lateral support

results from this study were found to stiffer than those from the modeling results plotted by [50]. The primary difference noted between these methods was the transfer of forces at the connections, particularly bimoment. Both methods in this study and the previous work by Baigent and Hancock allow for the end of an element to be defined as continuous, fixed, or free for warping. The difference is the effects of bimoment due to changes in the cross section and orientation. The work by Baigent and Hancock included a development of bimoment due to the offset shear center and bending moment and the compatibility with the adjacent connection bracket. This additional bimoment would introduce additional twist to the system which would cause additional weak-axis bending of the section due to the rotation of the section and thus an overall softer response. While not fully explored in this study, the free to warp (zero bimoment) condition at the end of the connection brackets resulted in a bimoment distribution within the channel per [50] that could not be reproduced within either of the non-symmetric line elements in this study. The selected elements do not have an ability to relate applied forces at the end of the member to internal bimoments. The internal bimoment can only develop at a continuous or fixed warping condition.

3.4 Roof System with Z-Section Purlins

3.4.1 Roof System Description

When assessing a structural design, an engineer will often utilize a general understanding of how the structure will behave to simplify the necessary evaluations. For example, an engineer may evaluate a roof purlin as an individual element and separately design the supporting beams and bracing. However, this process requires an assumption of the underlying response. In a roof system, the consideration of an unrestrained bending response with non-symmetric sections introduces additional biaxial bending and twisting effects which may not be considered in a simplified component analysis. To study the combined response of the entire system, the single slope roof shown in Figure 3.8 was considered which included non-symmetric roof members supported by rolled I-beams. The cross-section designations that follow are listed by the equivalent metric size followed by the standard American section size.

The four inclined W310x38.7 (W12x26) I-beams carry continuous Z-section purlins, 305Z76-254M (1200Z300-100). As the design assumed no bracing from the roof deck, the purlins were considered discretely braced by channels, 203S70-144M (800S275-57). A single channel brace at midspan was used based on work by Sputo *et al.* [51] that a single brace could provide adequate restraint. Figure 3.9 depicts the stacked configuration of the purlin and I-beams as well as the angle, L51x51x3.2 (L2x2x1/8), fly bracing included at the •'s in Figure 3.8(a) which braced the I-beam bottom flanges. The I-beam and angle members were modeled with a modulus of elasticity of 200 GPa and the Z-section and channel members were modeled with a modulus of elasticity of 203 GPa. All members were modeled with a Poisson's ratio of 0.3.

The roof system was evaluated for the application of a downward vertical load simulating dead/live loading and an upward load perpendicular to the roof slope to simulate wind loading. This loading was applied as a uniform distributed load at the purlin centroid. The roof system was evaluated for two cases. Case 1 considered a finite 1.5 kN/m load to establish a baseline comparison point. Case 2 considered the elastic stability limits to identify the analysis behavior at high loading levels.

3.4.2 Roof System Modeling Details

Support reactions were only applied at the I-beams. All beam ends were supported in the vertical direction and lateral restraints were applied as shown in Figure 3.8. The longitudinal reactions at the bottom of the I-beams allowed each beam line to resist wind

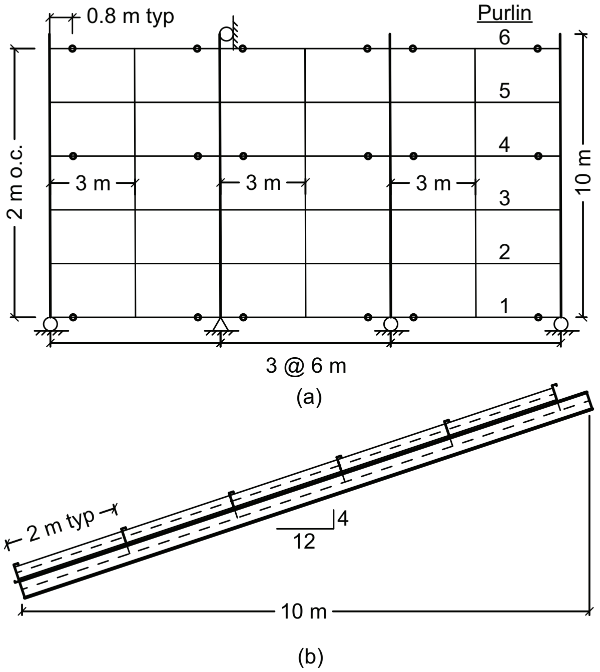

(a)

(b)

Figure 3.8: Roof layout (a) Plan view (b) Section view

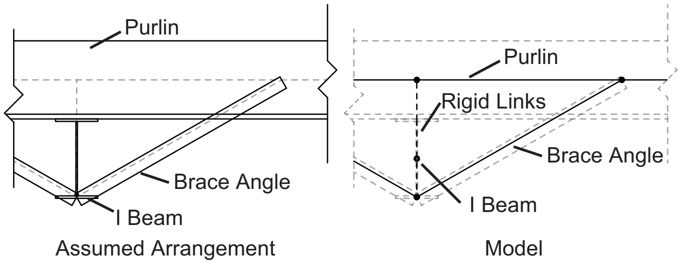

Assumed Arrangement

Model

Figure 3.9: Kicker brace positioning

pressure. Minimal reactions were applied in the transverse direction to provide stability. The ends of the I-beams were free to warp and torsional restraint was provided by the fly-bracing.

The purlins were modeled as continuous members across the I-beams. Each support connection allowed for the transfer of shear, axial load, and torsion out of each purlin. The ends of the purlins were free to warp. The midspan channel bracing was treated as a torsional brace through a web only connection. This configuration only precluded the transfer of weak axis moment at the connection and allowed the ends of the channel to be free to warp.

The continuous purlins were modeled in a prismatic condition with a constant cross section. Epstein *et al.* [52] investigated the design of purlins with continuous top flange bracing so that full cross section yield could be achieved for positive moment. A nonprismatic condition accounting for the lap length with increased stiffness was found to give conservative and more accurate results. The increased stiffness resulted in larger negative moments at the supports which was led to more critical conditions at the common limiting locations, either the end of the lap or at the support. A consequence of the nonprismatic modeling approach was that the maximum positive moment decreased as well. In this study, the long unbraced length of the purlin would preclude reaching full yield of the section in actual design. As a result, the maximum positive moment at midspan was considered a critical value and could be best obtained using a prismatic evaluation.

The section properties of the cold-formed members were based on a thin-walled model with sharp corners. While common bend radii are available, the exact radius used by the reference manufacturer was not indicated. Variability was also found in the bend angle of the Z-section flange. As a result, this study opted for a simplified geometry to aid repeatability.

The line element models were meshed with a seed of 200 mm for all members. The stacked geometry and offset connection shown in Figure 3.9 were obtained using rigid links. The distributed loading mentioned above was applied along the length of each element.

The shell element model was meshed with a seed of 5 mm for all members. The I-beam restraints were applied to a rigid tie across the height of the web. Similarly, the purlin to I-beam connections included a rigid tie over the height of the purlin web to transfer shear forces along the full height of the member. These rigid ties were then connected to the top flange of the I-beam using a MPC constraint that allowed for the transfer of torsion but no other moments. The distributed load was applied as point loads at the centroid of the purlin based on the tributary length of the element.

The evaluation of elastic stability needed as part of Case 2 was completed using a nonlinear static analysis in all analysis programs and an eigenbuckling analysis where possible. The nonlinear analyses were determined to have reached a maximum loading when an instability was observed. The onset of instability was identified by a significant change in deformations or if the model would fail to converge due to the instability. In either instance, the results were verified to have a similar loading and deformation response as the eigenbuckling analysis or to have indicated a negative or zero stiffness near failure. As the selected doubly symmetric structural analysis programs could not complete an eigenbuckling evaluation considering moments, conventional doubly symmetric elements ignoring warping were evaluated in MASTAN2 and Abaqus to confirm the underlying behavior.

Table 3.3: Analysis results for roof system with 1.5 kN/m distributed load

Downward Loading

Results	DS-1	DS-2	NSW-1	NSW-2	Shells
Beam Mx (N-m)	59551 (2.1%)	59600 (2.0%)	59526 (2.1%)	59197 (2.7%)	60810
Beam Uy (mm)	38.3 (2.0%)	38.0 (2.8%)	37.9 (3.1%)	38.0 (2.8%)	39.1
Purlin Uy (mm)	41.0 (5.7%)	40.6 (6.7%)	40.7 (6.4%)	40.9 (6.0%)	43.5
Purlin 1 Ratio	37.6%	35.9%	32.8%	33.0%	37.5%
Purlin 4 Ratio	33.0%	28.7%	22.6%	23.1%	21.4%

Uplift Loading

Results	DS-1	DS-2	NSW-1	NSW-2	Shells
Beam Mx (N-m)	63297 (1.7%)	63331 (1.7%)	63193 (1.9%)	62935 (2.3%)	64420
Beam Uy (mm)	40.9 (1.9%)	40.5 (2.9%)	40.3 (3.4%)	40.4 (3.1%)	41.7
Purlin Uy (mm)	43.2 (2.9%)	42.8 (3.8%)	42.9 (3.6%)	43.1 (3.1%)	44.5
Purlin 1 Ratio	36.2%	36.6%	35.1%	35.9%	34.2%
Purlin 4 Ratio	45.5%	44.5%	43.1%	43.4%	44.4%

3.4.3 Roof System Results

For this study, the primary results of interest are the forces and displacements of the various members. Based on the magnitude of loading alone though, it is difficult to have an understanding of how heavily loaded the structure is. To provide context, a demand capacity ratio for purlins based on the interaction of strong and weak axis moment was provided. While not detailed in this paper, the capacity limits of the purlin relative to the AISI Specification [32] were considered including combined effects from shear, web crippling, and torsion. A preliminary investigation considering these effects found that the moment demand capacity ratio was the limiting relationship and provided a useful metric for how much additional loading could be expected to be supported by the roof. The values provided in Table 3.3 were determined using the Direct Strength Method with a 3 m unbraced length considering the principal orientation [53].

The results of the finite 1.5 kN/m loading were similar among all the analysis methods when comparing the maximum vertical deflections, the moment along the supporting I-beams, and the demand capacity ratio for the purlins considering major and minor axis bending at midspan. A sampling of the results are shown in Table 3.3 with absolute error relative to the shell solution. An interesting result across all analysis methods was the change in moment at the supports. The largest moments at the interior supports could be observed in the first purlin, which is labeled on the right side of Figure 3.8(a), due to no differential displacements of the support beams. These interior support moments were found to decrease as the differential deflection of the I-beams increased as one moved away from the supports. This change resulted in larger positive moments at midspan which aligned with the prismatic model decision discussed earlier.

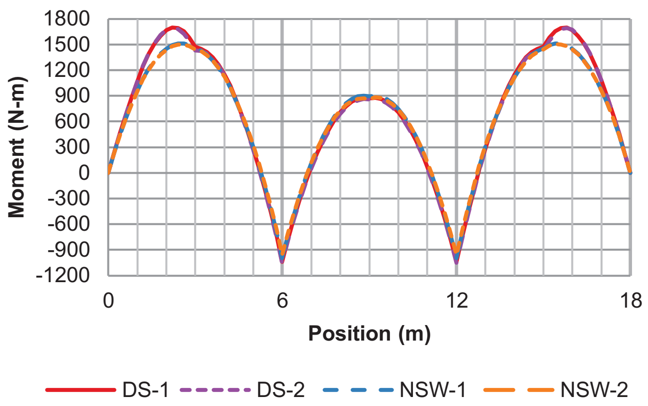

Figure 3.10: Geometric weak axis moment from vertical loading along 4th purlin. Position = 0 is the left side of Figure 3.8a

The point symmetric geometry of the Z-section means that two different orientations, geometric or principal, can be considered for the section. Either orientation may be appropriate for moment comparison depending on the design approach taken with the geometric orientation associated with the Effective Width Method and the principal orientation with the Direct Strength Method. Therefore, the variation of moment in both orientations was evaluated with the results along the fourth purlin discussed as an example. The strong axis moment for both loading scenarios, in either orientation, were still in good agreement. However, variations existed in the weak axis moment distributions in both the geometric orientation, Figure 3.10, and the principal orientation, Figure 3.11, for the vertical loading. In either orientation, there was a consistent overestimate of the weak axis moment between the end of the member and the first brace in the doubly symmetric analyses. While vertical loading introduced an increased demand prior to the brace, a more complex variation in the weak axis moment was observed in the uplift load case as shown in Figure 3.12 and Figure 3.13. As the applied loading was aligned with the geometric orientation, Figure 3.12 provides a helpful means to understand the response. The weak axis moment distribution is a combined response due to the torsional support reactions from braces and the I-beams and second-order twisting effects dues to the applied loading and lateral displacements. In the non-symmetric analyses, the increased torsional stiffness from including warping meant that minimal second-order twisting effects were included in the response. In contrast, the softer torsional stiffness of the doubly symmetric analyses allowed for significant second-order effects. This variation was amplified in the uplift case as the loading was oriented 7° further from the principal orientation than the vertical loading resulting in more initial lateral displacement to cause a larger second-order response.

When evaluating the roof systems for elastic stability, the different analysis methods

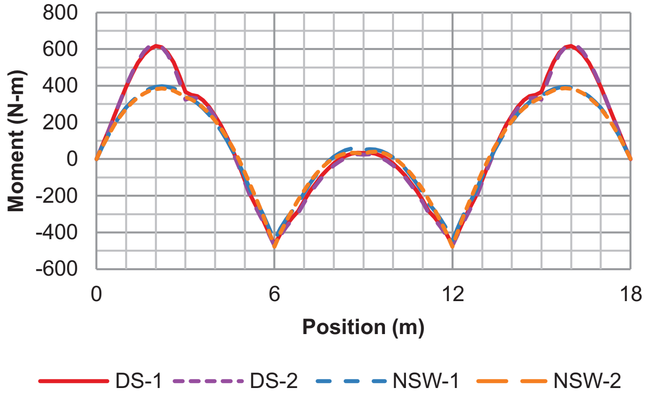

Figure 3.11: Principal weak axis moment from vertical loading along 4th purlin. Position = 0 is the left side of Figure 3.8a

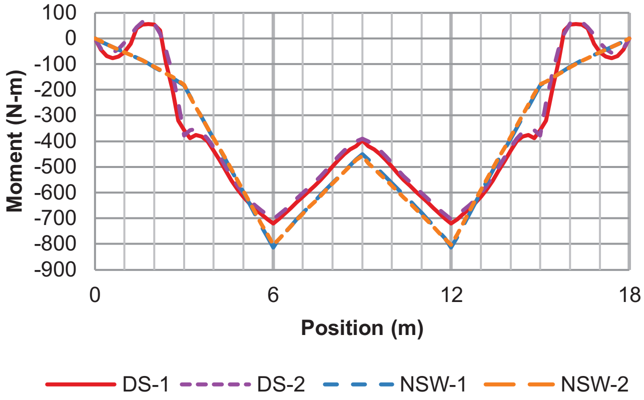

Figure 3.12: Geometric weak axis moment from uplift loading along 4th purlin. Position = 0 is the left side of Figure 3.8a

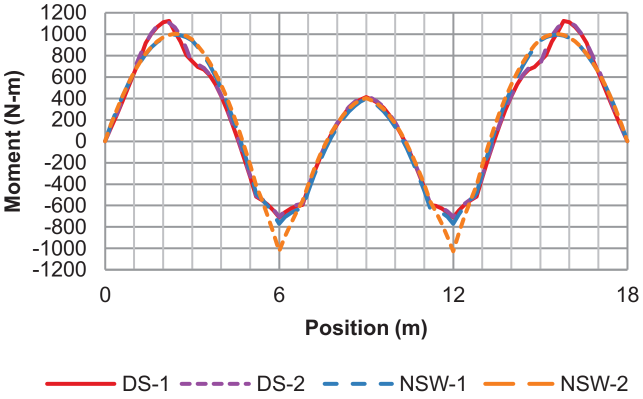

Figure 3.13: Principal weak axis moment from uplift loading along 4th purlin. Position = 0 is the left side of Figure 3.8a

Table 3.4: Maximum distributed load applied [kN/m]

Case	DS-1	DS-2	NSW-1	NSW-2	Shells
Down	1.67	1.80	3.63	3.58	3.78
Uplift	1.80	1.92	3.99	4.03	3.42

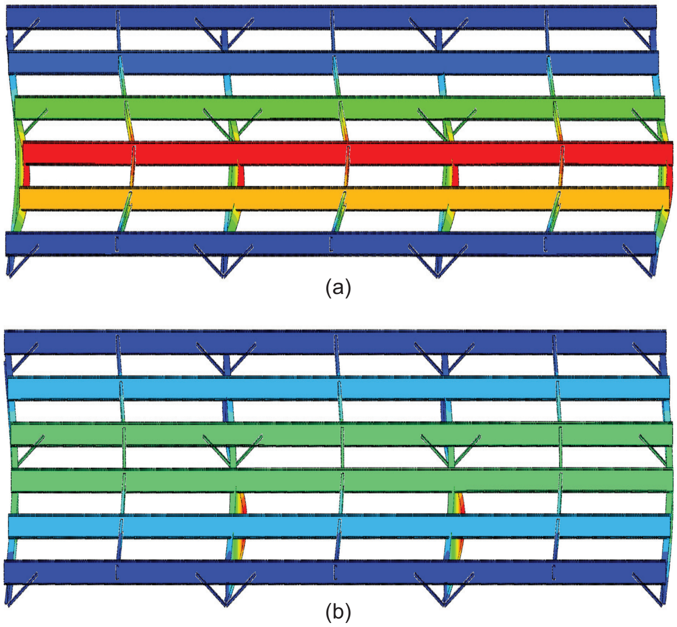

Figure 3.14: Roof system with Z-Section purlins buckling (a) due to downward vertical load and (b) due to uplift

indicated significant variations in the controlling response as summarized in Table 3.4 for the nonlinear static analysis. The observed failure of the system in more sophisticated analyses methods was the full roof system buckling laterally for the vertical loading and the interior beams buckling under uplift as depicted in Figure 3.14(a) and (b), respectively. The shell element model nonlinear analysis was in good agreement with the eigenbuckling evaluation which found limiting loads of 3.7 kN/m downwards and 3.3 kN/m in uplift. While identifying the same failure mode, the non-symmetric line element nonlinear analyses found stability limits at slightly lower values in the downward loading scenario and slightly larger values in uplift which followed with the eigenbuckling results, 3.5 kN/m downwards and 3.8 kN/m in uplift. The doubly symmetric analyses introduced a different failure mode where the central channel braces were buckling due to the applied moment. In the eigenbuckling evaluation, the first channels were observed to buckle at loads of 1.3 kN/m downwards and 1.6 kN/m in uplift. In the nonlinear analysis, the system was able to accommodate multiple braces reaching the elastic limit as depicted by the eigenbuckling shown in Figure 3.15. However, after the failure of three braces the purlins were not able to support additional loading to reach the stability limit of the full system.

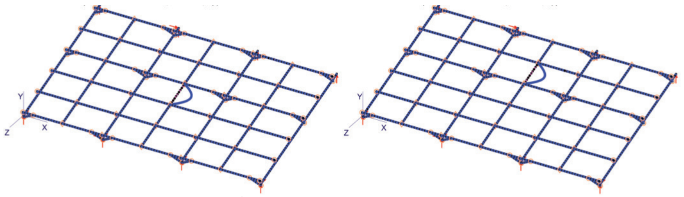

Mode 1 - 1.3 kN/m

Mode 2 - 1.4 kN/m

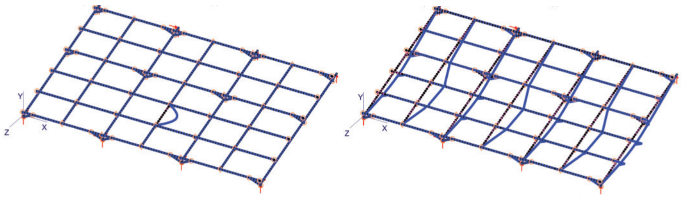

Mode 3 - 1.6 kN/m

Mode 4 - 1.9 kN/m

Figure 3.15: First 4 buckling modes using doubly symmetric analysis for roof system with Z-Section purlins due to downward vertical load

3.5 Roof System with Channel Purlins

3.5.1 Roof System Overview

The investigation into the roof system thus far has shown the importance of the appropriate evaluation of member stiffness to obtain accurate results. Prior results from an early part of this study [47] indicated that point symmetric Z-section variations could largely be attributed to warping stiffness effects. As such, it was desired to further investigate this system with channels to account for non-symmetric section properties related to a non-coincident shear center and centroid. As such, the single slope roof from the previous section was evaluated again with lipped channel purlins, 305Z51-300M (1200C200-118), replacing the original Z-section purlins.

The updated roof system was evaluated for the application of a downward vertical load simulating dead/live loading and an upward load perpendicular to the roof slope to simulate wind loading. This loading was applied as a set of discrete point loads at the locations shown in Figure 3.16 with an ‘x’. The point loads were applied at the centroid of the channel for two different loading cases. Case 1 considered a finite 1.5 kN load to establish a working load comparison point. Case 2 again considered the elastic stability limits of the consistent loading configuration.

3.5.2 Roof System Modeling Details

The updated roof system was modeled in line with the description in Section 3.4.2 with updates for the new purlin section and load distribution. The updated channel purlins

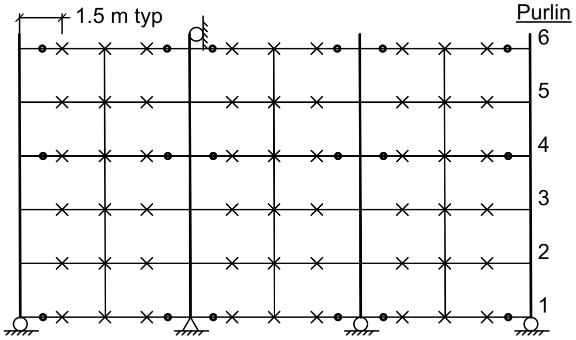

Figure 3.16: Roof Point Load Location

Table 3.5: Analysis Results for Roof System with 1.5 kN Point Loads

Downward Loading

Results		DS-1	DS-2	NSW-1	NSW-2	Shells
Beam Mx	(N-m)	31214 (0.3%)	31239 (0.2%)	30821 (1.6%)	30545 (2.5%)	31315
Beam Uy	(mm)	7.4 (7.5%)	7.4 (7.5%)	7.6 (5.0%)	7.7 (3.8%)	8.0
Purlin Uy	(mm)	25.7 (7.5%)	25.6 (7.1%)	22.3 (6.7%)	28.9 (21%)	23.9
Purlin 1 Ratio		69.5%	68.6%	67.8%	75.8%	64.9%
Purlin 4 Ratio		69.4%	69.0%	67.7%	68.1%	70.5%

Uplift Loading

Results		DS-1	DS-2	NSW-1	NSW-2	Shells
Beam Mx	(N-m)	12667 (2.1%)	12660 (2.1%)	12666 (2.1%)	12690 (1.9%)	12934
Beam Uy	(mm)	20.9 (2.3%)	20.7 (3.3%)	20.7 (3.3%)	20.7 (3.3%)	21.4
Purlin Uy	(mm)	13.5 (4.9%)	13.4 (5.6%)	13.7 (3.5%)	17.5 (23%)	14.2
Purlin 1 Ratio		31.4%	31.3%	31.3%	32.8%	29.9%
Purlin 4 Ratio		33.8%	33.8%	33.9%	33.9%	35%

were similarly modeled as prismatic and continuous members across the support beams with discrete bracing supports. The centroid of the purlin was assumed to remain constant despite the change in cross section.

In addition to the alterations described above, the other main modification to the line element models was to the NSW-2 model. An additional rigid link was defined to connect the origin of the section to the centroid where the point loads could be defined.

The shell element model was constructed similarly with the purlin to beam connections still located at the web. The first major update was to shift the channel and angle braces down the slope of the roof to align with the new web location. The other addition was a rigid tie over the height of the web at each point load location. Each tie was connected to the centroid where the point load could then be applied and distributed across the shell model.

3.5.3 Roof System Results

The primary results of interest are the same as for the roof with z-purlins: the internal forces and displacements of members. To provide similar context on the level of loading, a demand capacity ratio is provided for the interaction of strong and weak axis moment. The necessary moment capacities were determined using the Direct Strength Method with a 3 m unbraced length.

The 1.5 kN point load case for channel purlins presented consistent results among the different structural analysis methods. Table 3.5 summarizes a sampling of the maximum vertical deflection of the beams, the vertical deflection at the centroid of the purlin, the moment applied to the supporting beams, and the demand capacity ratio for the purlins considering strong and weak axis bending. Overall, the new roof was exhibiting greater variability in the deflection of the purlins. The variation in the channel deformation between the doubly symmetric and more sophisticated analyses was attributed primarily to the introduction of different amounts of torsion in the different analyses. The more sophisticated analyses were able to capture the initial loading eccentricity resulting from the difference between the shear center and centroid that was absent in the doubly symmetric analyses.

Taking a closer look at the purlin, the moment diagrams again show variation between the different analysis methods. The strong axis moment was quite similar along the length of the purlin, but the doubly symmetric underestimated the maximum midspan moments as shown in Figure 3.17. Similar to the Z-section, the more interesting behavior was observed in the weak axis moment direction depicted for vertical loading in Figure 3.18 and uplift in Figure 3.19. Once again, the softer torsional stiffness in the doubly symmetric analyses are resulting in larger twisting of the cross section which causes larger second-order effects. In the fourth purlin, the doubly symmetric analyses was actually unconservative and completed missed a negative moment that developed near the applied load, shown in Figure 3.20. Overall, the largest variations in the moments in the purlin were observed in the outer section between the last brace and the final support, especially in the weak axis.

When evaluating the roof system for elastic stability, the channel purlins are susceptible to lateral torsional buckling failures under vertical loading first while the uplift case is still controlled by the support beam as depicted in Figure 3.21. Once again, the different analysis methods indicated significant variations in the controlling response as summarized in Table 3.6 for the nonlinear static analysis. While completing the nonlinear evaluation of NSW-1 and NSW-2, both methods captured nonlinearly increasing deflections prior to the controlling failure of the roof system which was a global lateral response similar to the example in Section 3.4. A closer look comparing the displacement with the eigenbuckling

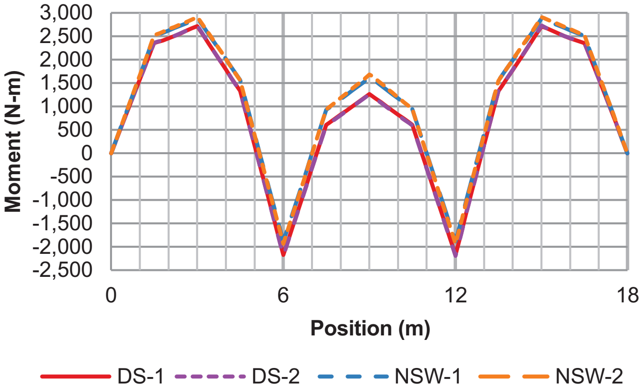

Figure 3.17: Strong axis moment from vertical loading along the 5th purlin. Position = 0 is the left side of Figure 3.16

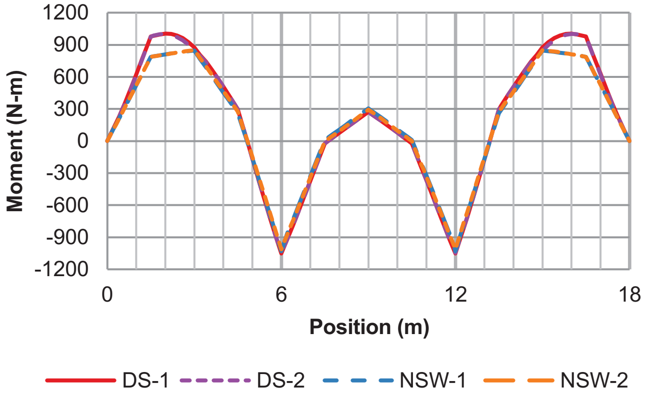

Figure 3.18: Weak axis moment from vertical loading along 5th purlin. Position = 0 is the left side of Figure 3.16

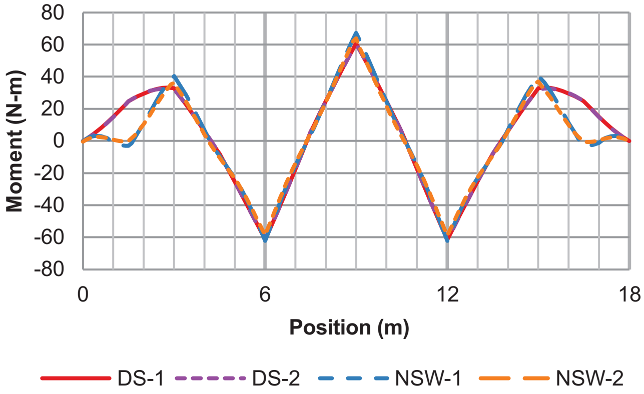

Figure 3.19: Weak axis moment from uplift loading along 5th purlin. Position = 0 is the left side of Figure 3.16

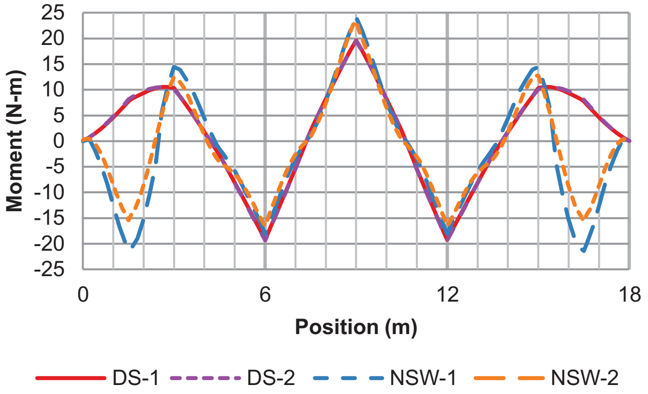

Figure 3.20: Weak axis moment from uplift loading along 4th purlin. Position = 0 is the left side of Figure 3.16

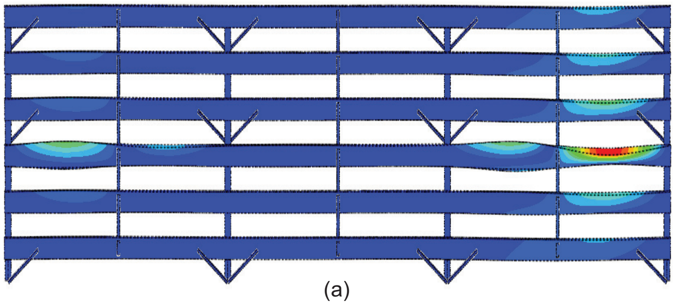
(a)

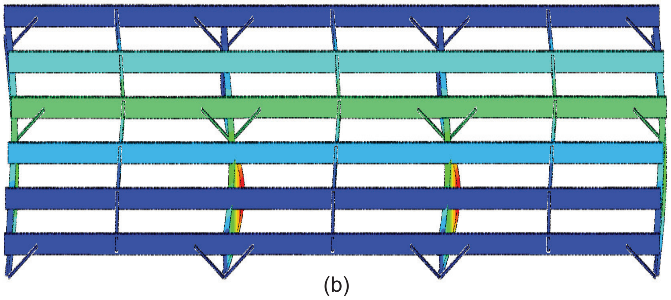
(b)

Figure 3.21: Roof system with channel purlins buckling (a) due to downward vertical load and (b) due to uplift

Table 3.6: Maximum point load applied [kN]

Case	DS-1	DS-2	NSW-1	NSW-2	Shells
Down	3.0	3.2	7.1	6.9	6.3
Uplift	2.9	3.2	7.7	7.5	7.5

behavior provided content for the apparent disagreement in buckling response noted in Figure 3.21(a). The eigenbuckling evaluation using NSW-1 indicated 10 different purlin buckling modes between 6.1 kN and 7 kN where a system buckling response was observed. These buckling modes represented various deflection patterns in the purlins that canceled and amplified each other. Approaching this lower limit, localized large changes to the deflection pattern occurred; however, additional load could still be readily applied to the system. Only upon reaching the lateral beam buckling mode did the system fail.

The numerous purlin buckling modes caused difficulties in determining a stability limit for the nonlinear shell element analysis. In the shell evaluation, it was not possible to immediately determine the next stable orientation at the given load due to the purlin behavior, and as such required an arc length evaluation to gradually transition to the next stable orientation. The channels starting to buckle caused the outer support beams to move slightly laterally and a local rotation of a purlin. The nonlinear analysis was able to evaluate this behavior through two regions of brief negative stiffness until a stable configuration was found and additional total loading applied. During the third iteration of this behavior, the analysis failed due to a near zero stiffness at the transition to a positive stiffness with small time steps resulting in the maximum value shown.

Similar to the previous example in Section 3.4, the doubly symmetric analyses encountered a premature failure due to buckling of the channel braces. Once the braces began reaching their maximum load, the channel purlins began to deflect more which lead to failure.

3.6 Discussion

The evaluation of structural systems requires accounting for the appropriate load sharing and deformation of the components. The inclusion of non-symmetric cross sections complicates this evaluation with more complex behavior including significant twisting effects in most applications. As shown in Section 3.3.3 with the modeling of the portal frame, a different structural response could be observed between the doubly symmetric and non-symmetric analyses when the the channels were only laterally supported. With the channels more free to move, different deformations existed not only out-of-plane, but in-plane as well. When the channels were torsionally restrained by the addition of interior lateral supports, the variation in the deflection of the system nearly disappeared. While some torsion was still applied with exterior and interior lateral supports, the available restraints limited the ability of non-symmetric sections to move and helped to constrain the response to a single plane which improved agreement for the doubly symmetric analyses. However as loading and deflection increases, variations will begin to appear as observed in Figure 3.13 where the different torsion behaviors caused incorrect secondary weak-axis loading. This variation is at an extreme when considering the higher loading associated with elastic stability in the roof examples. Despite the agreement among the different analysis methods at the lower applied discrete load, eventually the applied load caused the inherent variations in the underlying models to start controlling the overall response resulting in significant differences. The proper consideration of non-symmetric section properties becomes a critical factor under larger loading.

The response of a structural system with non-symmetric behavior could not be readily predicted due to the interaction of competing factors. As a consequence, the results of a doubly symmetric analysis including these sections could not easily be determined to be conservative or unconservative. In the roof system examples, the doubly symmetric analyses were slightly conservative at the lower loading levels. The softer twisting response in these non-symmetric sections resulted in minimal differences at the lower load level. When evaluating the stability of the system, the softer twisting response caused premature elastic failure at half the value of the expected ultimate load. In contrast, the doubly symmetric results of the portal frame captured an unconservative stiffer response than is expected. In this instance, the softer twisting response from ignoring warping did not cause larger rotations as it was accompanied with an underestimation of the additional torsional loading by not considering the shear center position. This localized interaction can often be readily discussed after the fact; however, quantifying how significant each factor is beforehand is challenging. As is, the most consistent ways to predict the response of a non-symmetric section to loading is either to directly account for the non-symmetric behavior or to directly limit the twist of the member to improve doubly symmetric predictions.

3.7 Conclusion

Comparisons are made with finite element analysis programs that use various formulations to model two structural systems with non-symmetric cross sections. As previous work showed the ability of these analysis methods to accurately model minimum structural analysis requirements, this investigation was able to focus on more complex examples including structural systems. Evaluation of these examples highlighted the importance of the interacting twist and non-symmetric properties through the entire structural system. While specific components of the result could occasionally be attributed to the underlying model assumptions, it was difficult to predict the cumulative effect of the excluded behavior. The more freedom an element had to rotate the more critical it was to capture the true behaviour of non-symmetric response. This interaction was amplified when the loading increased causing greater deformations. Torsional restraint of non-symmetric cross sections was identified as a significant factor in achieving an appropriate response with a simplified analysis, but no specific recommendation was developed. As a result, it is recommended that additional guidance be developed and provided to engineers as to when the effects of twisting and non-symmetric section properties should be included in structural analysis.

4 EXPERIMENTAL VERIFICATION OF ECCENTRICALLY LOADED STEEL JOIST ANALYSIS WITH NON-SYMMETRIC SECTIONS

Sippel, Edward J., Ziemian, Ronald D., and Blum, Hannah B. “Experimental verification of eccentrically loaded steel joist analysis with non-symmetric sections.” Submitted to Journal of Structural Engineering

Abstract

The non-symmetric sections commonly found in open-web steel joists present difficulties when evaluating eccentric loads applied to a single chord angle, which result in additional bending moments and torsion that are not typically considered in standard design practice. This study presents an experimental and computational approach towards qualifying the response of a steel joist with non-symmetric sections and eccentric loading. An experiment was conducted where a joist was subjected to uniform top chord loading with an eccentric hanging load applied to one chord angle, while recording displacements and strains along the bottom chord. A second-order structural analysis with a novel beam element formulation that considers non-symmetric sections was able to accurately estimate the deflections and rotations of the joist bottom chord. Several alternative computational models were created to determine the effects of common design assumptions on the analysis output. It was found that model variations including using a first-order analysis, simplifying the hanging load condition, and using doubly-symmetric section behavior only resulted in changes to the applied torsion and corresponding rotations, which led to worse predictions of stresses and deflections on the chord angle. Detailed measurements of each cross-section geometry in the joist were obtained using a handheld three-dimensional laser scanner. Despite the significant changes in torsional cross-section properties, the computational model with measured cross-section properties resulted in minimal variations compared to the model with nominal section properties. The work presented herein provides insight into the torsional response of steel joists with eccentric loads.

4.1 Introduction

Open-web steel joists are structural building components that allow practicing engineers to efficiently design floor and roof systems. The optimized use of steel allows joists to be an economical solution for supporting the specified loading condition that is often a uniformly distributed load applied to the top chord. When deviating from uniform loading, engineers rely on recommendations from industry experts, such as the Steel Joist Institute (SJI), on how to properly assess the integrity of the joist. However, engineers currently have limited guidance on assessing eccentric point loads on steel joists, even though these loads commonly occur when supporting raceways, signs, or scoreboards. Therefore, this study completed an experimental evaluation on a open-web steel joist subjected to eccentric loading to provide insight on the torsional response of steel joists as a step towards improved analysis methods. The paper provides the details of a unique system that can be used to verify a wide range of analysis programs and was applied to the non-symmetric analysis method implemented in MASTAN2 [7].

The addition of point loads to a joist takes careful consideration to ensure that there is no overstressing of the individual components, particularly the chords from additional bending effects. With general guidance, SJI recommends that point loads up to 100 pounds, which are concentrically applied to a chord as shown in Fig. 4.1(a), can likely be supported by the joist without modifications, provided the current bending moment and shear forces are enveloped by the original design loading [9]. If the point load exceeds 100 pounds, it is recommended to add a strut to reinforce the joist to reduce bending, or to analyze the joist in more detail. SJI recommends evaluating a steel joist for modified loading by considering a two-dimensional frame with doubly-symmetric line elements and assumes the load is applied equally to both chords [54]. Loading a chord eccentrically as shown in Fig. 4.1(b) is not recommended by SJI because it introduces torsional effects that the joist is not designed for. Nevertheless, many hangers are available on the market for this expressed purpose. The eccentric loading complicates the analysis as it requires further investigation into the effects of combined torsion, bending, and tension on a single angle with limited guidance for engineers.

The complicated response of open-web steel joists, which are commonly constructed with chords composed of double angles and webs composed of channels, single angles, or double angles, is partially due to the non-symmetric cross-section geometries. These non-symmetric sections often exhibit behavior differing from doubly-symmetric sections as the nonconcentric shear center and centroid, nonzero Wagner coefficients, and inclined principal orientations alter the mechanical response. To accurately account for this in routine design requires the use of more sophisticated analysis software. Recent work [4]–[6] has resulted in new line element formulations that directly account for the twisting effects associated with the non-symmetric behavior. The work by Liu et al. [5] has been implemented into the structural analysis algorithms within MASTAN2, along with additional tools to readily model these sections. Previous verification has shown that

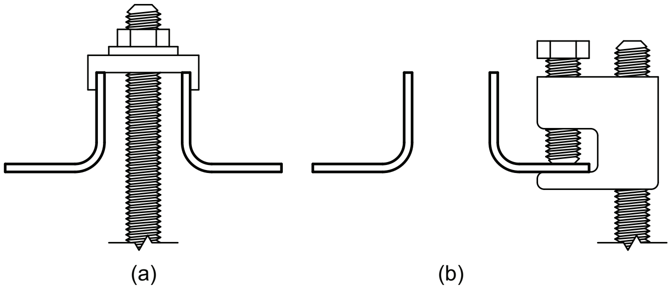

Figure 4.1: Point load applied to bottom chord using a: (a) concentric connection (b) eccentric connection

use of this line element accurately produces solutions that agree with theoretical results as well as other line element and shell finite element models [5], [6], [47], [55]. With most MASTAN2 verification studies based on individual members, this study focuses on systems and expands the verification process to comparing the computational results with an experimental investigation on a steel joist with an eccentric load. It also provides valuable insight to the special but not uncommon situation of designing for hanging loads on chords of open-web steel joists.

As this study was interested in the response of a member within an assembly, an open-web steel joist system was loaded with multiple magnitudes of uniform load and then subjected to an eccentric hanging load on one of the bottom chord angle members. The experimental results and the computational models were used to compare the stress distributions calculated in the bottom chord members and displacements. Stresses are discussed more than internal forces because the evaluation of members subjected to torsion is not covered by the current Steel Joist Institute (SJI) Specification [9] and the applicable section of the American Institute for Steel Construction (AISC) Specification for Structural Steel Buildings [1] is based on stress limit state checks.

4.2 Overview

The design joist for this study was a 6.1-meter (20-foot) 16K2 steel joist with the loading applied at the locations shown in Fig. 4.2. The joist was analyzed for three loading scenarios with an increasing hanging load summarized in Table 4.1, where LL is the design live load from SJI's standard joist load tables [9]. The joist was fabricated with cold-formed steel sections with the nominal centerline profiles shown in Fig. 4.3. The top and bottom chords were double equal leg angles with the nominal dimensions provided in Table 4.2 with a 29 mm (1-1/8 inch) gap between the angles. Table 4.2 also summarizes the dimensions of the three different rolled channels used for the webs. The majority of web members were the

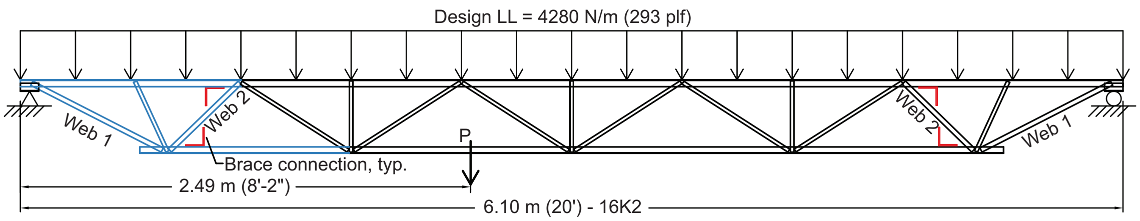

Figure 4.2: Overall steel joist with applied loads. Web members without a cross-section label are all Web 3. Members highlighted in blue were scanned for imperfections, which is discussed in Section 4.6.4.1.

Table 4.1: Test load matrix

Loading Scenario	Uniform Load	Maximum Hanging Load (P)
LS 1	0.5 LL	445 N (100 lb)
LS 2	1.0 LL	445 N (100 lb)
LS 3	0 LL	1245 N (280 lb)

LL = 4280 N/m (293 plf)

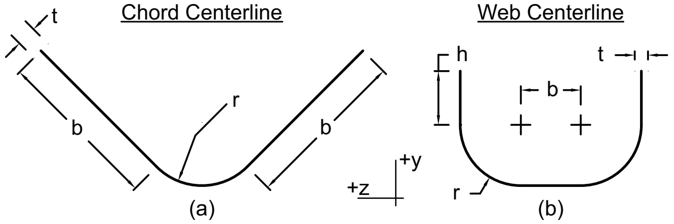

Figure 4.3: Typical cross-section centerlines

cross section identified as Web 3, except the first two web diagonals from each end which were Web 1 and Web 2, respectively, as labeled in Fig. 4.2. The top chord was continually braced by connection to the metal deck, while the bottom chord was only braced at each end by diagonal cross bracing.

4.3 Experimental Setup

Testing was performed on a dual-joist system as shown in Fig. 4.4 in the Jun and Sandy Lee Wisconsin Structures and Materials Testing Laboratory at the University of Wisconsin-Madison. Two 6.1 m (21 ft) 16K2 steel joists were placed 1.2 m (4 ft) on center with diagonal

Table 4.2: Joist element cross-section nominal centerline dimensions in accordance with Fig. 4.3

Section	b [mm (in)]	h [mm (in)]	r [mm (in)]	t [mm (in)]
Top Chord	26.759 (1.0535)	-	9.639 (0.3795)	3.404 (0.1340)
Bottom Chord	25.654 (1.0100)	-	9.398 (0.3700)	2.921 (0.1150)
Web 1	6.858 (0.2700)	14.844 (0.5844)	9.398 (0.3700)	2.921 (0.1150)
Web 2	7.366 (0.2900)	13.355 (0.5258)	9.271 (0.3650)	2.667 (0.1050)
Web 3	8.804 (0.3466)	7.879 (0.3102)	8.913 (0.3509)	1.948 (0.0767)

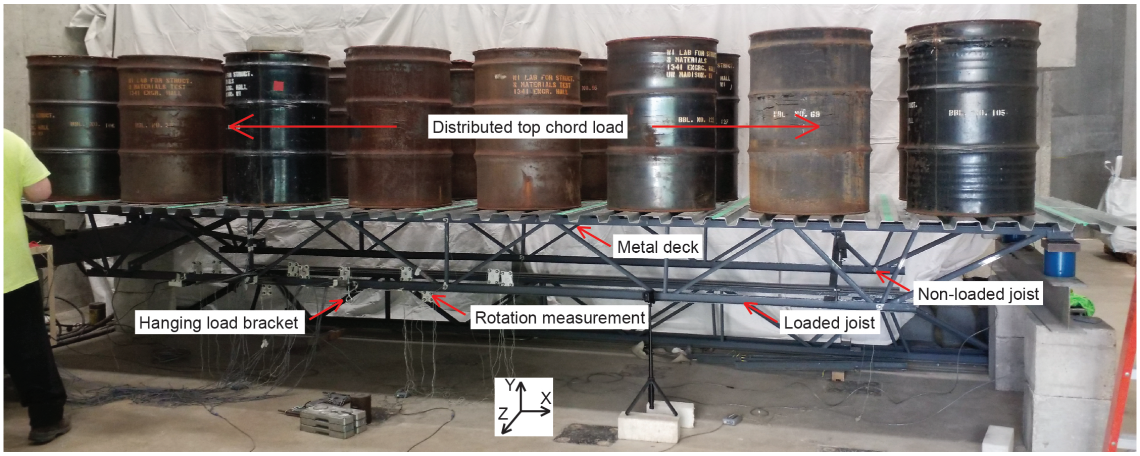

Figure 4.4: Experimental joist configuration

cross bracing at each end of the joists. A 1.8 m (6 ft) wide section of metal decking was attached to the top chords of each joist with #12 Teks 5 self-drilling screws at 305 mm (12 in) on center alternating top chord members with 2 additional sidelap fasteners. The two joists with decking and bracing in place provided a self-stabilizing system such that external lateral support was not required during testing. The hanging load, strain gauges, and optical tracking markers were primarily applied to the front joist as this was the test joist, while the back joist and decking served only to stabilize the system.

Uniform gravity load was simulated using barrels of aggregate distributed along the length and width of the deck. The target 4280 N/m (297 plf) design live load was achieved with a total of 27.03 kN (6077 lbs) in 8 barrels and 54.15 kN (12173 lbs) in 16 barrels applied to the deck to obtain the desired 0.5LL and 1.0LL, respectively. This applied loading corresponded with a uniformly distributed load of 2.22 kN/m (152 plf) and 4.44 kN/m (304 plf). Once the appropriate live load was applied, the hanging load was applied to only the front joist as shown in Fig. 4.5 using a 9.5 mm (3/8 in) rod beam clamp attached to the bottom chord, which caused an eccentric loading condition similar to Fig. 4.1(b).

Deflections and strain gauge measurements were recorded during each loading scenario using the self-weight of the system as the zero condition. Displacements in all three directions were captured using the Optotrak Certus optical tracking system. The Optotrak system utilizes three optical sensors to track the position of markers that are attached to the structure with up to an accuracy of 0.1 mm (0.004 in). The translation of the bottom chord was recorded at the location of the applied hanging load on the test joist and at midspan on both joists, which was the only measurements taken of the support joist. Rotations were recorded at the ten locations indicated in Fig. 4.6 along the bottom chord of the eccentrically loaded joist, which are identified by “R". The rotations were calculated based

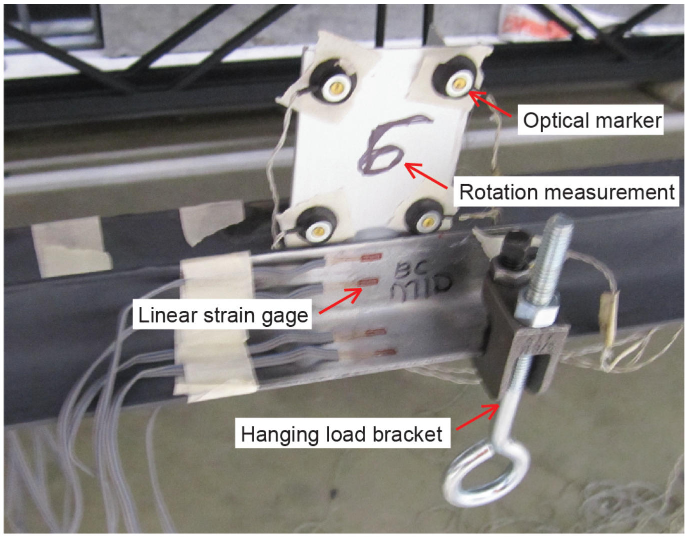

Figure 4.5: Hanging load application

on the displacements of a group of four markers attached to the vertical leg of the chord. Fig. 4.6 also depicts the five positions where strain gauge measurements were recorded, including two locations on the web marked with a “W" and three locations on the bottom chord marked with an “A". Measurements were recorded for the loaded chord angle of the test joist unless the label includes a “u" meaning the information was instead taken on the unloaded chord angle of the test joist. At each strain location, a torsional strain and four linear strain measurements were recorded for the calculation of the internal stresses including the possibility of a non-zero bimoment. The linear strain information was used to calculate internal forces based on the assumption of a linear elastic response according to the relationship shown in Eq. 4.1:

$$\sigma = \frac{P}{A} - \frac{M_y z}{I_y} - \frac{M_z y}{I_z} + \frac{B\omega}{C_w} \tag{4.1}$$

where σ is the normal stress at a position (y, z) on the cross section, P is the axial force, M_y and M_z are the bending moments about the y- and z-axes respectively, B is the bimoment, A is the cross-sectional area, I_y and I_z are the area moments of inertia about the y- and z-axes respectively, ω is the normalized warping coordinate, and C_w is the warping constant. This calculation of stress occurred in the local principal orientation. After back-solving for the internal forces, the same equation could then be used to determine the stress at any point on the cross section.

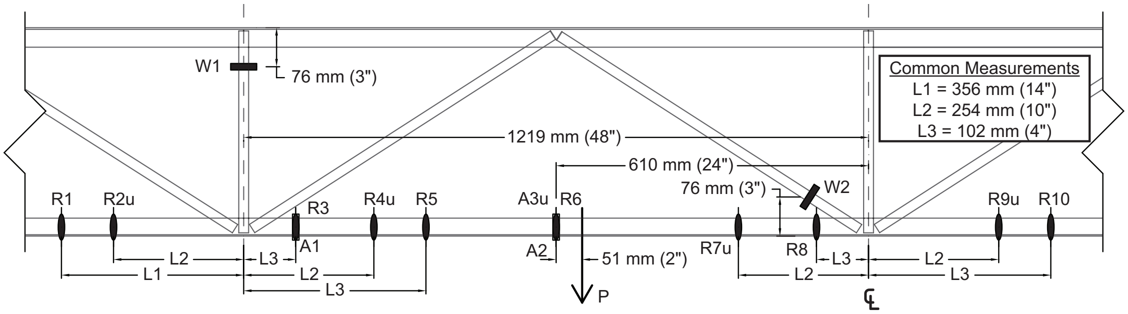

Figure 4.6: Locations where strain measurements and rotations were recorded on the bottom chord. Measurements were recorded on the loaded chord angle unless marked with an additional “u".

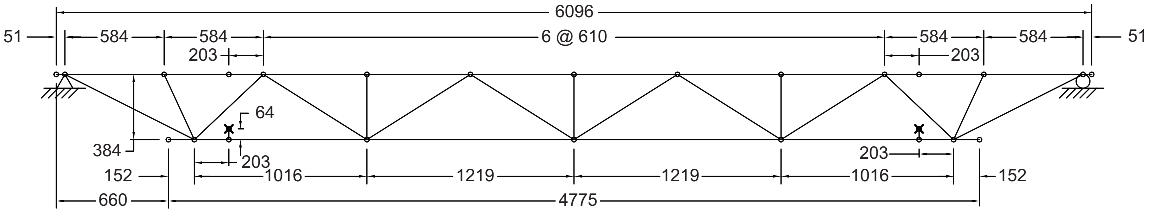

Dimensions in mm [25.4 mm = 1 in]

Figure 4.7: Joist model critical dimensions in plan

4.4 Computational Model

The computational modeling considered an isolated joist, as would commonly be done in practice. The model aligns with SJI’s recommendations for the evaluation of existing joists [54]. The geometry, shown in Fig. 4.7, assumed no joint eccentricity at the webs. The web members were pinned in-plane to match the typical design approach, but the webs were fixed for bending out-of-plane and warping at the ends to resist the out-of-plane forces from the eccentric loading. The individual angles in the top and bottom chords were modeled as separate elements to allow for the independent response of the angles and a better prediction of stability [56]. Fixed-end rigid links that were free to warp were used to connect the webs to the chord members. Boundary conditions were applied at the centerline of the joist using the middle node of the aforementioned rigid links. The bearing supports of the joist were treated as a pin and roller combination. A lateral support was applied to the top chord at all chord-to-web connections to approximate the deck restraint. The bottom chord was restrained with a lateral support at each end, noted by the ‘×’ in Fig. 4.7, which simulated the eccentric position of the cross-bracing connection using rigid links. To complete the structural analysis considering non-symmetric behavior, the necessary cross-section properties were determined using the MSASect tool within MASTAN2 and are based on the nominal centerline model of each cross section shown in Fig. 4.3 in a principal orientation. The modulus of elasticity was taken as 200 MPa (29,000 ksi) with a

Poisson's ratio of 0.3 for all steel elements [9].

Additional details of the joist model in this study can be found in the AISI Tutorial for MASTAN2 [57] as the tutorial incorporates the same joist geometry. The use of a warping continuous line element resulted in significant bimoments at connections, so a mesh convergence study was conducted to refine the element mesh until a minimal change in the maximum value of the bimoment was observed. The top chord was refined into 102 mm (4 inch) line element segments. The webs were divided into 12 elements resulting in 33 to 61 mm (1.3 to 2.4 inch) long segments. The bottom chord was predominately meshed into 51 mm (2 inch) segments. The bottom chord bay where the hanging load was located was further refined into 13 mm (0.5 inch) segments within 51 mm (2 inches) of the applied load and 25 mm (1 inch) segments for the rest of that bay plus 102 mm (4 inches) beyond the web intersection.

The uniform loading of 0.5 LL and 1.0 LL – 1.11 N/mm (6.33 lbs per inch) and 2.22 N/mm (12.68 lbs per inch), respectively – was applied equally to the two parallel top chord angles. The eccentric load was applied at the bottom of the eye bolt. The bracket was modeled with a 38 mm (1.5 inch) horizontal rigid link that supported a 63.5 mm (2.5 inch) long, 9.5 mm (3/8") round vertical steel section representing the eye bolt shaft. The models were evaluated using a second-order elastic analysis with the uniform loading and hanging loading applied sequentially. The results of the analysis were labeled NS-2 in reference to the non-symmetric, second-order analysis.

4.5 Experimental and Analytical Results

The overall behavior of the joist model from a second-order elastic analysis was validated against the experimental data using the vertical deflection at midspan and the axial force in the bottom chord, given that this force was the dominant internal response. The initial axial forces prior to the application of the hanging loads in the joist bottom chords were in agreement, with less than a 2.5% difference between the experiments and the computational models as presented in Table 4.3. The physical experiments had approximately 20% greater vertical deflections in the test joist compared to the analysis models as summarized in Table 4.4. Minimal lateral deflections were observed in the experimental results, which agreed with the modeled behavior. Despite this initial variation, it was observed that the net displacements near the applied load during the experiment were similar as shown in Fig. 4.8. The agreement improved, as illustrated in Fig. 4.9, when no uniform load was applied (LS 3). Overall, there was acceptable agreement in the baseline behavior to validate the models and continue with further comparisons of the stress distributions.

Table 4.3: Axial force in bottom chord before hanging load applied

Loading Scenario	Experiment at A2	Experiment at A3u	NS-2
LS 1 w/ 0 N (0 lb)	12.37 kN (2781 lb)	12.46 kN (2801 lb)	12.46 kN (2802 lb)[1]
LS 2 w/ 0 N (0 lb)	25.54 kN (5741 lb)	25.54 kN (5741 lb)	24.99 kN (5617 lb)[1]

[1] The force is the same in both angles in the analysis model prior to the application of the hanging load.

Table 4.4: Vertical deflection at midspan of joists before hanging load applied

Loading Scenario	Test Joist	Support Joist	NS-2
LS 1 w/ 0 N (0 lb)	9.17 mm (0.361 in)	10.24 mm (0.403 in)	7.62 mm (0.300 in)
LS 2 w/ 0 N (0 lb)	18.31 mm (0.721 in)	19.74 mm (0.777 in)	15.27 mm (0.601 in)

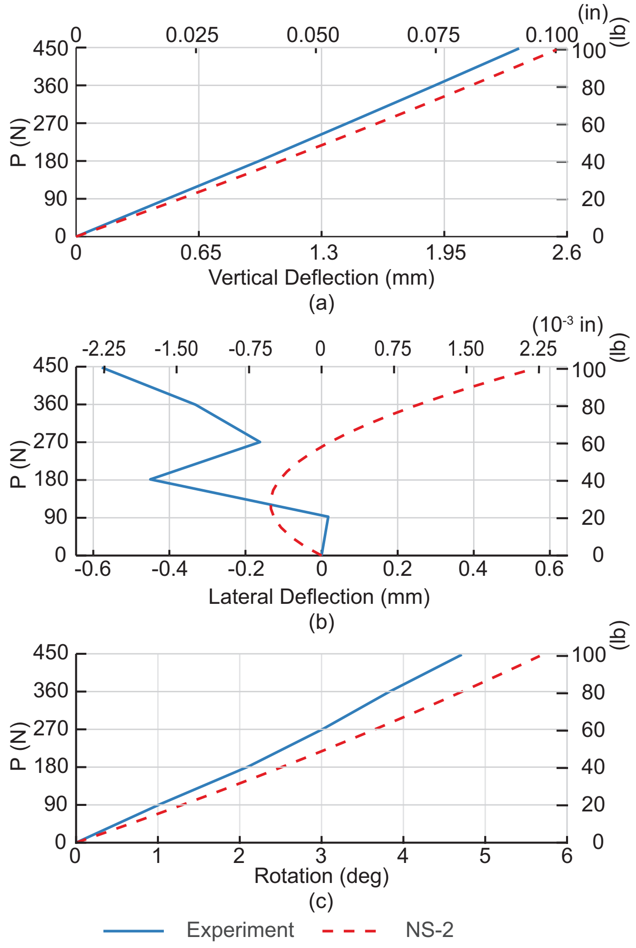

Figure 4.8: Net displacement of bottom chord at the hanging load in LS 2. (a) Downward vertical deflection (b) Lateral displacement in the global (-)Z-direction (c) Torsional rotation about the X-axis

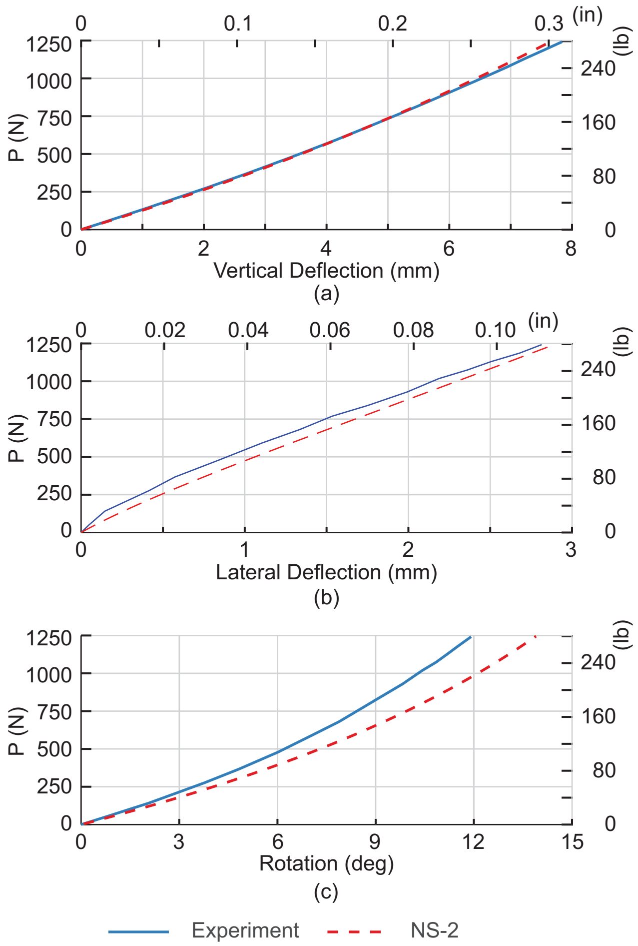

Figure 4.9: Displacement of bottom chord at the hanging load in LS 3. (a) Downward vertical deflection (b) Lateral displacement in the global (-)Z-direction (c) Torsional rotation about the X-axis

The stress distribution comparison considered both the stress resulting from the total load as well as the net change in stresses from the addition of the hanging load. The general distributions of stresses in the bottom chord from the experiment and the finite element analysis results were found to be in agreement. The internal stresses were primarily in tension with similar distributions during LS 1 and LS 2 as shown in Fig. 4.10 for position A1, with the full live load and full hanging load applied. Fig. 4.11 shows the stress distribution due to the uniform loading subtracted from the full live load results given in Fig. 4.10 - this was done to highlight the similar pattern of stresses across the section resulting from the hanging load only.

The maximum tensile stress can be considered a significant design value when evaluating non-HSS members for torsion because AISC [1] specifies stress limits and Eurocode [16] allows the use of elastic verification of yield which is currently dominated by the normal stress. Despite the agreement shown in Table 4.3 and Fig. 4.10, the maximum tensile

Table 4.5: Maximum tensile stress in bottom chord

ID	Loading	Stress - MPa (ksi) [Error to Experiment]			
		Experiment		Second-Order	
		Total	Net	Total	Net
A1	LS 1 - Start	75.57 (10.96)	-	68.67 (9.96) [-9.2%]	-
	LS 1 - End	88.67 (12.86)	33.44 (4.85)	94.67 (13.73) [6.8%]	40.54 (5.88) [21.4%]
	LS 2 - Start	154.0 (22.34)	-	138.4 (20.08) [-10.1%]	-
	LS 2 - End	149.0 (21.61)	30.06 (4.36)	144.4 (20.95) [-3.1%]	36.96 (5.36) [22.9%]
A2	LS 1 - Start	70.05 (10.16)	-	68.74 (9.97) [-1.9%]	-
	LS 1 - End	115.9 (16.81)	45.85 (6.65)	103.5 (15.01) [-10.7%]	36.40 (5.28) [-20.7%]
	LS 2 - Start	140.9 (20.44)	-	137.9 (20.00) [-2.2%]	-
	LS 2 - End	181.3 (26.30)	40.40 (5.86)	164.6 (23.88) [-9.2%]	30.96 (4.49) [-23.4%]
A3u	LS 1 - Start	76.81 (11.14)	-	68.74 (9.97) [-10.6%]	-
	LS 1 - End	84.05 (12.19)	7.24 (1.05)	77.91 (11.30) [-7.3%]	9.24 (1.34) [27.4%]
	LS 2 - Start	156.9 (22.76)	-	138.0 (20.01) [-12.1%]	-
	LS 2 - End	164.4 (23.85)	7.52 (1.09)	145.5 (21.11) [-11.5%]	7.65 (1.11) [1.3%]

[1] Start = 0 N (0 lb)

[2] End = 445 N (100 lb)

stresses observed in the bottom chord computational results from the uniform loading was found to be less than the experimental results and are most likely due to variations in the internal moments as shown in Table 4.5. This trend continued under the total effect of the combined uniform loading and hanging load. Isolating the net effect of adding the hanging load, the maximum net tensile stress at position A2 was similarly found to be underestimated in the computational model when compared to the experiment. However, the net tensile stress was found to be conservative at position A1 and A3u. Despite the apparent discrepancy, all three positions were consistently displaying larger net stresses on the vertical leg and smaller net stresses at the heel of the angle in the computational models when compared to the experimental results as shown in Fig. 4.12. At position A1 and A3u, the added negative moment from the hanging load resulted in a larger tension stress in the vertical leg that combined with the axial tension of the chord. At position A2, the added positive moment resulted in smaller tensile stresses near the heel of the angle, which was the critical location for maximum tension. Obscured by the comparison of maximum tension values was the increased applied compression to the vertical leg. Overall, the computational model was found to add a conservative bending response to the angle chords. It should be noted that the larger errors associated with position A2 were likely influenced by the proximity of the hanging load. While measurements of distortion were not taken during the experiment, the loading was applied only 50 mm (2 in) away from the strain gauges, which may have captured additional bending of the horizontal flange.

While strain data was recorded within the webs, no values are presented in this paper.

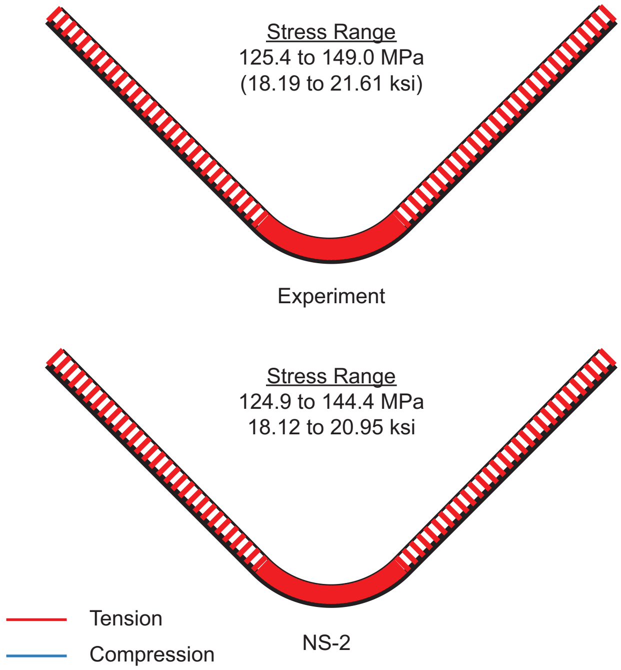

Figure 4.10: Normal stresses on bottom chord at A1 for LS2 (1.0LL with 445 N (100 lb) hanging load)

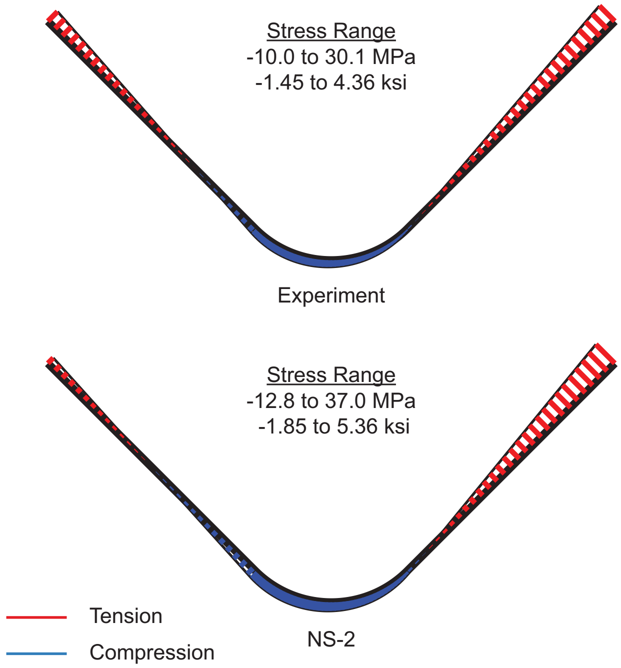

Figure 4.11: Net normal stresses on bottom chord at A1 for LS2 (1.0LL with 445 N (100 lb) hanging load)

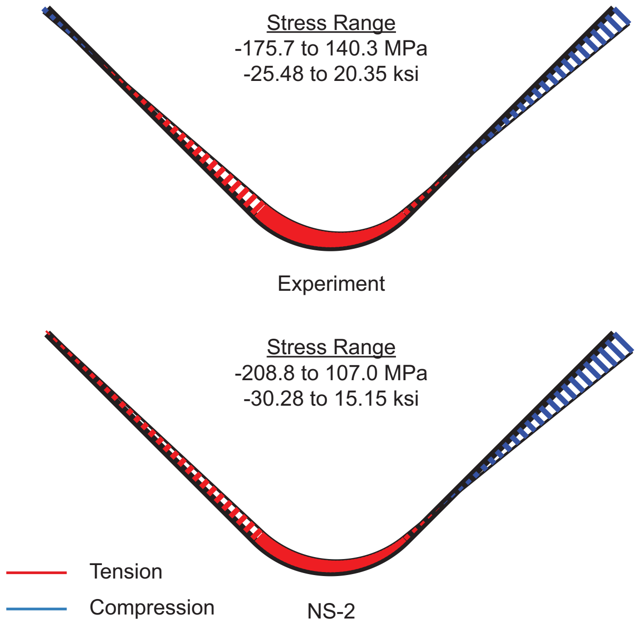

Figure 4.12: Normal stresses on bottom chord at A2 for LS3 (0LL with 1245 N (279 lb) hanging load)

The values were recorded near the ends to verify the fixity of the connection of the web members to the chords in the out-of-plane orientation. However, the resulting experimental data did not correspond to the assumption of a linear stress distribution defined by Eq. 4.1. The strains were indicative of a stress concentration due to the proximity of the welded connection. At the bottom of position W2, the leg of the channel attached to the chord angle with the applied hanging load had a significantly larger stress. Position W1 at the top of a web presented a more balanced distribution of force to both sides of the channel, but the large difference between the measurements over the height of the channel implied a stress concentration or that significant bimoment and bending in both directions would need to exist. In both cases, the measured results reflected a complicated local stress effect that a line element could not reproduce and, as such, were excluded from the study.

4.6 Computational Model Comparison

The computational results given in Section 4.5 were produced from a second-order analysis of a model that considered non-symmetric behavior, nominal cross sections, and a deformable vertical hanging rod. Each of these features was identified as an option that an engineer could decide whether or not to include in their structural analysis model. As such, the model described in Section 4.4 was modified to study the effects of individually changing these assumptions. A total of four additional scenarios were considered as

Table 4.6: Alternative model summary

Model	Label	Alteration
Baseline	NS-2	-
1	NS-1	First-order analysis
2	NS-2-R	Vertical rod segment is excluded
3	DS-2	Doubly-symmetric line elements
4	NS-2-M	Measured section properties

Table 4.7: Vertical deflections near applied load from the various analysis methods. Error relative to NS-2 result.

Model	LS1 w/ 445 N (100 lb)		LS2 w/ 445 N (100 lb)	
	Defl.-mm(in)[Error]	Rotation [Error]	Defl.-mm(in)[Error]	Rotation [Error]
NS-2	10.1 (0.40)	-6.1°	17.1 mm (0.67 in)	-5.7°
NS-1	10.9 (0.43) [8.4%]	-8.0° [31.2%]	18.3 (0.72) [7.1%]	-8.0° [41.3%]
NS-2-R	10.3 (0.40) [1.8%]	-7.2° [17.9%]	17.2 (0.68) [0.9%]	-6.6° [16.2%]
DS-2	9.1 (0.36) [-10.0%]	-5.0° [-17.9%]	16.1 (0.63) [-5.8%]	-4.7° [-16.6%]
NS-2-M	10.0 (0.39) [-0.9%]	-6.0° [-1.2%]	16.9 (0.67) [-0.7%]	-5.6° [-1.5%]

summarized in Table 4.6. For the first alternative, the second-order analysis, NS-2, was replaced with a first-order analysis of the existing model, NS-1, because steel joists are commonly designed based on first-order results. The second alternative, NS-2-R, excluded the vertical rod because the exact hanging elevation might not be readily available or the rod may be assumed to have negligible bending stiffness. Instead, the hanging load was applied at the end of the rigid horizontal member. The third alternative ignored the effects of non-symmetric behavior and evaluated the joist with doubly-symmetric elements with warping, DS-2. The section properties for the chords and webs were updated to exclude the non-symmetric values calculated by MSASect. The cross sections were still modeled in the principal orientation, similar to the approach used in many commercial structural analysis programs, and this improved the prediction of bi-axial bending response. The fourth alternative, NS-2-M, considered the effects of the imperfect cross sections. While retaining the overall joist geometry, the cross-section properties of all members were updated based on the measured geometry, which is presented in Section 4.6.4.1.

After modifying each model, similarities were still observed across the different analysis methods, such as the midspan deflection for Loading Scenario 1 and 2 was within 1% error for all models. However, the results diverged as other information was investigated including deformations as highlighted in Table 4.7 and Fig. 4.14, as well as by the stresses depicted in Fig. 4.13 and internal forces as shown in Table 4.8.

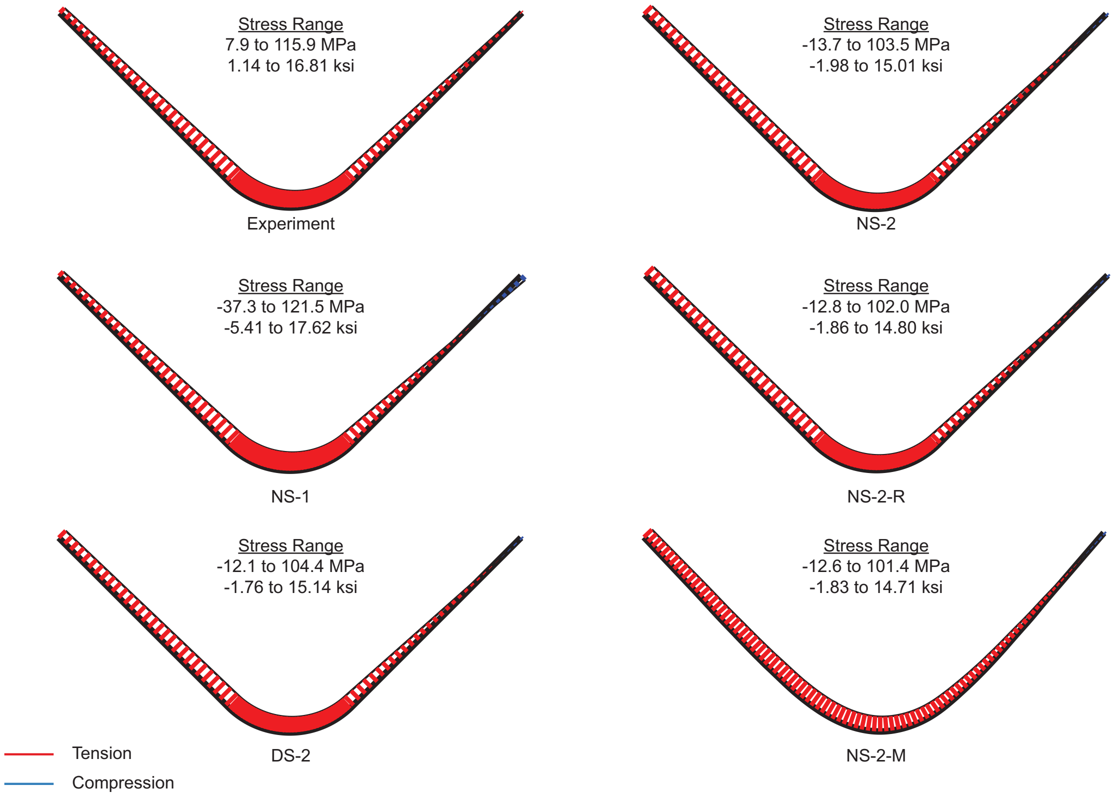

Figure 4.13: Normal stresses on bottom chord at A2 for LS1 (0.5LL with 445 N (100 lb) hanging load)

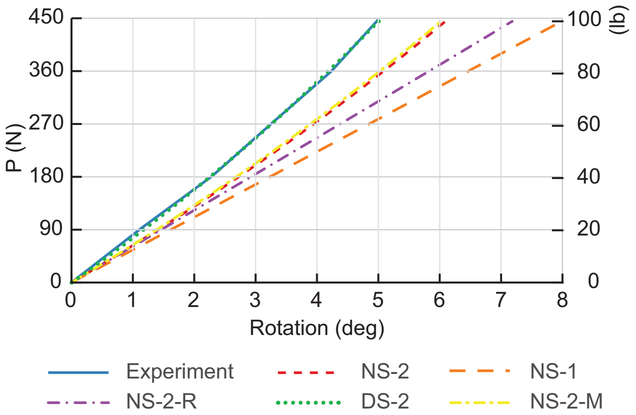

Figure 4.14: Twist of loaded bottom chord at A2 for LS 1

Table 4.8: Change in net axial force in loaded chord at hanging load

Model	Axial Force [Error to NS-2]	
	LS2 w/ 445 N (100 lb)	LS3 w/ 1240 N (279 lb)
NS-2	792 N (178 lb)	1761 N (396 lb)
NS-1	336 N (75.5 lb) [-57.6%]	937 N (211 lb) [-46.8%]
NS-2-R	801 N (180 lb) [1.2%]	1647 N (370 lb) [-6.5%]
DS-2	621 N (140 lb) [-21.6%]	1559 N (351 lb) [-11.4%]
NS-2-M	792 N (178 lb) [0.0%]	1737 N (390 lb) [-1.4%]

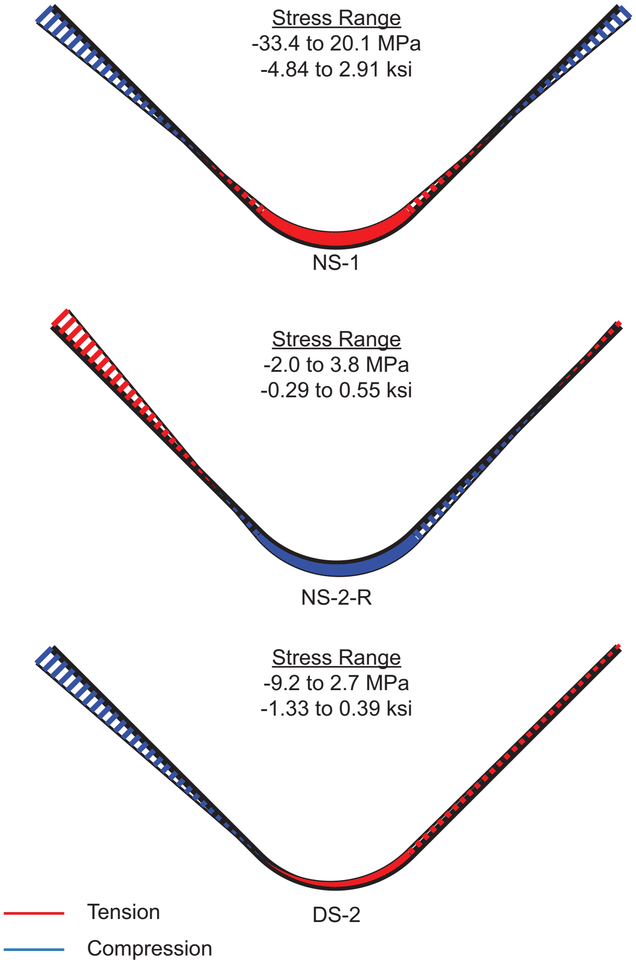

Figure 4.15: Variation in normal stresses on bottom chord at A2 compared to NS-2 for LS2 (0.5LL with 445 N (100 lb) hanging load)

4.6.1 First- vs. second-order (NS-1 vs. NS-2)

The first-order analysis, NS-1, consistently resulted in larger rotations, translations, and stresses relative to NS-2. By only considering equilibrium on the undeformed geometry, the effects of reduced applied torsion and increased bending stiffness of the rotated chord angle were not included. Instead, the NS-1 angles supported significantly larger weak axis bending moments. This combination led to the 5% errors in NS-1 compared to NS-2 in Fig. 4.13 due to the larger bending stresses captured by NS-1. This difference in internal response is better illustrated by Fig. 4.15 which shows the net stress differences between NS-2 and the analysis result (i.e., the additional stresses needed to be added to the NS-2 distribution to obtain the indicated analysis result, which is NS-1 in this case).

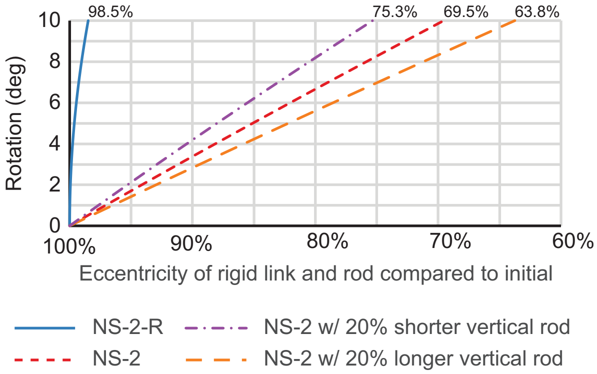

Figure 4.16: Variation in eccentricity of hanging load

4.6.2 Including vs. excluding vertical hanging rod (NS-2 vs. NS-2-R)

The analysis which excluded the direct modeling of the hanging rod, NS-2-R, resulted in negligible reductions in the eccentricity, which caused larger twist and deflections relative to NS-2, which is similar to the results from NS-1. While both NS-1 and NS-2-R captured increased torsional demands, the updated orientation from the second-order analysis in NS-2-R allowed for more bending moment to be supported about the strong axis of the angle, thereby resulting in a better agreement with the baseline than for NS-1, as noted in Fig. 4.15.

In typical applications, a small rod is generally considered to have minimal bending stiffness. However, in this joist application the flexural stiffness is relatively rigid compared to the much lower torsional stiffness of the individual angle. The rotation of the chord thus leads to a rapid change in the effective eccentricity of the applied hanging load as highlighted in Fig. 4.16.

4.6.3 Non-symmetric vs. doubly-symmetric elements (NS-2 vs. DS-2)

The different mechanical response of the DS-2 analysis resulted in an underestimation of the expected displacements as shown in Fig. 4.17. Of the various mechanics not fully captured by the doubly-symmetric analysis, the inaccurate center of rotation at the centroid led to an underestimation of the applied torsion due to the hanging load. The corresponding reduced rotation had a similar effect as a first order analysis (NS-1), which caused additional weak axis bending moment to be supported by the chord angle, thereby resulting in the stress variation highlighted in Fig. 4.15. It should be noted that prior to the applied hanging load where only top chord loading was present, the variations were less critical due to minimal rotation of the chord.

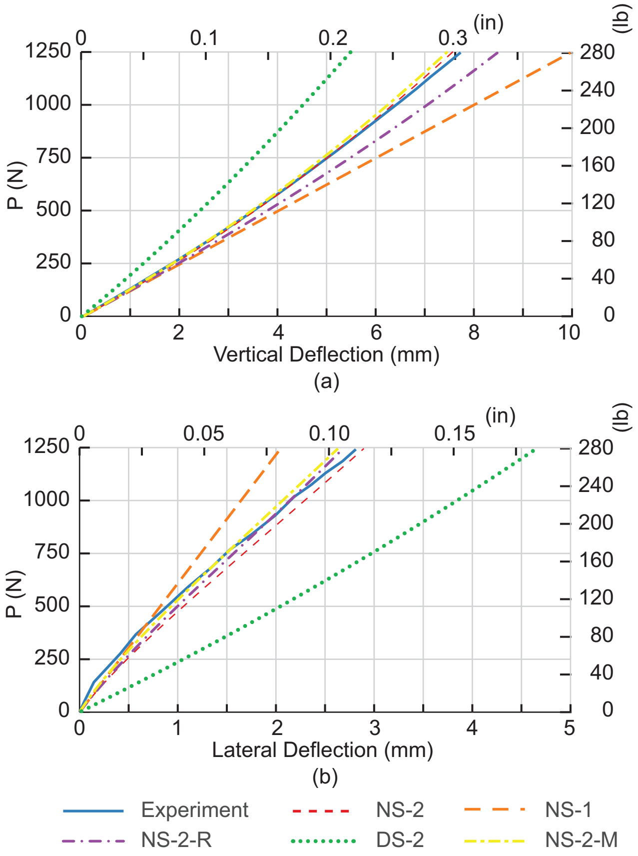

Figure 4.17: Displacement of chord at hanging load for LS 3

4.6.4 Measured vs. nominal cross-section geometry (NS-2-M vs. NS-2)

During the experimental phase, visible variations from the nominal geometry were noted for the cold-formed members. Hand measurements had been taken to confirm the overall dimensions of each member before testing, but the true curved profile was not obtained. Noting the variations between the experimental results and computational analyses, detailed information on the imperfect geometry was obtained so the exact sections could be considered during the analysis.

4.6.4.1 Measured Cross-Section Data

Measurements of the joist cross-section member geometry were obtained with the Artec Leo, which is a handheld 3D scanner, utilizing the methodology discussed by Xia and Blum [58]. After completion of the experiments detailed in Section 4.3, the joist was scanned to obtain the necessary point cloud information to determine the member cross sections for the five different cold-formed sections. The corresponding analysis only accounted for the cross-section variations and not the member imperfections - thus any slight alteration due to the experiment was not of concern. To ensure the original geometry was captured, the measurements were taken away from any location where plastic deformation would have been plausible (although very little was expected), which included the joints and other areas of high stresses. The joist was scanned in four different orientations to obtain overlapping point cloud data, which would be used to reconstruct a section of the joist in the Artec Studio software [59]. After creating a sharp fusion model of the data, the point cloud information was imported into MATLAB [60]. The data was then divided into the different structural components (e.g. web 1, web 2, chord angle). Each separate component was then segmented every 3.2 mm (1/8 inch) along its length to determine the cross section at any location along the member longitudinal axis. The data for each segment was used to create a curve using a Savitzky-Golay smoothing filter that defined the exterior profile of the section. This curve was offset based on the nominal thickness of the member to define the approximate centerline profile of the scan as shown in Fig. 4.18(a). The nominal value was used instead of measured value because measurements at the tip of the various cross sections were consistently within 0.03 mm (0.001 in) of the nominal value and a more accurate average across the complete geometry was not obtained due to the limited flat surfaces. Fig. 4.18(a) depicts the ideal case where the entire cross section could be completely captured; however, line of sight constraints caused gaps in some profiles. To consistently evaluate the different sections, the estimated centerline profile was modified to only include data from the more readily scanned surface of each cross section including the exterior face for the channel webs and interior face for the angle chords. The data processing tends to smooth sharp corners resulting in a rounded profile compared to the actual sharp edge of the plate, which is evident in the end of the centerline profile. The end of the estimated profile was replaced with a straight-line section to agree with the observed geometry. The estimated centerline profile was evaluated at each end to identify where the leg became a straight-line beyond the corner bends and then deviated off that straight line. Beyond that deviation, the centerline was replaced with a straight-line segment that extended to match extreme value of the exterior profile, such that a perpendicular line to the final centerline would touch the tip of the scan data as shown in Fig. 4.18(b).

The scan data from the left end of the joist, highlighted in blue in Fig. 4.2, was used to determine measurements for the five cross sections listed in Table 4.2. For the purposes of this project, a single updated cross-section profile, uniform along the member length, was desired for each of the five cross sections. The final cross-section profiles were selected from the middle of each member to avoid any potential plastic deformations, where the best agreement between the interior and exterior scan data based on the centerline profile was found. Due to the similarity between the loaded and non-loaded angle geometries, only

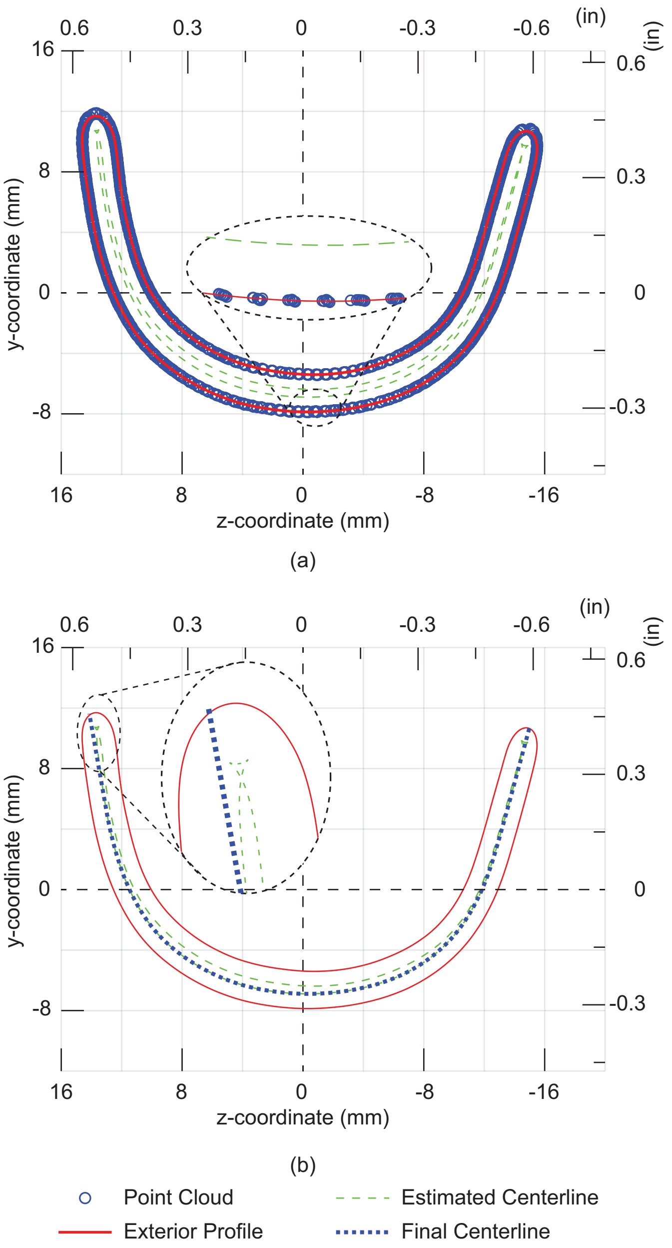

Figure 4.18: Point cloud data with calculated profiles. (a) Point cloud data with exterior profile. (b) Exterior profile and resulting centerline information.

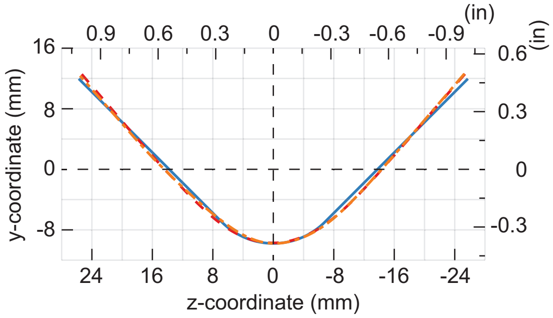

(a) Top Chord

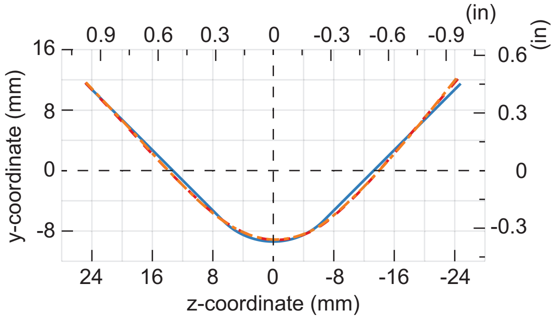

(b) Bottom Chord

Figure 4.19: Measured versus nominal cross-section geometry. (a) Top Chord (b) Bottom Chord

Table 4.9: Section properties of measured chords with percent difference to nominal values

Section Property	Top Chord	Bottom Chord
A [mm^2 (in^2)]	235 (0.365) [0.7%]	194 (0.301) [0.5%]
J [mm^4 (in^4)]	909 (2.18 x 10^{-3}) [0.7%]	551 (1.32 x 10^{-3}) [0.5%]
Iz [mm^4 (in^4)]	11289 (2.71 x 10^{-2}) [6.3%]	8304 (1.99 x 10^{-2}) [2.4%]
Iy [mm^4 (in^4)]	55486 (1.33 x 10^{-1}) [1.7%]	43024 (1.03 x 10^{-1}) [2.9%]
ys [mm (in)]	-13.3 (-0.525) [5.5%]	-12.6 (-0.495) [3.3%]
zs [mm (in)]	0.05 (0.002) [N/A]	0.58 (0.023) [N/A]
Cw [mm^6 (in^6)]	46104 (1.72 x 10^{-4}) [289.0%]	42137 (1.57 x 10^{-4}) [380.9%]

the cross-section properties of the loaded chord members were used in the analysis model, which are summarized in Table 4.9 and shown in Fig. 4.19. The channel web scan results are shown in Fig. 4.20 with the updated cross-section properties summarized in Table 4.10. To validate the consistency of the measured result, a second Web 3 cross-section profile was measured and analyzed. As seen in Fig. 4.20(c), the second web profile (interior web) presented a slightly less curved geometry at the channel base and a small variation on the inclination of the right side; however, these differences were insignificant compared to the variation from the nominal profile.

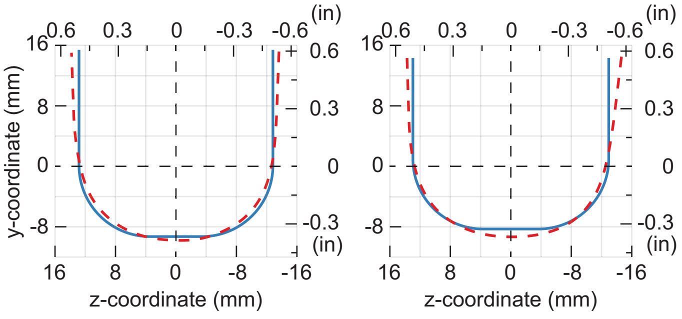

(a) Web 1 (b) Web 2

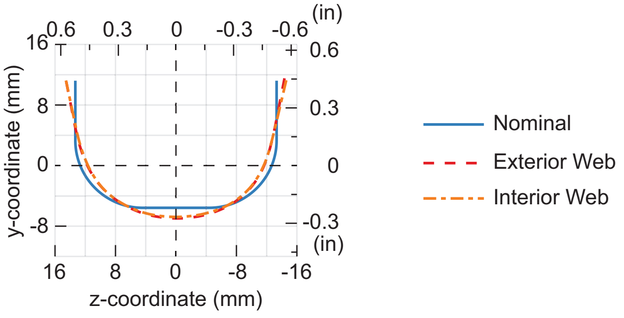

(c) Web 3

Figure 4.20: Measured versus nominal cross-section geometry. (a) Web 1 (b) Web 2 (c) Web 3

Table 4.10: Section properties of measured webs with percent difference to nominal values

Section Property	Web 1	Web 2	Web 3
A [mm^2 (in^2)]	191 (0.296) [-2.3%]	171 (0.264) [1.2%]	102 (0.158) [-0.2%]
J [mm^4 (in^4)]	544 (1.31 x 10^{-3}) [-2.3%]	404 (9.72 x 10^{-4}) [1.2%]	129 (3.11 x 10^{-4}) [-0.2%]
Iz [mm^4 (in^4)]	11962 (2.87 x 10^{-2}) [-4.7%]	9952 (2.39 x 10^{-2}) [9.4%]	3445 (8.28 x 10^{-3}) [13.9%]
Iy [mm^4 (in^4)]	23285 (5.59 x 10^{-2}) [0.6%]	21086 (5.07 x 10^{-2}) [6.4%]	11214 (2.69 x 10^{-2}) [-2.5%]
ys [mm (in)]	-18.7 (-0.738) [-3.1%]	-17.8 (-0.702) [2.5%]	-12.7 (-0.500) [6.1%]
zs [mm (in)]	0.20 (0.008) [N/A]	-0.48 (-0.019) [N/A]	0.24 (0.010) [N/A]
Cw [mm^6 (in^6)]	684637 (2.55 x 10^{-3}) [-29.6%]	530953 (1.98 x 10^{-3}) [-22.9%]	113620 (4.23 x 10^{-4}) [-44.5%]

4.6.4.2 Results

Despite the significant changes to the cross-section properties particularly in the warping constant, the NS-2-M analysis was found to be in good agreement with NS-2. The NS-2-M analysis results indicated small differences from the baseline analysis (NS-2) for LS 1 and LS 2. The two main differences were the total torsion supported by the webs and the calculated bimoment across the whole joist. Additional torsion was observed in the webs of NS-2-M compared to NS-2, but the maximum 730 N-mm (6.5 in-lb) torque resulted in a negligible stress. Bimoment presented an interesting issue because typical practice would assume no warping stiffness of angles and not include bimoment effects. However, the utilized analysis method requires a warping stiffness and one can be calculated for each cross sections, including the chord angles due to the rounded radius in addition to mentioned deviations from the nominal geometry. Focusing on the angle chords, the

NS-2-M bimoment results were 75% larger than the NS-2 baseline results. Despite the large variation, the resulting maximum normal stresses, 41 MPa (5.9 ksi) for NS-2 versus 63 MPa (6.2 ksi) for NS-2-M, were comparable due to the different warping constants. In either case, these values would be a significant stress if considered. However, this stress is highly localized to the heel of chord angles near applied torques and the adjacent supports. Additional work would be required to determine the appropriate approach on how to address any such bimoments and how they should be used when designing for the strength of the angle.

4.7 Non-Loaded Chord Angle Behavior

Throughout the experiment, bottom chord rotations were recorded along the length of each angle in the test joist. As previously shown in Fig. 4.8c, Fig. 4.9c, and Fig. 4.14, the non-symmetric analysis was able to capture similar rotation of the loaded chord angle, including the decreasing rate of rotation associated with the changing eccentricity. The analysis methods were also observed to predict the rotation of the non-loaded chord angle away from the applied load as shown in Fig. 4.21(a). However, the non-loaded chord angle adjacent to the applied load exhibited an asymptotic response that was not captured by the line element analyses as depicted in Fig. 4.21(b). This limited twist combined with the stress concentration at position W2 (Fig 4.6), previously mentioned in Section 4.5, indicated there were likely additional in-plane cross-section deformations that contributed to the discrepancies. While such behavior cannot be directly incorporated into the existing line element, the existing lateral connection between the webs and chords provide a plausible means to improve the response in future work. The current rigid link connection results in a bending and twisting response that is nearly a fixed-fixed boundary condition on the chords. One possible alternative would be the use of a more flexible connection element that causes internal forces to stay in the loaded chord. This could also include semi-rigid connections to limit the maximum moment transferred to simulate the asymptotic behavior observed in Fig. 4.21b.

4.8 Conclusions

This study presented the testing and evaluation of a steel joist structural assembly subjected to an eccentric hanging load. A pair of steel joists were connected with bracing and decking to form a self-stabilizing system. A simulated uniform design live load was applied to the deck followed by the application of an eccentric hanging load to one of the bottom

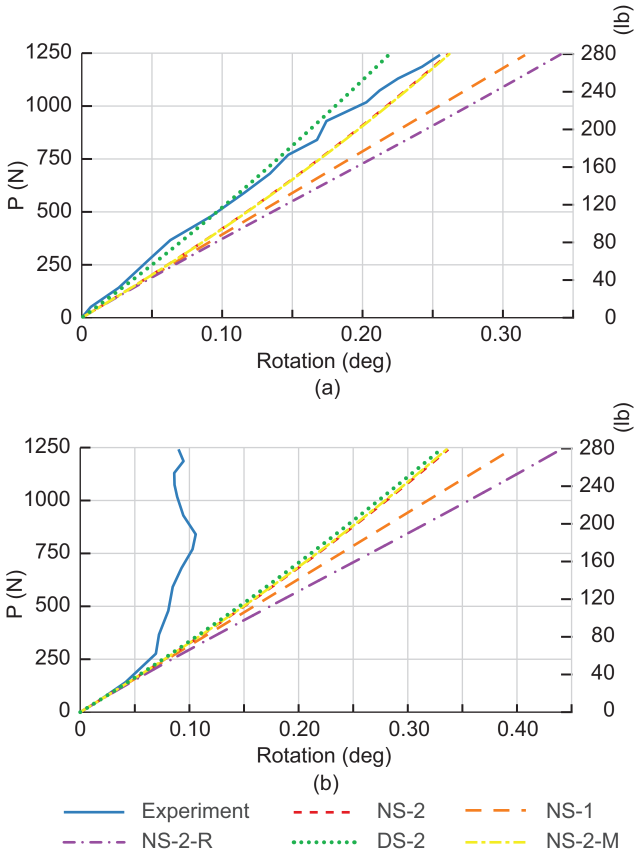

Figure 4.21: Rotation of non-loaded bottom chord angle for LS 3. (a) In panel to the left of applied load (R2u) and (b) In same panel as applied load (R4u)

chord angle members on the tested joist. During the experiment, strain and displacement information was recorded along the bottom chord. The imperfections of the joist were measured and analyzed to determine the true cross-section dimensions of all members. A computational model using a novel beam element formulation, which incorporates non-symmetric section behavior, was created. The displacement and stress output were compared to the experimental results. The computational model was able to accurately calculate deformations for the full experiment; however, it produced an incorrect stress estimate resulting from the hanging load by adding excessive compression to tension-controlled regions.

Additional computational models were created to study the effects of a first- vs. a second-order analysis, a non-symmetric vs. a doubly-symmetric analysis, nominal vs. measured cross-section geometry, and the effect of the hanging rod position on the analysis of a steel joist with an eccentric handing load. It was found that underestimating the rotation of the cross-section at equilibrium, whether due to underestimating the applied torque with a doubly-symmetric analysis or assuming the initial orientation associated with a first-order analysis, led to excessive weak-axis moments and compressive stresses on the horizontal legs. Likewise, the analysis captured excessive rotations and displacements of the cross section when not adequately accounting for the reduced eccentricity of the hanging load, which is associated with a first-order analysis or excluding the relatively stiff hanging rod, due to the low torsional stiffness of the chord. Although significant variations in the actual torsional cross-section properties relative to nominal were measured, it had minimal impact on the observed displacements and stresses. It is recommended that future work to improve joist modeling with line elements should focus on properly defining the out-of-plane web to chord connections.

5 FLEXURAL-TORSIONAL BUCKLING AND DOUBLE ANGLE JOIST AND JOIST GIRDER CHORDS

Sippel, Edward J., Ziemian, Ronald D., and Blum, Hannah B., "Influence of torsional stiffness in double angle open-web joist and joist girder chords." Submitted to *Journal of Constructional Steel Research*, (2022).

Abstract

The double angle chords of open-web steel joists are often designed to efficiently support loading with relatively slender sections, which introduces buckling instabilities that are treated differently by various design standards. This study investigated the buckling behavior of double angles, focusing on the importance of flexural-torsional buckling. A theoretical inelastic buckling investigation considering current design practices and known steel behavior demonstrated how flexural-torsional buckling does not control for all double angle configurations. Subsequent investigation focused on double angles theoretically susceptible to flexural-torsional buckling, while implementing finite element modeling of full joist structures and isolated chord segments. The resulting elastic and inelastic buckling analyses captured significant twisting of individual angles in the built-up section; however, global flexural-torsional buckling was not observed to control. Most double angle configutions were controlled by flexural buckling due to an increased flexural-torsional buckling capacity. This result was attributed to the observed increased torsional stiffness of the chords, which is typically not considered in design. A supplementary investigation indicated this torsional stiffness was primarily a result of torsion being transferred through the stiff chord-to-chord connections, which do not exist in all double angle members. Accounting for the additional torsional stiffness in a theoretical inelastic buckling calculation led to flexural-torsional buckling not controlling the design of most double angle cross sections considered in this study. Overall, this study indicates that designing double angles in joist structures by only considering flexural buckling with local buckling is reasonable with current industry practices.

5.1 Introduction

The elastic buckling behavior of members subjected to compression includes a combination of global flexural and torsional buckling in addition to local buckling effects. Typical steel design provisions utilize this elastic behavior as a basis to calculate the design capacity of a member. When working with non-doubly symmetric sections, Eurocode 3 [16], the Australian Standard for Steel Structures, AS 4100, [17] and the American Institute of Steel Construction's (AISC) Specification for Structural Steel Buildings, AISC 360, [1] all require that flexural-torsional buckling be considered in the design process in addition to flexural buckling and local buckling effects. However, exceptions to neglect flexural-torsional buckling exist, such as single angles designed per AISC 360. Instead, single angles are allowed to be evaluated for only flexural buckling with local buckling reductions as this procedure was determined to adequately predict the buckling capacity of single angles [8]. The idea that accounting for both flexural-torsional behavior and local buckling reductions with current design procedures is overly conservative has been indicated by other researchers [61], [62]. They demonstrated how the flexural-torsional buckling capacity in single angles was equivalent to the plate buckling capacity underlying the local buckling reduction indicating that applying both reductions effectively double counted the same phenomenon. To address the resulting conservative results for flexural-torsional buckling, Behzadi-Sofiani *et al.* [62] suggested a modified buckling relationship that considered the flexural buckling capacity to adjust the design capacity when flexural-torsional buckling controls.

Double angles are typically designed considering flexural-torsional buckling in addition to flexural buckling and local buckling. However, some standards, such as in the Structural Standard for Antenna Supporting Structures and Antennas, TIA-222-G, [63] and the Steel Joist Institute (SJI) Standard Specification for K-Series, LH-Series, DLH-Series Open Web Steel Joists and for Joist Girders, SJI 100, [9], require that only flexural and local buckling effects be considered in design. Currently, there is no clear reference to why these provisions were implemented. Nevertheless, the well-established history of existing joist performance and various production testing has indicated that double angle chords in joists and joist girders are adequately designed by only considering flexural buckling. Additionally, a study on double angle buckling by Simpson Gumpertz & Heger Inc. [10] noted that the consideration of flexural-torsional buckling produced overly conservative results at low slenderness ratios while the exclusion of flexural-torsional buckling was unconservative for some geometries.

This paper summarizes an investigation into the behavior of double angles, specifically focused on double angles used for joist and joist girder chords. A discussion of the theoretical buckling response is followed by a finite element-based parametric study utilizing full-scale joists and joist chord segments. Further investigation of the observed torsional response was completed to provide insight on the composite behavior of built-up double angle members.

5.2 Background

Kennedy and Murty [64] subjected equal-leg double angles spaced 6.4 mm apart to concentric compression through a support bracket, which was tested for both a fixed and pinned condition. Each angle pair was attached to the supports with three bolts through the vertical legs with an additional bolt at midspan for composite action. The experimental results consistently exceeded the controlling theoretical buckling response. When flexural-torsional buckling controlled, the experiments also exceeded the local buckling limit except when flexural buckling was more critical. Kitipornchai and Lee [65], [66] investigated double angles spaced 5 mm apart with pinned supports. The experimental compression tests resulted in deformed geometries that were difficult to separate into distinct flexural, flexural-torsional, and local buckling modes, but generally exceeded the controlling theoretical buckling mode. The analytical investigation of inelastic buckling indicated that flexural-torsional buckling would be a critical factor in unequal-leg double angles but would not be prevalent in equal-leg double angles based on the strong-axis to weak-axis moments of inertia ratio. Astaneh-asl *et al.* [67] noted similar combinations of buckling behaviors but also that the buckling capacity of the double angles was greater when using welded connections instead of bolts. Temple and Tan [68] did not observe a significant variation between bolted and welded connections for weak-axis flexural buckling when angles were widely spaced, which captured primarily flexural buckling. A deeper investigation of bolted double angles by Sherman and Yura [69] found that the end connection slip directly impacted buckling capacity, but there was minimal increased buckling capacity when increasing the number of interior bolts from the minimum allowed to the number required to achieve full elastic buckling, two and five bolts per AISC, respectively.

The underlying mechanics of the built-up member interaction has been studied by many researchers with a focus on cold-formed steel sections [70]–[80]. Directly related to the previous hot-rolled steel research, Rasmussen *et al.* [81] presented the mechanics behind how variable connection stiffness would impact the flexural and torsional stiffness of built-up cold-formed steel members. Recently, Alenezi and Mohareb [82] provided a solution for the mechanics of a double angle in compression that considered individual angle response between the constrained displacement of the build-up section at connected locations. While considering global buckling phenomena, Alenezi and Mohareb determined that flexural-torsional buckling is underestimated by AISC 360 [1] when accounting for angle-to-angle connections that ensured uniform displacements of the chords except for allowing free torsional rotation of the connection itself. With this limitation on the chord interaction, flexural-torsional buckling was still found to be a critical failure mode in various applications.

5.3 Theoretical Buckling Behavior

The basis of compression member design is elastic buckling that incorporates the global limits of flexural, torsional, or combined flexural-torsional buckling and local effects. Building upon the elastic buckling response, inelastic buckling design utilizes a tangential buckling approach based on flexural buckling behavior to convert the limiting elastic buckling stress to the critical buckling stress. Typically, the same relationship is used to convert elastic flexural-torsional buckling to the critical stress. However, previous research [8], [65], [83] has shown that there is a different change in stiffness observed for the modulus of elasticity, E, and the shear modulus, G. Galambos [8] demonstrated how different stiffness reductions for shear and longitudinal behavior could combine into a single equation representing the full design provisions, which is explained in more detail in work by Sippel et al. [84]. The standard elastic buckling relationship can be modified to determine the inelastic critical buckling stress, f_{in}, as shown in Eq. 5.1;

$$\begin{aligned}\left(f_{in} - f_{xb}\tau_E\right)\left(f_{in} - f_{yb}\tau_E\right)\left(f_{in} - \frac{\tau_G GJ + \tau_E \pi^2 E C_w/L^2}{r_0^2}\right)\\ -f_{in}^2\left(f_{in} - f_{yb}\tau_E\right)\frac{x_0^2}{r_0^2} - f_{in}^2\left(f_{in} - f_{xb}\tau_E\right)\frac{y_0^2}{r_0^2} = 0\end{aligned} \tag{5.1}$$

where $f_{xb} = \pi^2 E/\left(L/r_x\right)^2$ and $f_{yb} = \pi^2 E/\left(L/r_y\right)^2$ are the critical flexural buckling stresses about the principal x- and y-axis, respectively, $r_x = \sqrt{I_x/A}$ and $r_y = \sqrt{I_y/A}$ are the radii of gyration about the principal x- and y-axis, I_x and I_y are the moments of inertia about the principal x- and y-axis, A is the cross-sectional area, J is the torsion constant, C_w is the warping constant, G is the shear modulus, L is the effective length, τ_E and τ_G are the stiffness reduction factors for longitudinal and shear stiffness, $r_0 = \sqrt{r_x^2 + r_y^2 + x_0^2 + y_0^2}$ is the polar radius of gyration about the shear center, and (x_0, y_0) are the coordinates of the shear center relative to the centroid.

Eq. 5.1 was evaluated using a τ_E factor based on the SJI 100 steel design provisions, which are similar to the requirements in AISC 360-16 and AS 4100. The two-stage buckling relationship was rearranged to define the design τ_E given by Eq. 5.2;

$$\tau_E = \begin{cases} 0.877 & \text{if } \frac{f_{in}}{f_y} \leqslant 0.877/2.25 \\ \frac{1}{\ln(0.658)}\frac{f_{in}}{f_y}\ln\left(\frac{f_{in}}{f_y}\right) & \text{otherwise} \end{cases} \tag{5.2}$$

where f_y is the yield stress.

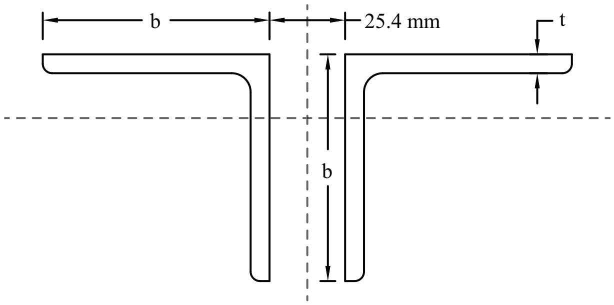

Figure 5.1: Typical double angle chord geometry

Galambos [8] previously used this relationship to indicate that flexural-torsional buckling was not likely to control the design of single angles but found that when considering the breadth of plausible double angle geometries, which included both unequal- and equal-leg sections, multiple spacings between the vertical legs of the angles, and different connection methods, flexural-torsional buckling could actually control in some applications. This study limited the scope to only equal-leg double angles spaced with 25.4 mm between the vertical legs as depicted in Fig. 5.1 to determine if the same generalization still applied. Seventy-one equal-leg double angle cross sections were evaluated for this study, spanning b between 32 mm and 203 mm with b/t ratios ranging from 6 to 16, which are representative of joist designs per SJI.

This flexural-torsional buckling study included variations in the shear stiffness via two values for τ_G and in the warping stiffness of double angles via three values for C_w. In line with previous research [8], [65], [83], an upper limit of $\tau_G = 1.0$ was used to capture the full shear stiffness of the section as minimal reduction was observed. A reduction was estimated as $\tau_G = 0.877$ to account for imperfections and residual stresses based on critical elastic flexural buckling. The minimum value for C_w was defined based on AISC's [1] conservative design recommendation that C_w of double angles can be taken as 0 and the shear center, $S_{\mathtt{low}}$, is positioned along the axis of symmetry at the middle of the horizontal flanges similar to a tee section as shown in Fig. 5.2. An alternative conservative recommendation by the Canadian Institute of Steel Construction [85] uses the same shear center position but references a C_w equal to twice that of the single angle. Limited information was available on the twist response of built-up double angles; therefore, an estimate of a fully composite behavior was determined using a thin-walled approximation by assuming a connection between the angle heels with no thickness which resulted in a new shear center, $S_{\mathtt{high}}$, and a significantly increased C_w, greater than $100\times(\text{Low } C_w)$ in some configurations. These three C_w values were considered to investigate the impact of warping stiffness and are identified as $C_w = 0$, Low C_w, and High C_w, respectively.

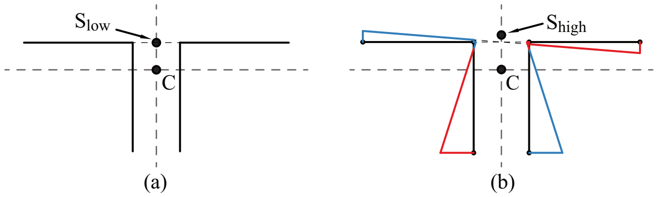

Figure 5.2: Assumed double angle warping behavior (a) AISC/CISC (b) Est. upper bound

For each alternative C_w, four inelastic buckling curves were determined for lengths up to 200 times the minimum radius of gyration. The upper bound was determined considering flexural buckling effects and labeled "FB". The lower bound for capacity was determined considering both flexural and torsional buckling effects and labeled "FTB". Two intermediate solutions were found using the τ_G factors discussed above to capture the increased shear stiffness in torsional buckling. The results labeled "$\tau_G = 1.0$" account for the maximum increase in strength while the results labeled "$\tau_G = 0.877$" include a small reduction to account for imperfections. All calculations included local buckling reductions based on the SJI provisions [9]. These provisions vary between different specifications but are based on the same local plate buckling concepts. While this variation does alter the final capacities, the impact is not discussed in further detail in this paper because the focus of this study is on ability to exclude flexural-torsional buckling checks, not the appropriate local buckling reduction.

This study identified multiple double angle cross sections expected to be controlled by flexural buckling over flexural-torsional buckling. Compact sections, such as the 2-L203x203x25 shown in Fig. 5.3, were controlled by flexural buckling about the x-axis when accounting for the increased shear stiffness. This response was reinforced by accounting for a non-zero C_w, further increasing the flexural-torsional buckling capacity. However, this trend was not absolute and flexural-torsional buckling became the controlling mechanism as the legs became more slender as depicted in Fig. 5.4 and Fig. 5.5. Despite the increases indicated, multiple double angle cross sections were still controlled by flexural-torsional buckling with significantly lower capacities in agreement with past research. However, this result does not align with the well-established history of existing joist performance and various production testing that indicate joists and joist girders are adequately designed by only considering flexural buckling. As a consequence, further investigation using advanced finite element models was implemented to validate whether flexural-torsional buckling or flexural buckling was observed at failure.

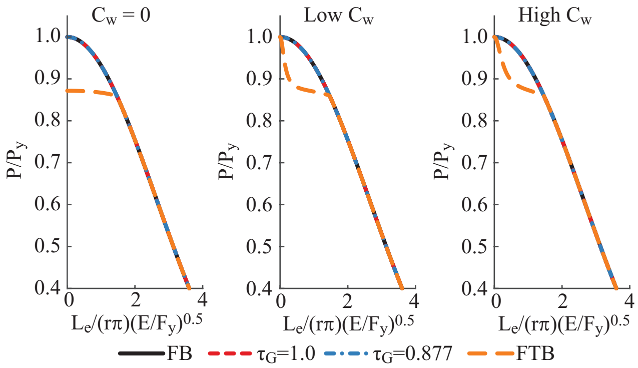

Figure 5.3: Inelastic buckling of a 2-L203x203x25 controlled by flexural buckling

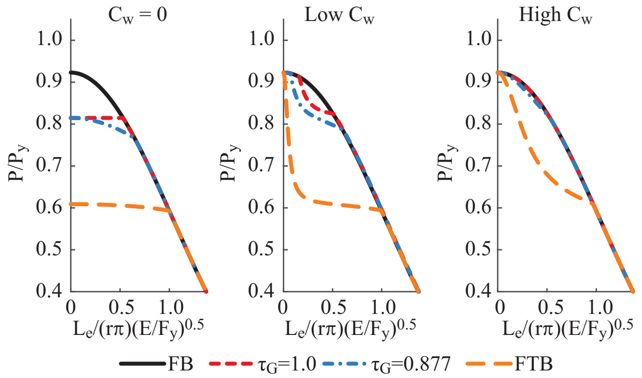

Figure 5.4: Inelastic buckling of a 2-L76x76x5.8 with limited critical flexural-torsional buckling

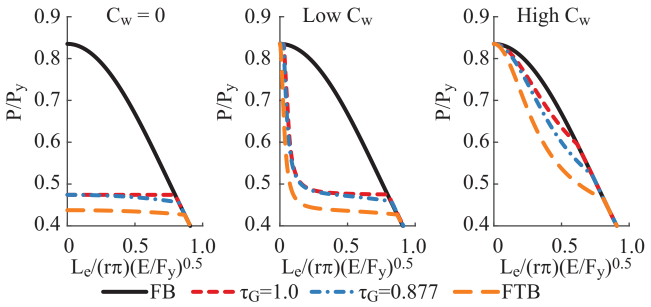

Figure 5.5: Inelastic buckling of a 2-L51x51x3.2 with significant flexural-torsional buckling

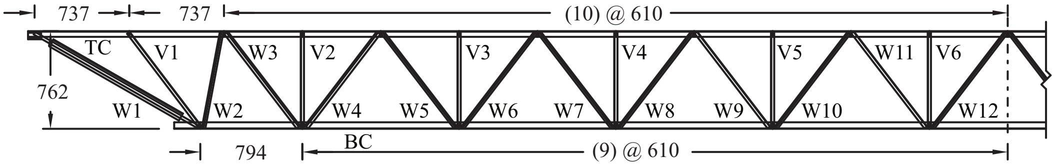

(a) Joist A

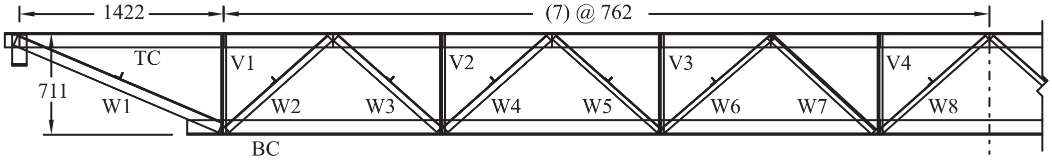

(b) Joist girder B

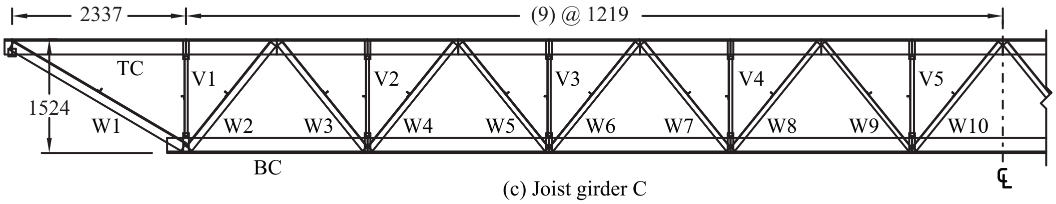

(c) Joist girder C

Figure 5.6: Elevation views of full joist models (Adapted from manufacturer's design package)

5.4 Full Joist and Joist Girder Buckling Study

A buckling study utilizing full joists and joist girders finite element models was completed to investigate the effects of flexural-torsional buckling including continuity and connection effects. The joists and joist girders were designed to have the chords fail in compression before the webs. Three different reference designs were considered as shown in Fig. 5.6 with members listed in Table 5.1. Each joist structure was evaluated for multiple chord angle sizes, listed in Table 5.2, for a total of eighteen variations, which covered a range of anticipated buckling behaviors based on the analysis in Section 5.3.

5.4.1 General Modeling Provisions

Each joist and joist girder was modeled as a simply-supported span with the appropriate lateral bracing to test buckling of the bottom chord including continuity and connection effects. The webs were sized to not fail in buckling prior to the chords. Based on the results from the validation study detailed in Sippel et al. [84], the double angle, single angle, and crimped angle members were modeled with SR4 shell elements, and the solid rod webs were modeled using C3D8R solid elements. The web-to-chord connections were modeled by connecting only the edge along the physical fillet weld without contact to simulate the fillet welds, Fig. 5.7. The flare bevel weld connecting the solid rod web to the double angle chord was modeled using a surface-to-surface tie over the approximate welded area as

Table 5.1: Full joist modeling member sizes

Label	Joist A	Joist girder B	Joist girder C
TC	2-L44x44x4.3	See Table 5.2	See Table 5.2
BC	See Table 5.2	See Table 5.2	See Table 5.2
W1	22mm Rod + L64x64x4.8	2-L76x76x9.5	2-L127x127x9.5
W2	CC32x32x4.8	2-L51x51x9.5	2-L127x127x15.9
W3	CC38x38x6.4	2-L51x51x6.4	2-L89x89x9.5
W4	CC38x38x3.5	2-L51x51x6.4	2-L102x102x12.7
W5	CC32x32x3.2	CC38x38x6.4	2-L76x76x9.5
W6	CC32x32x3.2	CC38x38x6.4	2-L76x76x12.7
W7	CC32x32x3.2	CC51x51x6.4	2-L76x76x9.5
W8	CC32x32x3.2	CC38x38x5.8	2-L76x76x9.5
W9	CC32x32x3.2	-	2-L64x64x8
W10	CC32x32x3.2	-	2-L76x76x5.8
W11	CC32x32x3.2	-	-
W12	CC32x32x3.2	-	-
V1	L25x25x2.8	CC38x38x4.3	2-L44x44x4.3
V2	L25x25x2.8	CC38x38x4.3	2-L44x44x3.9
V3	L25x25x2.8	CC38x38x4.8	2-L44x44x4.3
V4	L25x25x2.8	CC38x38x3.5	2-L51x51x4.1
V5	L25x25x2.8	-	2-L51x51x4.1
V6	L25x25x2.8	-	-

CC = Continuously crimped angle

Table 5.2: Alternative chord cross section dimensions

Reference Model	Leg (mm)	Thickness (mm)				Length (mm)	Theoretical Failure
Joist A	51	3.2	2.9	2.8	2.4	1219	Flexural-torsional
	44	3.2	2.9	2.8			Flexural-torsional
Joist girder B	102	9.5	8.7	7.9		1524	Flexural
	102	6.4	4.8				Flexural-torsional
Joist girder C	203	19	15.9	13.9		2438	Flexural
	203	12.7	11.1	9.5			Flexural-torsional

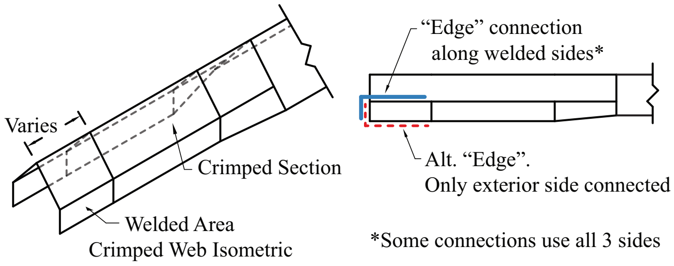

Figure 5.7: Crimped web end weld model

depicted in Fig. 5.8. The double angle chords were connected using vertical segments of 22 mm solid rods modeled in a similar fashion.

The joists were modeled as nominal 345 MPa yield steel with an elastic-plastic relationship following Eurocode 3 with a post-yield modulus of elasticity equal to $E/10,000$ [86]. Imperfections were applied in a sinusoidal pattern to each built-up double angle chord

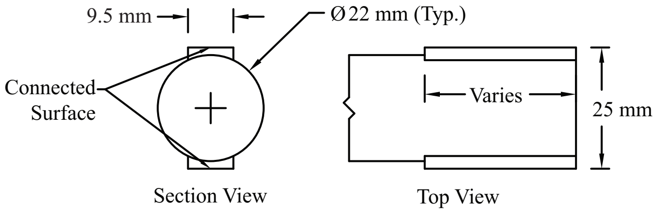

Figure 5.8: Typical solid rod to angle connection model

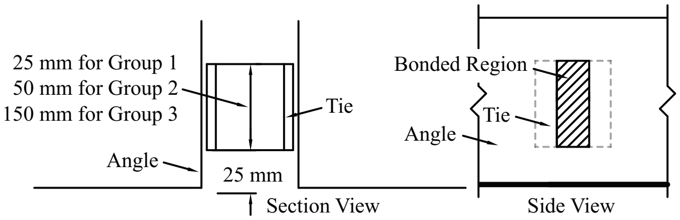

Figure 5.9: Tie between angle chord details

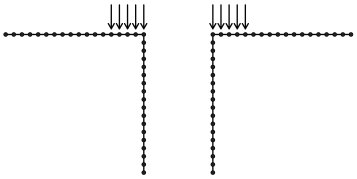

Figure 5.10: Uniform loading approximation on Group 1 top chord angles

with a half wavelength between the panel points incorporating a L/1000 displacement out-of-plane, a L/1000 displacement in-plane, and a 1° rotation. Each model was evaluated in a Riks load-controlled analysis to allow for a consistent distribution of load.

5.4.2 Individual model details

The joist A test series was subjected to uniform uplift to investigate buckling of the bottom chord. The joists were modeled as a simply-supported span with the top chord laterally supported on one chord angle at 12 inch o.c. and the bottom chord braced at all panel points. The bottom chord bracing was achieved by incorporating a horizontal bracing angle, which was laterally supported at the ends. A uniformly distributed load was applied over the entire length of the joist top chord via equal point loads on the interior 25% of the cross section as shown in Fig. 5.10.

The joist girder B test series was subjected to concentrated point loads in uplift to investigate buckling of the bottom chord. The joist girder model was a simply supported span with a discretely braced top and bottom chord at the panel points. A modified 1520 mm section of Joist A was used to model the joist bearing on joist girder interaction and to

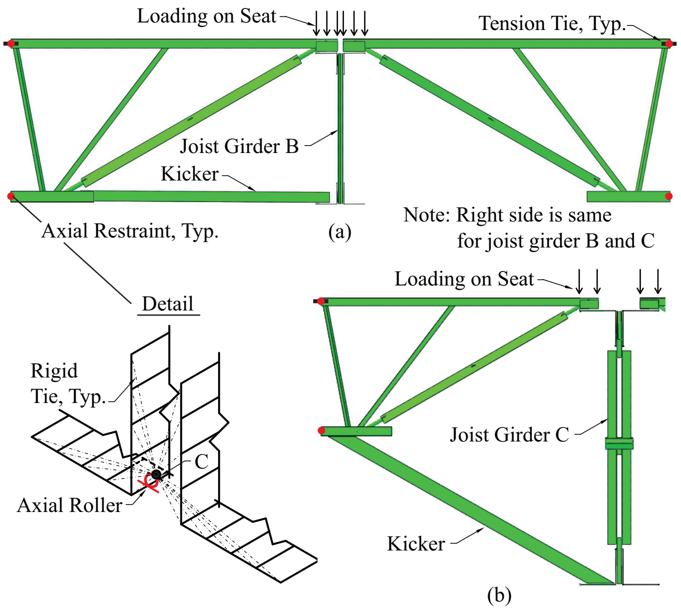

Figure 5.11: Joist girder loading and lateral bracing with axial restraint detail. (a) Joist girder B variation (b) Joist girder C variation

provide lateral support as shown in Fig. 5.11(a). The top and bottom chord axial restraints were defined separately utilizing a rigid tie between a reference node at the centroid and all end nodes on the cross section. These reaction forces combined with the L51x51x6.4 kicker on one side of the joist girder to brace the bottom chord. Aligned with typical construction practice, a second kicker was not considered to avoid creating moment continuity between the supported joists. The joist girder point loading implemented discrete loads over the length of the seat to the top chord of the modified joist A joist section, which allowed the flexibility of the joist seat and joist girder top chord to define the force distribution. To aid in model convergence, a 25-mm x 6.4-mm tension tie was pin connected to the top chord axial restraints to limit free rotation of the joist sections.

The joist girder C test series was modeled and evaluated similar to Joist girder B. Due to the larger size of the joist girder and increased applied loads, the chords of the modified joist A section were increased to 6.4-mm thick, and the kicker was replaced with a L76x76x6.4. Additionally, plasticity was eliminated from the joist A section seat material model as the applied load exceed the yield stress of the standard seat angles. The standard elastic-plastic stress-strain relationship described in Section 5.4.1 was still implemented for the remainder of the model.

Table 5.3: Full joist and joist girder modeling inelastic buckling results

Expected Buckling Mode		Cross Section	Model (kN)	SJI Design (kN)	Model/SJI
Expected Buckling Mode	Flexural-Torsional	2-L51x51x3.2	164	134	1.22
		2-L51x51x2.9	143	120	1.19
		2-L51x51x2.8	137	104	1.22
		2-L51x51x2.4	88.5	86.3	1.03
		2-L44x44x3.2	135	112	1.21
		2-L44x44x2.9	125	101	1.24
		2-L44x44x2.8	117	89.4	1.31
		2-L102x102x6.4	734	625	1.17
		2-L102x102x4.8	387	389	0.99
		2-L203x203x12.7	2938	2633	1.12
		2-L203x203x11.1	2236	2135	1.05
		2-L203x203x9.5	1600	1619	0.99
	Flexural	2-L102x102x9.5	1171	1070	1.09
		2-L102x102x8.7	1081	965	1.12
		2-L102x102x7.9	994	853	1.17
		2-L203x203x19	4728	4555	1.04
		2-L203x203x15.9	3975	3612	1.10
		2-L203x203x13.9	3380	2994	1.13
		(Model/SJI) per category		Mean	COV
		Expected Flexural-Torsional Buckling		1.15	0.10
		Expected Flexural Buckling		1.11	0.04
		All Specimens		1.14	0.09

5.4.3 Complete structure results

The joist and joist girder chords exhibited a number of complex displacement patterns at the maximum loading as noted in Table 5.3. The joist chord capacity was consistently observed to be greater than or equal to the SJI Specification's flexural buckling limit, including the effective length factor defined by SJI. The predominant deformation of the chord was in the vertical direction due to the span deflection and twisting of the chord angles as depicted in Fig. 5.12. The twisting of the chords included a combination of global and local twisting effects that made observations of post-buckling behavior difficult. The complex interaction was confirmed by evaluating the elastic buckling response, which captured five or more buckling modes within 5% of the first mode for each of the 51-mm leg angles. Each mode indicated a combination of competing individual angle and built-up chord lateral-torsional buckling shapes, all primarily located in the middle three spans.

5.5 Chord Segment Study

A simplified double angle chord segment buckling study was conducted to validate the full joist modeling results while considering both elastic and inelastic buckling. The eighteen bottom chord cross sections from the full joist modeling, listed in Table 5.2, were evaluated

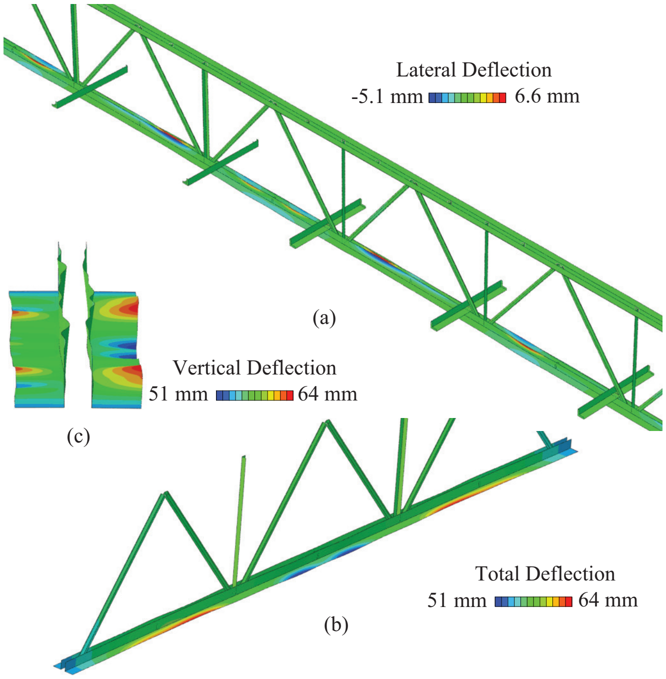

Figure 5.12: 2-L51x51x2.4 joist chord at failure. (a) Lateral displacement of full model. (b) Isometric view of bottom chord. (c) Angled end view of bottom chord.

with the same nominal effective length, L, as the full-scale model with both a pinned-pinned and fixed-fixed boundary condition. This portion of the study also varied the number of ties between the chords to account for any alteration to the observed composite behavior due to additional connections. While one connection between the double angle chords is typically adequate to meet the minimum requirements of a built-up member per the SJI Specification, this large spacing does not meet the limits for built-up members in most design standards, such as AISC 360, Eurocode 3, and AS 4100, and significant independent twisting of the individual angles was observed in the full joist investigation.

5.5.1 Modeling Details

The double angle chord segment models were based on the same modeling provisions as discussed in Section 5.4.1 using shell elements for the angles and solid elements for the ties. Each cross section was evaluated with 0, 1, 3, 7, 15, and 31 (23 for Group 1) ties evenly spaced along the length of the chords. The first subset considered a simply supported boundary condition for bending about both the weak and strong axis with a length, L. The pinned boundary condition utilized a rigid tie between a reference node at the centroid and all end nodes on the double angle as shown in Fig 5.13(a). This node was then subjected to axial load to apply uniform compression to each member. A consequence

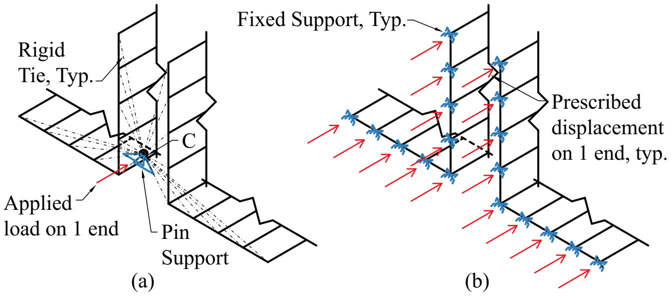

Figure 5.13: Chord segment end condition. (a) Pinned alternative (b) Fixed alternative

of this modeling approach was that the ends were fixed for warping, which resulted in a different theoretical effective length for flexural and torsional buckling. The alternative fixed-fixed series individually restrained each node as shown in Fig 5.13(b) to have the same effective length for flexural and torsional buckling. This fixed-fixed model was evaluated with a length of 2L to have an equivalent nominal effective flexural buckling length as the pinned-pinned variation. The fixed support model was loaded by providing a uniform axial displacement across the section. Each model was evaluated for elastic eigenbuckling and then inelastic buckling using the iterative-incremental Riks analysis. The first elastic buckling mode, regardless of the buckled shape, was used as an initial imperfection for the inelastic analyses with a consistent L/1000 imperfection for all models. An exception was made for the fixed end models with 0 ties because the unconnected angles behaved as separate models. To apply the first elastic mode imperfection to both angles, the first and second elastic buckling modes were applied. This was not required for the pin support as the angles interacted due to the rigid tie.

5.5.2 Elastic Chord Behavior

The elastic buckling investigation depicted a variety of flexural, flexural-torsional, and local buckling responses. Local buckling was observed as either twisting deformations in both flanges of one chord angle, which was classified as individual angles exhibiting flexural-torsional buckling as shown in Fig. 5.14(a), or different buckling patterns in the horizontal and vertical legs, which will be identified as flange buckling for simplicity, as depicted in Fig. 5.14(b). This change in local buckling mode was not driven solely by consideration of higher buckling modes but also by the amount of tie connectivity between the chords. Considering the results for the 2-L51x51x3.2 in Table 5.4 and 5.5, flange buckling behavior was largely limited to configurations with a significant number of connections between the angle members. For most practical joist applications, local buckling of the double angles resulted in single angle flexural-torsional buckling between the ties. Global

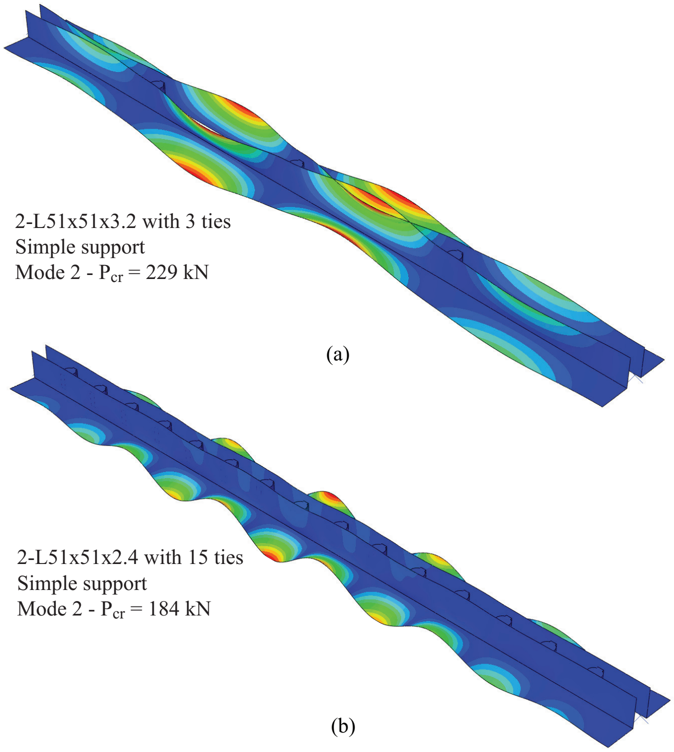

Figure 5.14: Two local buckling behaviors of double angles. (a) Individual angle flexural-torsional buckling (b) Different flange local buckling

Table 5.4: Elastic buckling of 2-L51x51x3.2 chord segment with simple support

Mode		Ties					
		0	1	3	7	15	23
1	P_{cr}	141 kN	176 kN	198 kN	204 kN	206 kN	207 kN
	Shape	g-FB+i-FTB	g-FB+i-FTB	g-FB	g-FB	g-FB	g-FB
2	P_{cr}	178 kN	195 kN	229 kN	317 kN	426 kN	440 kN
	Shape	g-FTB	i-FTB	i-FTB	i-FTB	L	L
3	P_{cr}	189 kN	198 kN	231 kN	320 kN	426 kN	440 kN
	Shape	i-FTB	i-FTB	i-FTB	i-FTB	L	L
4	P_{cr}	189 kN	200 kN	233 kN	323 kN	434 kN	448 kN
	Shape	i-FTB	i-FTB	i-FTB	i-FTB	L	L
5	P_{cr}	198 kN	206 kN	234 kN	325 kN	434 kN	448 kN
	Shape	i-FTB	g-FTB	i-FTB	i-FTB	L	L

FB = Flexural Buckling; FTB = Flexural-Torsional Buckling; L = Flange Buckling
g = Global/composite response; i = Individual angle response

flexural-torsional buckling was only identified when the ties rotated along with the angles.

It was anticipated that the advanced finite element modeling would capture the same global buckling behavior described in Section 5.3 with additional local effects. Conforming to that expectation, most cross sections with 102 mm and 203 mm legs failed in elastic global flexural-torsional buckling, regardless of inelastical response. Despite the apparent agreement, the observed buckling capacity was greater than the theoretical value with

Table 5.5: Elastic buckling of 2-L51x51x3.2 chord segment with fixed support

Mode		Ties					
		0	1	3	7	15	23
1	P_{cr}	83.6 kN	145 kN	174 kN	198 kN	204 kN	205 kN
	Shape	i-FB	g-FTB	g-FTB	g-FB	g-FB	g-FB
2	P_{cr}	83.6 kN	172 kN	175 kN	209 kN	290 kN	376 kN
	Shape	i-FB	i-FTB	g-FB+i-FTB	g-FTB	g-FTB	g-FTB
3	P_{cr}	149 kN	173 kN	192 kN	227 kN	314 kN	399 kN
	Shape	i-FTB	g-FB+i-FTB	g-FTB	i-FTB	i-FTB	g-FB
4	P_{cr}	149 kN	177 kN	193 kN	228 kN	315 kN	403 kN
	Shape	i-FTB	g-FTB	i-FTB	i-FTB	i-FTB	L
5	P_{cr}	169 kN	177 kN	194 kN	229 kN	316 kN	404 kN
	Shape	i-FB	i-FTB	g-FTB	i-FTB	i-FTB	L

FB = Flexural Buckling; FTB = Flexural-Torsional Buckling; L = Flange Buckling
g = Global/composite response; i = Individual angle response

ties spaced at L/2, which would have been reduced due to local effects. The smaller leg sizes provided a more complex result. For example, a 2-L51x51x3.2 would theoretically flexural-torsional buckle around 116 kN, but the advanced model with fixed end supports was able to reach 174 kN before failing in global flexural-torsional buckling. While the pinned variation failed at a similar load of 176 kN, flexural buckling with individual angle flexural-torsional buckling was now observed to be the controlling mode. For many of the 44 mm and 51 mm cross sections, flexural buckling replaced global flexural-torsional behavior, especially when considering the pinned boundary condition.

Additional ties were observed to consistently increase buckling capacity, but the effect varied by buckling modes. Flexural buckling exhibited initial gains due to composite behavior, but an excessive number of ties produced a negligible increase in strength. Reducing the spacing between ties increased the individual flexural-torsional response until the strength of the unsupported horizontal flange limited capacity, which aligned with a new controlling failure mode. In this study, no limit for increased elastic global flexural-torsional buckling capacity was observed.

5.5.3 Inelastic Chord Behavior

An iterative-incremental inelastic buckling analysis was conducted, and the results indicated that the double angle cross sections primarily failed in flexural buckling, which was typically initiated by the local twisting of the individual angle sections. The buckling capacity typically increased with an increase in ties, Table 5.6, as additional ties delayed the initial on-set of local buckling in the angles, especially for slender cross sections as shown in Fig. 5.15 and Fig. 5.16. Note that the additional values in the footnote of Table 5.6 provide the buckling capacity based on a different initial imperfection to verify the jump

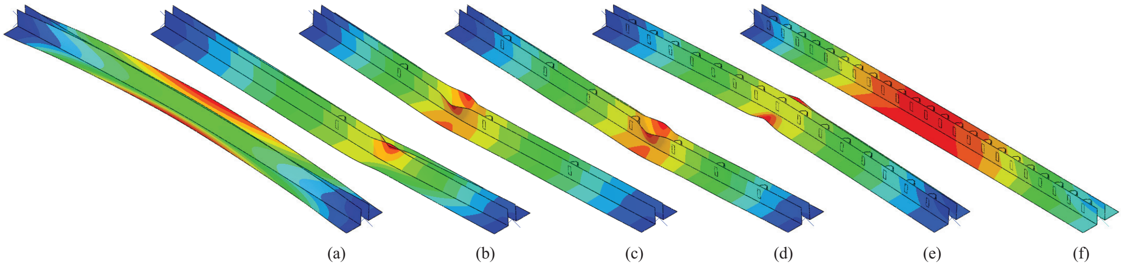

Figure 5.15: Composite behavior effect on inelastic buckling in a 2-L51x51x2.4 with (a) 0, (b) 1, (c) 3, (d) 7, (e) 15 and (f) 23 ties

in capacity was due to the study methodology and not other underlying behavior. Some global twisting of the cross sections was observed at failure due to the initial imperfection including flexural-torsional buckling; however, it was generally combined with a distinct weak-axis flexural response. The results of the simplified chord models, summarized in Table 5.7, were found to be consistent between the fixed and pinned boundary conditions as well as with the full joist models. The modeled capacities were conservatively predicted by both the flexural and flexural-torsional buckling design provisions. However, as the section slenderness increased, the conservatism of the flexural buckling prediction was reduced.

The inelastic model results provided an interesting deviation from the typical design assumptions. The various full and isolated joist models incorporate different effective lengths for flexural-torsional buckling; however, each exhibited comparable torsional behavior and similar ultimate capacities. The additional warping restraint in the simply supported alternative should have resulted in flexural buckling being more dominant compared to the other modeling alternative results. Therefore, it was theorized that the stiff connection between the chords and the continuity of the chords provide similar warping restraint that would typically be conservatively ignored in design. Additionally, the results consistently depicted flexural-torsional buckling to be greater than standard design predictions. Considering the increased shear stiffness, which is excluded for simplicity in design, along with the typical J and C_w of double angles, increased design predictions; however, it wasnot enough to match the observed failure or to cause flexural buckling to control indicating additional torsional stiffness was ignored in design calculations. Alenezi and Mohareb [82] also noted increased torsional section properties for double angles; however, the impact of a complete moment connection between the chords was not considered.

Table 5.6: Inelastic buckling of simply supported chord

	Axial buckling load (kN) with _ ties					
Cross Section	0	1	3	7	15	31
2-L203x203x19	4980	5030	5030	5030	5030	4940
2-L203x203x15.9	4150	4140	4200	4220	4230	4220
2-L203x203x13.9	3470	3480	3600	3670	3710 [1]	3630
2-L203x203x12.7	2930 [2]	2860	3190	3310	3400 [3]	3280
2-L203x203x11.1	2180 [4]	2160	2540	2700	2790	2780
2-L203x203x9.5	1560 [5]	1540	1860	2110	2220	2250

[*] Evaluations with different elastic buckling mode resulted in reduced buckling load

[1] Mode 2 = 3670 kN

[2] Mode 4 = 2740 kN

[3] Mode 3 = 3300 kN

[4] Mode 4 = 2030 kN

[4] Mode 4 = 1430 kN

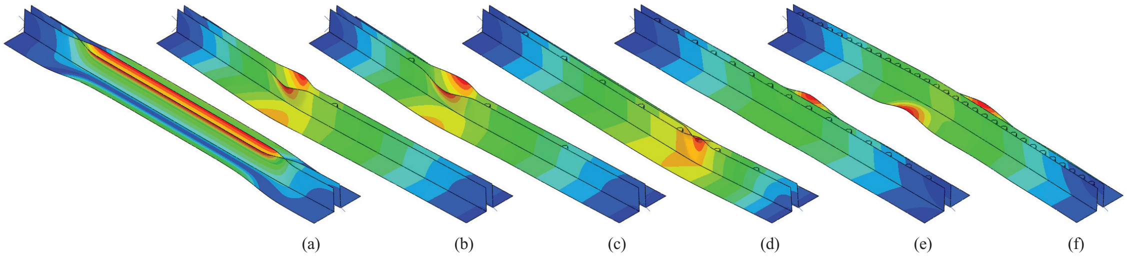

Figure 5.16: Composite behavior effect on inelastic buckling in a 2-L102x102x6.4 with (a) 0, (b) 1, (c) 3, (d) 7, (e) 15 and (f) 31 ties

5.6 Double Angle Chord in Torsion

The torsional stiffness of the chords was assessed by subjecting cantilevered double angle chord segments to a defined twist. The simply supported double angle base models described in Section 5.5.1 were modified to have a fully-fixed constraint on one end, while the other end was only subjected to a torsional rotation of 0.01 radians in a second-order elastic Riks analysis. The resulting torsional reaction moments for each model were recorded and found to be equal to or greater than the theoretical support moment associated with two times the C_w of a single angle due to the composite behavior caused by the tied end condition. Two different effective section properties were calculated for each model to compare the different support moments. An effective torsional stiffness, J_e, was determined neglecting warping, Fig. 5.17. An effective warping stiffness, $C_{w,e}$, was calculated accounting for the fixed warping at the boundaries and the nominal torsional stiffness, Fig. 5.18. These section properties would not coexist but provide different context for how much the stiffness increased. The inclusion of a single tie resulted in a measurable increase in stiffness causing $C_{w,e}$ to at least double for all cross sections, which translated to more

Table 5.7: Buckling capacity comparison between modeling and SJI-100 based design values

Cross Section	Maximum Model Compression (kN)					Design* (kN)	
	Ties at L/2			Ties at L/4			
	Joist	Pinned	Fixed	Pinned	Fixed	FB	FTB[1]
2-L51x51x3.2	163	153	163	162	158	126	107
2-L51x51x2.9	143	138	137	148	137	112	91
2-L51x51x2.8	127	114	121	113	118	104	81
2-L51x51x2.4	89	82	85	81	96	82	60
2-L44x44x3.2	134	111	113	117	116	101	102
2-L44x44x2.9	125	101	104	108	107	92	87
2-L44x44x2.8	117	96	98	102	102	86	78
2-L102x102x9.5	1170	1214	1254	1205	1263	1072	979
2-L102x102x8.7	1076	1125	1152	1143	1161	965	850
2-L102x102x7.9	992	1023	1041	1032	1054	854	721
2-L102x102x6.4	734	694	743	694	796	627	472
2-L102x102x4.8	389	368	387	389	449	389	261
2-L203x203x19	4728	5026	5053	5026	5066	4555	4008
2-L203x203x15.9	3959	4141	4212	4199	4235	3612	2940
2-L203x203x13.9	3261	3483	3572	3599	3652	2998	2282
2-L203x203x12.7	2931	2865	3020	3189	3194	2633	1913
2-L203x203x11.1	2246	2162	2220	2544	2420	2135	1446
2-L203x203x9.5	1601	1539	1530	1859	1730	1619	1019

* Effective length factors taken as k=1 for all calculations

[1] Flexural-torsional buckling applied per AISC 360 with local buckling reduction per SJI-100 to match flexural buckling calculation

than a 20% jump in J_e for 44-mm and 51-mm angles. The inclusion of more ties resulted in greater torsional stiffness that was linearly proportional to the spacing between ties. Overall, the increased stiffness directly corresponds to the observed buckling capacities. The larger impacts were observed in slender sections that were originally expected to be controlled by flexural-torsional buckling, while the compact sections encountered modest gains.

5.7 Parallel Plates in Torsion

The underlying mechanics of the torsional response was assessed by evaluating a simplified example of rectangular bars connected by intermediate ties, Fig 5.19, which was selected to isolate the composite response. The parametric study of 51-mm rectangular plates considered the influence of length, thickness, spacing of plates, and tie variations as detailed in Table 5.8. The pair of cantilevered parallel plates were subjected to a defined rotation in MASTAN2 [7] to determine a J_e. Each side plate was defined as 96 warping continuous line elements with the ends free to warp. A two segment line-element tie was provided at the end of the cantilevered plates to connect the system in addition to n_t ties

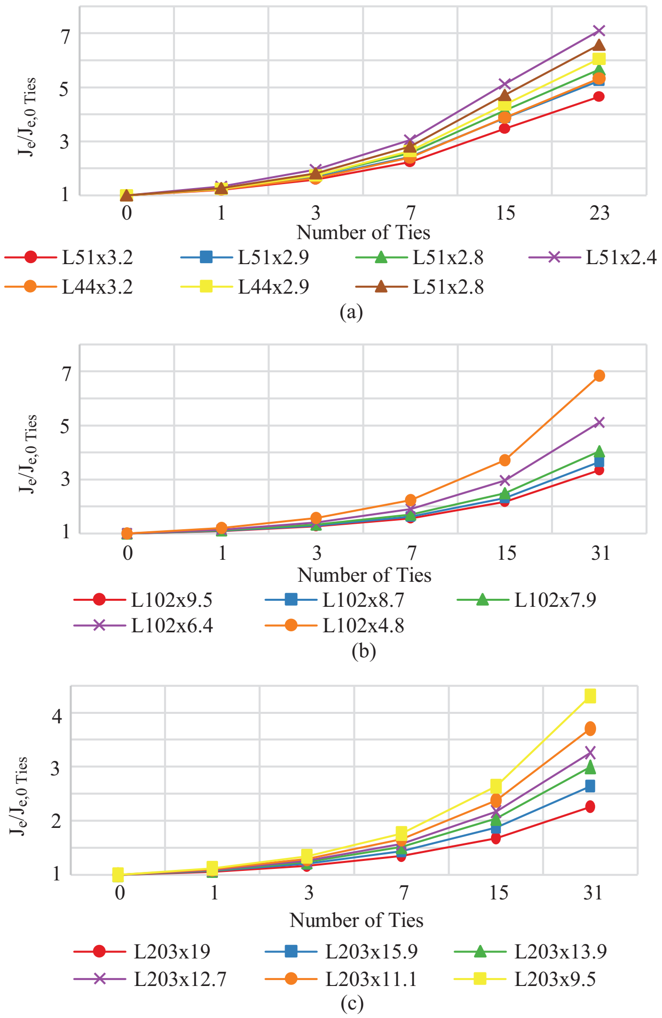

Figure 5.17: Influence of composite behavior on J_e of double angles

evenly spaced along the model. The system was supported by a fully fixed support applied at the middle of one end tie, while the other end tie was subjected to a torsional rotation of 0.01 radians. The “Tie End" condition defined whether the ties were fixed or pinned for bending moment to the plates. The corresponding connection was applied to both ends of the end ties; however, intermediate ties were only modified on one end to allow for shear force transfer between the plates in addition to axial forces and torsion.

Similar to the double angle study, the parallel plate examples exhibited an increased torsional stiffness as additional ties were included. Table 5.9 shows that J_e was in agreement with the expected theoretical results, $J_{nom} = 2/3bt^3$, when no intermediate ties were included, but J_e significantly increased as additional ties were added. The thicker plate configurations were significantly stiffer than the thinner plate variations; however, the benefit of composite behavior was greater with thinner plates. The addition of one tie was

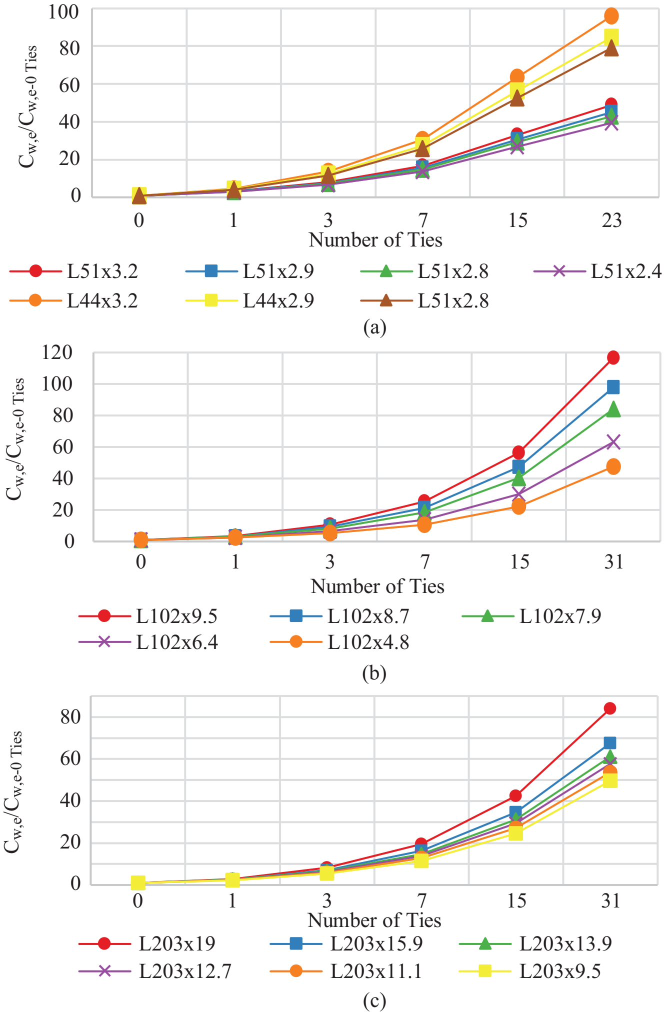

Figure 5.18: Influence of composite behavior on C_w of double angles

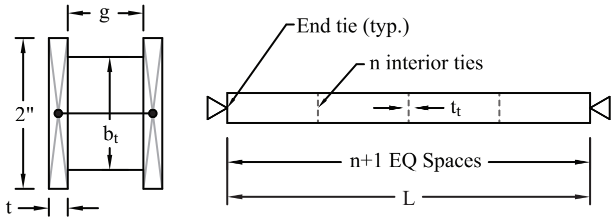

Figure 5.19: Geometry of parallel plates in torsion

Table 5.8: Variables for parametric torsion study

Variable	Options					
L (mm)	1219	2438				
t (mm)	2.1	2.5	3.2	4.2	6.4	
g (mm)	12.7	25.4	20.8			
n_t	0	1	2	3	7	15	31
b_t (mm)	3.2	38.1				
t_t (mm)	3.2	12.7				
Tie End	Fixed	Pinned				

Table 5.9: J_e/J_{nom} for 51 mm × t plates spaced 12.7 mm apart with (n_t) 38.1 mm x 12.7 mm ties for L = 2438 mm

	t (mm)	2.1	2.5	3.2	4.2	6.4
	J_{nom} (mm^4)	321	555	1084	2569	8671
Number of ties, n_t	0	1.04	1.03	1.02	1.01	1.01
	1	1.15	1.11	1.07	1.04	1.02
	2	1.31	1.22	1.14	1.08	1.04
	3	1.51	1.36	1.23	1.13	1.06
	7	2.63	2.10	1.68	1.36	1.14
	15	5.61	3.99	2.76	1.88	1.33
	31	12.64	8.31	5.13	2.97	1.70

Table 5.10: J_e/J_{nom} for 51mm × t plates spaced 12.7 mm apart with (n_t) 38.1 mm x 12.7 mm ties for L = 1219 mm

	t (mm)	2.1	2.5	3.2	4.2	6.4
	J_{nom} (mm^4)	321	555	1084	2569	8671
Number of ties, n_t	0	1.15	1.11	1.07	1.05	1.02
	1	1.53	1.37	1.24	1.14	1.06
	2	2.05	1.72	1.46	1.25	1.11
	3	2.68	2.13	1.70	1.37	1.15
	7	5.71	4.06	2.80	1.90	1.34
	15	12.80	8.42	5.20	3.01	1.71
	31	28.02	17.59	10.14	5.25	2.46

found to increase the stiffness of the 2.1-mm plate variation by 10.4%, while only a 1.4% increase was observed with the 6.4-mm plate alternative. The torsional stiffness increase varied with the tie spacing, which can be seen in Table 5.9 and Table 5.10 where the stiffness is equivalent for the same tie spacing.

While the exact details of the mechanics were not evaluated in this study, the increased stiffness was attributed to a combined warping response. The rectangular plates behaved analogous to the flanges of an I-beam where the rectangular plates supported equal and opposite bending moments, shown in Fig. 5.20(a). The torsional stiffness of the built-up plate member increased as the gap between the plates increased similar to how the C_w varies with I-beam depth (Table 5.11). However, a deviation in this comparison was the distribution of bending moments in the plates. While an I-beam under a discrete torsional loading would have a linearly increased moment distribution in the flange, the plates instead exhibited a saw-tooth moment pattern that required torsion to be transferred through the tie connections. When utilizing a tie with a low torsional stiffness or one unable to transfer torsion, minimal internal bending moments were developed as shown in Fig. 5.20(b) resulting in minimal composite behavior.

Table 5.11: J_e/J_{nom} for 51mm × t plates spaced 51mm apart with (n_t) 38.1 mm x 12.7 mm ties for L = 1219 mm

	t (mm)	2.1	2.5	3.2	4.2	6.4
	J_{nom} (mm^4)	321	555	1084	2569	8671
Number of ties, n_t	0	2.62	2.09	1.67	1.35	1.14
	1	5.50	3.90	2.68	1.82	1.29
	2	8.71	5.85	3.73	2.29	1.44
	3	12.06	7.85	4.79	2.75	1.58
	7	25.87	16.01	9.06	4.60	2.15
	15	53.93	32.44	17.60	8.28	3.28
	31	110.14	65.25	34.60	15.59	5.53

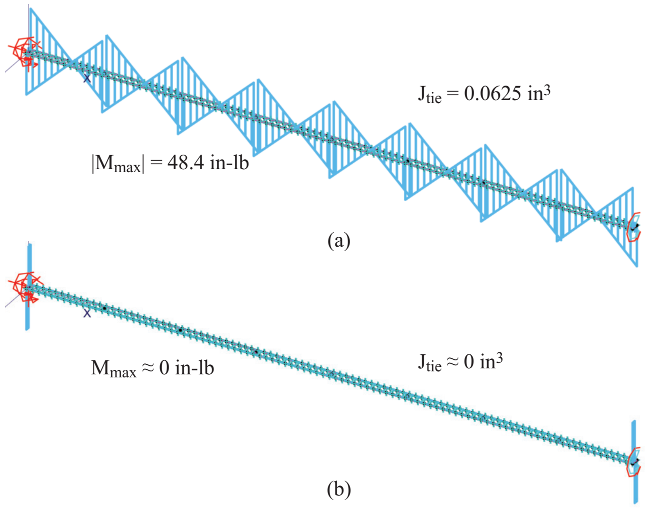

(a)

(b)

Figure 5.20: Strong-axis moment in parallel plates subjected to torsion. (a) Standard fixed tie connection (b) No torsion transferred through tie

5.8 Effect of increased torsional stiffness

As mentioned in Section 5.3, AISC recommends ignoring the warping stiffness of double angles in design. However, the composite nature of double angles was found to significantly increase torsional stiffness, particularly through warping. The impact of this increase was evaluated by updating the inelastic buckling study, while considering the nominal J and the calculated $C_{w,e}$ from Section 5.6 for one tie between the chords. The effective end restraint observed in the full joist and chord segment modeling was implemented by considering effective torsional buckling length factors of 1.0 and 0.5. In addition to the original conditions, the tangential buckling response without any local buckling reduction, labeled '$\tau_G = 1.0$ w/o Q', is provided to understand the influence of the local buckling reduction. As depicted in Fig. 5.21, the increased torsional restraint and torsional stiffness resulted in minimal difference between the expected behavior and the flexural buckling design provisions after the application of local buckling reductions. However, global

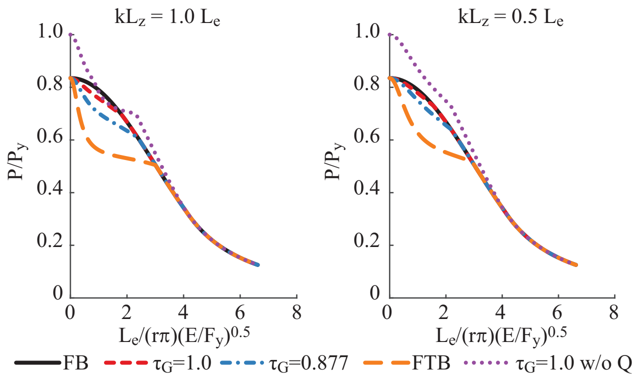

Figure 5.21: Theoretical buckling capacity of 2-L203x203x12.7 with effective section properties

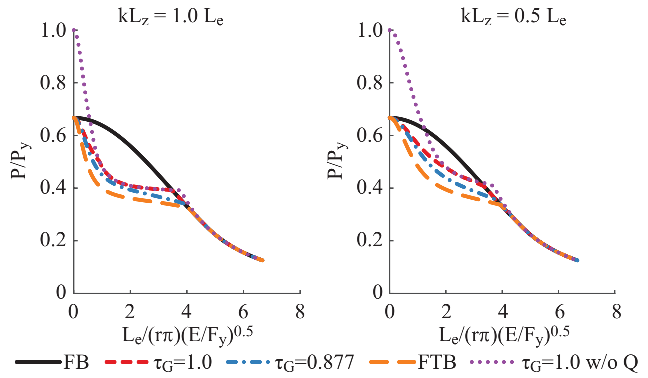

Figure 5.22: Theoretical buckling capacity of 2-L203x203x9.5 with effective section properties

flexural-torsional buckling was observed to be the controlling behavior for cross sections with high slenderness, $b/t > 16$, Fig. 5.22. In these instances, local buckling reductions were not large enough to simulate the low global flexural-torsional buckling capacity, which was so low that local buckling reductions do not apply. Although this observation indicates there is a limit when flexural-torsional buckling is critical, none of the representative cross-section sizes recommended by SJI exceeded the $b/t > 16$ limit, and therefore only applied to the theoretical sizes considered in the extended study. To validate this result, the complete set of representative cross sections was evaluated for theoretical inelastic buckling with an estimated $C_{w,e}$ equal to 70% of the "High C_w" based on the typical results of torsional study in Section 5.6 and a partial warping fixity with an effective torsion length factor of 0.7. The resulting buckling analysis found most sections were controlled by flexural buckling. When flexural-torsional buckling did control, the capacity was found to be within 3% of the flexural buckling result.

5.9 Discussion

The torsional stiffness of built-up members was observed to be greater than conventional design assumptions. While the double angle geometry exhibits similarities to a tee section, the separation between the vertical legs causes the analogy to fail for the description of warping and underestimates the member torsional stiffness. This underestimation of torsional stiffness causes flexural-torsional buckling to appear more critical in design provisions than it actually is, which was demonstrated in the theoretical inelastic buckling study in Section 5.3. Whereas Alenezi and Mohareb [82] indicated that double angle have some increased warping stiffness due to partial composite behavior, the drastic increases noted in this study relied on the relatively stiff ties over the height of the double angle members, which would readily transfer forces and moments including torsion between the chord angles. As shown with the plate example, if the connection is too flexible or unable to transmit torsion, like a single bolt, the benefit of composite behavior is reduced.

The increased torsional stiffness of the double angles considered in this study resulted in flexural buckling controlling the design behavior. However, that does not mean torsional behavior is not an important component of the limit state. All modeled cross sections were noncompact or slender, which requires the incorporation of local buckling reductions. This local buckling would equate to the flexural-torsional buckling mode of each angle as an independent member [61], [62]. For single angles, the flexural-torsional buckling condition does not need to be checked as the local buckling criteria adequately reduces the flexural buckling capacity to address torsional concerns [8], [61], and hence avoids penalizing the capacity of the member twice for the same effect. For double angles, standard engineering practice currently accounts for minimal torsional stiffness benefits but applies the full penalty of non-compact sections. As a result, designs according to the SJI Specification are only reduced due to local buckling while designs according to the AISC 360 or Eurocode 3 are reduced due to both global and local buckling. Determining an appropriate balance of these factors will be critical to establishing a uniform design approach for all double angle configurations. Behzadi-Sofiani *et al.* [62] have proposed a design approach for Eurocode 3 to address the same issue for equal-leg single angles, but additional work would be required to determine the applicability to double angles.

The results of this study indicate that the design approach of only considering flexural buckling with local buckling reductions seems to be appropriate for joist and joist girder chords. The joist chord configuration results in an increased torsional stiffness section property in addition to increased torsional restraint due to continuity and web members. All these factors cause global flexural-torsional buckling behavior to be less significant than the current AISC Specification design approach. The individual twisting of angles cannot be eliminated, but this behavior can be accounted for in the local buckling reductions. This recommendation is based on assuming there is adequate stiffness at the connection to ensure composite warping behavior, an appropriate local buckling reduction, and restraint provided to the chord from the webs. The ties in this study were quite stiff and could transmit torsion in contrast to the connection assumed by Alenezi and Mohareb [82] that excluded torsion, which directly impacts the flexural-torsional buckling capacity. Local buckling reductions were observed to be adequate for double angles with $b/t \leqslant 16$; however, the alternative reduction methods might require a different limiting slenderness ratio. Additionally, applications with more slender cross sections or yield stresses greater than 50 ksi need to be addressed. Lastly, no consideration in this study was given to the minimum stiffness needed to provide the desired restraint at connection to the chord. Typical joist systems may be less stiff than those evaluated in this study; however, the fixed-fixed isolated chord results indicate a stiff member-to-member connection alone may be adequate such that the stiffness of webs is irrelevant. Future work should refine each of these limitations if this design approach were to be extended to other applications.

5.10 Conclusion

This paper summarized a study on flexural-torsional buckling in double angle cross sections for joist and joist girder chords. Following existing design provisions in AS 4100, Eurocode 3, and AISC 360, double angles are required to be evaluated for flexural-torsional buckling and to consider local buckling reductions. An inelastic buckling investigation found that while flexural-torsional buckling is not as critical as treated by current AISC design procedures, flexural-torsional buckling is theoretically important for a number of double angle cross sections when considering nominal torsional stiffness. A series of double angles were evaluated using full joist finite element models, which implemented three base models with eighteen different cross sections, to determine if flexural-torsional buckling would be observed in a system. The resulting analysis found that these chords were buckling at or above the SJI flexural buckling limit, while capturing a combination of local behaviors interacting with the global buckling modes. These results were validated with an isolated chord segment buckling study. Elastic buckling evaluations indicated that local angle behavior between ties was a significant factor in defining the overall deformation of the cross sections. The inelastic buckling capacities were found to be greater than the expected theoretical design-based results, while capturing significant individual angle flexural-torsional buckling and more flexural buckling than would be expected. This behavior was due to increased torsional stiffness of the built-up section, which was confirmed by additional finite element analysis, but is often ignored in design. The increased torsional stiffness caused the inelastic buckling capacity to be controlled by flexural buckling with local twisting of the individual angles. A reevaluation of the original inelastic buckling calculations with updated section properties and a reduced effective length for torsional buckling resulted in agreement between the observed behavior and the underlying theory.

6 PARAMETRIC STUDY OF BUCKLING IN STAINLESS STEEL UNEQUAL-LEG ANGLES

6.1 Introduction

This chapter presents a summary of a computational study on the behavior of concentrically loaded austenitic stainless steel unequal-leg single angles. After a discussion of existing research, details of the modeling procedure and related validation is provided. This work served as the foundation of a parametric study that incorporated 12 cross sections, nominal and measured material properties, and varied boundary conditions. The results are presented and discussed with a focus on the importance of flexural-torsional buckling.

6.2 Background

The recent release of American Institute of Steel Construction (AISC) Specification for Structural Stainless Steel Buildings, AISC 370, [12] has provided additional opportunities to implement stainless steel members and take advantage of corrosion resistance, thermal properties, and aesthetics among other benefits [87]. AISC 370 provides an updated design procedure to evaluate members in compression including compact, equal-leg single angles. Unlike carbon steel members designed according to AISC 360 [1], the stainless steel provisions incorporate a three stage buckling model that separates the response into full member yield, inelastic buckling, and elastic buckling. Another modification to the design procedure is the consideration of flexural-torsional buckling with single angles. The design provisions for carbon steel single angles permit excluding the direct calculation of flexural-torsional buckling, unless the legs are highly slender, since the local buckling reduction adequately reduces the flexural buckling capacity to produce a safe design [8]. These conditions outline the key areas of interest for this research: expanding the available data on unequal-leg angles subjected to uniform compression and the importance of flexural-torsional buckling in stainless steel single angles.

6.2.1 Material Properties

Stainless steel exhibits a nonlinear stress-strain response, as shown in Fig. 6.1, unlike typical structural carbon steels. While carbon steels have a well-defined yield behavior, stainless steels have no definitive yield point. Stainless steel behavior is characterized by a departure from the linear elastic response at low stresses, which varies with the exact material grade.

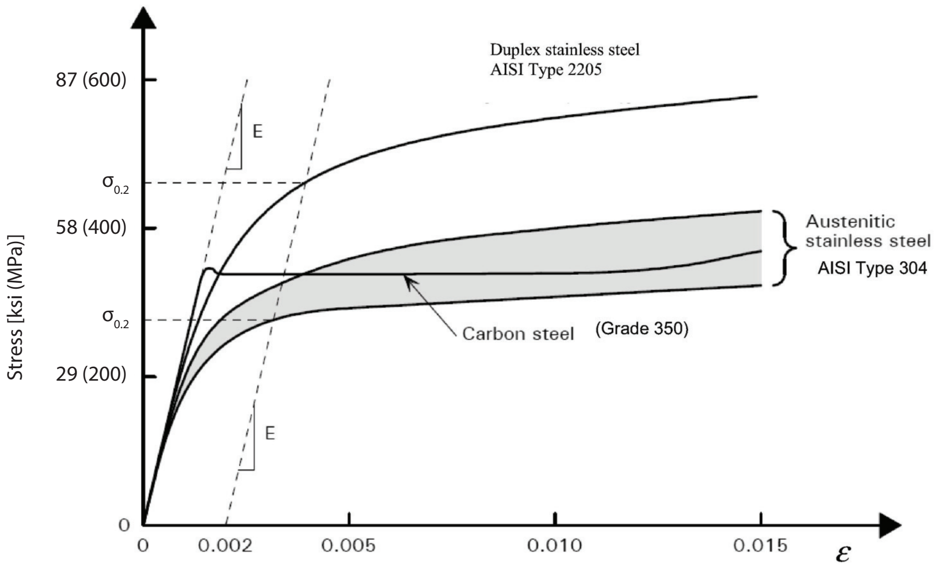

Figure 6.1: Typical stress-strain curves of carbon and stainless steels. (Modified from [88])

The yield point is alternatively defined using a specified offset strain, commonly 0.2% strain as highlighted in Fig. 6.1.

While various models [88] have been considered to capture the nonlinear behavior of stainless steel, the modified Ramberg-Osgood model [89] has been a popular choice for defining many nonlinear materials. The Ramberg-Osgood model [90] allows users to define the material behavior based on the initial modulus of elasticity, E_0, and two points along the stress-strain curve. The original recommendation utilized values defined by the secant stiffness. The first value was chosen to approximately correspond with the 0.2% offset yield stress using $0.7E_0$, and the second value was taken as $0.85E_0$ to capture the intermediate response. Hill [89] updated the model by selecting the two points via an offset strain condition. He suggested the use of the 0.2% offset yield stress, $\sigma_{0.2}$, and the 0.1% offset yield stress, $\sigma_{0.1}$, resulting in Eq. 6.1.

$$\epsilon = \frac{\sigma}{E_0} + 0.002\left(\frac{\sigma}{\sigma_{0.2}}\right)^n \tag{6.1}$$

where ϵ is the current strain, σ is the current stress, and n is the strain hardening exponent, which can calculated using Eq. 6.2.

$$n = \frac{\ln 20}{\ln\left(\frac{\sigma_{0.2}}{\sigma_{0.1}}\right)} \tag{6.2}$$

Although this modified Ramberg-Osgood model [89] has been shown to effectively present stresses below the yield stress, it regularly over-predicts observed stresses at higher

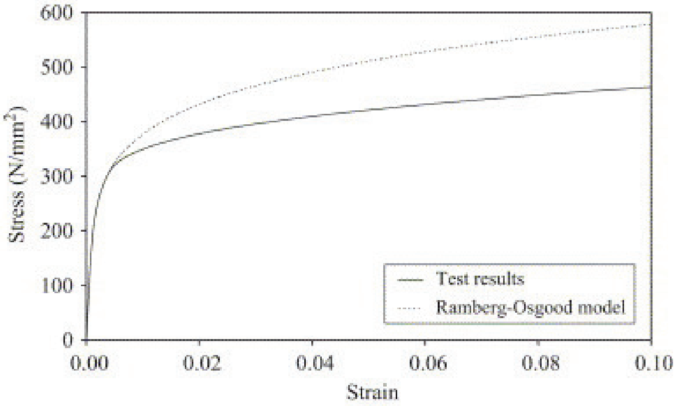

Figure 6.2: Comparison of modified Ramberg-Osgood model and experimental stress-strain curves [91]

strains as shown in Fig 6.2. Researchers [92]–[99] have addressed this issue in different ways; however, one of the more common solutions is the application of a two-stage, modified Ramberg-Osgood stress-strain relationship as shown in Eq. 6.3;

$$\epsilon = \begin{cases} \frac{\sigma}{E_0} + 0.002\left(\frac{\sigma}{\sigma_{0.2}}\right)^n & \text{if } \sigma \leqslant \sigma_{0.2} \\ \frac{\sigma-\sigma_{0.2}}{E_{0.2}} + \epsilon_{\max}\left(\frac{\sigma-\sigma_{0.2}}{\sigma_{\max}-\sigma_{0.2}}\right)^{n_{0.2,\max}} + \frac{\sigma_{0.2}}{E_{0.2}} + 0.002 & \text{otherwise} \end{cases} \tag{6.3}$$

where $E_{0.2} = E_0/\left(1 + 0.002nE_0/\sigma_{0.2}\right)$ is the tangent modulus of elasticity at $\sigma_{0.2}$, $\sigma_{\max}$ is the maximum reference stress, $\epsilon_{\max}$ is the maximum reference strain, $n_{0.2,\max}$ is the Ramberg-Osgood strain-hardening coefficient for the second stage.

The standard modified Ramberg-Osgood model is still used below the yield stress. However, at this point the Ramberg-Osgood model is updated by defining another Ramberg-Osgood curve starting at $\sigma_{0.2}$ with an initial slope of $E_{0.2}$ and passes through another set stress-strain pair. Early work by Rasmussen [95] considered the ultimate stress and ultimate strain to capture the entire material response range, which aligns with the current material model recommended in AISC 370 [12]. Limitations of using the ultimate behavior to define the strain-strain curve included that the largest errors in stress-strain predictions occurred shortly after yield and that compression testing could not readily define the needed parameters due to the lack of fracture [96]. To improve the accuracy at lower strains, researchers have alternatively recommended using intermediate strain values [96], [98], [99]. This study follows the model recommended by Gardner and Nethercot [96] and updated by Arrayago *et al.* [100], which defines second reference point as the 1% offset strain stress, $\sigma_{1.0}$. Arrayago *et al.* found that the resulting material model was capable of predicting the stress-strain response for up to 10% strains when fit from tension results and 2% strains when fit from compression results. Quach *et al.* [98] noted previous work had been focused on defining separate engineering stress-engineering strain formulas for tension and compression due to distinct behaviors at higher strains, but the difference was primarily a artifact of considering engineering stress-engineering strains. Upon comparing the true stress-true strain behavior, the distinction between tension and compression stress-strain curves was minimal.

6.2.2 Compression Testing

The buckling behavior of concentrically loaded angles has been studied for a number of years. The majority of research has focused on carbon steel equal-leg angles with some consideration of stainless steel or unequal-leg geometries. However, work considering stainless steel unequal-leg angles was not located.

6.2.2.1 Stainless Steel Equal-Leg Angles

In recent years, research on stainless steel equal-leg angles subjected to uniform compression has become an active topic. Before this, Kuwamura [101] and Sun *et al.* [102] provided some of the limited relevant results. Kuwamura [101] was primarily concerned with the local buckling behavior of thin-walled stainless steel sections. As part of that study, twelve cold-formed austenitic equal-leg angle stub-columns were tested to failure with nominally fixed-fixed end conditions. Flexural-torsional buckling was observed at failure of the columns with compact cross sections having ultimate loads greater than the yield stress. As the slenderness of individual legs increased, the buckling load decreased and was found to be less than the yield stress for slender legs. As part of a study on laterally constrained bending behavior of hot-rolled stainless steel equal-leg angles, Sun *et al.* [102] similarly completed a series of stub-column tests. All ten tests were also found to exhibit flexural-torsional buckling with most exceeding the nominal yield stress.

Reynolds [103] investigated the behavior of laser-welded duplex equal-leg angles. Thirty-three specimens were subjected to concentric compression with the ends pinned for weak-axis bending, fixed for strong-axis bending, and fixed for warping. Weak-axis flexural buckling was observed in 28 of the specimens, while the remaining five were found to exhibit flexural-torsional buckling. Reynolds found that the evaluation of flexural-torsional buckling design provisions resulted in overly conservative results, while the accuracy of flexural buckling provisions varied among different specifications. A parametric study using shells indicated the flexural-torsional buckling became increasingly critical as the cross-section slenderness increased.

Liang *et al.* [104] subjected 16 fixed-ended hot-rolled austentitic stainless steel equal-leg angles to concentric compression. All members depicted flexural-torsional buckling, but longer members also incorporated an interaction with flexural buckling. The experimental results and a complementary parametric study were compared to existing design provisions indicated that flexural-torsional buckling was conservatively predicted. Comparisons to proposed direct strength method provisions for flexural-torsional buckling, which were based on carbon steel behavior, resulted in improved accuracy of the expected capacity. However, approximately half of the estimated capacities were unconservative due to not accounting for the softer response of stainless steel compared to carbon steel. A comparable study was completed by Sirqueira *et al.* [105] with 18 fixed-end hot-rolled austentitic stainless steel equal-leg angles obtained similar conclusions. Additional numerical work with slender equal-leg angles noted that observed local buckling did not correspond with the behavior indicated by the Eurocode 3 provisions [106].

An extended series of compression tests were completed at the University of Belgrade including hot-rolled [107], laser welded [108], and cold-formed [109] stainless steel equal-leg angles. All columns were fixed for strong-axis bending and torsion while pinned for weak-axis bending. The measured yield stress was consistently found to exceed the specified nominal value with the largest variation of 55% noted for the hot-rolled sections. The shorter stub column tests were found to fail in flexural-torsional buckling. The slender cold-formed section exhibited failure below the yield stress, while the laser welded and hot-rolled specimens exceeded the yield stress. Flexural-torsional buckling was observed throughout the shorter specimens with a gradual transition to flexural buckling behavior at long lengths. The test results indicated that existing design procedures resulted in safe, but inaccurate strength predictions. These design calculations only considered flexural buckling, which aligned with the recommendation of the first edition of the AISC Design Guide 27 [11] to not consider flexural-torsional buckling.

Another test series of 24 hot-rolled stainless steel equal-leg angles including short and long member lengths studied by Zhang *et al.* [110], [111] observed similar global buckling behaviors and inaccurate strength predictions by existing design procedures.

Behzadi-Sofiani *et al.* [112] completed an experimental and numerical study on fixed-end stainless steel equal-leg angle columns. The flexural buckling controlled capacities were reasonably estimated using existing design provisions, but flexural-torsional buckling could be widely underestimated. They noted that the flexural-torsional buckling behavior of columns can be effectively double counted in column design based on current practices considering combined global and local buckling.

6.2.2.2 Unequal-Leg Angles

Despite the growing database for equal-leg angles, only minimal existing research on unequal-leg angles subjected to uniform compression, including none for stainless steel members, was located. Early work by Liu and Chantel [113] considered 26 carbon steel unequal-leg angles subjected to compression with varying amounts of eccentricity. All five concentrically loaded angles failed primarily in flexural buckling at less than 40% of the yield stress. Dinis *et al.* [114] evaluated four carbon steel unequal-leg angles to investigate the elastic flexural-torsional response in asymmetric sections. Experimental results and subsequent modeling were found to be in agreement with the standard theoretical elastic buckling capacity used in the AISC Specifications. Ojalvo [115] summarized the results of three fixed end aluminum unequal-leg angles tests [116], [117]. The inelastic response of the fixed ended columns captured additional post-critical strength excluded in standard elastic buckling assumptions. Recently, Zhang *et al.* [118] and Zhang *et al.* [119] tested a combined 22 pinned end aluminum unequal-leg angle columns. Experimental results consistently exhibited flexural-torsional buckling. The response was dominated by torsional behavior at short lengths with a gradual transition to significant flexural behavior at long lengths.

6.2.3 Design Provisions

In the late 1800's, Engesser demonstrated how inelastic buckling capacity could be determined by considering the tangential stiffness of a perfectly straight column, which was in agreement with experimental results [120]. By simply replacing the E_0 with the tangential modulus of elasticity, E_t, the existing elastic global buckling relationships could be used to determine inelastic behavior. Further investigation demonstrated that this theory alone did not accurately depict the internal behavior of the column as it started to fail. As a result, Engesser developed a more refined relationship for the effective modulus of elasticity identified as the reduced modulus of elasticity which accounted for the redistribution of forces as the column buckled. While mechanically correct, inelastic capacities calculated by this method were higher than the tangent modulus approach and did not agree with experimental capacities.

The discrepancy between the tangent modulus and reduced modulus was finally resolved by Shanley [121]. Shanley demonstrated that the reduced modulus approach was capturing an ideal upper bound, including the additional column capacity required to move a perfectly straight column. Similarly, the tangent modulus approach was shown to be a lower bound capacity representing the bifurcation solution. By considering the deformed column geometry, an intermediate solution transitioning between the tangent modulus and reduced modulus results was developed. From a practical design perspective, the increased capacity from this method was deemed to not be worth the effort. Noting that the actual strength of the member would be reduced by initial imperfections, the tangent modulus approach was determined to be an appropriate simplification and is currently used as the basis of inelastic column buckling for various design approaches.

The current AISC Structural Stainless Steel Specification [12] can be depicted with a tangential modulus, but for simplicity, the provisions are typically presented as converting the elastic buckling stress, F_e, into the critical buckling stress, F_{cr}. Since stainless steel is a more expensive material, the desire for efficient material usage has resulted in buckling being defined by a three-stage response. Similar to carbon steel, low compressive stresses correspond to an elastic buckling behavior with minor reduction for imperfections and residual stresses. As the stress increases, the response transitions to include inelastic buckling behavior. Unlike carbon steel, designs with stainless steel allow for full yield in compression at short lengths. Based on existing research, Meza *et al.* [122] developed the current flexural design provisions for compression members, given by Eq. 6.4;

$$F_{cr} = \begin{cases} F_y & \text{if } \frac{F_y}{F_e} \leqslant \left(\frac{\beta_0}{\pi}\right)^2 \\ 1.2\left[\beta_1^{\left(\frac{F_y}{F_e}\right)^{\alpha}}\right] F_y & \text{if } \left(\frac{\beta_0}{\pi}\right)^2 < \frac{F_y}{F_e} \leqslant 3.20 \\ \beta_2 F_e & \text{if } \frac{F_y}{F_e} > 3.20 \end{cases} \tag{6.4}$$

where α, β_0, β_1, β_2 are flexural buckling coefficients that vary based on the member type as shown in Table 6.1. Multiple column curves have been adopted to capture the increased strength associated with different geometries buckling. Research has developed similar multiple column curves for carbon steel sections [123], but these are not considered in the AISC Structural Steel Specification, AISC 360, for simplicity [1]. The minimum global buckling stress, F_e, is determined by evaluating the cubic relation given by Eq. 6.5 to assess the interaction of flexural and torsional buckling;

$$\begin{gathered}(F_e - f_{xb})(F_e - f_{yb})\left(F_e - \frac{GJ + \pi^2 E C_w / L^2}{r_0^2}\right) \\ -F_e^2 (F_e - f_{yb}) \frac{x_0^2}{r_0^2} - F_e^2 (F_e - f_{xb}) \frac{y_0^2}{r_0^2} = 0\end{gathered} \tag{6.5}$$

where $f_{xb} = \pi^2 E / (L/r_x)^2$ and $f_{yb} = \pi^2 E / (L/r_y)^2$ are the critical flexural buckling stresses about the principal x- and y-axis, respectively, $r_x = \sqrt{I_x/A}$ and $r_y = \sqrt{I_y/A}$ are the radii of gyration about the principal x- and y-axis, I_x and I_y are the moments of inertia about

Table 6.1: Flexural buckling coefficients for stainless steel

Member Type	Curve	α	β_0	β_1	β_2
I-shaped sections buckling about the minor axis and other sections not specified in this table	A	0.56	0.759	0.409	0.690
I-shaped sections buckling about the major axis, welded box sections, and round HSS	B	0.58	0.891	0.455	0.820
Rectangular HSS	C	0.69	1.195	0.501	0.820

the principal x- and y-axis, A is the cross-sectional area, J is the torsion constant, C_w is the warping constant, G is the shear modulus, L is the effective length, $r_0 = \sqrt{r_x^2 + r_y^2 + x_0^2 + y_0^2}$ is the polar radius of gyration about the shear center, and (x_0, y_0) are the coordinates of the shear center relative to the centroid. For unequal-leg angles, this relationship cannot be simplified meaning the controlling response is always technically a flexural-torsional buckling mode.

Following AISC 370, single angle compression member design is limited to equal-leg, compact cross sections. Despite the current buckling coefficients being based on flexural buckling, the design procedures require the determination of the minimum controlling elastic global buckling behavior including flexural-torsional buckling, which is then adjusted using Eq. 6.4 with Curve A coefficients from Table 6.1. The singly symmetric geometry of equal-leg angles normally exhibit flexural buckling about the weak-axis at longer lengths with a transition to flexural-torsional buckling at short lengths. This transition is typically associated with a significant drop in buckling capacity per design. While not covered by the current AISC 370, an asymmetric unequal-leg angles would behave similarly, including flexural behavior depicted at long lengths that transition to torsional behavior at short lengths. However, the controlling response is always flexural-torsional buckling, which means there is consistently an additional reduction applied to the buckling capacity.

Local buckling reductions are defined in the AISC 370 based on elastic local plate buckling, but do not currently apply to single angles as slender cross sections are not covered. If local buckling was considered, the reduced capacity is determined by calculating an effective area, A_e, over which F_{cr} can be supported based on Eq. 6.6,

$$A_e = A - (b - b_e)t - (h - h_e)t \tag{6.6}$$

where b_e and h_e are the effective length of the horizontal and vertical legs, respectively, calculated using Eq. 6.7;

$$b_e = \begin{cases} b & \text{if } \frac{b}{t} \leqslant 0.41\sqrt{\frac{E}{F_{cr}}} \\ 0.772b\left(1 - 0.10\sqrt{\frac{F_{el}}{F_{cr}}}\right)\sqrt{\frac{F_{el}}{F_{cr}}} & \text{if } \frac{b}{t} > 0.41\sqrt{\frac{E}{F_{cr}}} \end{cases} \tag{6.7}$$

where F_{el} is the elastic local buckling stress, which for angles can be determined by Eq. 6.8.

$$F_{el} = 0.425 \frac{\pi^2 E}{12\left(1-\nu^2\right)} \left(\frac{t}{b}\right)^2 \tag{6.8}$$

An interesting phenomenon in single angles is the equivalency of flexural-torsional buckling and local buckling, both in terms of the deformed shape and buckling capacity [61], [112]. As a result, existing design provisions run the risk of double counting the same effect when evaluating flexural-torsional buckling and local buckling in single angles. This issue is addressed in AISC 360 for carbon steel members [1] by not requiring flexural-torsional buckling to be considered in compression member design for single angles. Galambos [8] demonstrated that carbon steel single angles could safely be designed using the flexural buckling capacity reduced for local buckling concerns. This provision was carried forward to the original AISC Stainless Steel Design Guide [11] as it was modeled after AISC 360 with additional reductions for the nonlinear behavior of stainless steel. However, the exception was not incorporated into the current AISC 370 or updated Design Guide.

6.3 Experimental Reference

This computational study was based upon the experimental work led by Max Laracuente at the University of Wisconsin - Madison as part of his Masters of Science degree. The following is a brief summary of the stainless steel unequal-leg angle compression testing program and relevant results with complete details available in Laracuente's thesis [15].

6.3.1 Material Properties

The stress-strain behavior of the 304/304L stainless steel angles was determined using six tensile coupon tests taken around the cross section of two different specimen as indicated in Fig. 6.3. Table 6.2 summarizes the best fit of the experimental results using a two-stage modified Ramberg-Osgood model.

At the time of finalizing this paper, work was ongoing related to the residual stresses in the unequal-leg sections. Final results were not available, but preliminary trends were similar to previous research.

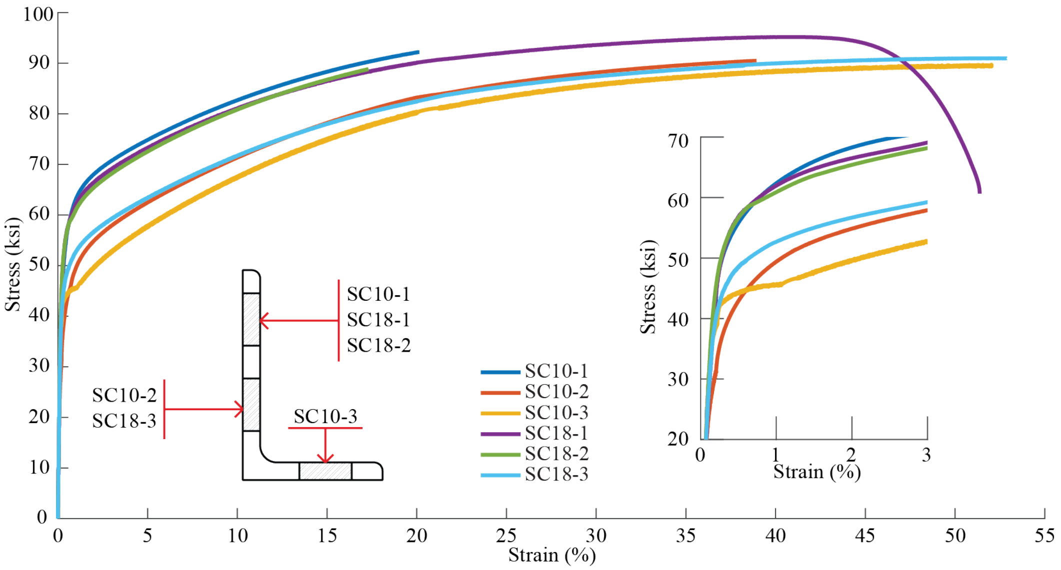

Figure 6.3: Experimental stress-strain curves including relative position of coupons and detail of low strain behavior

Table 6.2: Experimental mechanical properties

Curve #	Specimen	E_0 (ksi)	σ_y (ksi)	$\sigma_{1.0}$ (ksi)	n	$n_{0.2,1.0}$
1	SC10-1	28745	52.6	64.7	5.35	2.57
2	SC10-2	27779	38.9	50.9	4.23	2.20
3	SC10-3	28353	43.4	46.2	10.45	1.51
4	SC18-1	25755	54.9	63.5	8.78	2.12
5	SC18-2	27799	54.5	62.3	9.13	2.55
6	SC18-3	27757	46.1	53.7	8.83	2.29
Average		27698	48.4	56.9	7.80	2.21

6.3.2 Geometry

The experimental series evaluated 18 hot-rolled stainless steel unequal-leg angles with three specimens at six different lengths. Prior to testing, the dimensions and imperfections of the angles were obtained by hand. Table 6.3 summarizes the measured dimensions, where L is the length of the specimen, b and h are the width and height of the section, respectively, and t_b and t_h are the corresponding leg thicknesses as depicted in Fig. 6.4.

The initial geometric imperfections of the specimens were measured through a non-contact three-dimensional laser scanning technique using the Artec Leo Scanner. The angles were scanned in three orientations to create a three-dimensional point cloud of the complete surface. Reconstruction of the data in Artec Studio 15 [59] was aided by the use of a background with unique texture and geometry created from metal decking and various markings on the angle itself as shown in Fig. 6.5. Post-processing of the data established the coordinates of the angle heel and inclination of each leg (twist) along the length of the member through linear-fits of the exterior face of the angle referencing Zhang et al.'s work

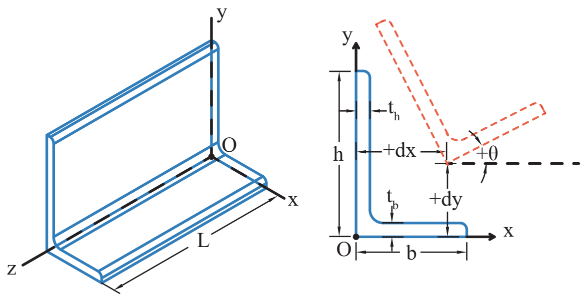

Figure 6.4: Unequal-leg angle conventions for dimensions, axes, and displacements

Table 6.3: Measured geometric properties of test specimens

Specimen	L (in)	b (in)	h (in)	t_b (in)	t_h (in)	Area (in^2)
S10-A1-1	10	2.049	2.979	0.257	0.266	1.251
S10-A2-1	10	2.055	2.977	0.258	0.243	1.191
S10-A2-2	10	2.052	2.966	0.258	0.244	1.192
S20-A1-1	20	2.030	2.981	0.253	0.253	1.203
S20-A2-1	20	2.063	2.958	0.258	0.241	1.182
S20-A2-2	20	2.063	2.965	0.259	0.243	1.190
S36-A1-1	36	2.019	2.985	0.251	0.253	1.198
S36-A1-2	36	2.014	2.991	0.251	0.253	1.198
S36-A2-1	36	2.076	2.964	0.259	0.241	1.190
S72-A5-1	72	2.005	2.987	0.250	0.250	1.185
S72-A5-2	72	2.010	2.985	0.251	0.249	1.184
S72-A6-1	72	2.034	2.980	0.253	0.256	1.214
S100-A3-1	100	2.057	2.957	0.258	0.252	1.210
S100-A4-1	100	2.067	2.933	0.258	0.252	1.208
S100-A4-2	100	2.063	2.939	0.258	0.253	1.209
S148-A1-1	147.9375	2.006	2.999	0.249	0.254	1.199
S148-A2-1	147.9375	2.033	2.972	0.256	0.244	1.182
S148-A3-1	147.9375	2.020	2.989	0.255	0.254	1.210

[124] with additional details in Appendix A. The lateral imperfections along the length of the member, dx and dy in the x- and y- direction, respectively, were determined based on Eq. 6.9 where (x, y) are the coordinates of the heel, i is the current cross section along the length z of the member, and n is the total number of cross sections as shown in Fig. 6.4;

$$[dx, dy]_i = \left[x_i - x_1 + (x_n - x_1)\frac{i-1}{n-1}, y_i - y_1 + (y_n - y_1)\frac{i-1}{n-1} \right] \tag{6.9}$$

The evaluation process separately determined the horizontal and vertical leg rotations and did not constrain the angle to a perfect 90° heel. As a result, the imperfection information was influenced by both global and local effects. For analysis, a single global rotational imperfection was defined as the average rotation of the two legs. The rotational imperfection along the length of the specimen, $d\theta$ about the z-axis, was calculated by Eq. 6.10 where θ_b and θ_h are the orientation of the horizontal and vertical legs, respectively.

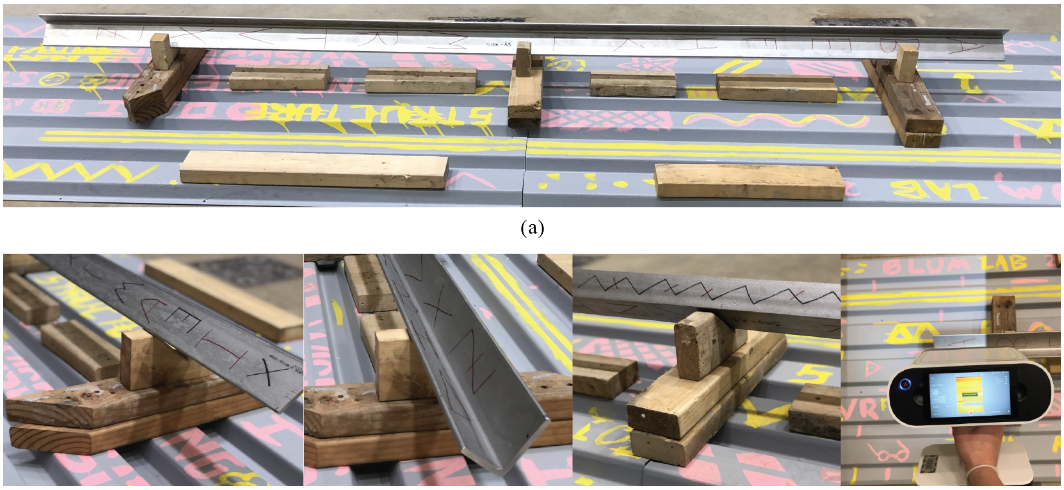

(a)

(b) (c) (d) (e)

Figure 6.5: Imperfection scanning process. (a) Overview of angle to be scanned on background (b) Angle positioned to scan complete exterior face (c) Angle positioned to scan complete interior face (d) Angle positioned to scan majority of both faces at same time (e) Leo scanner capturing data of background and angle.

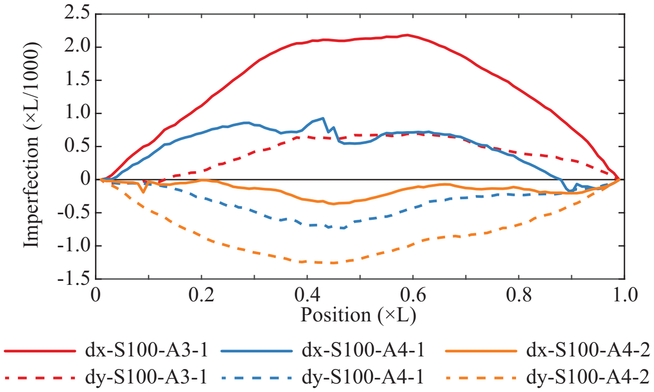

Figure 6.6: Initial lateral imperfection of the 100" specimens

$$d\theta = 0.5\left(\theta_{b,i} + \theta_{h,i} - \theta_{b,1} - \theta_{h,1} + (\theta_{b,n} + \theta_{h,n} - \theta_{b,1} - \theta_{h,1})\,\frac{i-1}{n-1}\right) \tag{6.10}$$

Table 6.4 summaries the maximum imperfection measured along the length of each member with a typical example of lateral imperfections in Fig. 6.6 and rotational imperfections in Fig. 6.7.

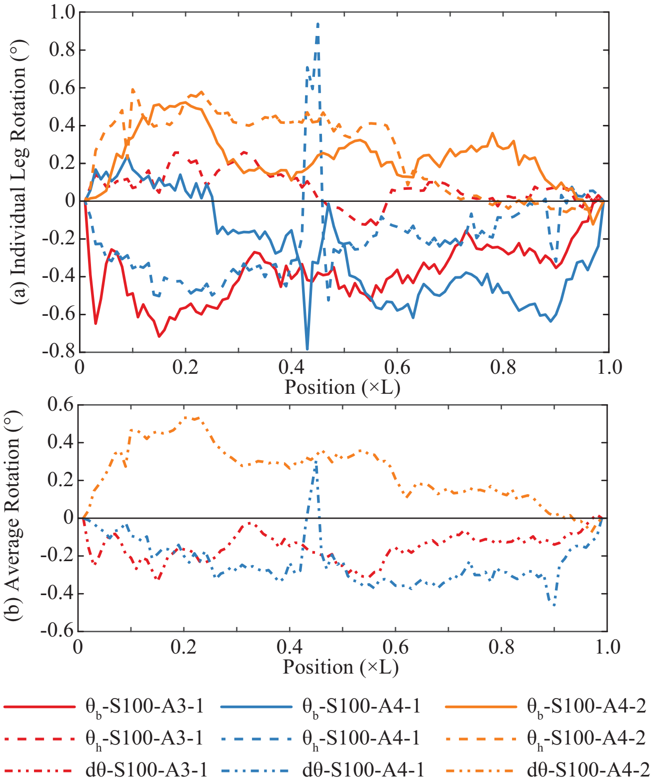

Figure 6.7: Initial rotational imperfection of the 100" specimens. (a) Individual leg rotation (b) Average rotation of specimen

Table 6.4: Maximum measured imperfections

Specimen	Measured			Normalized		
	dx (in)	dy (in)	θ (deg)	dx/(L/1000)	dy/(L/1000)	$\theta/\tan^{-1}(L/1000h)$
S10-A1-1	-0.014	-0.007	-0.20	-1.434	-0.705	-1.05
S10-A2-1	0.003	0.002	0.04	0.347	0.197	0.21
S10-A2-2	0.003	0.002	N/A[1]	0.300	0.150	N/A[1]
S20-A1-1	-0.016	-0.013	-0.22	-0.787	-0.639	-0.56
S20-A2-1	-0.006	-0.003	0.04	-0.288	-0.160	0.09
S20-A2-2	0.005	-0.009	0.05	0.236	-0.442	0.13
S36-A1-1	0.018	-0.018	-0.12	0.494	-0.499	-0.17
S36-A1-2	-0.011	-0.036	-0.18	-0.299	-1.000	-0.26
S36-A2-1	-0.048	-0.022	-0.21	-1.339	-0.603	-0.31
S72-A5-1	0.063	-0.064	0.26	0.873	-0.893	0.19
S72-A5-2	-0.142	-0.134	0.15	-1.978	-1.857	0.11
S72-A6-1	0.035	-0.037	0.10	0.483	-0.520	0.07
S100-A3-1	0.218	0.070	-0.30	2.183	0.695	-0.16
S100-A4-1	0.086	-0.073	-0.37	0.858	-0.732	-0.19
S100-A4-2	-0.037	-0.126	0.35	-0.369	-1.259	0.18
S148-A1-1	-0.070	-0.141	-0.20	-0.472	-0.955	-0.07
S148-A2-1	0.470	0.206	-0.33	3.178	1.389	-0.12
S148-A3-1	0.287	-0.070	-0.20	1.943	-0.474	-0.07

[1] Value not determined. Provided measurements confirmed by hand due to scan issues

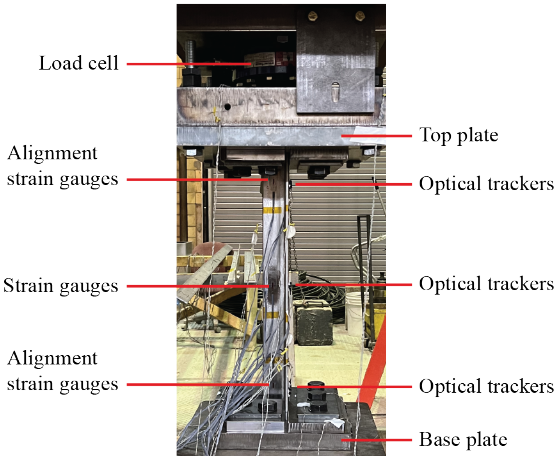

Figure 6.8: Typical compression testing set-up

Table 6.5: Experimental failure loads compared to design loads using nominal and measured material properties

Specimen	Load (kip)	Specimen	Load (kip)	Specimen	Load (kip)
S10-A1-1	62.1	S36-A1-1	57.1	S100-A3-1	19.2
S10-A2-1	69.5	S36-A1-2	52.7	S100-A4-1	18.4
S10-A2-2	68.8	S36-A2-1	53.3	S100-A4-2	18.0
S20-A1-1	61.3	S72-A5-1	30.8	S148-A1-1	7.8
S20-A2-1	66.8	S72-A5-2	24.8	S148-A2-1	5.6
S20-A2-2	65.4	S72-A6-1	34.4	S148-A3-1	6.7

6.3.3 Compression Tests

The full-scale compression tests were completed using a Southwark Emery Testing Machine with a 1 million pound capacity. As illustrated in Fig. 6.8, the tests were completed with nominal fixed-fixed boundary conditions using reusable 50 ksi base plates. Before starting the test series, the base plates and end of each angle were milled flat to provide full end bearing. Three 3/4" thick, A36 clamping brackets were then used to lateral position angle. All test specimens were observed to exhibit flexural-torsional buckling at the failure loads summarized in Table 6.5. The buckling response was dominated by torsional deformations for short specimens, which transitioned to flexural bending for longer ones.

6.4 Modeling Methods

The computational investigation was completed using finite element analysis via Abaqus [20]. This section summarizes the underlying modeling decisions and assumptions used in the later validation process and parametric study.

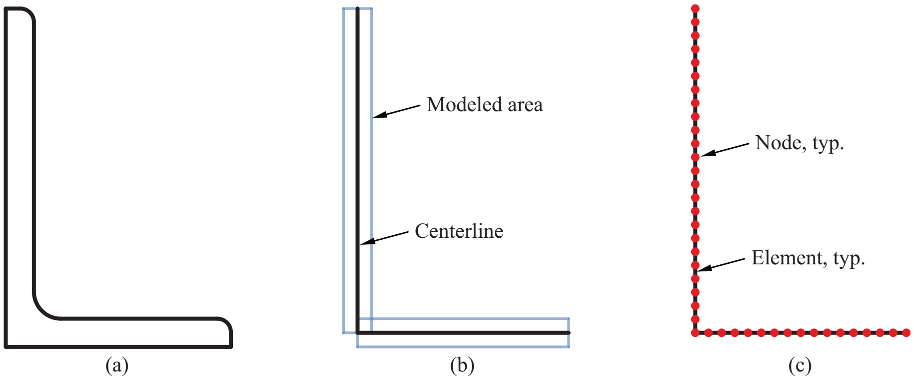

Figure 6.9: Typical model of unequal-leg cross section. (a)Actual cross section. (b) Modeled cross section. (c)Meshed cross section

6.4.1 Geometry

The unequal-leg cross sections were modeled as S4R shell elements, which has a four node linear formulation with reduced integration, hour-glass control, and a general formulation that includes both thick and thin shell behavior [21]. The shell element model was chosen over a solid element because a shell element could accurately model members with a cross-section width to thickness ratio of 3 or larger [22], and solid element models have been observed to capture excessive bending stiffness. Additionally, multiple other researchers [103]–[105], [110]–[112], [114], [125], [126] have shown that shell elements can be used to accurately model angles in compression.

The unequal-leg geometry was modeled using the centerline model shown in Fig. 6.9(b) using centered elements. Some researchers, e.g. [112], have considered more complex layouts to capture the exact hot-rolled angle area without overlap of shell elements at the heel. However, this technique is not always equally applied to the tips of the legs, accounting for a slight increase in area, and cannot account for the complete connectivity of the heel due to shell element limitations. Since other researchers has shown adequate computational results with use of simple shell geometries, including comparisons to solid element models [103], [114], this study chose to work with the simplified geometry. The preliminary mesh, indicated in Fig. 6.9(c), was defined using an approximately square element mesh configuration with 16 elements along the short leg based on prior work discussed in Chapters 2 and 3. Mesh refinement was re-evaluated after defining the material behavior.

The boundary condition for the unequal-leg angle models was applied using the connection illustrated in Fig. 6.10. A single reference node at the angle centroid was connected to all nodes across the end of the angle through a rigid tie constraint. As a result, the angle was always full constrained against warping, and the flexural boundary condition could

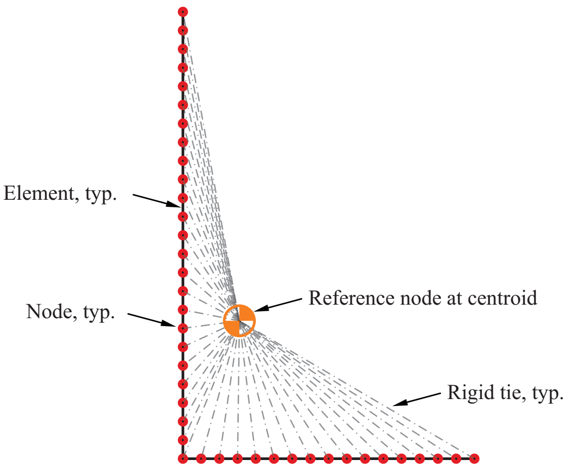

Figure 6.10: End restraint of unequal-leg model

be readily defined as fixed or pinned in the geometric orientations.

6.4.2 Material Model

The material model for stainless steel was developed using a combination of elastic and plastic behavior to depict the material nonlinearity. The model implemented an isotropic elastic response based on a single E and an assumed Poisson's ratio of 0.3 [12]. The anisotrophic behavior of stainless steel was not included in the analysis as previous research has shown minimal impact of considering anisotrophy in compression members[127]. The gradual nonlinearity of stainless steel required a piece-wise linear relationship to approximate the two-stage, modified Ramberg-Osgood model mentioned in Section 6.2.1. To properly model the response in Abaqus, the engineering stress-engineering strain values, σ and ϵ, respectively, were converted to the true stress-true plastic strain response, σ_t and $\epsilon_{t,pl}$, respectively, using Eq. 6.11 and Eq. 6.12.

$$\sigma_t = \sigma(1+\epsilon) \tag{6.11}$$

$$\epsilon_{t,pl} = \ln{(1+\epsilon)} - \frac{\sigma_t}{E_0} \tag{6.12}$$

Previous work has highlighted that the inclusion of any plastic behavior can negatively impact modeling, even when the impact should be negligible [128]. As a result, proper selection of the material model also required determining the appropriate initial plastic stress condition. Two possible extremes would be the proportional limit and the yield stress as depicted in Fig. 6.11. Implementing plasticity at the proportional limit would capture all

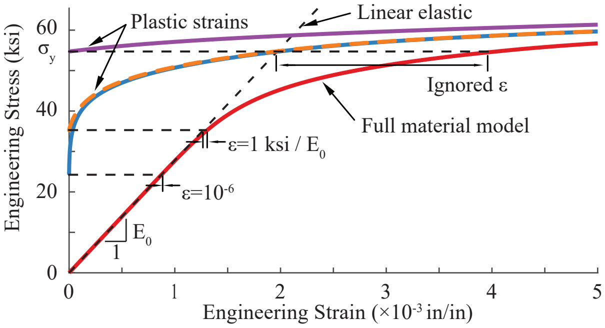

Figure 6.11: Defining the initial plastic strain

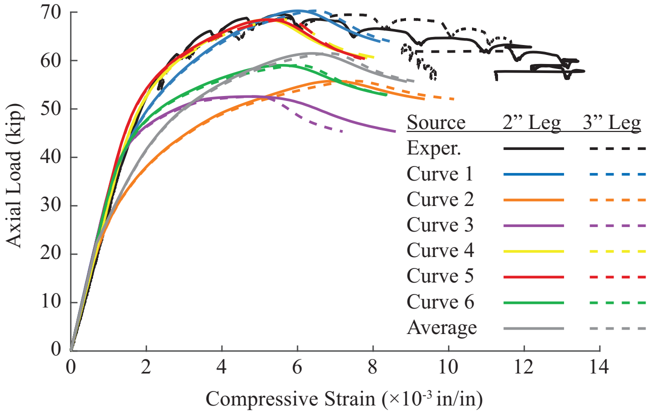

Figure 6.12: Stress-strain response of S10-A2-1 column

of the expected plastic strain, but could lead to an underestimation of the capacity. Starting plasticity at a higher stress can result in higher buckling loads, but also introduces an amount of plastic strain that is ignored in analysis.

The material model for this study was selected from the experimental results listed in Table 6.2. Since the 10-inch column tests corresponded with a typical stub column test, each of the material models could be compared to a compressive stress-strain curve that averages the cross-section response. The axial strain in the angle was determined by averaging a pair of strain gauges at middle of each leg. Comparisons between the experimental and computational results, Fig. 6.12, indicated multiple material models underestimated the stiffness of the full cross section causing premature failure. Only Curve 1, Curve 4, and Curve 5 were able capture the desired failure capacity. However, Curve 1 also incorporated an undesirable reduced stiffness at intermediate stresses; thus leaving Curve 4 and Curve 5 as the primary options with E_0 being the most significant variation.

The material model selection process was expanded to the full experimental series to incorporate stability effects. The preliminary study considered nominal dimensions with the smoothed lateral imperfections, which is defined in Section 6.4.4. The results,

Table 6.6: Ultimate capacity of columns with different stress-strain relationships

	Test	Ultimate load (kip) for Stress-Strain Curve						
Specimen	(kip)	1	2	3	4	5	6	Ave.
S10-A1-1	62.1	66.6	52.3	51.2	65.4	65.5	56.3	58.2
S10-A2-1	69.5	70.3	55.8	52.6	68.5	68.5	59.0	61.5
S10-A2-2	68.8	70.5	56.0	52.6	68.6	68.6	59.1	61.7
S20-A1-1	61.3	60.8	47.6	48.6	60.5	60.6	52.2	53.3
S20-A2-1	66.8	63.6	49.8	50.0	62.7	62.8	54.0	55.7
S20-A2-2	65.4	63.1	49.4	50.1	62.4	62.5	53.8	55.2
S36-A1-1	57.1	49.9	38.7	43.1	51.8	52.2	45.0	43.9
S36-A1-2	52.7	51.7	40.1	44.0	53.5	53.7	46.2	45.8
S36-A2-1	53.3	47.8	37.1	41.6	49.7	50.2	43.4	41.8
S72-A5-1	30.8	29.7	23.1	29.8	31.2	32.7	29.8	24.3
S72-A5-2	24.8	25.9	20.4	25.3	26.8	27.9	25.4	21.9
S72-A6-1	34.4	30.1	23.3	30.3	31.7	33.2	30.3	24.5
S100-A3-1	19.2	16.8	13.8	16.7	16.7	17.7	16.6	14.5
S100-A4-1	18.4	19.9	16.4	20.3	19.5	20.8	20.0	17.4
S100-A4-2	18.0	19.8	16.2	20.2	19.4	20.7	19.9	17.2
S148-A1-1	7.8	10.3	9.2	10.4	9.6	10.3	10.1	9.7
S148-A2-1	5.6	8.4	7.2	8.4	8.2	8.7	8.3	7.5
S148-A3-1	6.7	9.4	8.1	9.4	8.9	9.5	9.2	8.5
Full Series	Mean	1.05	0.85	0.96	1.05	1.08	0.98	0.92
	CoV	0.17	0.22	0.25	0.15	0.17	0.21	0.20
0"-72" Series	Mean	0.97	0.76	0.82	0.98	1.00	0.87	0.84
	CoV	0.07	0.07	0.11	0.05	0.06	0.08	0.08

summarized in Table 6.6, confirmed the importance of having adequate stiffness as the variations in Fig. 6.12 extended to the entire series. Likewise, the stiffness variations at intermediate stresses noted with Curve 1 led to reduced buckling capacities at the intermediate lengths of 36- and 72-inch. Overall, Curve 5 was adopted as the the measured material model. While the buckling results for Curve 4 and Curve 5 were quite similar, Curve 4 was ultimately eliminated as the reduced E_0 was an outlier compared to all material testing.

The measured material model based on Curve 5 was refined by varying the stress where plasticity started. For this study, five alternatives ignored an amount of plastic strain as depicted in Fig. 6.11 ranging from a negligible measurement, 10^{-6} in/in, to $(1\text{ksi})/E_0$ of strain. The corresponding initial plastic stresses are summarized in Table 6.7, along with the resulting ultimate capacities when considering measured cross-section dimensions and the smoothed lateral imperfections. In this application, the different initial conditions resulted in negligible variation in the ultimate capacity. While the effect was minimal, the previous research [128] noted a drastic drop in capacity if plasticity was encountered prematurely which could be applicable to the longer test lengths in the parametric study. Therefore it was opted to start plasticity after ignoring $(0.5\text{ksi})/E_0$ strain, which corresponded to approximately 1% of the actual yield stress, raising the effective yield 36%.

Table 6.7: Effect of initial plastic strain on ultimate failure load

	Test	Ultimate load (kip) for ignored initial plastic strain				
Specimen	(kip)	10^{-6}	0.1ksi/E_0	0.2ksi/E_0	0.5ksi/E_0	1.0ksi/E_0
S10-A1-1	62.1	70.3	70.3	70.3	70.3	70.3
S10-A2-1	69.5	68.9	68.9	68.9	68.9	68.9
S10-A2-2	68.8	69.1	69.1	69.1	69.1	69.1
S20-A1-1	61.3	62.0	62.0	62.0	62.0	62.0
S20-A2-1	66.8	63.4	63.4	63.4	63.4	63.4
S20-A2-2	65.4	63.5	63.5	63.5	63.5	63.5
S36-A1-1	57.1	53.0	53.0	53.0	53.0	53.0
S36-A1-2	52.7	54.4	54.4	54.4	54.4	54.4
S36-A2-1	53.3	51.7	51.7	51.7	51.7	51.7
S72-A5-1	30.8	32.8	32.8	32.9	33.2	33.4
S72-A5-2	24.8	28.1	28.1	28.2	28.3	28.4
S72-A6-1	34.4	34.7	34.7	34.8	35.1	35.4
S100-A3-1	19.2	19.0	19.0	19.0	19.1	19.1
S100-A4-1	18.4	22.7	22.7	22.8	22.9	22.9
S100-A4-2	18.0	22.3	22.3	22.3	22.4	22.5
S148-A1-1	7.8	10.4	10.4	10.4	10.4	10.4
S148-A2-1	5.6	9.0	9.0	9.1	9.1	9.1
S148-A3-1	6.7	9.9	9.9	9.9	9.9	9.9
Full Series	Mean	1.12	1.12	1.12	1.12	1.12
	CoV	0.17	0.17	0.17	0.17	0.17
0"-72" Series	Mean	1.02	1.02	1.02	1.02	1.02
	CoV	0.06	0.06	0.07	0.07	0.07
Initial Plastic Stress (ksi)		24.2	27.6	29.8	33.1	35.3

Limited research exists on the topic of residual stresses in hot-rolled unequal-leg angles included no data for stainless steel sections besides the work mentioned above. Al-Sayed and Bjorhovde [129] completed some of the only measurements of unequal-leg angles via the sectioning method, which included two carbon steel specimens. The maximum compression was observed at the heel and tips of the angles with tension at the middle of each legs. There was similarity to the standard assumed single angle residual stress distribution [130], shown in Fig. 6.13; however, the actual distributions varied including having different responses in each leg, which was noted to be a common complexity of residual stresses in even equal-leg angles. Modeling residual stresses in stainless steel has been shown to have a small reduction in the member stiffness, but was not found to significantly impact the analysis [96], [131]. An additional study with stainless steel equal-leg angles indicated that considering residual stress had a negligible effect on the final buckling capacity [132]. Accounting for residual stress resulted in both increasing and decreasing the compression capacity, which varied inconsistently with different initial imperfections. Therefore, additional direct modeling of residual stresses was not considered in this study as the selected material model indirectly addresses the altered stiffness.

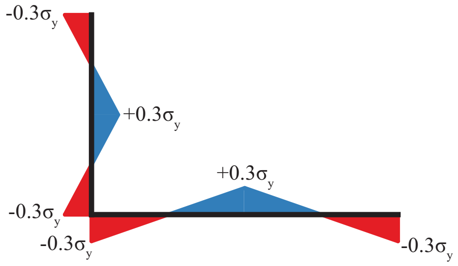

Figure 6.13: Typical residual stress distribution in a single angle

6.4.3 Convergence Study

The initial model mesh was implemented based on previous benchmarking that focused on elastic and perfect elastic-plastic materials. As this study incorporates non-linear elastic-plastic behavior, a confirmation study was completed. The model mesh was varied based on the number of elements across the short flange and the aspect ratio of the element with the long direction along the length of the member. The number of elements across the long flange was adjusted to best match the element size on the short flange.

The short leg was segmented into 4, 8, 16, 32, and 64 elements with nominal element aspect ratios of 1, 2, 3, 4, 5, and 8. Irregardless of the specified mesh, the base model was initially divided at the quarter points to ensure consistent nodes for comparison. Within each section, the length was divided to best match the desired aspect ratio.

The mesh convergence study considered member lengths of 10 in., 36 in., and 100 in. to capture flexural and torsional buckling dominated responses. Each model was subjected to lateral imperfections of $L/1000$ in the principal x- and y-axes and a rotation of 1° in a half-sine wave pattern. The finalized measured material, Curve 5 with plasticity starting ignoring $(0.5\text{ksi})/E_0$ strain, was considered.

Table 6.8 normalized the results based on the finest mesh size, 64 elements with an aspect ratios of 1. Similar to previous convergence study, dividing the short flange into 16 square elements was found to provide a high level of accuracy, less than 0.2% error. Alternate meshing schemes implementing a non-square mesh or reduced elements across a flange also indicated acceptable accuracy and possible speed increases; however, it decided to maintain a consistent approach.

6.4.4 Imperfections

Both measured and nominal imperfections were considered in this study for different application. In either instance, the displacement of cross section was defined by a single set of reference imperfections, dx, dy, and $d\theta$ aligning with Fig. 6.4, which translated to an

Table 6.8: Convergence study for stainless steel. Normalized to finest mesh size

Model length	Number of elements	Aspect ratio					
		1	2	3	4	5	8
10"	4	1.006	1.009	1.017	1.079	1.079	1.079
	8	1.003	1.005	1.009	1.009	1.017	1.080
	16	1.002	1.002	1.003	1.005	1.006	1.009
	32	1.000	1.000	1.002	1.002	1.002	1.005
	64	1.000	1.000	1.000	1.000	1.000	1.002
36"	4	0.994	0.998	1.004	1.006	1.015	1.056
	8	1.000	1.002	1.004	1.006	1.011	1.019
	16	1.000	1.000	1.002	1.002	1.004	1.009
	32	1.000	1.000	1.000	1.000	1.002	1.002
	64	1.000	1.000	1.000	1.000	1.000	1.000
100"	4	0.973	0.979	0.984	0.989	0.995	1.021
	8	0.995	0.995	0.995	1.000	1.005	1.016
	16	1.000	1.000	1.000	1.000	1.000	1.005
	32	1.000	1.000	1.000	1.000	1.000	1.000
	64	1.000	1.000	1.000	1.000	1.000	1.000

updated (x, y) coordinates for each cross section node.

The measured imperfections were critical for the validation analysis. As depicted in Figs. 6.6 and 6.7, imperfections were calculated at discrete locations along the member length. These measured imperfections were transferred to the model mesh using a linear interpolation. The sharp transitions of that piecewise distribution would add unintended stress concentrations to the simulation. Therefore, a modified ″exact" fit, Fig. 6.14, was defined using a Savitzky-Golay smoothing filter to maintain the local variations while eliminating the kinked behavior by fitting a cubic function that considers only 1-inch or 5% of the section. The resulting distribution was determined to be reasonable based on hand measurements; however, it was noted that the measured imperfection distribution contained some noise. For example, assuming the leg data was perfectly aligned at the heel and off by the tolerance of the scanner at the tip of leg would result in a 0.1° rotation error. This issue was addressed by defining a second ″smoothed" fit using a weighed average considering up to 10-inch length which balanced the variations, especially observed in the rotations. Finally, a simplified half-sine curve was provided for comparison. Other researchers have traditionally implemented imperfection in a similar pattern. Section 6.5 details how this information was used.

The parametric study, Section 6.6, implemented nominal half-sine wave imperfections with a magnitude of L/1000 in the lateral directions and a rotation of $\tan^{-1} L/(1000h)$, but limited to 1°. The orientation of worst case imperfection was determined by evaluating L3"x2"x1/4" columns with length matching the experimental study for various imperfection profiles. Separately, the dx, dy, and $d\theta$ imperfections were either excluded or applied in

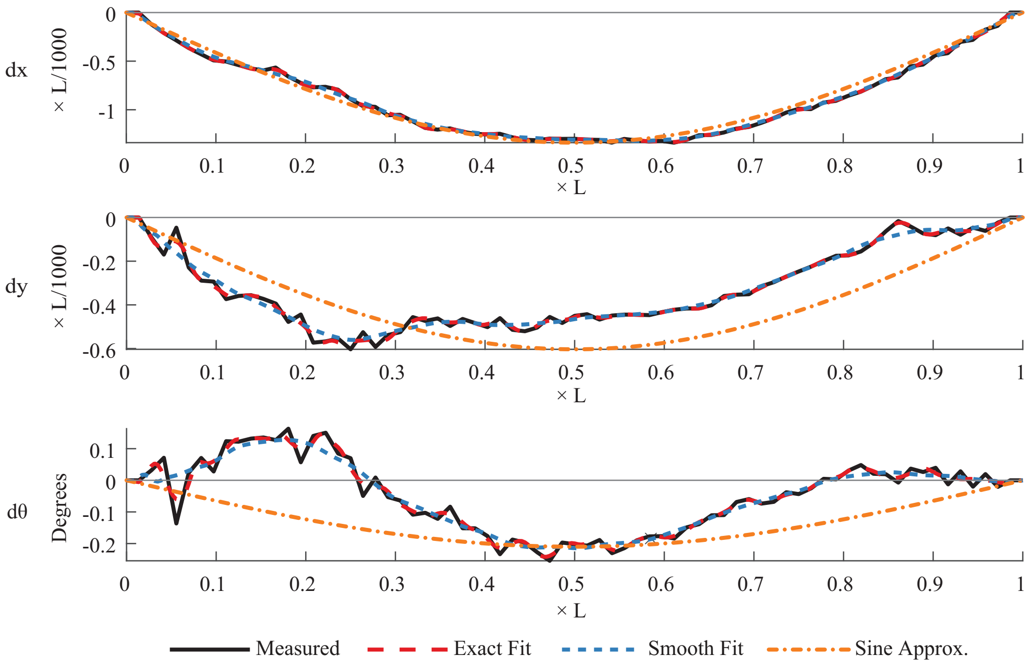

Figure 6.14: Initial imperfections as adjusted for finite element modeling for S36-A2-1

the positive or negative direction. Additionally, the displacements were evaluated for the geometric and principal orientation for a total of 54 combinations. No single combination was found to consistently provide the minimum buckling capacity, Tables 6.9 and 6.10. The default parametric study imperfection was selected as a negative dx and dy imperfection in the principal orientation plus a negative $d\theta$ rotation since this distribution was consistently capturing a one of the lower buckling capacity and a principal orientation allowed for better consistency between different unequal-leg geometries.

6.5 Model Validation

The model validation was completed against the experimental results noted in Section 6.3. All models were evaluated with material properties based on Curve 5 from Table 6.2 with plasticity starting at 33.1 ksi and a square mesh with 16 elements across the short flange with equivalent sized elements on the long flange. The angles were modeled using the measured dimensions in a fixed-fixed end condition. The model length was not shortened to consider effective restraint of the clamping brackets. Four variations of the measured imperfections were evaluated as summarized in Table 6.11 to investigate the effect of the imperfection shape with only minor variations noted, as indicated by Table 6.12.

The computational models matched well with the experimental results for all specimen

Table 6.9: Variation due to geometric initial imperfections

Column Length (in)			dθ								
			-1			0			+1		
			dy			dy			dy		
			-1	0	+1	-1	0	+1	-1	0	+1
10	dx	-1	0.932	0.944	0.908	0.914	0.982	0.921	0.901	0.937	0.939
		0	0.935	0.943	0.907	0.917	1.000	0.919	0.904	0.942	0.937
		+1	0.937	0.940	0.905	0.919	0.987	0.918	0.907	0.944	0.935
20	dx	-1	0.955	0.953	0.916	0.933	0.980	0.930	0.916	0.967	0.947
		0	0.947	0.963	0.921	0.928	1.000	0.935	0.914	0.958	0.953
		+1	0.942	0.975	0.924	0.925	0.977	0.941	0.911	0.952	0.961
36	dx	-1	0.816	0.787	0.753	0.793	0.806	0.767	0.776	0.843	0.782
		0	0.794	0.806	0.767	0.777	1.000	0.782	0.764	0.806	0.799
		+1	0.777	0.835	0.782	0.764	0.806	0.799	0.752	0.788	0.823
72	dx	-1	0.655	0.587	0.535	0.619	0.614	0.551	0.597	0.649	0.569
		0	0.594	0.640	0.564	0.578	1.000	0.583	0.565	0.646	0.606
		+1	0.558	0.639	0.601	0.549	0.614	0.628	0.540	0.597	0.664
100	dx	-1	0.952	0.883	0.814	0.935	0.909	0.835	0.918	0.944	0.857
		0	0.883	0.952	0.857	0.874	1.000	0.879	0.866	0.974	0.905
		+1	0.835	0.922	0.909	0.831	0.913	0.944	0.827	0.905	0.978
148	dx	-1	0.972	0.935	0.885	0.972	0.954	0.902	0.981	0.972	0.919
		0	0.926	0.981	0.918	0.935	1.000	0.935	0.935	1.009	0.954
		+1	0.894	0.944	0.954	0.900	0.954	0.981	0.906	0.963	1.000

Table 6.10: Variation due to principal initial imperfections

Column Length (in)			dθ								
			-1			0			+1		
			dy			dy			dy		
			-1	0	+1	-1	0	+1	-1	0	+1
10	dx	-1	0.915	0.908	0.901	0.930	0.921	0.912	0.953	0.939	0.928
		0	0.958	0.943	0.932	0.953	1.000	0.955	0.928	0.942	0.958
		+1	0.924	0.936	0.951	0.908	0.918	0.929	0.897	0.905	0.914
20	dx	-1	0.922	0.921	0.918	0.938	0.935	0.932	0.956	0.953	0.950
		0	0.964	0.963	0.960	0.992	1.000	1.008	0.952	0.958	0.963
		+1	0.942	0.947	0.952	0.924	0.928	0.933	0.910	0.914	0.919
36	dx	-1	0.758	0.765	0.771	0.773	0.779	0.787	0.788	0.797	0.806
		0	0.796	0.806	0.820	0.820	1.000	0.820	0.816	0.806	0.799
		+1	0.799	0.791	0.784	0.780	0.776	0.770	0.765	0.762	0.758
72	dx	-1	0.540	0.558	0.578	0.556	0.576	0.601	0.576	0.599	0.626
		0	0.603	0.640	0.674	0.635	1.000	0.637	0.689	0.646	0.614
		+1	0.614	0.587	0.567	0.592	0.572	0.555	0.576	0.560	0.546
100	dx	-1	0.823	0.848	0.879	0.840	0.870	0.905	0.866	0.896	0.935
		0	0.900	0.952	0.948	0.935	1.000	0.935	0.974	0.974	0.926
		+1	0.909	0.874	0.844	0.896	0.866	0.840	0.887	0.861	0.835
148	dx	-1	0.889	0.911	0.935	0.906	0.926	0.954	0.924	0.944	0.972
		0	0.944	0.981	0.963	0.963	1.000	0.972	0.991	1.009	0.972
		+1	0.944	0.921	0.899	0.954	0.926	0.906	0.954	0.935	0.911

Table 6.11: Imperfection Distributions considered in Validation Study

	Translations		Rotations	
Label	Smooth	Sine	Smooth	Sine
IV-1	x			
IV-2	x		x	
IV-3	x			x
IV-4		x		x

Table 6.12: Ultimate failure loads for validation modeling with variable imperfections

	Test	Ultimate load (kip) with			
Specimen	(kip)	IV-1	IV-2	IV-3	IV-4
S10-A1-1	62.1	70.3	69.5	69.5	69.6
S10-A2-1	69.5	68.9	68.4	68.4	68.4
S10-A2-2	68.8	69.1	69.1	69.1	69.1
S20-A1-1	61.3	62.0	61.4	61.5	61.6
S20-A2-1	66.8	63.4	63.5	63.6	63.3
S20-A2-2	65.4	63.5	63.5	63.3	63.0
S36-A1-1	57.1	53.0	53.1	53.2	53.7
S36-A1-2	52.7	54.4	54.0	53.9	52.9
S36-A2-1	53.3	51.7	51.3	51.4	51.3
S72-A5-1	30.8	33.2	33.0	32.9	33.4
S72-A5-2	24.8	28.3	28.3	28.4	28.4
S72-A6-1	34.4	35.1	35.1	35.0	36.7
S100-A3-1	19.2	19.1	19.1	19.1	19.2
S100-A4-1	18.4	22.9	22.9	23.0	22.9
S100-A4-2	18.0	22.4	22.6	22.7	22.2
S148-A1-1	7.8	10.4	10.4	10.4	10.2
S148-A2-1	5.6	9.1	9.1	9.1	9.0
S148-A3-1	6.7	9.9	9.9	9.9	9.9
Full Series	Mean	1.12	1.12	1.12	1.12
	CoV	0.17	0.17	0.17	0.17
0"-72" Series	Mean	1.02	1.02	1.02	1.02
	CoV	0.06	0.06	0.07	0.07

72 inches and shorter with additional information in Appendix B. The simulation was able to replicate the torsional buckling dominate response in short columns as shown in Fig. 6.15. The inclusion of additional flexural movement as the column length increased was also captured as depicted in Fig. 6.16. However, as the buckling transitioned to a primarily flexural buckling response at long lengths, see Fig. 6.17, significant variations between the modeled and actual response were noted. The same primary behavior captured, but at different magnitudes and more gradually in the computational result.

While investigating the different response, the larger flexural deformation of the buckling column combined with the fixed boundary condition was observed to cause tension to develop at the end of the specimens in the finite element analysis. While reasonable, this result was not realistic as there was no positive connection between the base plate and the angles. Instead, bearing would be lost when tensile flexural stresses exceeded the axial

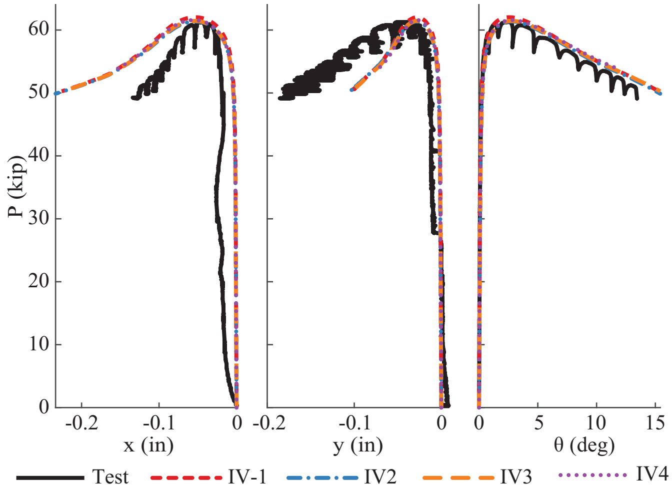

Figure 6.15: Torsion dominated buckling displacement of S20-A1-1

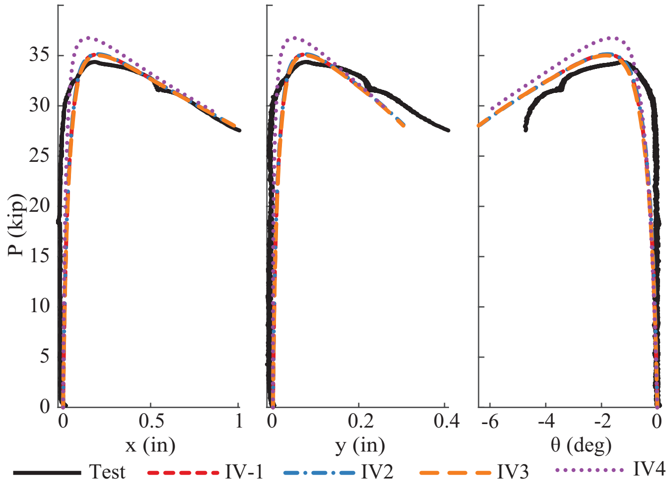

Figure 6.16: Intermediate flexural-torsional buckling displacement of S72-A6-1

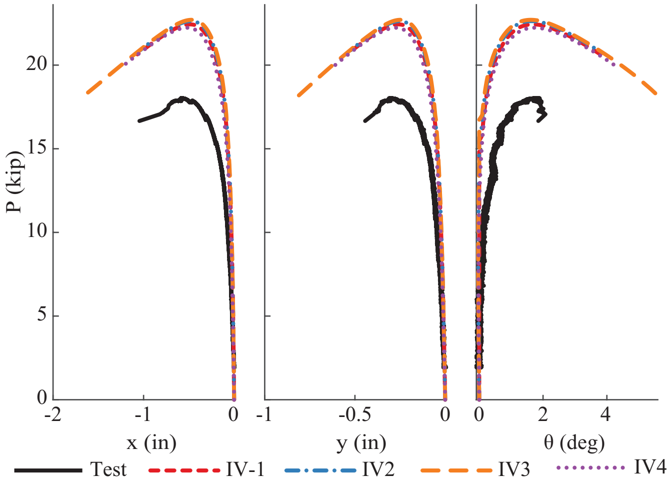

Figure 6.17: Flexure dominated buckling displacement of S100-A4-2

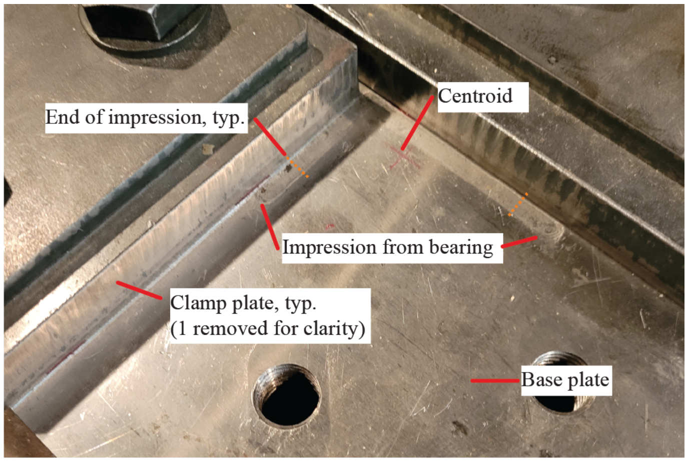

Figure 6.18: Base plate after final compression test series

compression. Exploratory work to directly account for contact at the base plate confirmed that uplift did occur at buckling for the longer specimens. Most investigations noted the angle lifted at the heel, which increased the bearing stress at the tip causing more localized yielding. A slightly reduced ultimate capacity and less post-buckling ductility were also noted, but not enough to match the experimental results. Further review highlighted that the base plate was permanently deformed after the compression tests as shown in Fig. 6.18. While the base plate was not anticipated to be plastically deformed under loads associated with nominal stainless steel material properties, the actual compression tests caused small impressions near the tips of each angle leg. The entire cross section was discolored from bearing, but only the final 5/8-inch of each leg was deformed, varying approximately linearly with a max impression of 0.02 inch at the tip. Modeling incorporating contact, the imperfect bearing surface, and deformation of the base plate resulted in only minor changes for shorter columns; however, the majority of 100-inch and 148-inch models captured a significantly reduced capacity and less overall deflection. While future work is needed to provide a detailed, exact comparison to these flexural buckling experiments, the validation study indicated that the modeling approach was capable of depicting the behavior of stainless steel unequal-leg angles with perfect boundary conditions, and thus acceptable to implement in a parametric study

6.6 Parametric Study

A parametric study was completed to expand the available data for unequal-leg single angles. This study focused on nominally compact cross sections, aligning with the current limitations for equal-leg angles given in AISC 370 [12]. Possible sections were identified

Table 6.13: Angles in Parametric Study

Section	h/b	h/t	b/t
L6"x5"x1/2"	1.2	12	10
L6"x4"x1/2"	1.5	12	8
L6"x3"x1/2"	2.0	12	6
L5"x3"x1/2"	1.67	10	6
L4"x3"x1/2"	1.33	8	6
L4"x3"x3/8"	1.33	10.7	8
L3"x2"x3/8"	1.5	8	5.3
L3"x2"x1/4"	1.5	12	8
L3"x1.5"x1/4"	2.0	12	6
L2"x1.5"x1/4"	1.33	8	6
L2"x1"x1/4"	2.0	8	4
L1.5"x1.25"x1/8"	1.2	12	10

Figure 6.19: Proportions of all available angles

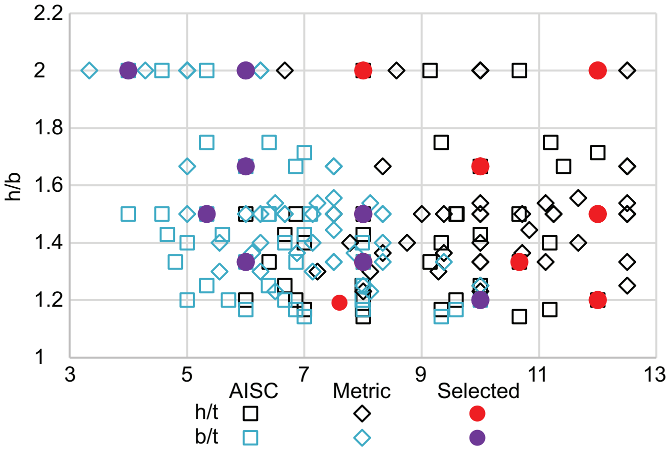

from the unequal-leg cross sections listed in the AISC carbon steel design manual [133] and from distributors [134]–[140]. A total of 90 different sections were noted; however, only 50 were determined to be compact while applying the stainless steel compression limit of $b/t \leqslant 0.41\sqrt{E/Fy}$ for both nominal 304 and 304L material properties. The final twelve representative sections, listed in Table 6.13, were selected to cover typical h/t, b/t, and h/b ratios, as depicted in Fig. 6.19, and were the sizes most commonly available from distributors.

Each cross section was evaluated with nominal dimensions, nominal imperfections, and an effective slenderness ratio, L_e/r_z, ranging from 5 to 200. All cross sections were modeled for both a fixed-fixed, $0.5L = L_e$, and pinned-pinned, $1.0L = L_e$, boundary condition. The angles were then modeled with either the measured material properties, matching the validation study, or nominal material properties for 304 or 304L based on the AISC list nominal values [12]. In the total 2,880 models, flexural-torsional buckling was consistently observed. Similar to the experimental results [15], flexural deformation were dominant at

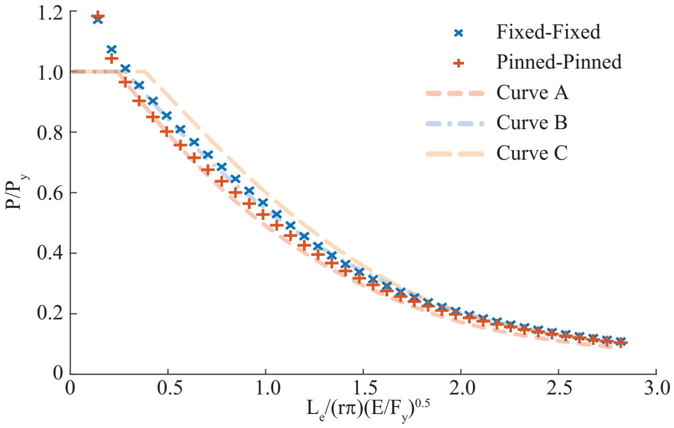

Figure 6.20: Buckling behavior of L2"x1"x1/4" with measured material properties

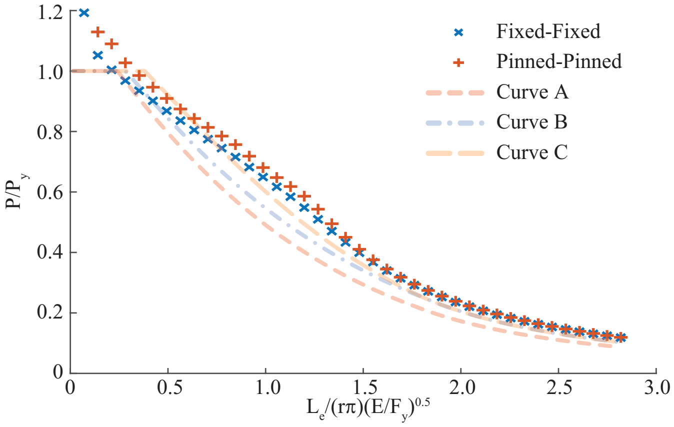

Figure 6.21: Buckling behavior of L6"x4"x1/2" with measured material properties

high slenderness ratios that transitioned to torsional deformation as the slenderness ratio decreased.

Plotting the ultimate capacity against normalized slenderness for a single section, for example Fig. 6.20 with additional results in Appendix C, depicted a gradual increase in strength as the column shortened. A significant strength plateau that corresponds with typical flexural-torsional buckling design provisions was not captured. The most comparable observation, such as Fig. 6.21, was an uncharacteristic early increase in strength that reverted to typical behavior. This localized increased was attributed to the reference imperfection. Exploratory simulations with variable imperfections captured reduced buckling capacities, particularly at the increased intermediate results. However, for consistently and clarity in the final data set, only results implementing the default imperfection are presented from this study.

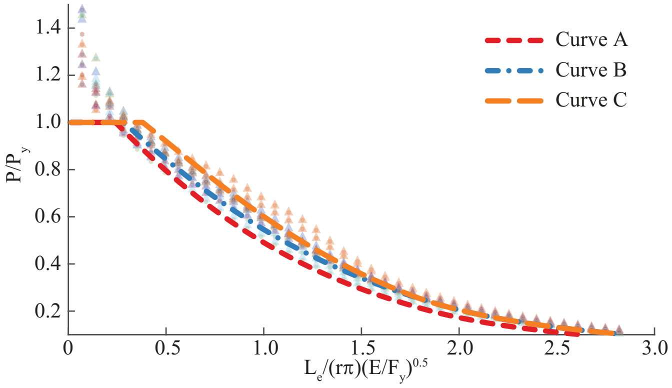

Figure 6.22: Buckling behavior with measured material properties

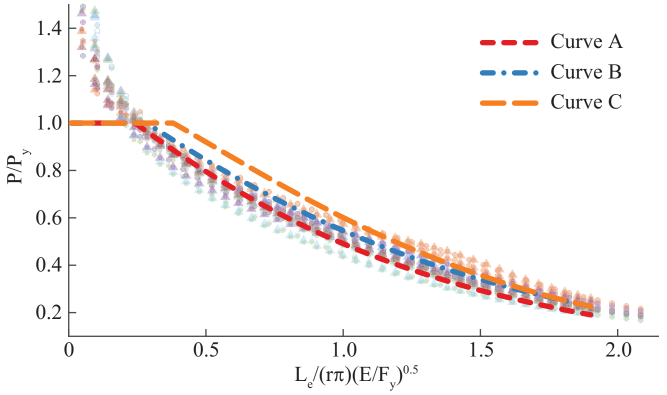

Figure 6.23: Buckling behavior with nominal material properties

6.7 Comparison to Design Provisions

The parametric study resulted in distinct variations depending on the material properties considered. Using the AISC 370 flexural buckling relationships as a reference, the measured material property results were found to be normally greater than Curve A, Fig. 6.22, while a number of nominal material property results were determined to be lower than Curve A, Fig. 6.23. By comparing the effective stiffness included in each model in Fig. 6.24, there is a distinct variation between the nominal assumed behavior and the measured behavior used in this study. The increased strain-hardening coefficient measured in this study, which agrees with previous research on hot rolled sections [102], [104], [112], [126], causes a stiffer material response. As a result, detailed discussion of design provisions will evaluated for the nominal and measured results separately.

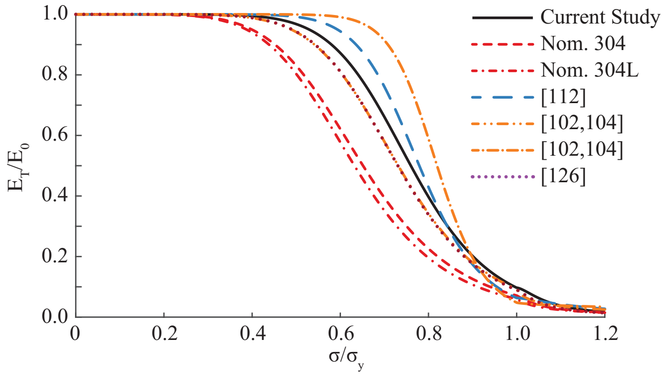

Figure 6.24: Effective modulus of elasticity within material models

6.7.1 Flexural-Torsional Buckling in the Design Provisions

For comparison purposes, the general compression design provisions presented in Section 6.2.3 were assumed to apply to unequal-leg angles. This approach is similar to carbon steel angles, in that unequal-leg and equal-leg angles are treated identically. Therefore, the sections in this parametric study would be controlled by flexural-torsional buckling for design purposes as the asymmetric sections will never be controlled by elastic flexural buckling. While this also applies to carbon steel angles, they are allowed to be designed using the flexural buckling provisions based on Galambos's work [8], partially to avoid double counting the local buckling and global flexural-torsional buckling response since they are effectively the same failure mode in single angles [61], [112]. Extending the method from Galambos [8] to stainless steel sections, the buckling capacity can be calculated by modifying Eq. 6.5 with stiffness reduction factors for the longitudinal stiffness and shear stiffness, τ_E and τ_G, respectively as given by Eq. 6.13;

$$\begin{aligned}(f_{in} - f_{xb}\tau_E)(f_{in} - f_{yb}\tau_E)\left(f_{in} - \frac{\tau_G GJ + \tau_E \pi^2 E C_w / L^2}{r_0^2}\right)& \\ -f_{in}^2 (f_{in} - f_{yb}\tau_E)\frac{x_0^2}{r_0^2} - f_{in}^2 (f_{in} - f_{xb}\tau_E)\frac{y_0^2}{r_0^2} = 0&\end{aligned} \tag{6.13}$$

where f_{in} is the critical buckling stress, equivalent to F_{cr}.

Eq. 6.13 can be evaluated for any effective longitudinal stiffness behavior, provided a τ_E factor can be defined. A design longitudinal stiffness reduction factor, $\tau_{E,D}$, would be defined by rearranging Eq. 6.4 as shown in Eq. 6.14 with an additional constraint that the calculated f_{in} must be reduced to a maximum of F_y;

$$\tau_{E,D} = \begin{cases} \beta_2 & \text{if } \frac{f_{in}}{F_y} \leqslant \beta_2/3.20 \\ \frac{f_{in}}{F_y}\left(\frac{\ln\left(f_{in}/(1.2F_y)\right)}{\ln \beta_1}\right)^{1/\alpha} & \text{otherwise} \end{cases} \tag{6.14}$$

Table 6.14: Specific Ramberg-Osgood parameters for different models

Reference	σ_{max}	ϵ_{max}	$n_{0.2,max}$
Nominal AISC values	σ_u	ϵ_u	m
Measured properties	$\sigma_{1.0}$	$\epsilon_{1.0}$	$n_{0.2,1.0}$

The buckling behavior can also be determined based on the nonlinear Ramberg-Osgood stress-strain relationship. A stress-strain longitudinal stiffness reduction factor, $\tau_{E,SSC}$, can be calculated using Eq. 6.15, which was derived by rearranging Eq. 6.3 and substituting $\sigma_{0.2} = F_y$;

$$\tau_{E,SSC} = \begin{cases} F_y / \left(F_y + 0.002En \left(\frac{f_{in}}{F_y} \right)^{n-1} \right) & \text{if } f_{in} \leqslant F_y \\ \frac{E_{0.2}}{E} f_r / \Bigg[f_r + E_{0.2} \left(\epsilon_{max} - 0.002 - \frac{F_y}{E} - \frac{f_r}{E_{0.2}} \right) & \text{otherwise} \\ \qquad \bullet\, n_{0.2,max} \frac{f_{in} - F_y}{f_r}^{n_{0.2,max}-1} \Bigg] & \end{cases} \tag{6.15}$$

where $f_r = \sigma_{max} - F_y$. Since the AISC nominal properties and measured material properties in this study use different reference stress in modified Ramberg-Osgood relationship, Table 6.14 summarizes the necessary substitutions.

Typical design calculations would assume an identical response for the longitutional and shear behavior, $\tau_G = \tau_E$, which is the lower bound for this comparison. Alternatively, Galambos [8] utilized $\tau_G = 1$ for carbon steel single angle since effectively no reduction in shear stiffness was observed prior to failure of a compression member. While carbon steel and stainless steel have different constitutive relationships, the equivalence of a partially yielded section and the initial linear-elastic response under a small torque presented by Neal [83] would still be applicable. Therefore like carbon steel, a reasonable approximation for an upper bound for the stainless steel response was $\tau_G = 1$ indicating there is no shear stiffness reduction due to axial compression.

Together, these stiffness relationships allow for the comparison of the current design provisions and the buckling strength based on the stress-strain relationship including variations on the importance of flexural-torsional buckling. The design provisions for compression members were directly evaluated to determine the buckling capacity when considering flexural-torsional buckling, labeled 'AISC 370-FTB', and evaluated again neglecting flexural-torsional buckling as done for carbon steel single angles, labeled 'AISC 370-FB'. Using Eq. 6.13 with $\tau_{E,D}$ and $\tau_G = 1$, the buckling capacity was determined considering flexural-torsional buckling while implementing the longitudinal stiffness defined

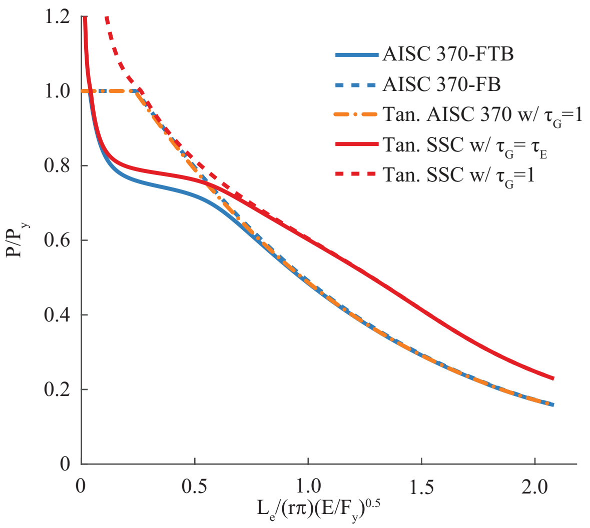

Figure 6.25: Compression member capacity for L6"x5"x1/2" with nominal 304 properties

implicitly by design and without shear stiffness reduction from compression, labeled ‘Tan. AISC 370 w/ $\tau_G = 1$’. The companion condition of $\tau_G = \tau_{E,D}$ was not calculated as it is equivalent to the flexural-torsional buckling values following AISC 370. Using Eq. 6.13 with $\tau_{E,SSC}$, the buckling capacities based on the stress-strain relationship were calculated for both values of τ_G with the results labeled ‘Tan. SSC w/ $\tau_G = 1$’ and ‘Tan. SSC w/ $\tau_G = \tau$’, respectively. Comparing the design based results with the stress-strain curve results assists in understanding where the imperfect nature of real systems reduces our system.

6.7.2 Design Provisions with Nominal Material Properties

When utilizing nominal material properties, for example Fig. 6.25, considering design flexural-torsional buckling was observed to cause a substantial decrease in strength compared to the flexural buckling capacity. Other cross-section geometries exhibited smaller reductions, but it was always observed to create a significant impact. Evaluating flexural-torsional buckling with the increased shear stiffness resulted in a minimal reduction from the flexural buckling limit, similar to the corresponding analysis with carbon steel. As a result, comparing parametric study capacities to the flexural buckling design values would be appropriate to determine if flexural-torsional buckling needs to directly evaluated or if it safely implicitly incorporated.

The nominal 304 stress-strain curve capacities were observed to be only slightly greater than the design values near the yield stress when evaluating both flexural-torsional and flexural buckling behavior. While there are differences at the higher normalized slenderness

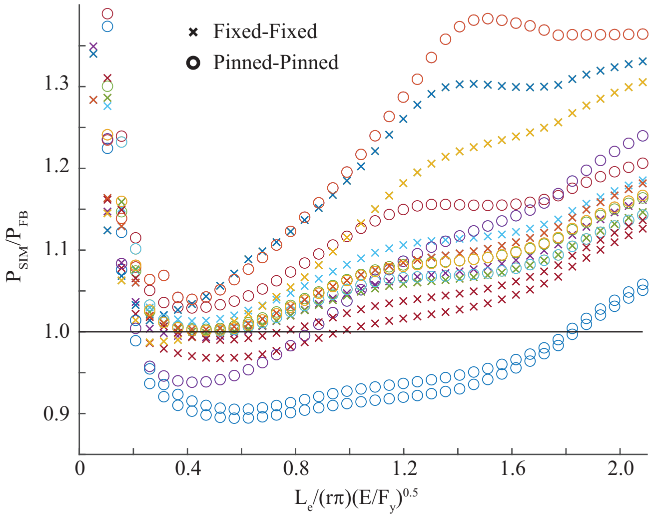

Figure 6.26: Nominal 304 modeled capacity versus design flexural buckling

ratios to account for member imperfections and other reductions to the column capacity, the behavior at low normalized slenderness ratios indicate the design provisions do not account for a reduction from the nominal response. This trend only becomes worse when considering 304L material as the resulting capacities drops below the design values.

The parametric study results were compared to the design buckling capacities considering and neglecting flexural torsional buckling. Despite stainless steel members being commonly dual-certified as 304/304L, each material group was evaluated with the grade specific yield stress. None of the following calculations account for local buckling reductions as all cross sections are compact for nominal material properties.

Flexural buckling alone was observed to be a poor predictor of the buckling capacity of the columns with nominal material properties as shown in Figs. 6.26 and 6.27. For 304, a majority of the cross sections approached unity at the worst-case normalized slenderness with approximately as many sections being unconservatively predicted as conservatively. However, the predictions for 304L columns were found to be worse with almost all sections becoming unconservatively designed at one point.

Predictions were improved by considering flexural-torsional buckling, see Figs. 6.28 and 6.29. This change left only the pinned-pinned L5"x3"x1/2" and L2"x1"x1/4" series as consistently unconservatively designed for both grades. The remainder of the 304 series were safely predicted, while a small number of 304L were slighly under unity.

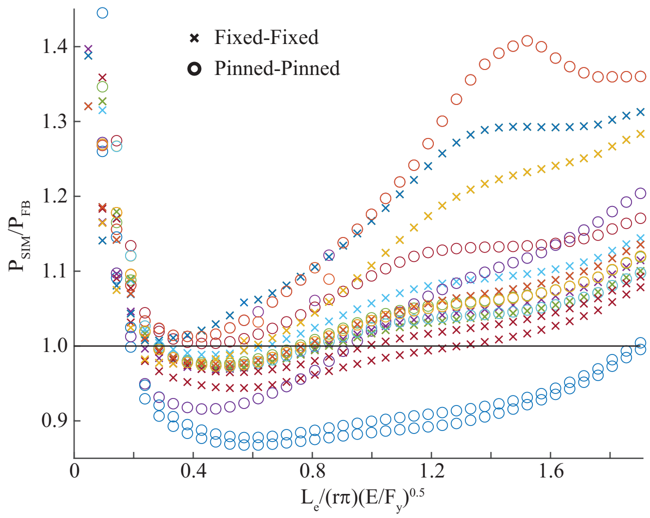

Figure 6.27: Nominal 304L modeled capacity versus design flexural buckling

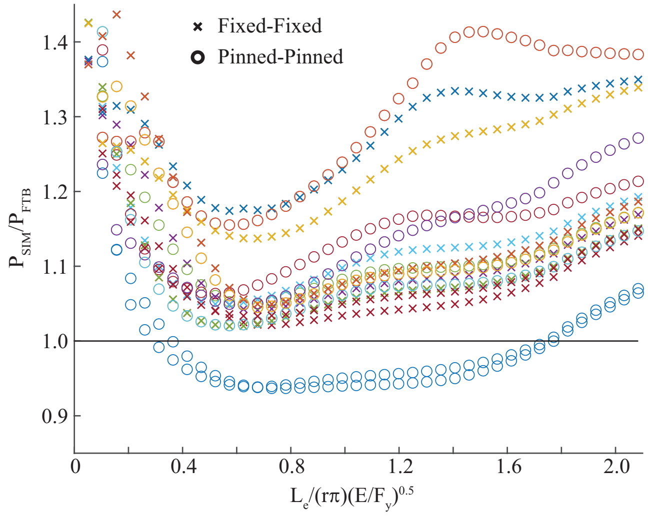

Figure 6.28: Nominal 304 modeled capacity versus design flexural-torsional buckling

6.7.3 Design Provisions with Measured Material Properties

When utilizing the measured material properties, for example Fig. 6.30, similar trends as noted with the nominal material properties between the design flexural buckling and design flexural-torsional buckling capacities were observed. The main difference was flexural-torsional buckling resulted in a larger reduction due to the increased yield stress. This behavior carried over to the 'Tan. AISC 370 w/ $\tau_G = 1$' causing a slightly greater variation from the pure flexural buckling response. However, the overall agreement still indicated that it might be acceptable to not explicitly evaluate flexural-torsional buckling.

The measured stress-strain curve buckling capacity was observed to approach the

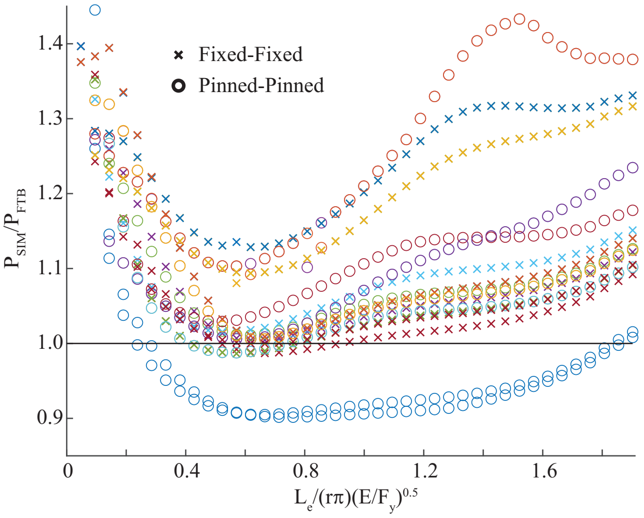

Figure 6.29: Nominal 304L modeled capacity versus design flexural-torsional buckling

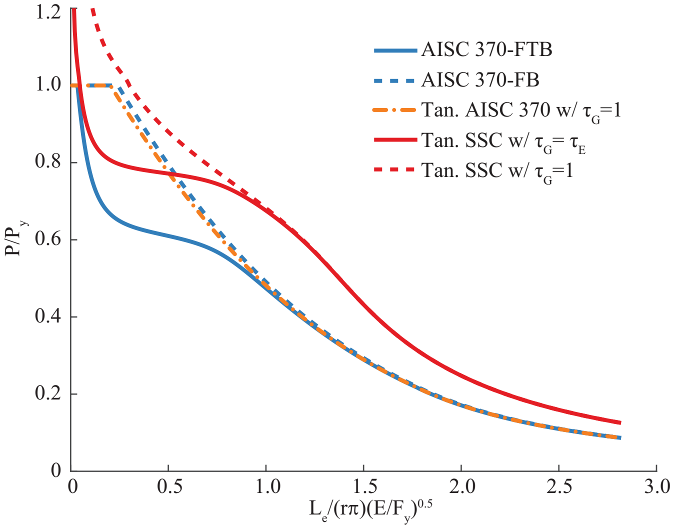

Figure 6.30: Compression member capacity for L6"x5"x1/2" with measured material properties

flexural-torsional buckling design capacity at yield similar to the nominal behavior comparison. However, the measured stress-strain curve buckling quickly deviated from the design provisions indicating additional capacity at both low and high normalized slenderness ratios. The concerns associated with the nominal response were not observed due to the increased stiffness encountered in the measured response.

Unlike the nominal, the measured material parametric study results were found to be conservatively predicted by flexural buckling alone as shown in Fig. 6.31. Only a few results were underestimated, with the majority associated with the same pinned-pinned L5"x3"x1/2" and L2"x1"x1/4" sections that were poorly predicted in the nominal material property portion of the study. Considering flexural-torsional buckling eliminated any

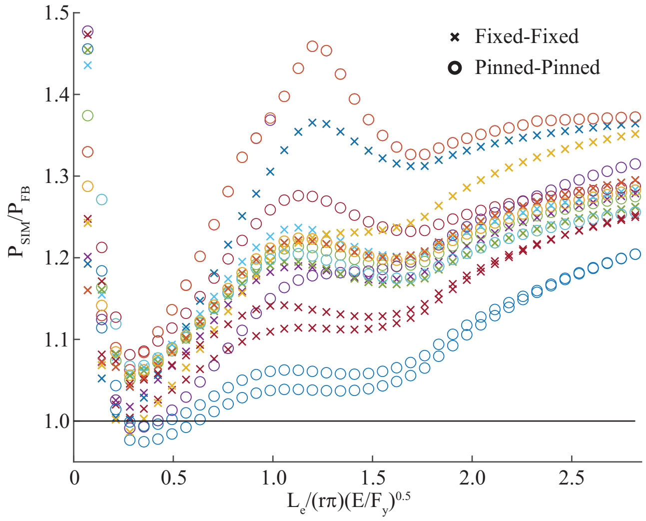

Figure 6.31: Modeled capacity with measured material properties versus design flexural buckling

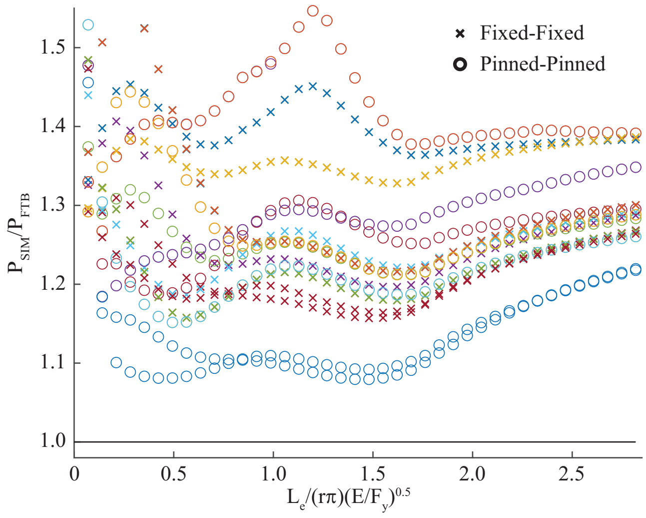

Figure 6.32: Modeled capacity with measured material properties versus design flexural-torsional buckling

unconservative results, see Fig. 6.32; however, the overall capacity predictions were worse, especially for low normalized slenderness.

As mentioned earlier, the cross section sizes were selected to be compact for nominal material properties. Considering the actual yield stress observed would reclassify some cross sections as slender since the critical b/t ratio reduced from 12.5 to 9.3. Combining the standard local buckling reduction for stainless steel section, noted in Section 6.2.3, with the flexural buckling design provisions reduced the number of unconservative results, as illustrated in Fig. 6.33. Local buckling reductions would also interact with flexural-torsional buckling values, but no plot was provided since the increased capacity at low slenderness ratios only worsen the prediction shown in Fig. 6.32.

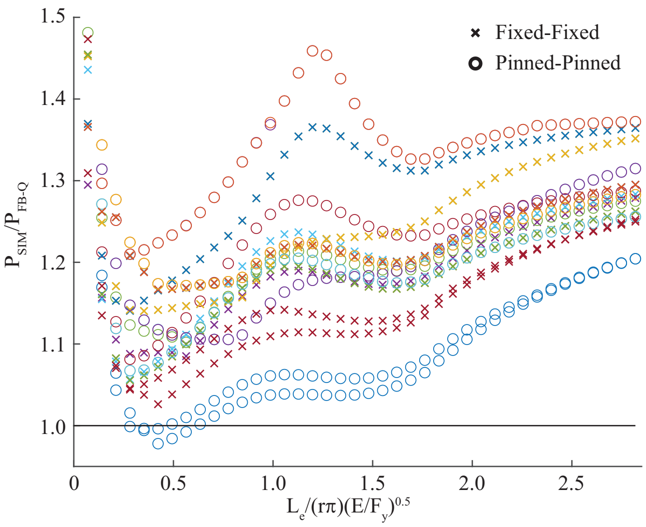

Figure 6.33: Modeled capacity with measured material properties versus design flexural-buckling plus local buckling reductions

6.8 Relevance to existing design provisions

At first glance, comparing the parametric study results to the design provisions indicated different conclusions depending on the material model. The nominal results indicated that accounting for flexural-torsional buckling in design was necessary to provide conservative capacities across a wide range of geometries. In contrast, the measured material results indicated that flexural buckling alone was adequate to appropriately design single angles with local buckling reductions eliminating most unconservative predictions. Despite this difference, both data sets were observed to have a gradual transition from the flexural dominated behavior at a high normalized slenderness to the torsion dominated behavior at a low one. The typical strength plateau associated with a controlling region of flexural-torsional was not observed. Simulations that depicted a small strength plateau also captured buckling capacities greater than the expected flexural buckling capacity and never occurred at the low normalized slenderness corresponding to where controlling flexural-torsional buckling would be expected to exist. Inspections of the buckled shape near these plateaus noted distinct trends before, within, and after the region. Combining this observation with the alternative initial imperfection work noted earlier, the author theorized that the selected initial imperfection cannot readily transition to the preferred buckling geometry at intermediate lengths with less issues at the extremes. As a result, a significant reduction in buckling capacity due to flexural-torsional buckling was not observed in this study.

The varied results of the parametric study highlighted the importance of defining the appropriate material response. With carbon steel sections, the majority of steel grades used for structural design exhibit a consistent material behavior that is readily simplified to an approximate elastic-plastic response. Despite a simple, consistent material model, multiple compression design curves have been developed that vary with the cross-section shape being analyzed [123]. This issue is complicated for stainless steel members as the variability of the nonlinear constitutive relationship adds an additional dimension. The nominal stress-strain relationship has experimental backing that it is appropriate for the baseline behavior of 304/304L stainless steel in a very broad range of applications. However, additional research, including the testing related to this study, has regularly noted significant increases in strength and stiffness when investigating structural stainless steel sections as highlighted in Fig. 6.24. As a result, the three design curves in AISC 370 are attempting to balance what is the impact of different geometries, including the variable cross sections and typical imperfections as had been done with carbon steel, as well as what is a realistic, average response of typical stainless steel members. Therefore, the trends observed in all the completed simulations are useful information, but evaluations of the design provisions should focus on the more realistic response associated with the measured material properties.

The completed study cannot directly assess the appropriateness of the buckling coefficients given in Curve A for compression design from AISC 370 for unequal-leg angles in general. Without first assessing the actual range of material stiffness, this study can only indicate that those parameters are conservative for this batch of stainless steel angles. While possibly improbable, stainless steel members that only meet the minimum grade requirements would realistically be under designed with these buckling coefficients. Despite that limitation, this parametric study agrees with previous research on equal-leg single angles that accounting for flexural-torsional buckling underestimates the capacity of single angles. The straight-forward simplification used in design to use the same reduction for the longitudinal stiffness and shear stiffness under axial load becomes less appropriate as a greater component of the total capacity relies on the torsional shear behavior. Therefore, implementation of a provision similar to what currently applies to carbon steel should be considered. Allowing single angles to be designed by only evaluating flexural buckling with local buckling reductions, thereby relying on the indirect evaluation of flexural-torsional buckling, would allow for a more efficient use of material. While further work is needed to assess the appropriateness of local-buckling provisions for all slender cross sections, the limited results in this study noted similarity to the carbon steel angle observations that the flexural buckling capacity was adequately reduced where flexural-torsional buckling concerns did arise.

6.9 Conclusions

This study investigated the flexural-torsional buckling behavior of stainless steel unequal-leg single angles. A modeling procedure was developed and validated by comparison to experimental results from 18 fixed-fixed 304/304L L3"x2"x1/4" columns with lengths ranging from 10 inches to 148 inches. The subsequent parametric study considered 12 cross sections, nonslender for nominal material properties, with a L_e/r_z ratio ranging from 5 to 200 to incorporate elastic and inelastic failures. Each cross section was evaluated for a fixed-fixed and pinned-pinned flexural end restraint and one of three material models based on either nominal 304 parameters, nominal 304L parameters, or the measured material properties determined through the validation study. The simulations captured flexural-torsional buckling of all cross sections with both flexural and torsional dominated failures. The variable stiffness of the constitutive relationships was observed to effect how the results compared to design provisions. It was determined that the existing buckling coefficients for generic cross-sections produced conservative results when considering realistic material properties. While flexural-torsional buckling was consistently observed, evaluation of existing flexural-torsional buckling design provisions resulted in excessive conservatism in design for most applications. It was determined that evaluating flexural buckling with local buckling reductions, similar to the design provisions for carbon steel single angles, addressed most flexural-torsional buckling concerns for the stainless steel single angles in this study. Additional work should focus on slender cross sections to validate the consistency of this result and to determine if a limiting slenderness of the cross section is applicable.

7 CONCLUSIONS

7.1 Summary and Conclusions

This dissertation summarized the advancements in providing guidance to engineers on how to appropriately evaluate structures with non-symmetric cross sections. Non-symmetric sections present multiple challenges in the structural design process including difficulties with the analysis and design phase. A significant issue that consistently arises is how important are the unique non-symmetric behaviors that are not encountered with the doubly symmetric cross sections and when do they matter. To address this issue, a better understanding of what is included in current practice was needed first.

When assessing the fundamental mechanics, it is understood that non-symmetric sections behave different from doubly symmetric sections. However, the implementation of this information into structural analysis varies. As discussed in Chapter 2 and 3, many practicing structural engineers utilize structural analysis software that assume doubly-symmetric cross sections and require intervention by the user to approximately model any non-symmetric cross-section specific response. An underlying issue with such considerations is moving from the two-dimensional focus that individuals are typically taught and can be appropriately applied to many structures to a three-dimensional reference frame requiring evaluation of combined axial, strong-axis bending, weak-axis bending, and torsional behaviors that are common with non-symmetric sections. While many benchmark solutions exist for two-dimensional analysis, only a few alternatives exist to confirm the three-dimensional response, which typically focused on doubly-symmetric cross sections. As a result, this project evaluated three individual member and three structural systems to provide additional benchmark solutions for non-symmetric cross sections, while also assessing the ability of conventional double-symmetric line elements and a novel non-symmetric line element to model the behavior.

Evaluations of the various benchmarks noted that the impact of twist was the most critical feature. When twist was constrained or small, there was better agreement between double symmetric analyses and the more complex methods. However, non-symmetric sections commonly rotate due to the cross section geometry whether due to direct torsion due to the shear center position relative to the load or bending moments applied about both principal axes, which drives increased differences. Depending on engineers interpretation of the minimum requirements for analysis, it is possible to miss these impacts as twist and torsion are not discussed as fundamental requirements. This issue highlights the importance of evaluating the equilibrium on the deformed geometry, especially with non-symmetric sections, which often requires incorporating the third dimension. Additionally, this extra deformation causes warping stiffness to become increasing important to efficiently utilize the section. Without warping stiffness, non-symmetric sections were observed to depict premature stability issues.

Building on the different twisting effects, the true impact on structural systems from not considering non-symmetric behavior was difficult to predict. Evaluations of individual beams and columns allowed for a single mechanism to be isolated for the observed variation. But once combining members, predicting how different inaccuracies would influence each other was inconsistent. The competing behaviors, such as an underestimated applied torsion combined with missing torsional stiffness, could result in reasonable or unrealistic results. As more complex structures and problems are evaluated, capturing the appropriate non-symmetric behavior becomes increasingly important as the ability to verify simplified models will be strained.

Open-web steel joists, which are discussed in Chapter 4, are such an application where a relatively common structural component requires complex analysis in nonstandard applications since it is composed of multiple members with non-symmetric cross sections. Assessing eccentric torsion applied to the chord angles has typically involved a combination of standard analysis with supplementary methods to access bending and torsion in the chord segment. For this study, an experimental evaluation was completed to validate the modeled response incorporating non-symmetric section behavior.

A pair of steel joists were connected with bracing and decking to form a self-stabilizing system. A simulated uniform design live load was applied to the deck followed by the application of an eccentric hanging load to one of the bottom chord angle members on the tested joist. During the experiment, data was recorded to compare internal stresses in the chord as well as displacements and rotations. The computational model was able to accurately calculate deformations for the full experiment and axial forces in the chords. Conservative predictions of the additional stresses due to the eccentric loading was determined by the model, which led to some undesirable results due to the excessive compression calculated on the chord in the tension-controlled regions.

Building on the challenges noted in predicting the behavior of simplified models noted above, additional computational models were created to study the effects of a first- vs. a second-order analysis, a non-symmetric vs. a doubly-symmetric analysis, nominal vs. measured cross-section geometry, and the effect of the hanging rod position on the analysis of a steel joist with an eccentric handing load. It was found that underestimating the rotation of the cross-section at equilibrium, whether due to underestimating the applied torque with a doubly-symmetric analysis or assuming the initial orientation associated with a first-order analysis, led to excessive weak-axis moments and compressive stresses on the horizontal legs. Likewise, the analysis captured excessive rotations and displacements of the cross section when not adequately accounting for the reduced eccentricity of the hanging load, which is associated with a first-order analysis or excluding the relatively stiff hanging rod, due to the low torsional stiffness of the chord. Although significant variations in the actual torsional cross-section properties relative to nominal were measured, it had minimal impact on the observed displacements and stresses.

The variations noted in the more simplistic models might be expected. However, addressing these after completing the analysis would be difficult to impractical. To improve the modeled behavior, the non-symmetric response needs to be directly included. Despite the improvements noted with following this approach, further work is needed to address the limitations of connecting different cross sections.

While determining demand with non-symmetric cross sections is imperfect, structures still incorporate non-symmetric cross sections meaning design capacities need to be available. Similar to analysis, this introduces the challenge of separating the underlying mechanics and an acceptable design procedure. This study focused on two groups of compression members, carbon steel equal-leg double angle joist chords and stainless steel unequal-leg single angles. Despite significant differences, both groups demonstrated how simplifications are acceptable when the complex true behavior varies from the streamlined behavior defined by design specifications.

Double angles provide an interesting example as different design specifications indicate different importance for flexural-torsional buckling. Some methodologies, like AISC-360, require flexural-torsional buckling to be treated equivalent to flexural buckling, while others, e.g. SJI-100, allow flexural-torsional buckling to be neglected. A numeric inelastic buckling investigation considering the known shear stiffness of axial-loaded columns found that flexural-torsional buckling is not as critical as treated by current AISC design procedures. However, flexural-torsional buckling is theoretically important for a number of double angle cross sections when considering only nominal torsional stiffness. Attempts to validate this observation using finite element models noted that double angles in full joist models buckled at loads at or above the SJI flexural buckling limit, while capturing a combination of local behaviors interacting with the global buckling modes.

Further investigation with isolated chord segment finite element models noted similar behavior. The inelastic buckling capacities were found to be greater than the expected theoretical design-based results, while capturing significant individual angle flexural-torsional buckling and more flexural buckling than would be expected. This behavior was confirmed with elastic buckling evaluations that indicated local angle behavior between ties was a significant factor in defining the overall deformation of the cross sections and global flexural-torsional buckling capacity substantially increased. The greater observed torsional stiffness of the composite section was confirmed, which could be attributed to combined warping of the full cross-section due to torsion transfer at the ties.

A reevaluation of the inelastic buckling calculations with the known shear stiffness, updated section properties, and a reduced effective length for torsional buckling observed in the study resulted in agreement between the observed behavior and the underlying theory. Twisting of the double angles was a critical factor; however, it was the individual angles and not the combined cross section. Flexural-torsional buckling was still possible, but the buckling capacity was substantially increased and normally exceeded the flexural buckling capacity.

A similar response was noted with stainless steel unequal-leg single angles, despite the simplified cross section and nonlinear material behavior. Implementing a parametric study validated using experimental results from 18 fixed-fixed 304/304L L3"x2"x1/4" columns with lengths ranging from 10 inches to 148 inches, a range of flexural-torsional buckling failures was observed in 12 nominally compact, unequal-leg angle cross sections. When considering measured material properties, the flexural buckling conservatively predicted the majority of buckling results despite not directly accounting for the observed behavior. Most of the unconservative predictions were eliminate when accounting for local buckling as well, which was attributed to the equivalent capacity and deflections associated with local buckling and flexural-torsional buckling in single angles.

In both applications, flexural buckling with local buckling reduction appropriately determines the buckling capacity in compression. For most practical hot-rolled geometries, flexural-torsional buckling was found to not control, in the case of double angles, or to cause minimal reductions, in the case of unequal-leg single angles. The simplified design procedure can obscure the underlying complex behavior, but in most applications, engineers only need to determine an appropriate capacity to safely and efficiently use material. An available description of the true behavior provides most of the benefit associated with completing more complex calculations that would directly assess flexural-torsional buckling. Combining the why with limitations on applicability then provides engineers with the guidance to further investigate the behavior if they opt to continue down that path.

Overall, non-symmetric cross sections continue to present interesting challenges in structural applications. There remains to be a consideration during design to balance the exact response with a reasonable approximation. This study has highlighted instances where the existing methods fail to capture the appropriate behavior as well as others where simplifications are acceptable. Providing this guidance to practicing engineers assists them in making better design decisions by understanding what they are actually evaluating and what is expected to occur.

7.2 Future Work

This project has highlighted the importance of understanding the actual behavior of a situation so that an appropriate evaluation can be applied. Engineers may be able to apply a simplified analysis or design calculation, but it is critical to define a reason why and the associated limitations. With respect to the use of non-symmetric cross sections, the following areas are a few future research topics that would further assist engineers in appropriately designing structures:

- While this research has shown that incorrect internal forces and displacements are calculated when not considering non-symmetric behavior, more parametric studies are needed to verify the importance to common design applications. The inherent variability between the real world and our design assumptions means engineers can rarely expect to perfectly capture the response. Therefore, before suggesting that any change is needed for normal situations, additional investigations considering member design capacities should be completed to determine how significant the observed variations are and if there are common conditions associated with significant variations.

- In Section 2.3.1, the current formulation of the novel line-element implemented in MASTAN2 was able to capture some of the desired interaction between torsion, bending, and axial responses. However, there was a distinct underestimation of the total interaction due to the current formulation only capturing part of the member shortening from torsion. Research should directly address the longitudinal strains developed due to helical displacements due to torsion. A related consideration would also be a distributed torsional moment, but this would likely require a fundamental change to the assumed torsion behavior to allow nonuniform torsion within a single element.

- Shear deflection could be added to the novel line-element. The primary challenge is developing an algorithm to determine the appropriate shear deflection factor that accounts for the shear distribution in any arbitrary cross section.

- Additional consideration needs to be given to the connection between line elements, especially when utilizing non-symmetric cross sections. Two primary areas of concern identified in this study were the definition of warping at connections and the behavior of bimoment when either the centroid or shear center are misaligned at a connection. Preliminary investigation by the author and other researchers have noted mechanics that cannot be captured by the current approach, which can be attributed to unintended bimoment due connected two different cross sections. This directly relates to the warping at connections, which becomes more complex with the variety of geometries that can intersect at a single location. These two concepts directly combine with the connection ideas noted in Chapter 4 and would allow engineers to better control what they are modeling.

- More investigation should be completed on the composite behavior of built-up sections considering the impact of torsional transfer between the elements. A closer inspection of this behavior could be used to refine an estimation of the torsional stiffness of a double angle which drastically increases the calculated buckling capacity of a short column.

- There is interest in industry to use higher strength steels in steel joists to reduce the amount of required material. However, this change could directly impact the recommendation to design double angles by only considering flexural buckling with local buckling reductions. Work needs to be completed to determine if existing local buckling reductions still appropriately address the cross section slenderness concerns related to global flexural-torsional buckling or if a limiting slenderness ratio can be determined.

- Non-compact stainless steel angles, both equal- and unequal-leg, need to be assessed to determine appropriate buckling provisions. Such sections are already available for use, so it would be beneficial to determine which buckling provisions apply and what local buckling reduction should be applied. The current provisions take an approach based on the elastic behavior, but an increased inelastic limit may be appropriate.

- Stainless steel design provisions have been created balancing complexity of the provisions, non-linear behavior, and the increased material cost compared to carbon steel. One possible area for significant increase would be a better classification of the material grades. Since the current ASTM defines a single set of material properties for a grade that applies across multiple manufacturing processes, observed strength is being excluded in design because hot-rolled and laser welded sections have regularly been observed to be significantly stronger compared to equivalent flat stock. Based on this study, some of the stiffness appears to be considered in defining the appropriate buckling curves; however, it is not consistently applied to the allowable strength or direct evaluation of stiffness.

BIBLIOGRAPHY

---

[1] AISC, *Specification for Structural Steel Buildings ANSI/AISC 360-16*. Chicago, IL: American Institute of Steel Construction, 2016, p. 676.

[2] R. D. Ziemian, J. C. Batista Abreu, M. D. Denavit, and T.-J. L. Denavit, "Three-Dimensional Benchmark Problems for Design by Advanced Analysis: Impact of Twist," *J. Struct. Eng.*, vol. 144, no. 12, p. 04 018 220, 2018. DOI: `10.1061/(asce)st.1943-541x.0002224`.

[3] L. H. Teh, "Beam element verification for 3D elastic steel frame analysis," *Computers & Structures*, vol. 82, no. 15-16, pp. 1167–1179, Jun. 2004. DOI: `10.1016/j.compstruc.2004.03.022`.

[4] Rinchen, G. J. Hancock, and K. J. Rasmussen, "Formulation and Implementation of General Thin-Walled Open-Section Beam-Column Elements in Opensees Research Report," The University of Sydney, Sydney, Australia, Tech. Rep., 2016.

[5] S.-W. Liu, R. D. Ziemian, L. Chen, and S.-L. Chan, "Bifurcation and large-deflection analyses of thin-walled beam-columns with non-symmetric open-sections," *Thin-Walled Struct.*, vol. 132, no. 135, pp. 287–301, 2018. DOI: `10.1016/j.tws.2018.07.044`.

[6] S.-W. Liu, W. L. Gao, and R. D. Ziemian, "Improved line-element formulations for the stability analysis of arbitrarily-shaped open-section beam-columns," *Thin-Walled Struct.*, vol. 144, no. July, p. 106 290, 2019. DOI: `10.1016/j.tws.2019.106290`.

[7] R. D. Ziemian, W. McGuire, and S.-W. Liu, *MASTAN2 v5.0.2*. 2019.

[8] T. V. Galambos, "Design of axially loaded compressed angles," in *Proceedings of the 1991 SSRC Annual Stability Conference: "Inelastic Behavior and Design of Frames"*, Chicago, IL: SSRC, 1991, pp. 353–367.

[9] SJI, *Standard Specifications: Load Tables and Weight Tables for Steel Joists and Joist Girders SJI 100-2020*, 45th. Florence, SC: Steel Joist Institute, 2020, p. 232.

[10] Simpson Gumpertz & Heger, "Parameter Study to Assess Modifications to the SJI Design Equations for Buckling of HSLA-V Steels," Simpson Gumpertz & Heger, Inc., San Francisco, CA, Tech. Rep., 2011, p. 708.

[11] N. R. Baddoo, *Structural Stainless Steel* (Design Guide 27). Chicago, IL: American Institute of Steel Construction, 2013, p. 150.

[12] AISC, *Specification for Structural Stainless Steel Buildings ANSI/AISC 370-21*. Chicago, IL: American Institute of Steel Construction, 2021, p. 376.

[13] J. R. Yost, D. W. Dinehart, S. P. Gross, J. J. Pote, and B. Gargan, "Strength and Design of Open Web Steel Joists with Crimped-End Web Members," *Journal of Structural Engineering*, vol. 130, no. 5, pp. 715–724, 2004. DOI: `10.1061/(ASCE)0733-9445(2004)130`.

[14] J. R. Yost, D. W. Dinehart, S. P. Gross, J. J. Pote, and J. Deeney, "Buckling Strength of Single-Angle Compression Members in K-Series Joists," *AISC Engineering Journal*, no. 2, pp. 141–152, 2006.

[15] M. E. Laracuente, "Behavior of Concentrically Loaded Austenitic Stainless Steel Single Unequal-Leg Angles," M.S. thesis, University of Wisconsin - Madison, 2022.

[16] EN 1993-1-1, *Eurocode 3: Design of steel structures - Part 1-1: General rules and rules for buildings*. European Committee for Standardisation, 2005.

[17] Standards Australia, *Australian Standard - Steel Structures, AS4100-1998*. 1998.

[18] CSI America, *SAP2000 v. 20.1.0*. Berkeley, CA: Computers & Structures, Inc., 2018.

[19] Dlubal, *RFEM v. 5.19*. Dlubal Software GmbH, 2012.

[20] Dassault Systems, *Abaqus/CAE v.6.16*. Johnston, RI: Dassault Systems, 2015.

[21] Dassault Systems, *Abaqus 2016 Documentation*, 2015. [Online]. Available: `http://130.149.89.49:2080/v2016/index.html`.

[22] J. E. Akin, *Finite element analysis concepts: Via solidworks*. 2010, pp. 1–335, ISBN: 9789814313025. DOI: `10.1142/7785`.

[23] E. J. Sippel, R. D. Ziemian, and H. B. Blum, "Analysis of non-symmetric cross-sections relative to the provisions of AISC 360-10," in *Struct. Stab. Res. Counc. 2020 Annu. Stab. Conf.*, SSRC, Ed., Atlanta, GA, 2020, pp. 1–28.

[24] R. C. Kaehler, D. W. White, and Y. D. Kim, *Frame Design Using Web-Tapered Members*. Chicago, IL: American Institute of Steel Construction, 2011, p. 204.

[25] M. M. Attard, "Nonlinear Shortening and Bending Effect Under Pure Torque of Thin-Walled Open Beams," *Thin-Walled Struct.*, vol. 4, no. 3, pp. 165–177, 1986. DOI: `10.1016/0263-8231(86)90001-7`.

[26] M. Gregory, "A Non-linear Bending Effect When Certain Unsymmetrical Sections are Subjected to a Pure Torque," *Austrailian J. Appl. Sci.*, vol. 2, pp. 33–48, 1960.

[27] M. M. Attard, "The Elastic Flexural-Torsional Response of Thin-Walled Open Beams," Doctor of Philosophy, The University of New South Wales, 1984, p. 389.

[28] Z. Li and B. W. Schafer, “Buckling analysis of cold-formed steel members with general boundary conditions using CUFSM: Conventional and constrained finite strip methods,” in *20th Int. Spec. Conf. Cold-Formed Steel Struct. - Recent Res. Dev. Cold-Formed Steel Des. Constr.*, 2010.

[29] S. S. Cheng, B. Kim, and L. Y. Li, “Lateral-torsional buckling of cold-formed channel sections subject to combined compression and bending,” *J. Constr. Steel Res.*, vol. 80, pp. 174–180, 2013. DOI: `10.1016/j.jcsr.2012.07.026`.

[30] W. McGuire and R. D. Ziemian, “Steel Frame Stability: Out-of-Plane Effects,” in *First Int. Conf. Struct. Stab. Dyn.*, Taipei, Taiwan, 2000, pp. 5–20.

[31] D. B. Moore, “A Non-linear Theory for the Behaviour of Thin-walled Sections Subject to Combined Bending and Torsion,” *Thin-Walled Struct.*, vol. 4, no. 6, pp. 449–466, 1986. DOI: `10.1016/0263-8231(86)90040-6`.

[32] AISI S100-16, *North American Specification for the Design of Cold-Formed Steel Structural Members*. Washington, DC, U.S.A.: AISI, 2016.

[33] M. H. El-Zanaty, D. W. Murray, and R. Bjorhovde, “Inelastic Behavior of Multistory Steel Frames,” Edmonton, Alberta, Canada, Tech. Rep., 1980.

[34] B. T. Rosson, “Major and Minor Axis Stiffness Reduction of Steel Beam-Columns Under Axial Compression and Tension Conditions,” in *Proc. Annu. Stab. Conf.*, San Antonio, TX: SSRC, 2017, pp. 1–17.

[35] R. D. Ziemian and W. McGuire, “Modified Tangent Modulus Approach, A Contribution to Plastic Hinge Analysis,” *J. Struct. Eng.*, vol. 128, no. 10, pp. 1301–1307, 2002. DOI: `10.1061/(asce)0733-9445(2002)128:10(1301)`.

[36] B. Dowswell, *Curved Member Design*. Chicago, IL: American Institute of Steel Construction, 2018, p. 156.

[37] C. Bernuzzi, G. Gabbianelli, A. Gobetti, and A. Rosti, “Beam design for steel storage racks,” *J. Constr. Steel Res.*, vol. 116, pp. 156–172, 2016. DOI: `10.1016/j.jcsr.2015.09.007`.

[38] N.-I. Kim and M.-Y. Kim, “Exact dynamic/static stiffness matrices of non-symmetric thin-walled beams considering coupled shear deformation effects,” *Thin-Walled Structures*, vol. 43, no. 5, pp. 701–734, 2005. DOI: `https://doi.org/10.1016/j.tws.2005.01.004`.

[39] C. Bernuzzi, A. Pieri, and V. Squadrito, “Warping influence on the static design of unbraced steel storage pallet racks,” *Thin-Walled Struct.*, vol. 79, pp. 71–82, 2014. DOI: `10.1016/j.tws.2014.01.024`.

[40] S.-W. Liu, R. D. Ziemian, L. Chen, and S.-L. Chan, “Bifurcation and large-deflection analyses of thin-walled beam-columns with non-symmetric open-sections,” *Thin-Walled Struct.*, vol. 132, no. 135, pp. 287–301, 2018. DOI: `10.1016/j.tws.2018.07.044`.

[41] N. S. Trahair, *Flexural-Torsional Buckling of Structures*, 1st. London; New York: Spon, 1993, p. 360, ISBN: 9780419181101. DOI: `10.1201/9781482271218`.

[42] S. Shayan and K. J. Rasmussen, “A model for warping transmission through joints of steel frames,” *Thin-Walled Struct.*, vol. 82, pp. 1–12, 2014. DOI: `10.1016/j.tws.2014.03.017`.

[43] E. J. Sapountzakis and I. C. Dikaros, “Advanced 3-D beam element including warping and distortional effects for the analysis of spatial framed structures,” *Eng. Struct.*, vol. 188, no. May 2018, pp. 147–164, 2019. DOI: `10.1016/j.engstruct.2019.03.006`.

[44] A. B. Hansen and J. Jönsson, “Modelling of steel frames using advanced beam and joint elements with interfaces governed by beam modes,” *Thin-Walled Struct.*, vol. 145, no. August, 2019. DOI: `10.1016/j.tws.2019.106430`.

[45] G. J. Hancock, “Portal Frames Composed of Cold-Formed Channel- and Z-Sections,” in *Steel Fram. Structrues - Stab. Strength*, R. Narayanan, Ed., 1st ed., CRC Press, 1990, ch. 8, pp. 241–276.

[46] Rinchen, K. J. Rasmussen, and H. Zhang, “Design of cold-formed steel single C-section portal frames,” *J. Constr. Steel Res.*, vol. 162, p. 105 722, 2019. DOI: `10.1016/j.jcsr.2019.105722`.

[47] E. J. Sippel, R. D. Ziemian, and H. B. Blum, “Structural analysis of non-symmetric cross sections with line elements,” *Submitted*, 2021.

[48] A. H. Baigent and G. J. Hancock, “Structural analysis of assemblages of thin-walled members,” *Eng. Struct.*, vol. 4, no. 3, pp. 207–216, 1982. DOI: `10.1016/0141-0296(82)90010-4`.

[49] A. H. Baigent, “Thin-Walled Structural Systems,” Ph.D. dissertation, The University of Sydney, 1980, pp. 291–610.

[50] A. H. Baigent and G. J. Hancock, “The Stiffness and Strength of Portal Frames Composed of Cold-Formed Members,” *Civ. Eng. Trans.*, vol. 24, no. 3, pp. 278–283, 1982.

[51] T. Sputo, J. Haynes, and D. S. Ellifritt, "Flexural Capacity of Discretely Braced C's and Z's," *11th Int. Spec. Conf. Cold-Formed Steel Struct.*, vol. 2, pp. 109–129, 1992. [Online]. Available: `https://scholarsmine.mst.edu/isccss/11iccfss/11iccfss-session3/2`.

[52] H. I. Epstein, E. Murtha-Smith, and J. D. Mitchell, "Analysis and design assumptions for continuous cold-formed purlins," *Pract. Period. Struct. Des. Constr.*, vol. 3, no. 2, pp. 60–67, 1998. DOI: `10.1061/(ASCE)1084-0680(1998)3:2(60)`.

[53] S. Wang, R. S. Glauz, and B. W. Schafer, "Inelastic Lateral-Torsional Buckling Strength Validation for Non-Principal Axis Bending Using Numerical Methods," Tech. Rep., 2020, p. 62.

[54] J. M. Fisher and P. S. Green, *Steel Joist Institute Technical Digest 12: Evaluation and Modification of Open-Web Steel Joists and Joist Girders*. Myrtle Beach, SC, 2007, p. 110.

[55] E. J. Sippel, R. D. Ziemian, and H. B. Blum, "Structural analysis using line elements to model members with non-symmetric cross sections," *Thin-Walled Structures*, vol. 169, p. 108 407, 2021. DOI: `https://doi.org/10.1016/j.tws.2021.108407`.

[56] G. M. K. Rojahn and R. D. Ziemian, "Finite element modeling of open-web steel joists comprised of nonsymmetric shapes," in *Proc. 2021 SSRC Annu. Stab. Conf.*, Louisville, KY: SSRC, 2021, pp. 1–12.

[57] Committee on Specifications for the Design of Cold-Formed Steel Structural Members, *Tutorials for MASTAN2 and Related Validation*. American Iron and Steel Institute, 2021. [Online]. Available: `https://scholarsmine.mst.edu/ccfss-aisi-spec/227`.

[58] Y. Xia and H. B. Blum, "Geometric imperfection measurements of cold-formed steel members using a portable non-contact 3D laser scanner," in *Proc. 2020 SSRC Annu. Stab. Conf.*, Atlanta, GA: SSRC, 2020, pp. 1–15.

[59] Artec 3D, *Artec Studio 15*. L-2328, Luxembourg: Artec 3D, 2020.

[60] MATLAB, *MATLAB (R2019a)*. Natick, MA: The MathWorks Inc., 2019.

[61] K. J. Rasmussen, "Design of angle columns with locally unstable legs," *Journal of Structural Engineering*, vol. 131, no. 10, pp. 1553–1560, 2005. DOI: `10.1061/(ASCE)0733-9445(2005)131:10(1553)`.

[62] B. Behzadi-Sofiani, L. Gardner, M. A. Wadee, P. B. Dinis, and D. Camotim, "Behaviour and design of fixed-ended steel equal-leg angle section columns," *Journal of Constructional Steel Research*, vol. 182, 2021. DOI: `10.1016/j.jcsr.2021.106649`.

[63] TIA-222-G, *Structural standard for antenna supporting structures and antennas*. Washington DC, USA: Telecommunications Industry Association, 2005.

[64] J. B. Kennedy and M. K. S. Murty, "Buckling of Steel Angle and Tee Struts," *Journal of the Structural Division*, vol. 98, no. 11, pp. 2507–2522, 1972.

[65] S. Kitipornchai and H. W. Lee, "Inelastic buckling of single-angle, tee and double-angle struts," *Journal of Constructional Steel Research*, vol. 6, no. 1, pp. 3–20, 1986.

[66] S. Kitipornchai and H. W. Lee, "Inelastic experiments on angle and tee struts," *Journal of Constructional Steel Research*, vol. 6, no. 3, pp. 219–236, 1986. DOI: `10.1016/0143-974X(86)90035-0`.

[67] A. Astaneh-asl, S. C. Goel, and R. D. Hanson, "Cyclic out-of-plane buckling of double-angle bracing," *Journal of Structural Engineering*, vol. 111, no. 5, pp. 1135–1153, 1985.

[68] M. C. Temple and J. C. Tan, "Interconnection of widely spaced angles," *Canadian Journal of Civil Engineering*, vol. 15, no. 4, pp. 732–741, 1988.

[69] D. R. Sherman and J. A. Yura, "Bolted double angle compression members," *Journal of Constructional Steel Research*, vol. 46, no. 1-3, pp. 470–471, 1998. DOI: `10.1016/S0143-974X(98)80092-8`.

[70] W. F. Maia, L. C. Vieira, B. W. Schafer, and M. Malite, "Experimental and numerical investigation of cold-formed steel double angle members under compression," *Journal of Constructional Steel Research*, vol. 121, pp. 398–412, 2016. DOI: `10.1016/j.jcsr.2016.03.003`.

[71] G. B. G. Ananthi, M. S. Deepak, K. Roy, and J. B. Lim, "Influence of intermediate stiffeners on the axial capacity of cold-formed steel back-to-back built-up unequal angle sections," *Structures*, vol. 32, pp. 827–848, 2021. DOI: `10.1016/j.istruc.2021.03.059`.

[72] M. Anbarasu and M. A. Dar, "Improved design procedure for battened cold-formed steel built-up columns composed of lipped angles," *Journal of Constructional Steel Research*, vol. 164, p. 105 781, 2020. DOI: `10.1016/j.jcsr.2019.105781`.

[73] A. M. Mahar, S. A. Jayachandran, and M. Mahendran, "Global buckling strength of discretely fastened back-to-back built-up cold-formed steel columns," *Journal of Constructional Steel Research*, vol. 187, p. 106 998, 2021. DOI: `10.1016/j.jcsr.2021.106998`.

[74] T. Zhou, Y. Li, L. Ren, L. Sang, and L. Zhang, "Research on the elastic buckling of composite webs in cold-formed steel back-to-back built-up columns – Part I: Experimental and numerical investigation," *Structures*, vol. 30, pp. 115–133, 2021. DOI: `10.1016/j.istruc.2020.12.059`.

[75] Y. Li, T. Zhou, L. Ren, L. Sang, and L. Zhang, "Elastic buckling of composite webs in back-to-back cold-formed steel built-up columns-Part II: Design formula," *Structures*, vol. 33, pp. 3515–3525, 2021. DOI: `10.1016/j.istruc.2021.05.100`.

[76] D. K. Phan, K. J. Rasmussen, and B. W. Schafer, "Tests and design of built-up section columns," *Journal of Constructional Steel Research*, vol. 181, p. 106 619, 2021. DOI: `10.1016/j.jcsr.2021.106619`.

[77] D. K. Phan, K. J. Rasmussen, and B. W. Schafer, "Numerical investigation of the strength and design of cold-formed steel built-up columns," *Journal of Constructional Steel Research*, vol. 193, p. 107 276, 2022. DOI: `10.1016/j.jcsr.2022.107276`.

[78] D. C. Fratamico, S. Torabian, X. Zhao, K. J. Rasmussen, and B. W. Schafer, "Experimental study on the composite action in sheathed and bare built-up cold-formed steel columns," *Thin-Walled Structures*, vol. 127, pp. 290–305, 2018. DOI: `10.1016/j.tws.2018.02.002`.

[79] S. Selvaraj and M. Madhavan, "Design of cold-formed steel built-up columns subjected to local-global interactive buckling using direct strength method," *Thin-Walled Structures*, vol. 159, p. 107 305, 2021. DOI: `10.1016/j.tws.2020.107305`.

[80] Q. Y. Li and B. Young, "Experimental and numerical investigation on cold-formed steel built-up section pin-ended columns," *Thin-Walled Structures*, vol. 170, p. 108 444, 2022. DOI: `10.1016/j.tws.2021.108444`.

[81] K. J. Rasmussen, M. Khezri, B. W. Schafer, and H. Zhang, "The mechanics of built-up cold-formed steel members," *Thin-Walled Structures*, vol. 154, p. 106 756, 2020. DOI: `10.1016/j.tws.2020.106756`.

[82] A. M. Alenezi and M. Mohareb, "Elastic compressive buckling resistance for back-to-back double angle assemblies," *Engineering Structures*, vol. 258, p. 114 120, 2022. DOI: `10.1016/j.engstruct.2022.114120`.

[83] B. G. Neal, "The lateral instability of yielded mild steel beams of rectangular cross-section," *Philosophical Transactions of the Royal Society of London. Series A, Mathematical and Physical Sciences*, vol. 242, no. 846, pp. 197–242, 1950. DOI: `10.1098/rsta.1950.0001`.

[84] E. J. Sippel, R. D. Ziemian, and H. B. Blum, “Buckling behavior of open-web steel joists and joist girders,” in *Proceedings of the 2022 SSRC Annual Stability Conference*, Denver, CO: SSRC, 2022, pp. 1–21.

[85] CISC, *Torsional Section Properties of Steel Shapes*. Canadian Institute of Steel Construction, 2002, p. 19.

[86] EN 1993-1-5, *Eurocode 3: Design of Steel Structures - Part 1-5: Plated Structural Elements*. European Committee for Standardisation, 2009.

[87] C. Houska, *Designing Stainless Steel Part 1*, Conference Presentation, NASSC: The Steel Conference, Toronto, Canada, 2014.

[88] M. Dundu, “Evolution of stress–strain models of stainless steel in structural engineering applications,” *Construction and Building Materials*, vol. 165, pp. 413–423, 2018. DOI: `10.1016/j.conbuildmat.2018.01.008`.

[89] H. Hill, “Determination of stress-strain relations from te offset yield strength values,” National Advisory Committee for Aeronautics, Washington DC, Tech. Rep. Technical Note No. 927, 1944.

[90] W. Ramberg and W. R. Osgood, “Description of stress-strain curves by three parameters,” National Advisory Committee for Aeronautics, Washington DC, Tech. Rep. Technical Note No. 902, 1943.

[91] M. Ashraf, L. Gardner, and D. A. Nethercot, “Compression strength of stainless steel cross-sections,” *Journal of Constructional Steel Research*, vol. 62, no. 1-2, pp. 105–115, 2006. DOI: `10.1016/j.jcsr.2005.04.010`.

[92] J. MacDonald M.; Rhodes and G. T. Taylor, “Mechanical Properties of Stainless Steel Lipped Channels,” in *CCFSS Proceedings of International Specialty Conference on Cold-Formed Steel Structures (1971 - 2018)*, vol. 4, St. Louis, MO., 2000. [Online]. Available: `https://scholarsmine.mst.edu/isccss/15iccfss/15iccfss-session11/4`.

[93] A. Olsson, “Stainless steel plasticity : Material modelling and structural applications,” Ph.D. dissertation, Luleå University of Technology, 2001, p. 298.

[94] E Mirambell and E Real, “On the calculation of deflections in structural stainless steel beams: An experimental and numerical investigation,” *Journal of Constructional Steel Research*, vol. 54, no. 1, pp. 109–133, 2000.

[95] K. J. Rasmussen, “Full-range stress–strain curves for stainless steel alloys,” *Journal of constructional steel research*, vol. 59, no. 1, pp. 47–61, 2003.

[96] L Gardner and D. Nethercot, “Experiments on stainless steel hollow sections—part 1: Material and cross-sectional behaviour,” *Journal of Constructional Steel Research*, vol. 60, no. 9, pp. 1291–1318, 2004.

[97] L. Gardner and M. Ashraf, “Structural design for non-linear metallic materials,” *Engineering structures*, vol. 28, no. 6, pp. 926–934, 2006.

[98] W. Quach, J. G. Teng, and K. F. Chung, “Three-stage full-range stress-strain model for stainless steels,” *Journal of Structural Engineering*, vol. 134, no. 9, pp. 1518–1527, 2008.

[99] P. Hradil, A. Talja, E. Real, E. Mirambell, and B. Rossi, “Generalized multistage mechanical model for nonlinear metallic materials,” *Thin-walled structures*, vol. 63, pp. 63–69, 2013.

[100] I. Arrayago, E. Real, and L. Gardner, “Description of stress–strain curves for stainless steel alloys,” *Materials & Design*, vol. 87, pp. 540–552, 2015. DOI: `https://doi.org/10.1016/j.matdes.2015.08.001`.

[101] H. Kuwamura, “Local buckling of thin walled stainless steel members,” *Steel Structures*, vol. 3, pp. 191–201, 2003.

[102] Y. Sun, Z. Liu, Y. Liang, and O. Zhao, “Experimental and numerical investigations of hot-rolled austenitic stainless steel equal-leg angle sections,” *Thin-Walled Structures*, vol. 144, p. 106 225, 2019. DOI: `10.1016/j.tws.2019.106225`.

[103] N. A. Reynolds, “Behavior and Design of Concentrically Loaded Duplex Stainless Steel Single Equal-Leg Angle Struts,” PhD Dissertation, Georgia Institute of Technology, 2013, p. 253.

[104] Y. Liang, V. V. K. Jeyapragasam, L. Zhang, and O. Zhao, “Flexural-torsional buckling behaviour of fixed-ended hot-rolled austenitic stainless steel equal-leg angle section columns,” *Journal of Constructional Steel Research*, vol. 154, pp. 43–54, 2019. DOI: `10.1016/j.jcsr.2018.11.019`.

[105] A. d. S. Sirqueira, P. C. S. Vellasco, L. R. O. de Lima, and F. R. Sarquis, “Experimental assessment of stainless steel hot-rolled equal legs angles in compression,” *Journal of Constructional Steel Research*, vol. 169, p. 106 069, 2020. DOI: `10.1016/j.jcsr.2020.106069`.

[106] F. R. Sarquis, L. R. O. de Lima, P. C. G. da S. Vellasco, and M. C. Rodrigues, “Experimental and numerical investigation of hot-rolled stainless steel equal leg angles under compression,” *Thin-Walled Structures*, vol. 151, p. 106 742, 2020. DOI: `10.1016/j.tws.2020.106742`.

[107] A. Filipović, J. Dobrić, N. R. Baddoo, and P. Može, “Experimental response of hot-rolled stainless steel angle columns,” *Thin-Walled Structures*, vol. 163, p. 107 659, 2021. DOI: `10.1016/j.tws.2021.107659`.

[108] A. Filipović, J. Dobrić, D. Buđevac, N. Fric, and N. R. Baddoo, “Experimental study of laser-welded stainless steel angle columns,” *Thin-Walled Structures*, vol. 164, 2021. DOI: `10.1016/j.tws.2021.107777`.

[109] J. Dobrić, A. Filipović, Z. Marković, and N. R. Baddoo, “Structural response to axial testing of cold-formed stainless steel angle columns,” *Thin-Walled Structures*, vol. 156, p. 106 986, 2020. DOI: `10.1016/j.tws.2020.106986`.

[110] L. Zhang, Y. Liang, and O. Zhao, “Experimental and numerical investigations of pin-ended hot-rolled stainless steel angle section columns failing by flexural buckling,” *Thin-Walled Structures*, vol. 156, p. 106 977, 2020. DOI: `10.1016/j.tws.2020.106977`.

[111] L. Zhang, Y. Liang, and O. Zhao, “Laboratory testing and numerical modelling of pin-ended hot-rolled stainless steel angle section columns failing by flexural-torsional buckling,” *Thin-Walled Structures*, vol. 161, p. 107 395, 2021. DOI: `10.1016/j.tws.2020.107395`.

[112] B. Behzadi-Sofiani, L. Gardner, and M. A. Wadee, “Stability and design of fixed-ended stainless steel equal-leg angle section compression members,” *Engineering Structures*, vol. 249, p. 113 281, 2021. DOI: `10.1016/j.engstruct.2021.113281`.

[113] Y. Liu and S. Chantel, “Experimental study of steel single unequal-leg angles under eccentric compression,” *Journal of Constructional Steel Research*, vol. 67, no. 6, pp. 919–928, 2011. DOI: `10.1016/j.jcsr.2011.02.005`.

[114] P. B. Dinis, D. Camotim, K. Belivanis, C. Roskos, and T. A. Helwig, “On the buckling, post-buckling and strength behavior of thin-walled unequal-leg angle columns,” in *Proceedings of the 2015 SSRC Annual Stability Conference*, Nashville, TN: SSRC, 2015, pp. 1–15.

[115] M. Ojalvo, “Opposing Theories and the Buckling Strength of Unequal-Leg Angle Columns,” *Journal of Structural Engineering*, vol. 137, no. 10, pp. 1104–1106, 2011. DOI: `10.1061/(ASCE)ST.1943-541X.0000389`.

[116] K. Liao, “Compression tests of unequal-leg angles,” M.S. thesis, Ohio State University, 1982.

[117] F.-h. Wu, “Experimental determination of buckling loads for unequal leg angles with concentric loads,” M.S. thesis, Ohio State University, 1982.

[118] Y. Zhang, Y. Wang, Z. Wang, Y. Bu, S. Fan, and B. Zheng, "Experimental investigation and numerical analysis of pin-ended extruded aluminium alloy unequal angle columns," *Engineering Structures*, vol. 215, p. 110 694, 2020. DOI: `10.1016/j.engstruct.2020.110694`.

[119] Y. Zhang, Y. Bu, Y. Wang, Z. Wang, and Y. Ouyang, "Study of flexural–torsional buckling behaviour of 6061-T6 aluminium alloy unequal-leg angle columns," *Thin-Walled Structures*, vol. 164, p. 107 821, 2021. DOI: `10.1016/j.tws.2021.107821`.

[120] S. Timoshenko and J. Gere, *Theory of Elastic Stability*, 2nd ed. McGraw-Hill Book Company Inc., 1961, p. 177.

[121] F. R. Shanley, "Inelastic column theory," *Journal of the aeronautical sciences*, vol. 14, no. 5, pp. 261–268, 1947.

[122] F. J. Meza, N. Baddoo, and L. Gardner, "Development of Flexural Buckling Rules for the New AISC Stainless Steel Design Specification," *ce/papers*, vol. 4, pp. 1537–1542, 2021. DOI: `https://doi.org/10.1002/cepa.1453`.

[123] R. D. Ziemian, *Guide to stability design criteria for metal structures*, 6th. John Wiley & Sons, 2010.

[124] Z. Zhang, G. Shi, L. Hou, and L. Zhou, "Geometric dimension and imperfection measurements of box-T section columns using 3D scanning," *Journal of Constructional Steel Research*, vol. 183, p. 106 742, 2021. DOI: `10.1016/j.jcsr.2021.106742`.

[125] L. Zhang, K. H. Tan, and O. Zhao, "Experimental and numerical studies of fixed-ended cold-formed stainless steel equal-leg angle section columns," *Engineering Structures*, vol. 184, no. September 2018, pp. 134–144, 2019. DOI: `10.1016/j.engstruct.2019.01.083`.

[126] A. A. de Menezes, P. C. G. da S. Vellasco, L. R. O. de Lima, and A. T. da Silva, "Experimental and numerical investigation of austenitic stainless steel hot-rolled angles under compression," *Journal of Constructional Steel Research*, vol. 152, pp. 42–56, 2019. DOI: `10.1016/j.jcsr.2018.05.033`.

[127] K. J. Rasmussen, T. Burns, P. Bezkorovainy, and M. R. Bambach, "Numerical modelling of stainless steel plates in compression," *Journal of Constructional Steel Research*, vol. 59, no. 11, pp. 1345–1362, 2003. DOI: `10.1016/S0143-974X(03)00086-5`.

[128] B. W. Schafer, Z. Li, and C. D. Moen, "Computational modeling of cold-formed steel," *Thin-Walled Structures*, vol. 48, no. 10-11, pp. 752–762, 2010. DOI: `10.1016/j.tws.2010.04.008`.

[129] S. H. Al-Sayed and R. Bjorhovde, “Inelastic behavior of single angle columns,” *Journal of Constructional Steel Research*, vol. 12, no. 2, pp. 103–118, 1989. DOI: `10.1016/0143-974X(89)90027-8`.

[130] M. Abambres and W.-M. Quach, “Residual stresses in steel members: A review of available analytical expressions,” *International Journal of Structural Integrity*, vol. 7, no. 1, pp. 70–94, 2016. DOI: `10.1108/IJSI-12-2014-0070`.

[131] K. J. Rasmussen and G. J. Hancock, “Design of Cold-Formed Stainless Steel Tubular Members. I: Columns,” vol. 119, no. 8, pp. 2349–2367, 1993.

[132] J. Dobrić, A. Filipović, N. Baddoo, D. Buđevac, and B. Rossi, “Design criteria for pin-ended hot-rolled and laser-welded stainless steel equal-leg angle columns,” *Thin-Walled Structures*, vol. 167, 2021. DOI: `10.1016/j.tws.2021.108175`.

[133] AISC, *Steel Construction Manual*, 15th. Chicago, IL: American Institute of Steel Construction, 2017.

[134] CFF Stainless Steels Inc., *Stainless Steel Angle Equal/Unequal Leg*, Available at `https://cffstainless.com/products/`, Accessed: 2021-01-22.

[135] Atlantic Stainless, *Unequal Leg Angles*, Available at `https://www.atlanticstainless.com/products/angle/unequal-leg-angles/`, Accessed: 2021-01-22.

[136] Stainless Structurals, *Unequal Leg Angles*, Available at `https://www.stainless-structurals.com/product-category/stainless-steel-angles/stainless-steel-angles-unequal-leg-angles/`, Accessed: 2021-01-22.

[137] Penn Stainless Products, *Unequal Leg Angle*, Available at `https://www.pennstainless.com/products/unequal-leg-angle/`, Accessed: 2021-01-22.

[138] Ryerson, *Stainless Steel Angle*, Available at `https://www.ryerson.com/stocklist/detail/e8a08d07-fe98-48c3-bc04-e4cdff2df3cf`, Accessed: 2021-01-22.

[139] Metal Supermarkets, *Stainless Steel Angle 304*, Available at `https://www.metalsupermarkets.com/product/stainless-steel-angle-304/`, Accessed: 2021-01-22.

[140] Montanstahl AG, *Stainless Steel Unequal Leg Angles American Sizes*, Available at `https://www.montanstahl.com/products/stainless-steel-structurals-bright-bars/stainless-steel-angles/unequal-leg-angles-american-sizes/`, Accessed: 2021-01-22.

[141] M. Haque, “Visualization Techniques For Structural Design Education,” in *2003 Annual Conference*, https://peer.asee.org/12260, Nashville, Tennessee: ASEE Conferences, 2003.

[142] H. Demirkaya and Y. Atayeter, "A study on the experiences of university lecturers and students in the geography field trip," *Procedia - Social and Behavioral Sciences*, vol. 19, pp. 453–461, 2011. DOI: `10.1016/j.sbspro.2011.05.154`.

[143] J. Barroso-Osuna, J. J. Gutiérrez-Castillo, M. C. Llorente-Cejudo, and R. V. Ortiz, "Difficulties in the incorporation of augmented reality in university education: Visions from the experts," *Journal of New Approaches in Educational Research*, vol. 8, no. 2, pp. 126–141, 2019. DOI: `10.7821/naer.2019.7.409`.

[144] A. McCabe and D. McPolin, "Virtual reality: Immersed in the structural world," *Structural Engineer*, vol. 93, no. 3, pp. 20–23, 2015.

[145] J. H. Falk and L. D. Dierking, "School Field Trips: Assessing Their Long-Term Impact," *Curator: The Museum Journal*, vol. 40, no. 3, pp. 211–218, 1997. DOI: `10.1111/j.2151-6952.1997.tb01304.x`. [Online]. Available: `http://doi.wiley.com/10.1111/j.2151-6952.1997.tb01304.x`.

[146] N. V. Hanh and N. H. Hop, "The effectiveness of the industrial field trip in introduction to engineering: A case study at Hung Yen University of Technology and Education, Vietnam," *International Journal of Electrical Engineering Education*, vol. 55, no. 3, pp. 273–289, 2018. DOI: `10.1177/0020720918773050`. [Online]. Available: `http://journals.sagepub.com/doi/10.1177/0020720918773050`.

[147] A. Fauzi and Z. I. Rizman, "Field trip education approach beyond classroom: Microwave course case," *Mediterranean Journal of Social Sciences*, vol. 6, no. 4S1, pp. 89–94, 2015. DOI: `10.5901/mjss.2015.v6n4s1p89`.

[148] M. Seifan, D. Dada, and A. Berenjian, "The effect of virtual field trip as an introductory tool for an engineering real field trip," *Education for Chemical Engineers*, vol. 27, pp. 6–11, 2019. DOI: `10.1016/j.ece.2018.11.005`.

[149] A. Barraclough and I. Guymer, "Virtual reality - A role in environmental engineering education?" *Water Science and Technology*, vol. 38, no. 11, pp. 303–310, 1998. DOI: `10.2166/wst.1998.0481`. [Online]. Available: `http://repositorio.unan.edu.ni/2986/1/5624.pdf`.

[150] L. Freina and M. Ott, "A literature review on immersive virtual reality in education: State of the art and perspectives," *Proceedings of eLearning and Software for Education (eLSE) (Bucharest, Romania, April 23–24, 2015)*, p. 8, 2015. DOI: `10.12753/2066-026X-15-020`. [Online]. Available: `http://proceedings.elseconference.eu/index.php?paper=b5bc8a20809b5689c689a7fec40255e6`.

[151] S. Kavanagh, A. Luxton-Reilly, B. Wuensche, and B. Plimmer, "A Systematic Review of Virtual Reality in Education.," *Themes in Science and Technology Education*, vol. 10, no. 2, pp. 85–119, 2017.

[152] J. A. di Lanzo, A. Valentine, F. Sohel, A. Y. Yapp, K. C. Muparadzi, and M. Abdelmalek, *A review of the uses of virtual reality in engineering education*, 2020. DOI: `10.1002/cae.22243`.

[153] E. Blümel and T. Haase, "Virtual Reality Platforms for Education and Training in Industry," in *East European Conference on Advances in Databases and Information Systems*, Berlin: Springer, 2009, pp. 1–7. DOI: `10.1007/978-3-642-12082-4_4`.

[154] S. K. Chaturvedi and K. A. Dharwadkar, "Simulation and Visualization Enhanced Engineering Education - Development and implementation of virtual experiments in a laboratory course," in *ASEE Annual Conference and Exposition, Conference Proceedings*, 2011.

[155] F. M. Dinis, A. S. Guimarães, B. R. Carvalho, and J. P. Pocas Martins, "Virtual and augmented reality game-based applications to civil engineering education," in *2017 IEEE Global Engineering Education Conference (EDUCON)*, IEEE, 2017, pp. 1683–1688. DOI: `10.1109/EDUCON.2017.7943075`. [Online]. Available: `https://ieeexplore.ieee.org/document/7943075/`.

[156] M. Noghabaei, A. Heydarian, V. Balali, and K. Han, "Trend Analysis on Adoption of Virtual and Augmented Reality in the Architecture, Engineering, and Construction Industry," *Data*, vol. 5, no. 1, p. 26, 2020. DOI: `10.3390/data5010026`. [Online]. Available: `https://www.mdpi.com/2306-5729/5/1/26`.

[157] J. M. Davila Delgado, L. Oyedele, T. Beach, and P. Demian, "Augmented and Virtual Reality in Construction: Drivers and Limitations for Industry Adoption," *Journal of Construction Engineering and Management*, vol. 146, no. 7, p. 04 020 079, 2020. DOI: `10.1061/(asce)co.1943-7862.0001844`.

[158] F. M. Bademosi, R. Tayeh, and R. R. Issa, "An Immersive Approach to Construction Cost Estimating," in *Computing in Civil Engineering 2019: Visualization, Information Modeling, and Simulation - Selected Papers from the ASCE International Conference on Computing in Civil Engineering 2019*, 2019, pp. 48–54. DOI: `10.1061/9780784482421.007`. [Online]. Available: `http://toc.proceedings.com/49478webtoc.pdf`.

[159] J. I. Messner, S. C. M. Yerrapathuruni, A. J. Baratta, and V. E. Whisker, "Using virtual reality to improve construction engineering education," in *American Society for Engineering Education Annual Conference and Exposition*, 2003, pp. 1–8.

[160] A. Z. Sampaio, P. G. Henriques, C. O. Cruz, and O. P. Martins, “Interactive Models Based on Virtual Reality Technology Used in Civil Engineering Education,” in *Teaching through Multi-User Virtual Environments*, 2011, pp. 18–25. DOI: `10.4018/9781616928223.ch021`.

[161] R. Sengupta and A. E. Sparkling, “Incorporating virtual reality in construction management education,” in *2021 ASEE Virtual Annual Conference Content Access*, https://peer.asee.org/37324, Virtual Conference: ASEE Conferences, 2021.

[162] G. N. de Almeida Mello and J. C. Almenara, “Aid-augmented reality for reinforced concrete class: students’ perception,” *Alteridad-Revista De Educacion*, vol. 15, no. 1, pp. 12–23, 2020. DOI: `10.17163/alt.v15n1.2020.01`.

[163] A. Hadigheh, J. Vulic, J. M. Burridge, T. Goldfinch, J. Thomas, and A. Opdyke, “Preliminary Evaluation of Immersive and Collaborative Virtual Labs in a Structural Engineering Unit of Study,” in *AAEE2019 Conference*, 2019.

[164] J. Fogarty, J. McCormick, and S. El-Tawil, “Improving Student Understanding of Complex Spatial Arrangements with Virtual Reality,” *Journal of Professional Issues in Engineering Education and Practice*, vol. 144, no. 2, pp. 1–10, 2018. DOI: `10.1061/(ASCE)EI.1943-5541.0000349`.

[165] G. Norman, “Likert scales, levels of measurement and the “laws” of statistics,” *Advances in Health Sciences Education*, vol. 15, pp. 625–632, 2010. DOI: `10.1007/s10459-010-9222-y`.

[166] J. F. de Winter and D. Dodou, “Five-Point Likert Items: t test versus Mann-Whitney-Wilcoxon (Addendum added October 2012),” *Practical Assessment, Research, and Evaluation*, vol. 15, no. 11, pp. 1–16, 2010. DOI: `https://doi.org/10.7275/bj1p-ts64`.

[167] InstaVR Inc, *InstaVR*. San Francisco, CA: InstaVR Inc: [Computer Software], 2019. [Online]. Available: `https://www.instavr.co/`.

[168] E. D. Ragan, K. J. Huber, B. Laha, and D. A. Bowman, “The effects of navigational control and environmental detail on learning in 3D virtual environments,” in *Proceedings - IEEE Virtual Reality*, IEEE, 2012, pp. 11–14. DOI: `10.1109/VR.2012.6180868`.

[169] Y. C. Chen, H. L. Chi, W. H. Hung, and S. C. Kang, “Use of tangible and augmented reality models in engineering graphics courses,” *Journal of Professional Issues in Engineering Education and Practice*, vol. 137, no. 4, pp. 267–276, 2011. DOI: `10.1061/(ASCE)EI.1943-5541.0000078`.

Appendices

A IMPERFECTION MEASUREMENTS

The general process used for evaluating the scan information is provided in this Appendix. After an initial description, results for the angles scanned for the work discussed in Chapter 6 are provided in Section A.3.

A.1 Imperfection Scanning

The geometric imperfections were measured through non-contact three-dimensional laser scanning utilizing the Artec Leo Scanner. The handheld scanner projects a structured light grid onto the specimen surface that allows for triangulation to define the three-dimensional coordinates across the surface. This information is recorded for each captured frame, which is then evaluated using the Artec Studio 15 proprietary machine learning-based high definition mode to reduce noise and better define edges and voids within the scanned region [59]. Afterwards, the individual frames are aligned to define the full surface area that can then be exported for use in other applications.

Obtaining quality scan data starts with the scanning procedure. The reconstruction considers both the texture and geometry of the underlying surface, so the setup significantly impacts the final result. Geometry is the primary factor for the initial alignment, while texture is incorporated in subsequent refinement. Additionally, unique texture is a key factor in validating the resulting alignment by allowing users to visually confirm the final configuration. Attempts to scan the angle standing vertically and against the concrete floor were ineffective as the analysis struggled to recombine the frame data appropriately. Fig. A.1 highlights the final configuration that was used to successfully determine imperfections. The background provided a larger surface area to align in each scan compared to the 2 inch and 3 inch dimensions of the angle legs. Additionally, the profile of the metal deck assisted in ensuring unique geometry and textures were captured in the various frames, especially compared to the relatively flat angle surface.

The Artec Leo scanner requires a line of sight with an acceptable angle from perpendicular to obtain information on a surface. The imperfections of the angle could have been determined using just the exterior face of the angle, Fig. A.1(b); however, this work also wanted to determine if it was possible to capture a complete surface of the angle. As a result, two additional orientations were captured to obtain the full geometry: the full interior surface, Fig. A.1(c), and the entire angle, Fig. A.1(d). The scan of the entire angle was then used as a base shell that was improved with the separate scans focused on the interior and exterior faces.

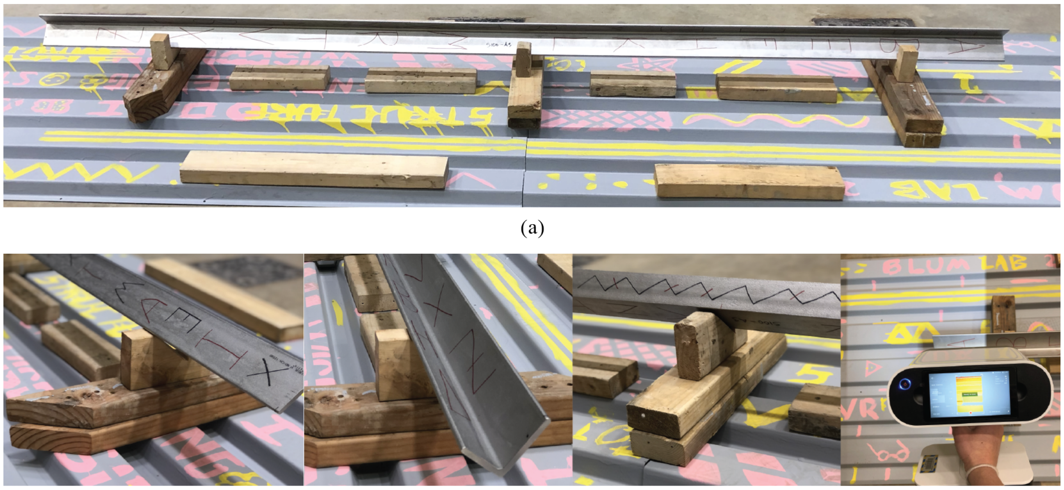
(a)

(b) (c) (d) (e)

Figure A.1: Imperfection scanning process. (a) Overview of angle to be scanned on background (b) Angle positioned to scan complete exterior face (c) Angle positioned to scan complete interior face (d) Angle positioned to scan majority of both faces at same time (e) Leo scanner capturing data of background and angle.

Each scan was processed separately to create a baseline geometry. During the alignment procedures, frames with larger errors (>0.2) or that were visually misaligned were either deleted or manually realigned. Once finalized, the background and ancillary blocking was removed from the scans of the interior and exterior surfaces. Then, the alignment of the full angle scan was locked before merging with the additional surfaces data. The same alignment procedure was then cared out for the full system. Once completed, the remaining background information was removed before purging the outliers. Finally, an sharp fusion model of the structure could be defined and exported for evaluation as a point cloud.

A.2 Data Evaluation

The first step was to align the point cloud to the desired coordinate systems shown in Fig. A.2. A preliminary alignment was obtained by selecting three nodes on three different faces: the base of the angle, the outside face of the 2-inch leg, and the outside face of the 3-inch leg. A plane was fit to each node group that was then used to create a preliminary selection by including all nodes within one-half the nominal thickness of the leg from the plane. An updated best-fit plane was calculated for the node group as well as the distance for each node to the plane. Any outlier nodes were removed from the group, and the process repeated until no outlier nodes remained. The normal direction of the final best-fit planes were then used as the tentative x-, y-, and z- axes. The vectors perpendicular to the

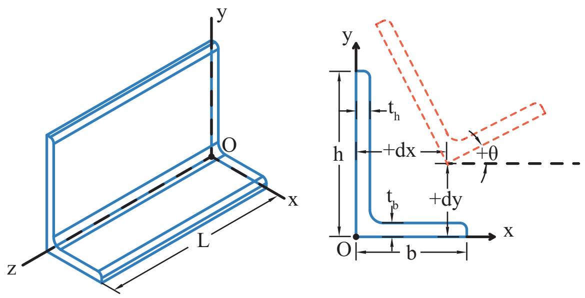

Figure A.2: Unequal-leg angle conventions for dimensions, axes, and displacements

legs were used to update the z-direction, which in turn was combined with the x-axis to finalize the y-direction. Lastly, the origin of the scan was defined as the intersection of the best-fit planes.

This initial alignment worked well for members with small imperfections; however, longer angles with localized end imperfections could cause the z-axis to be misaligned by significant distances. To reduce this misalignment, a preliminary evaluation of the heel location as discussed in the following paragraphs was completed at the extreme ends of the angle only. The vector connecting these two heels was defined as an improved z-axis, which was used to rotate the angle to the final orientation.

The imperfections along the length of the angle were obtained by dividing the angle at equal intervals along the z-axis. As each cut, nodes within a specified tolerance, 0.5 mm for most applications, were used to define the geometry of the cross section. Due to the density of the point cloud data, a significant number of nodes would be included in all locations with complete scan outlines. Therefore, the data was filtered prior to be sorted for later use. The filter process returned the average position of all nodes with 0.05 mm, which is one-half the accuracy of the scanner. These averaged nodes were then sorted by minimizing the distance around the angle perimeter.

The sorted nodes were then assessed to determine the four main faces of the angle. By modifying the approach described by Zhang *et al.* [124], each edge was determined using a linear fit starting from the middle of each face. Initial predictions for the center of the face were based on the nominal geometry; however, subsequent cross sections considered the center of the previous elevation. The end of the flat portion of each face was defined where the next node was greater than 0.3 mm from the linear line. After defining the edges, the intersection of the outside two faces were used to define the coordinates of the angle heel, (x, y). The lateral imperfections along the length of the member, dx and dy in the x- and y-direction, respectively, were calculated using Eq. A.1, i is the current cross section along the length z of the member, and n is the total number of cross sections as shown in Fig. A.2;

$$[dx, dy]_i = \left[x_i - x_1 + (x_n - x_1)\frac{i-1}{n-1}, y_i - y_1 + (y_n - y_1)\frac{i-1}{n-1}\right] \tag{A.1}$$

The evaluation process separately determined the horizontal and vertical leg rotations and did not constrain the angle to a perfect 90° heel. As a result, the imperfection information was influenced by both global and local effects. For analysis, a single global rotational imperfection was defined as the average rotation of the two legs. The rotational imperfection along the length of the specimen, $d\theta$ about the z-axis, was calculated by Eq. A.2 where θ_b and θ_h are the orientation of the horizontal and vertical legs, respectively.

$$d\theta = 0.5\left(\theta_{b,i} + \theta_{h,i} - \theta_{b,1} - \theta_{h,1} + (\theta_{b,n} + \theta_{h,n} - \theta_{b,1} - \theta_{h,1})\,\frac{i-1}{n-1}\right) \tag{A.2}$$

A.3 Imperfection Results

The imperfection of individual nodes was determined using the imperfections, dx, dy, and $d\theta$, discussed in the previous section. This required mapping the measured imperfections to the final computer mesh, particularly along the member length. An initial distribution was determined by assuming a linear interpolation between the measured imperfections, indicated by a '$\times$' on Fig. A.3. To eliminate the sharp transitions that introduced undesired stress concentrations, a Savitzky-Golay filter was applied to smooth out the distribution while retaining the local maximums, labeled 'Exact'. It was found that some distributions were relatively noisy, particularly for the rotation distribution where an 0.1° rotation was approximately equal to the leg being properly aligned at one edge and off by the accuracy of the scanner on the other edge. A final 'Smoothed' distribution was therefore determined by using a weighted average of the 'Exact' distribution. Additionally, imperfections have commonly been applied as assumed sine curves with the measured imperfection. Thus, an approximate 'Sine' distribution based on the maximum imperfections was also included for comparison purposes. Note this sine curve distribution was not attempting to replicate the shape of the measured imperfection, only provide a comparison point on how critical the shape of the imperfection distribution was during the validation process.

The processed scan results for the hot-rolled and laser-fused angles are provided, starting on the following page. This information was used to calculate the individual node imperfections assuming rigid body deformation as depicted in Fig. A.2.

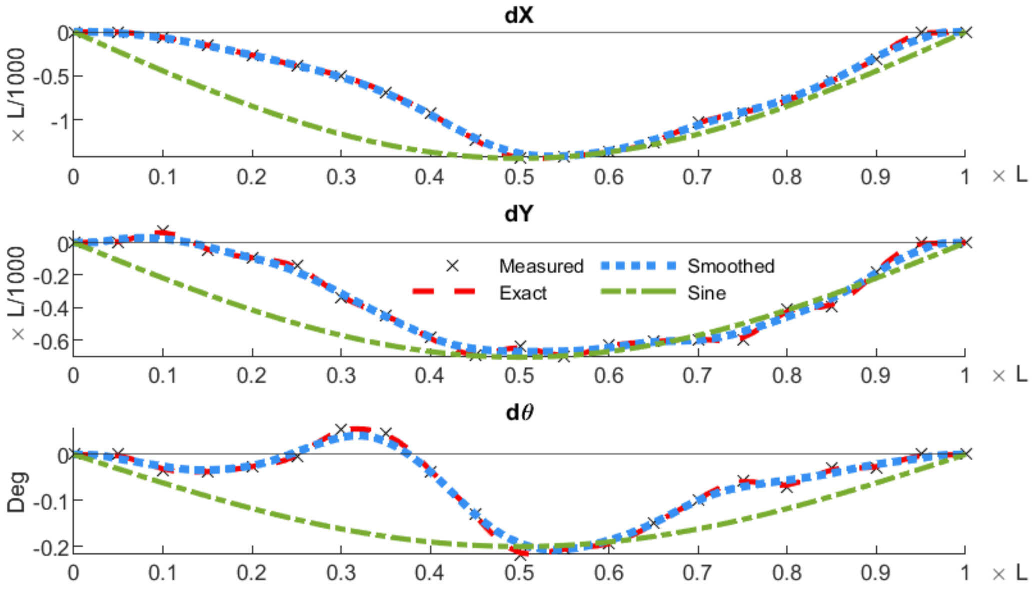

Figure A.3: Measured imperfections of S10-A1-1

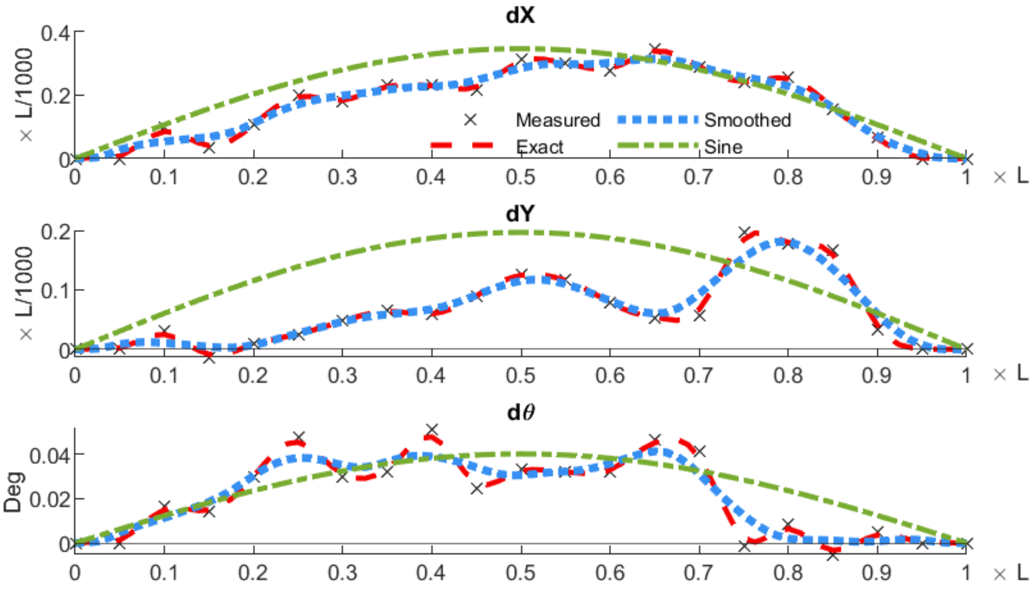

Figure A.4: Measured imperfections of S10-A2-1

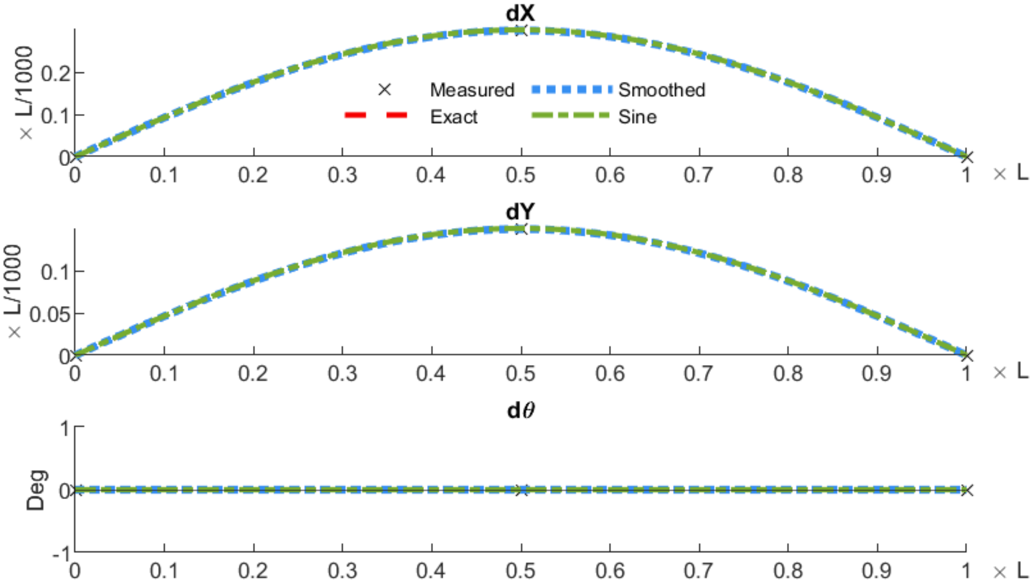

Figure A.5: Measured imperfections of S10-A2-2

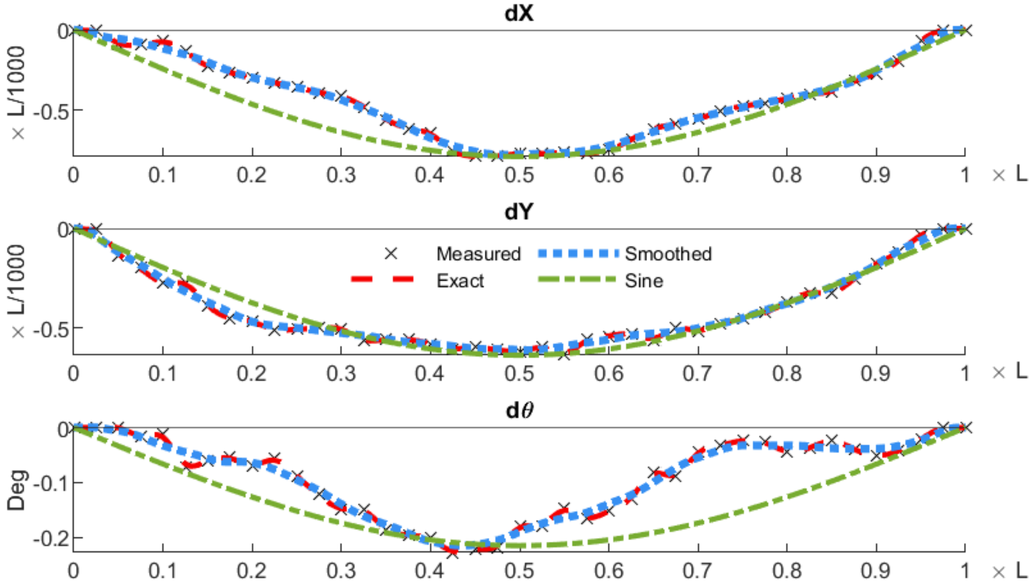

Figure A.6: Measured imperfections of S20-A1-1

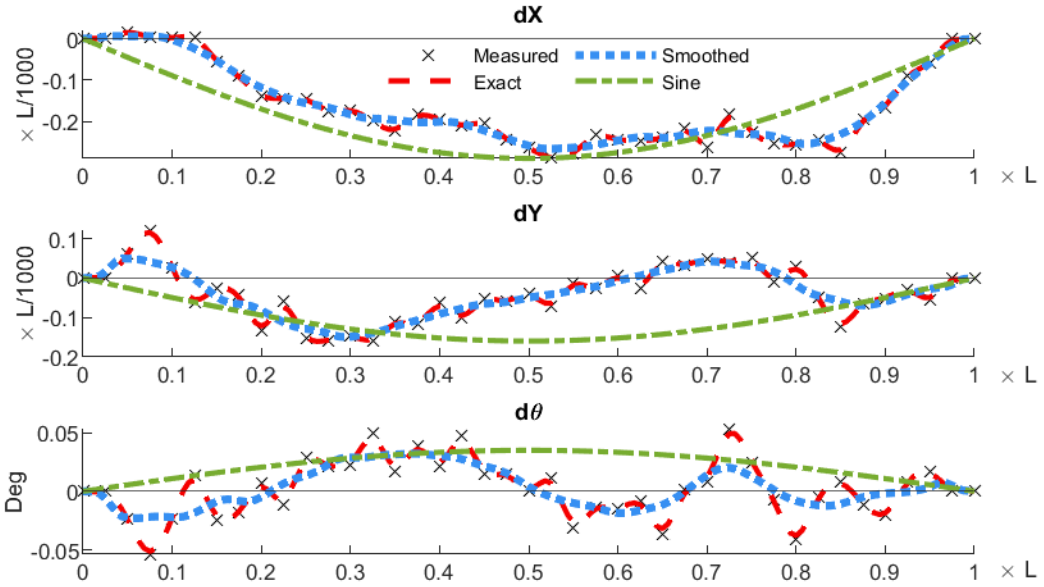

Figure A.7: Measured imperfections of S20-A2-1

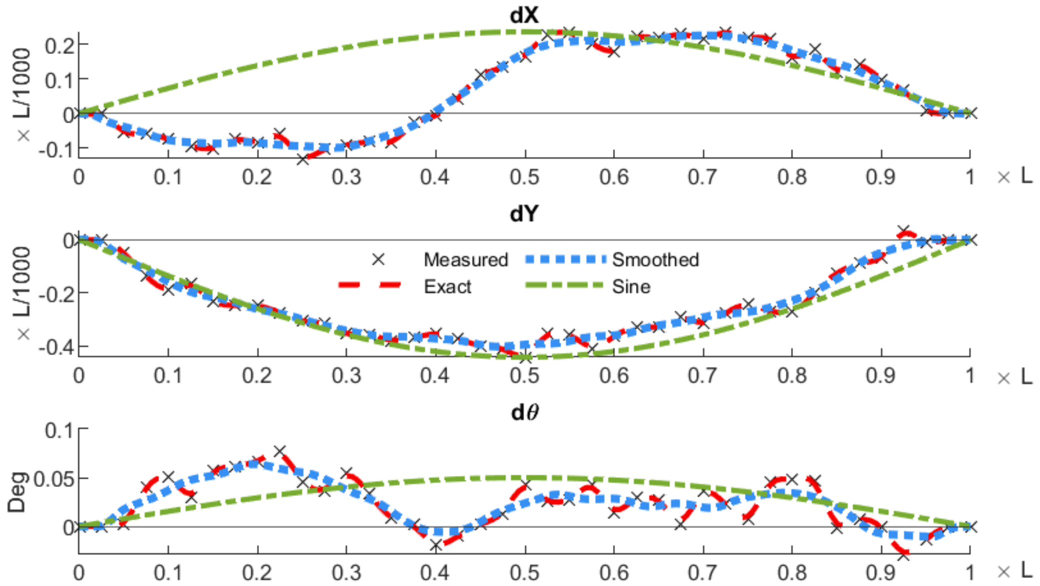

Figure A.8: Measured imperfections of S20-A2-2

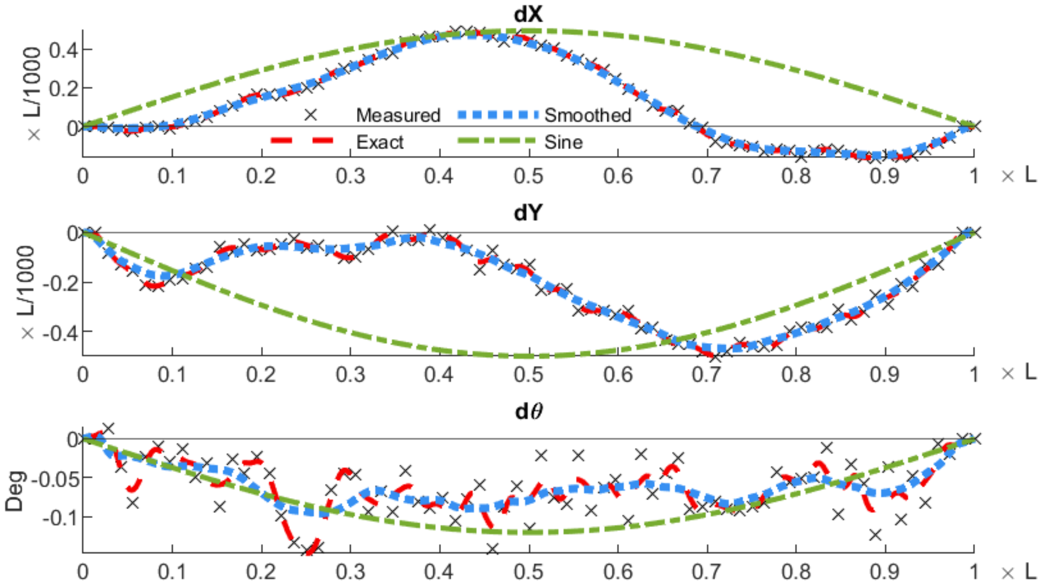

Figure A.9: Measured imperfections of S36-A1-1

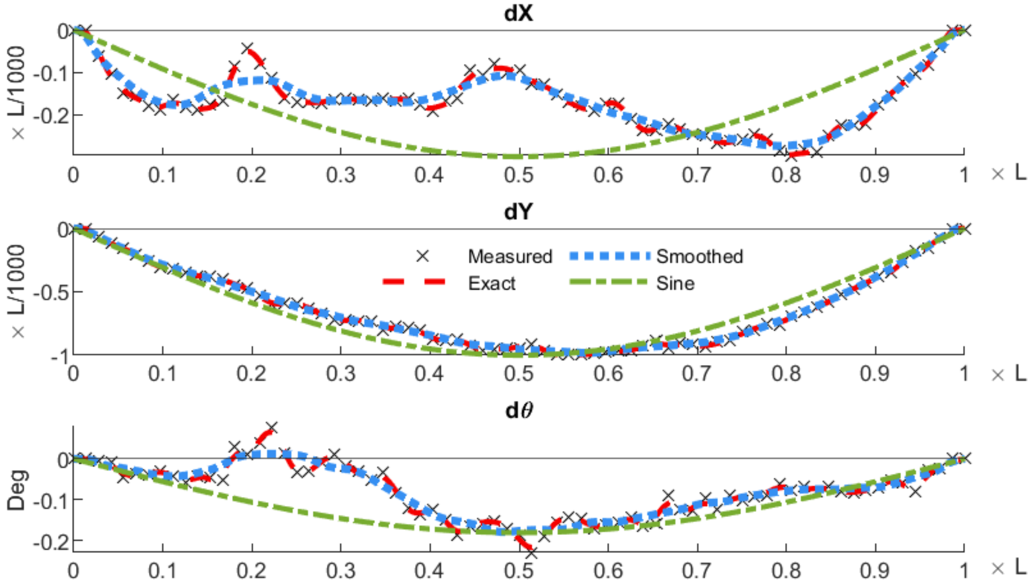

Figure A.10: Measured imperfections of S36-A1-2

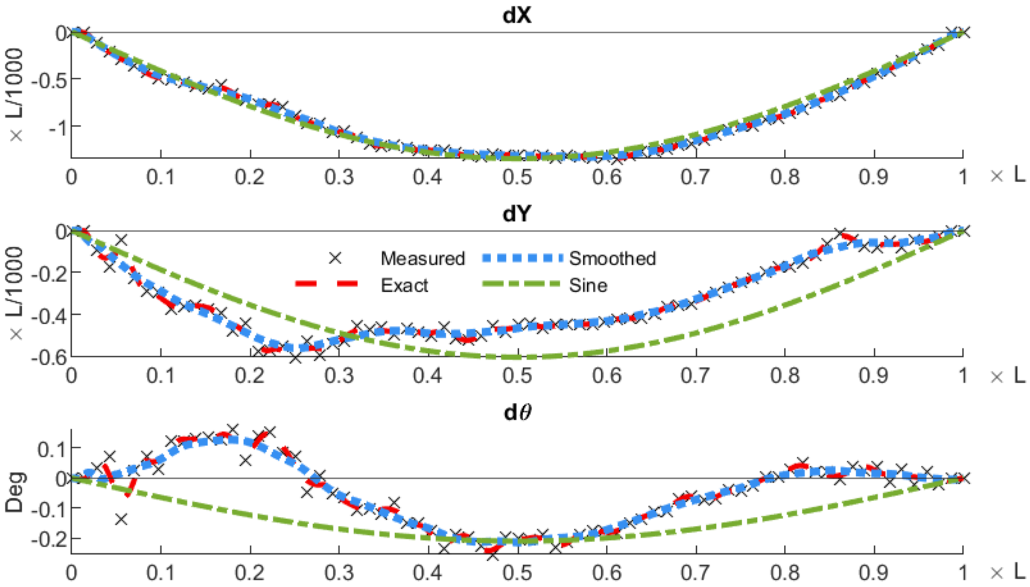

Figure A.11: Measured imperfections of S36-A2-1

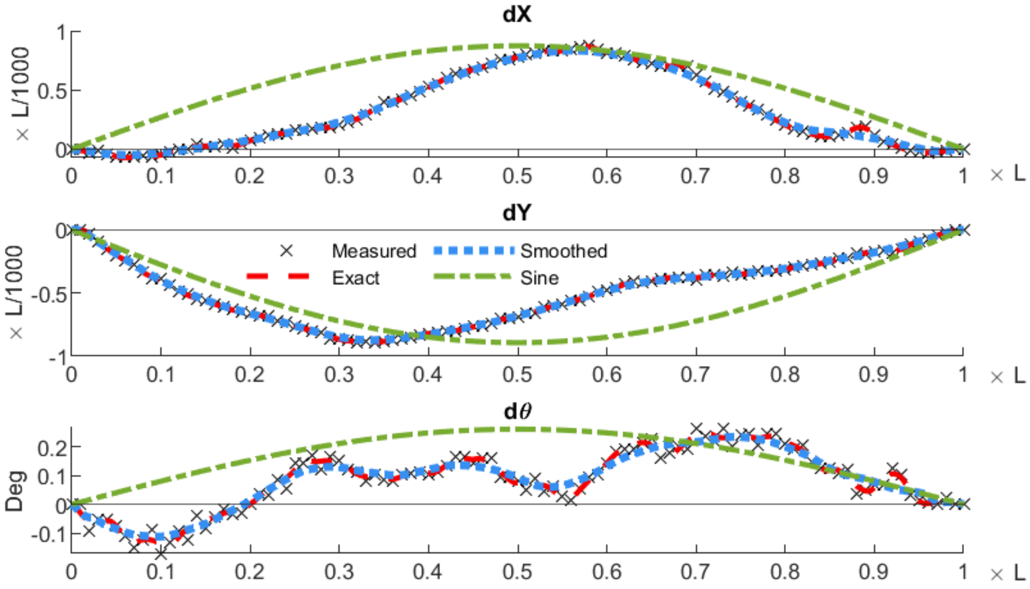

Figure A.12: Measured imperfections of S72-A5-1

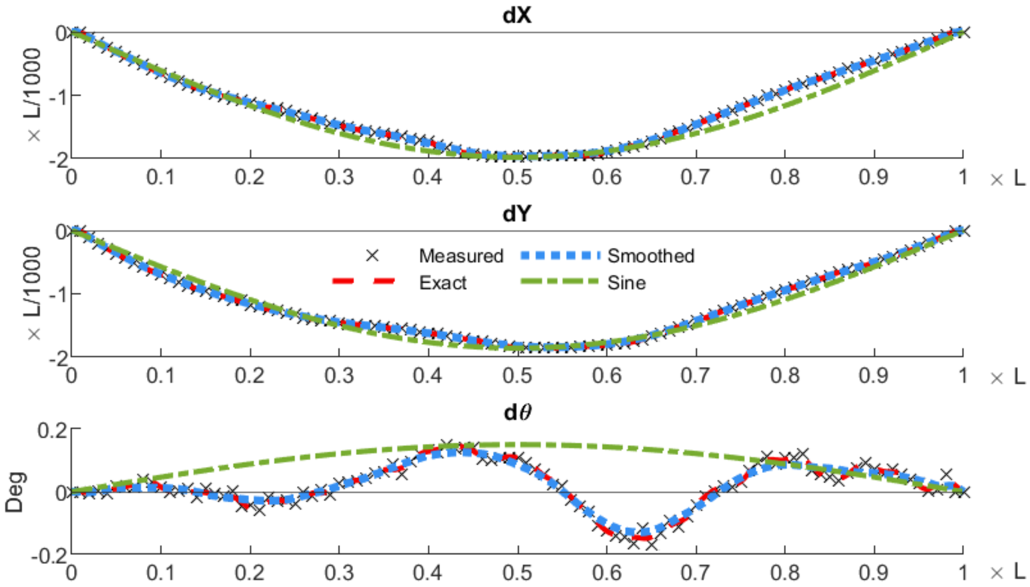

Figure A.13: Measured imperfections of S72-A5-2

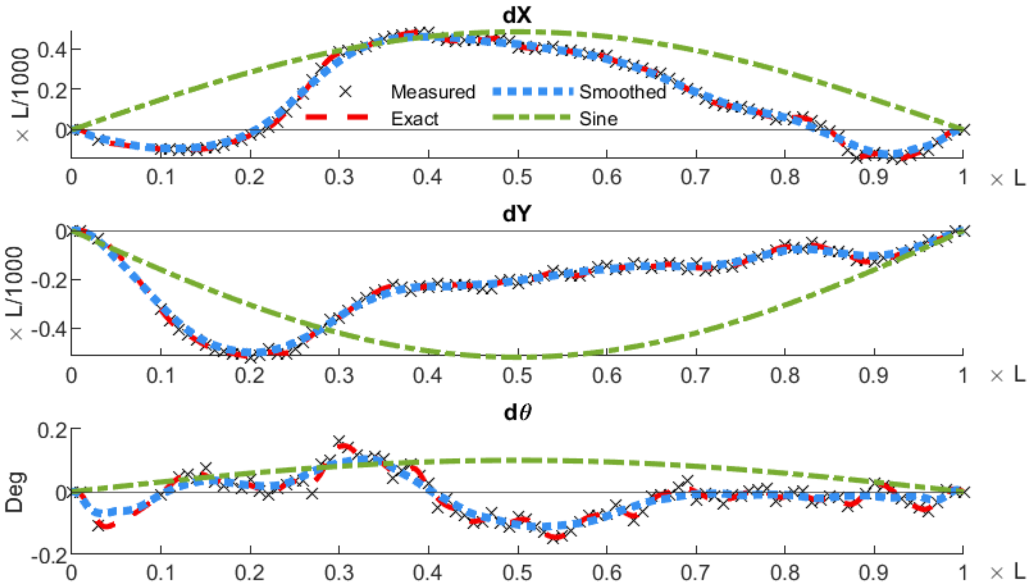

Figure A.14: Measured imperfections of S72-A6-1

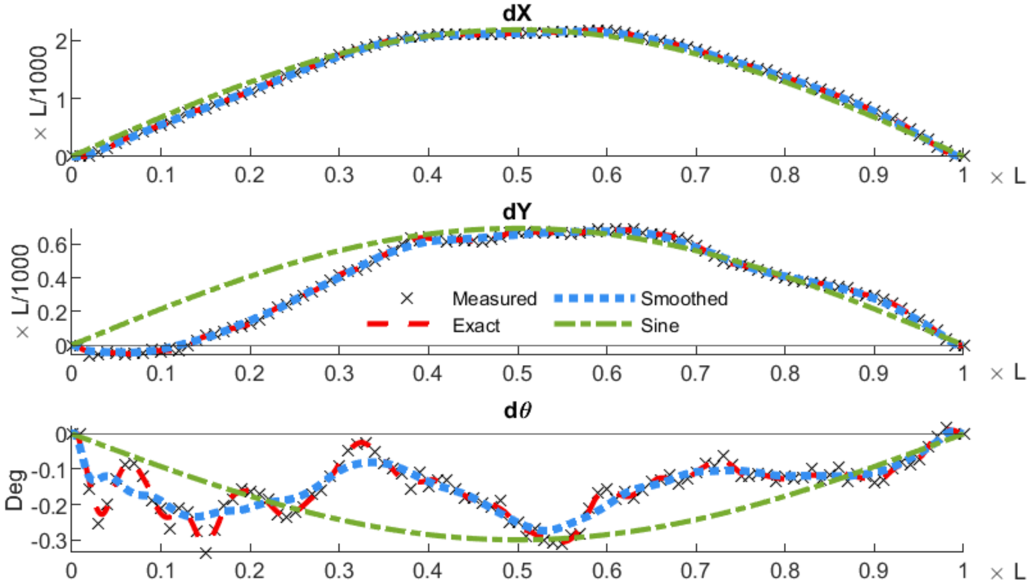

Figure A.15: Measured imperfections of S100-A3-1

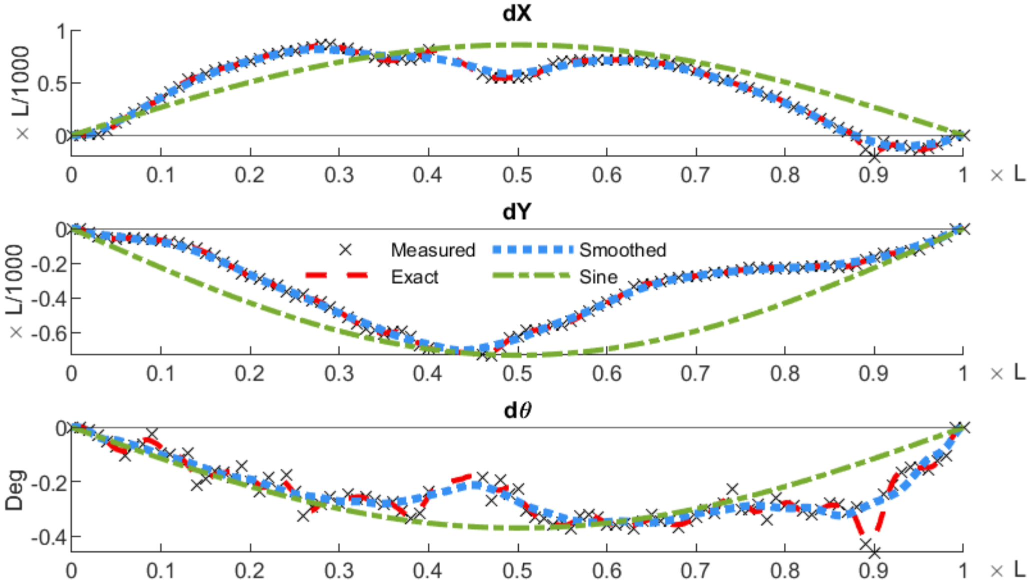

Figure A.16: Measured imperfections of S100-A4-1

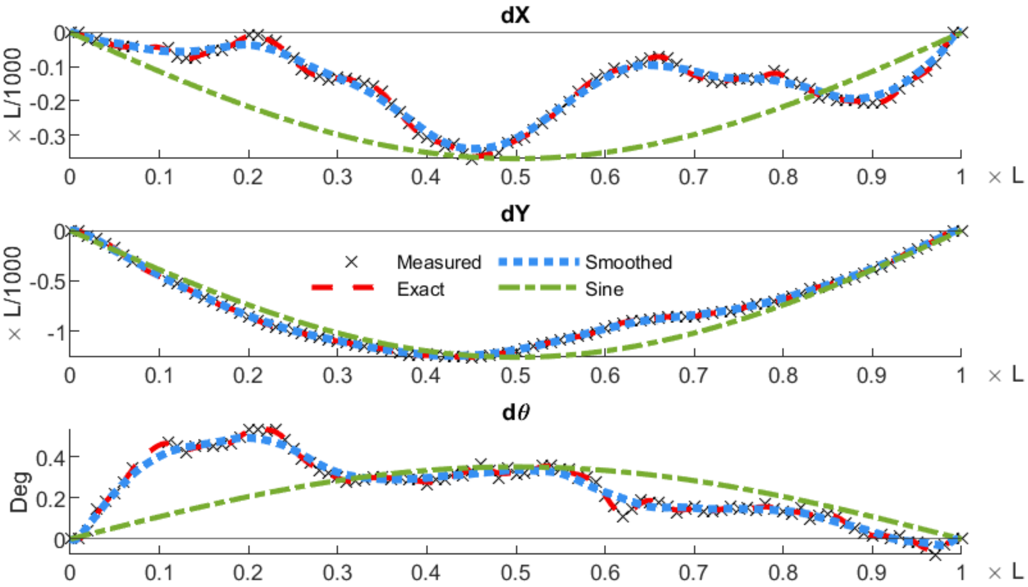

Figure A.17: Measured imperfections of S100-A4-2

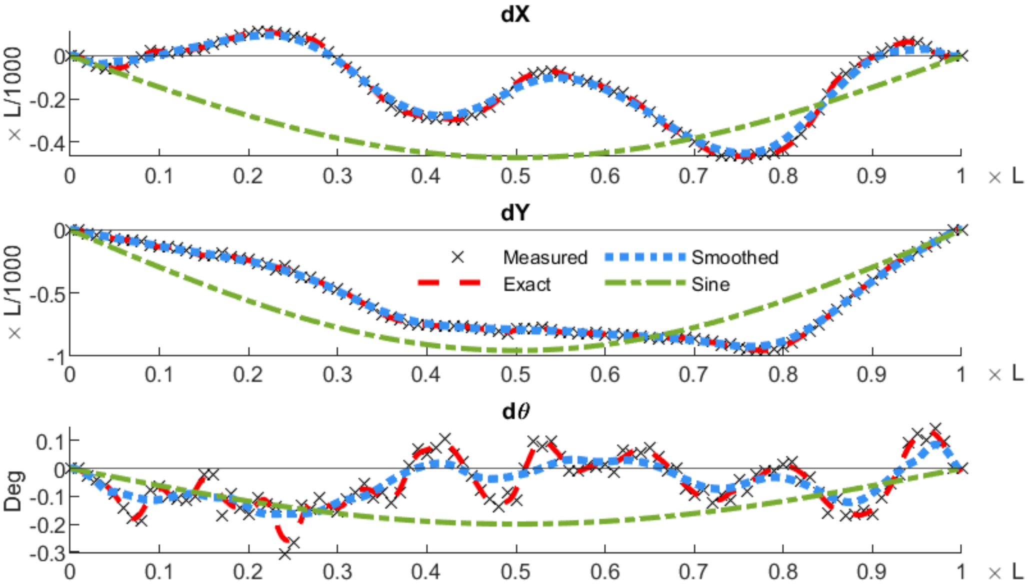

Figure A.18: Measured imperfections of S148-A1-1

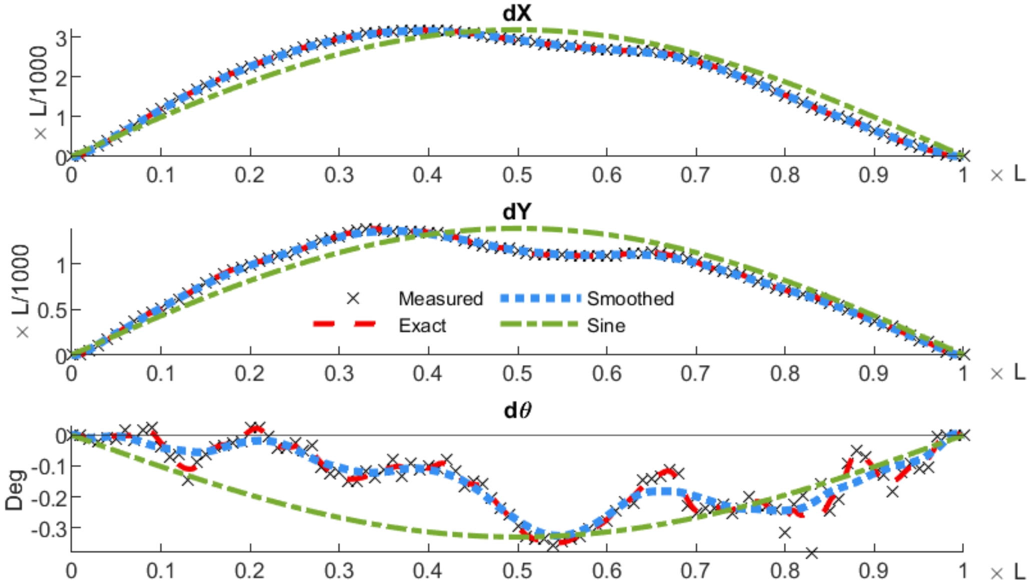

Figure A.19: Measured imperfections of S148-A2-1

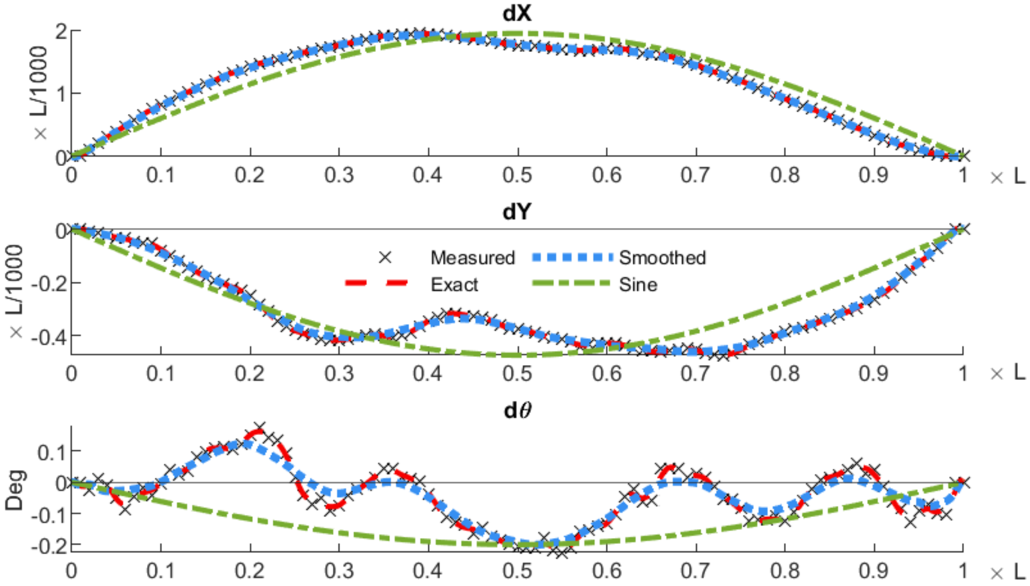

Figure A.20: Measured imperfections of S148-A3-1

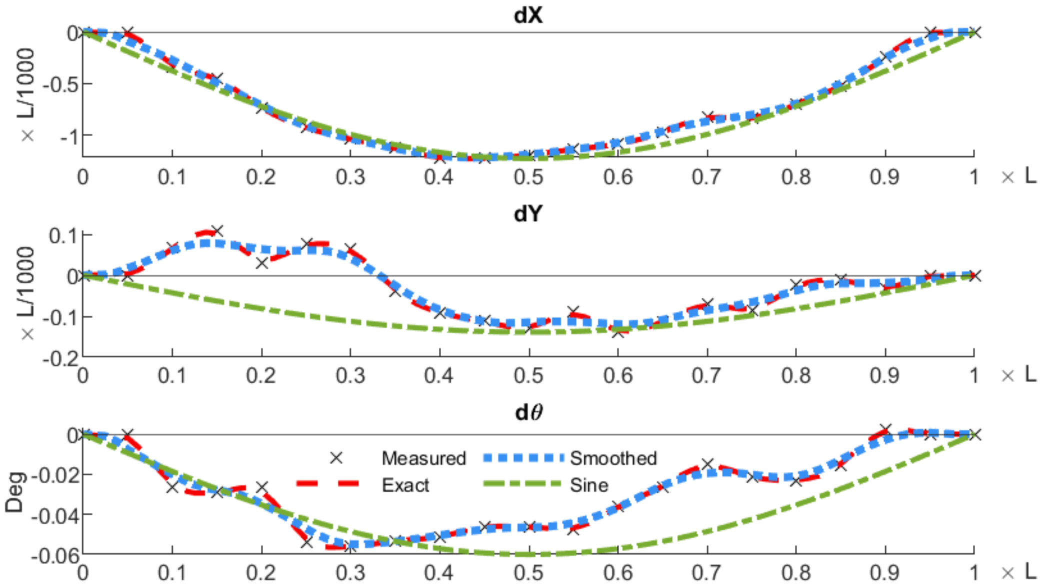

Figure A.21: Measured imperfections of L10-A1-1

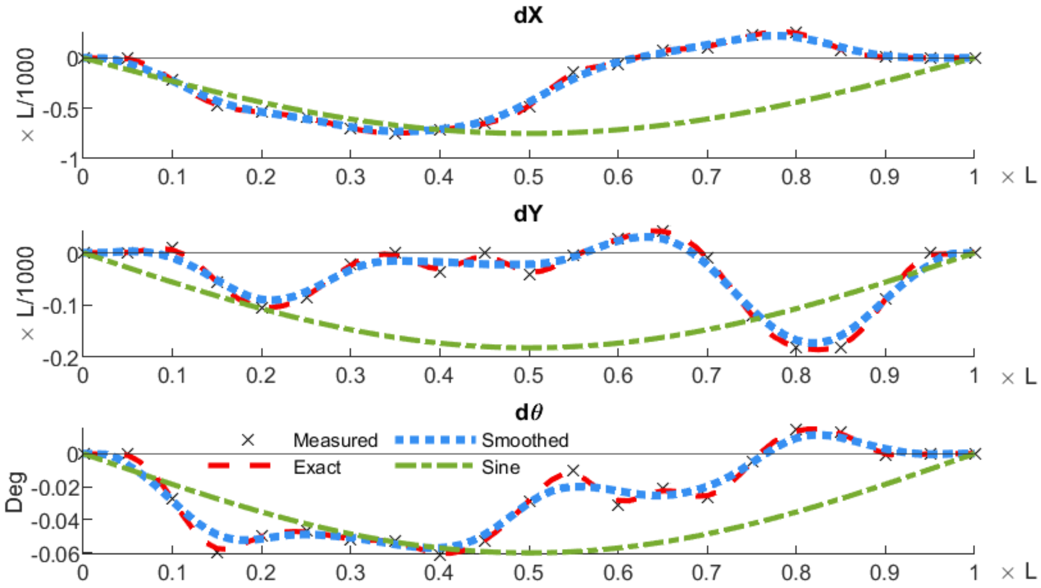

Figure A.22: Measured imperfections of L10-A2-1

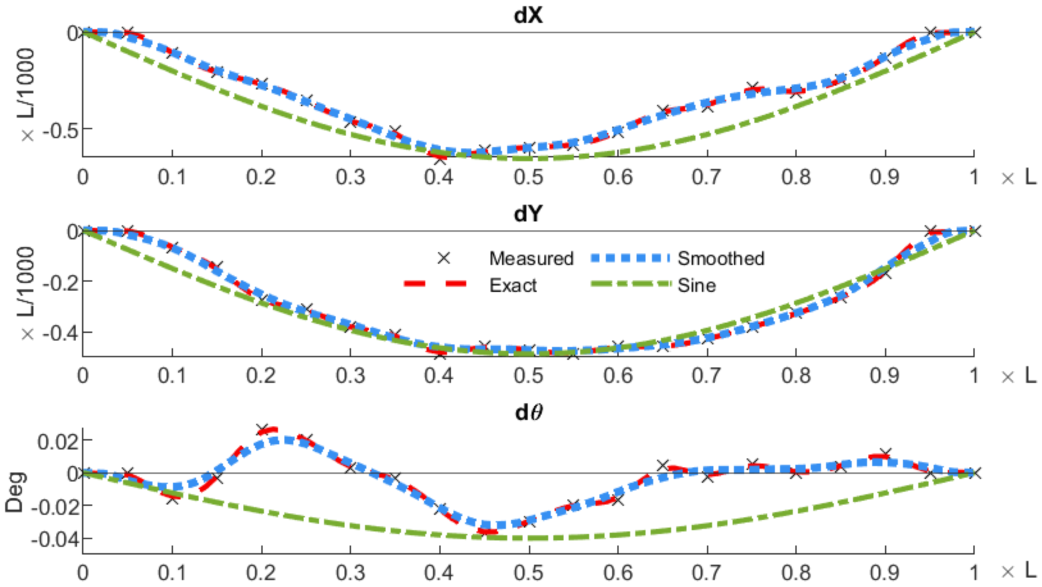

Figure A.23: Measured imperfections of L10-A3-1

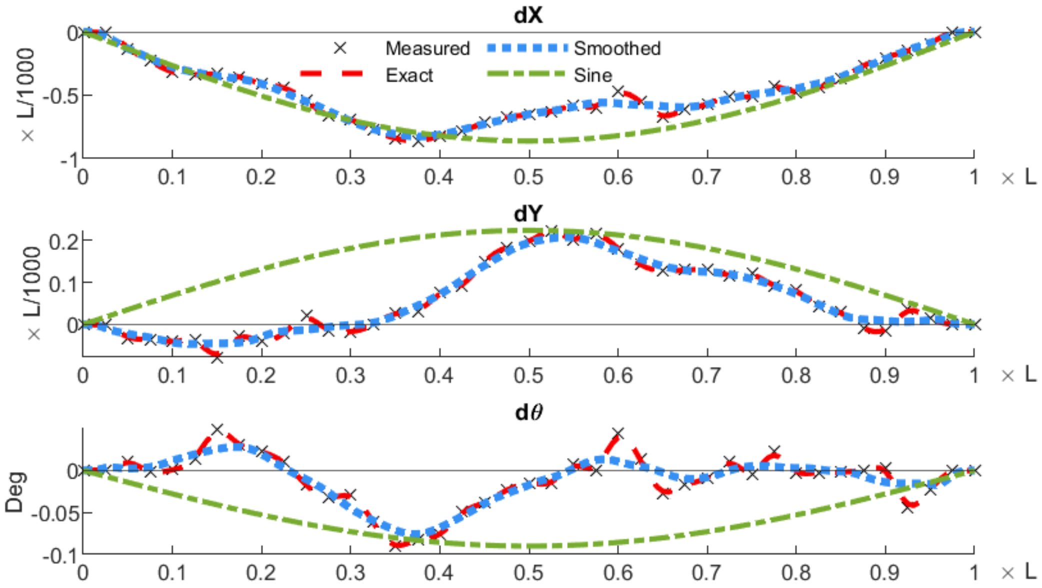

Figure A.24: Measured imperfections of L20-A2-1

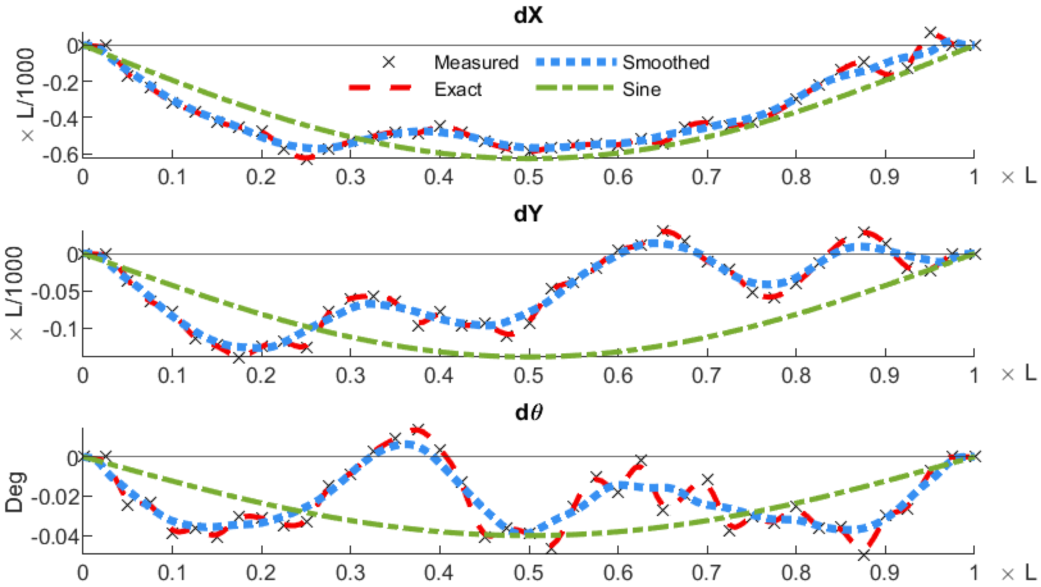

Figure A.25: Measured imperfections of L20-A2-2

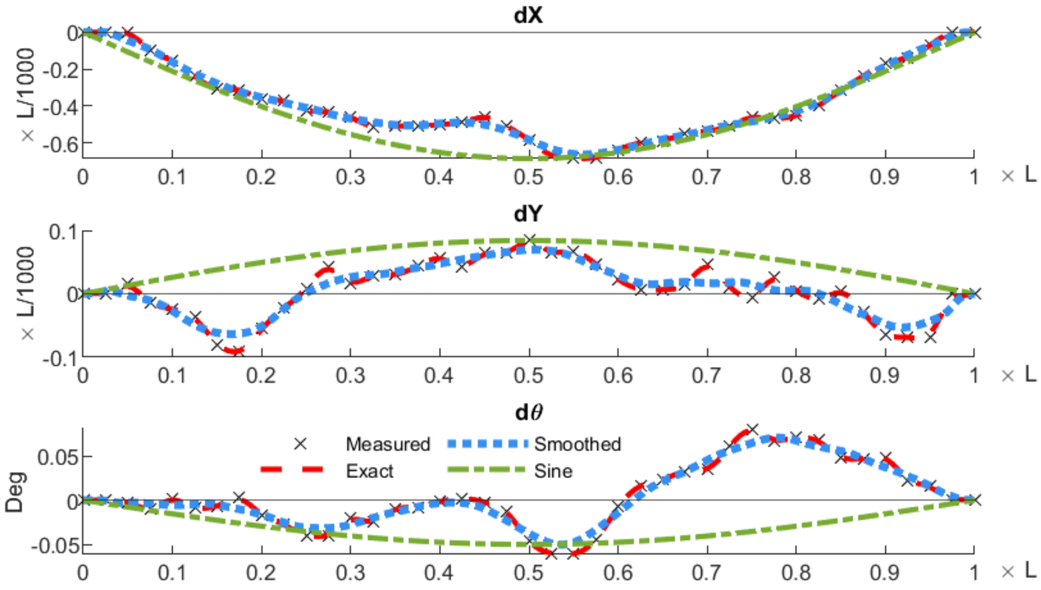

Figure A.26: Measured imperfections of L20-A4-1

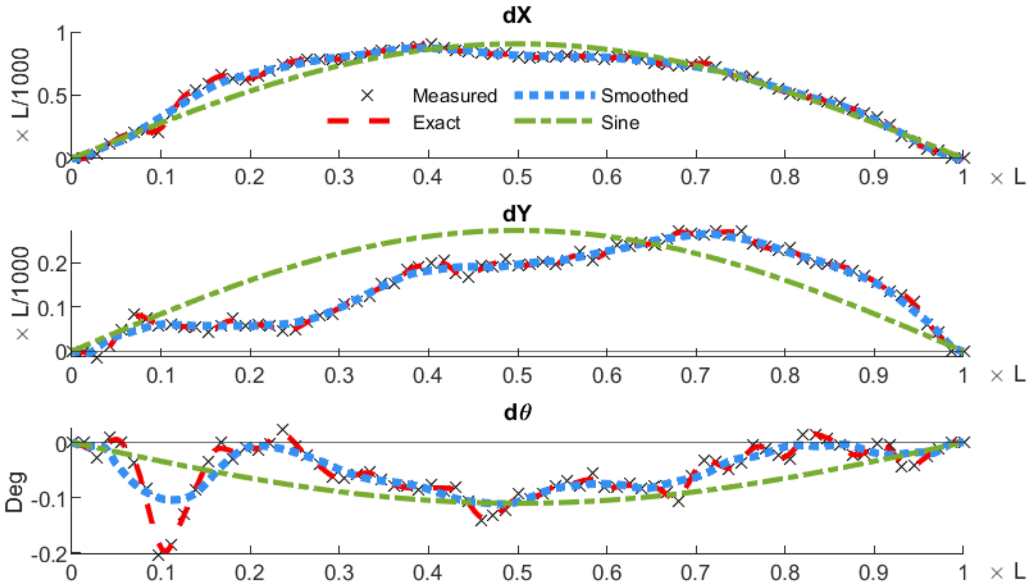

Figure A.27: Measured imperfections of L36-A1-1

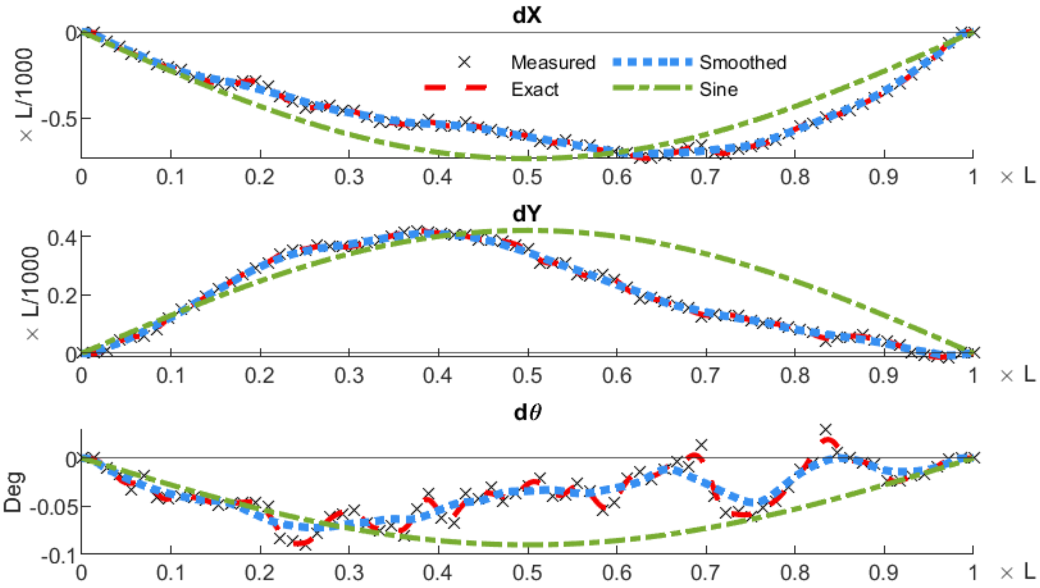

Figure A.28: Measured imperfections of L36-A1-2

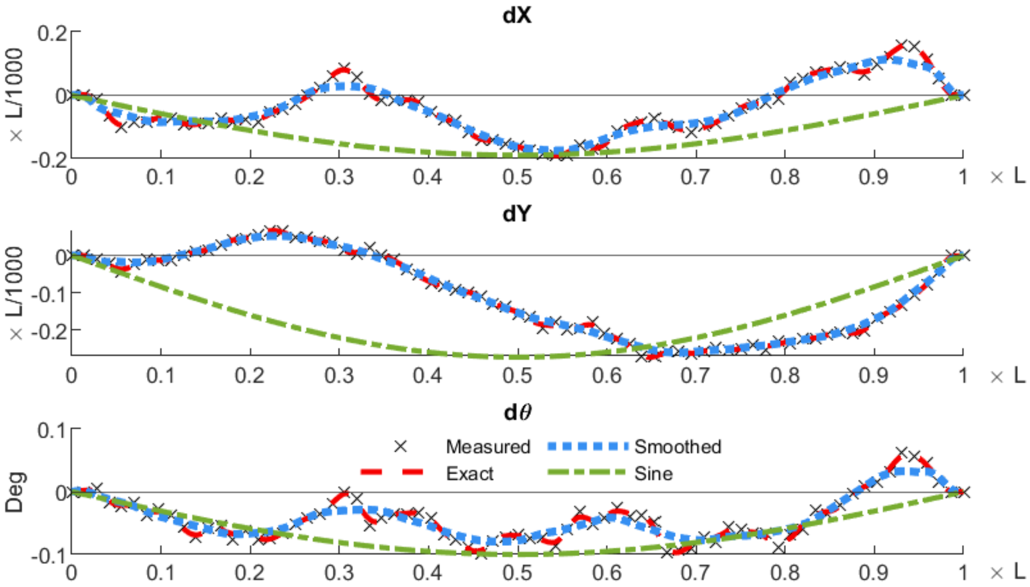

Figure A.29: Measured imperfections of L36-A2-1

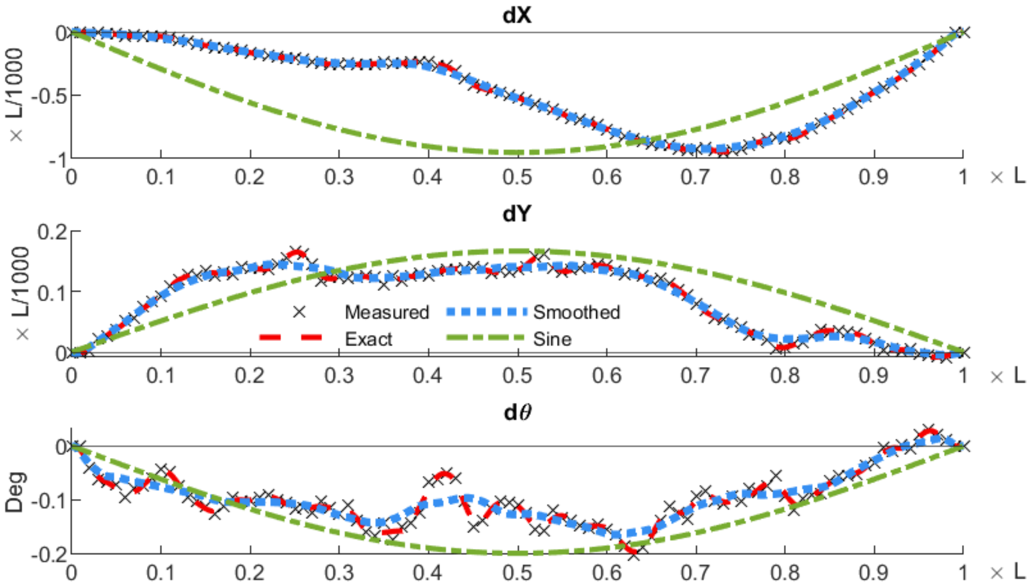

Figure A.30: Measured imperfections of L72-A3-1

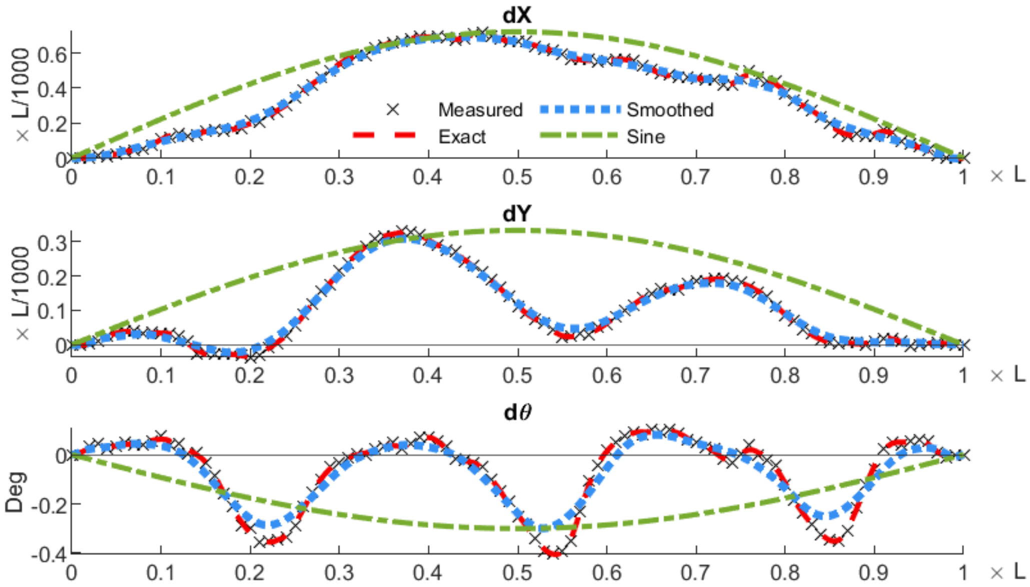

Figure A.31: Measured imperfections of L72-A5-1

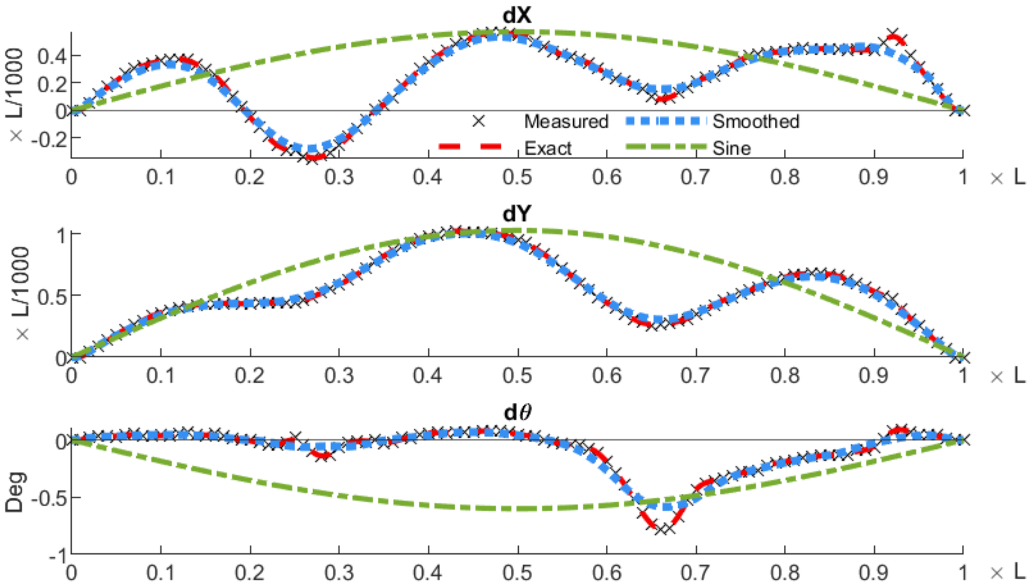

Figure A.32: Measured imperfections of L72-A6-1

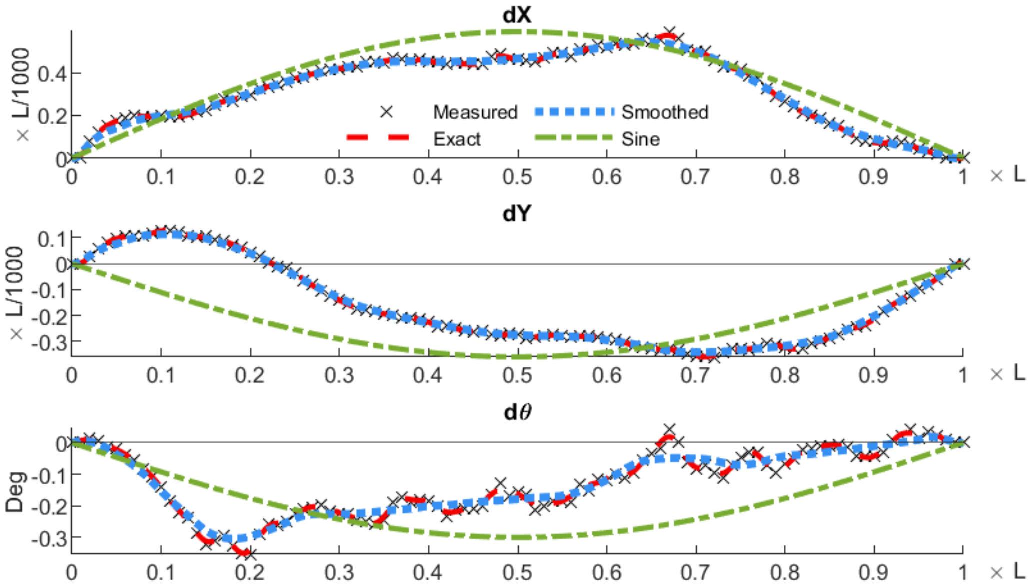

Figure A.33: Measured imperfections of L100-A4-1

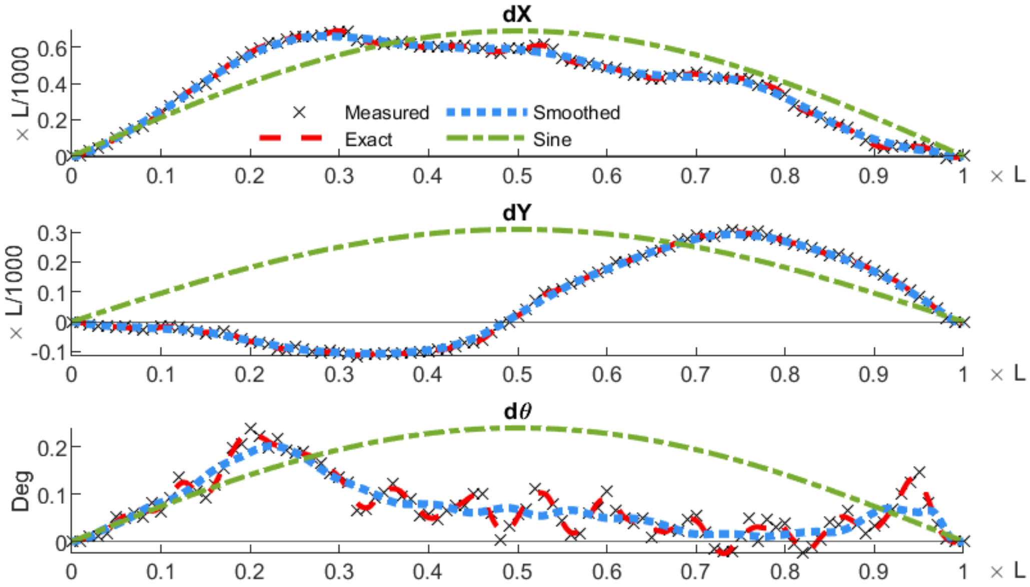

Figure A.34: Measured imperfections of L100-A4-2

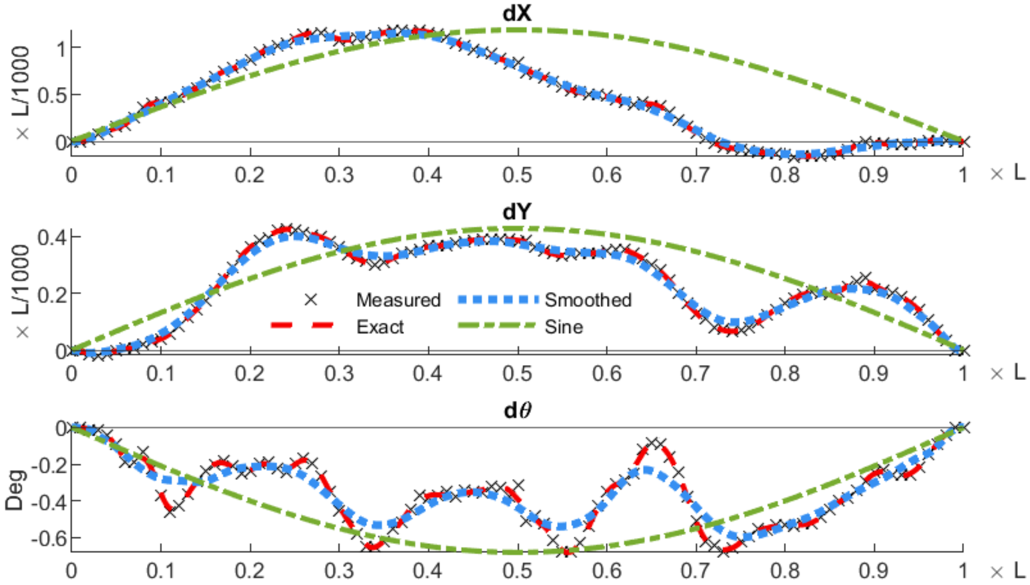

Figure A.35: Measured imperfections of L100-A5-1

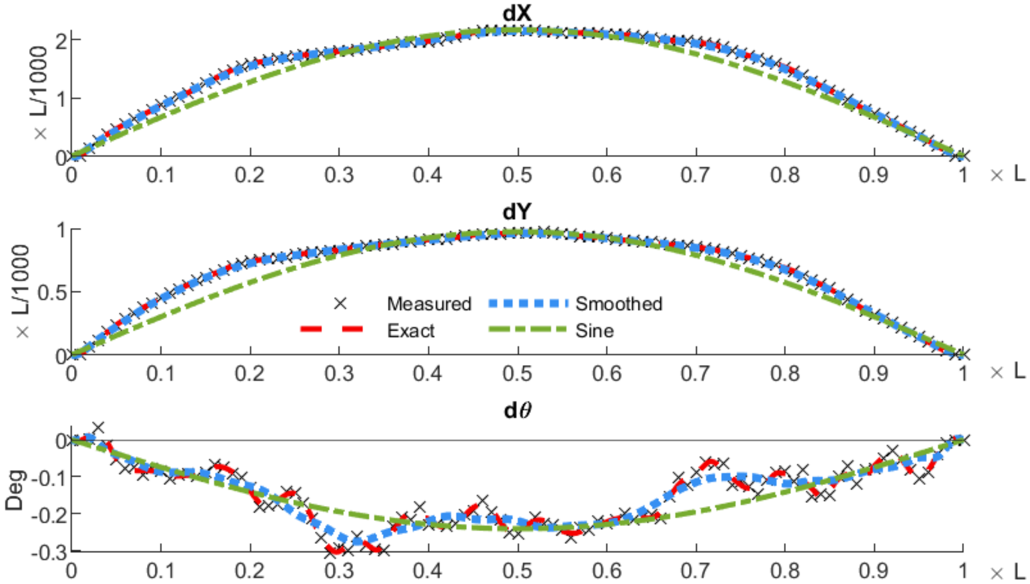

Figure A.36: Measured imperfections of L148-A1-1

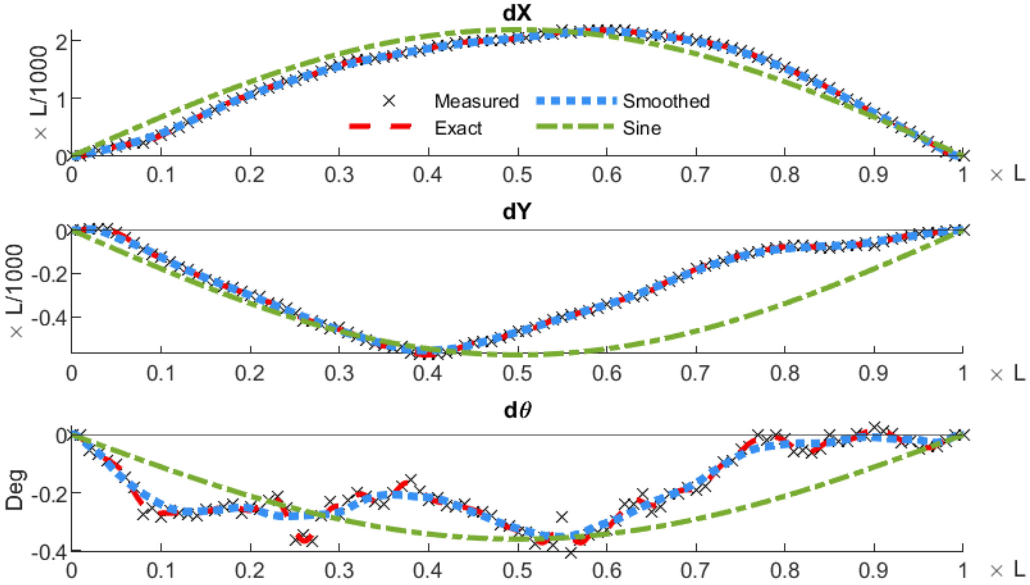

Figure A.37: Measured imperfections of L148-A2-1

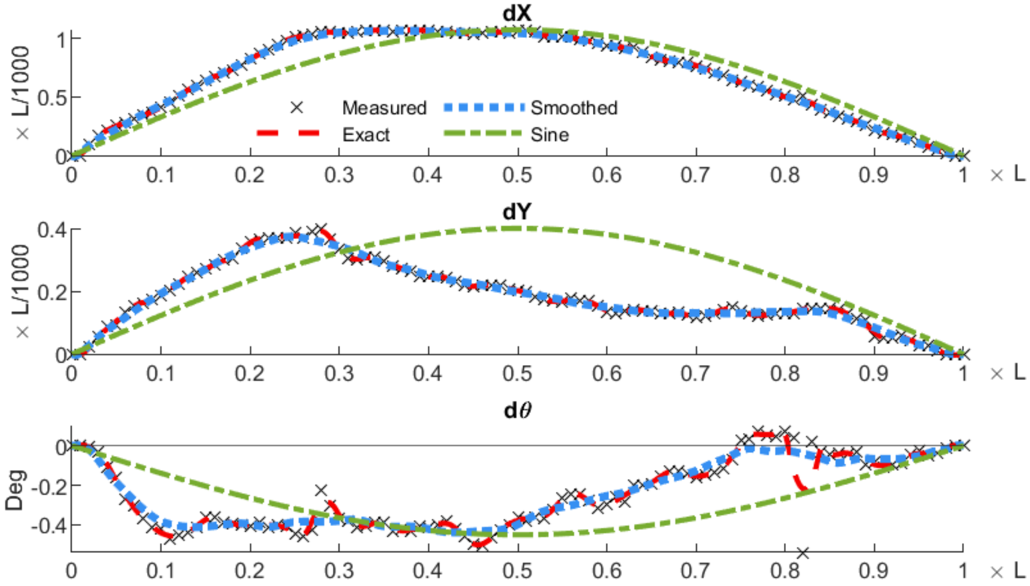

Figure A.38: Measured imperfections of L148-A3-1

B VALIDATION MODELING RESULTS

The following information is additional results from the validation study described in Section 6.5 based on the experiment work with stainless steel unequal-leg angles completed by Laracuente [15]. Information is provided on average axial strain at the middle of each leg as well as the translation and rotation of the cross section at mid-height for each test specimen when considering the measured material properties, measured dimensions, and various implementation of the measured imperfections.

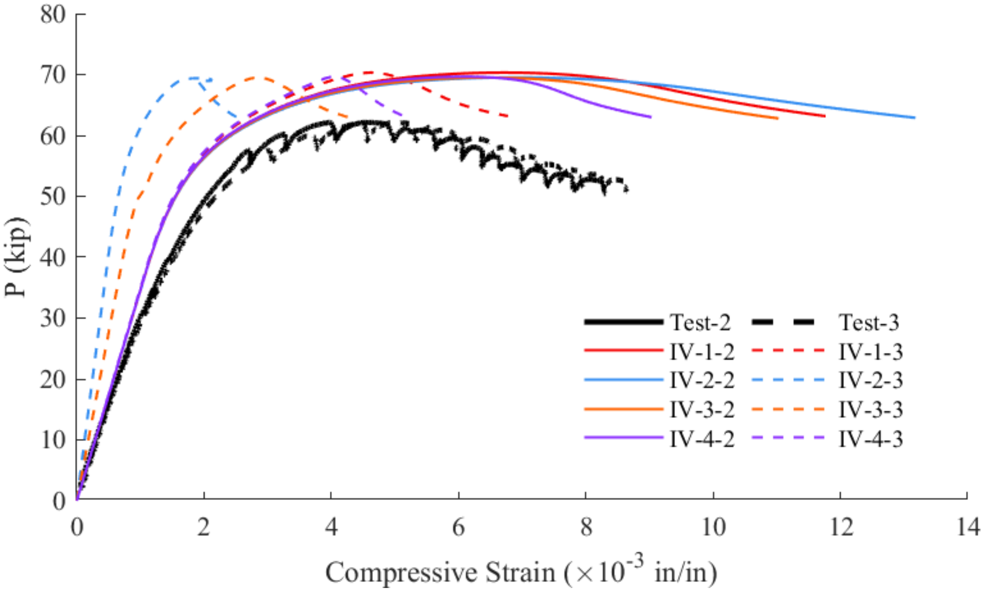

Figure B.1: Stress-strain response of S10-A1-1

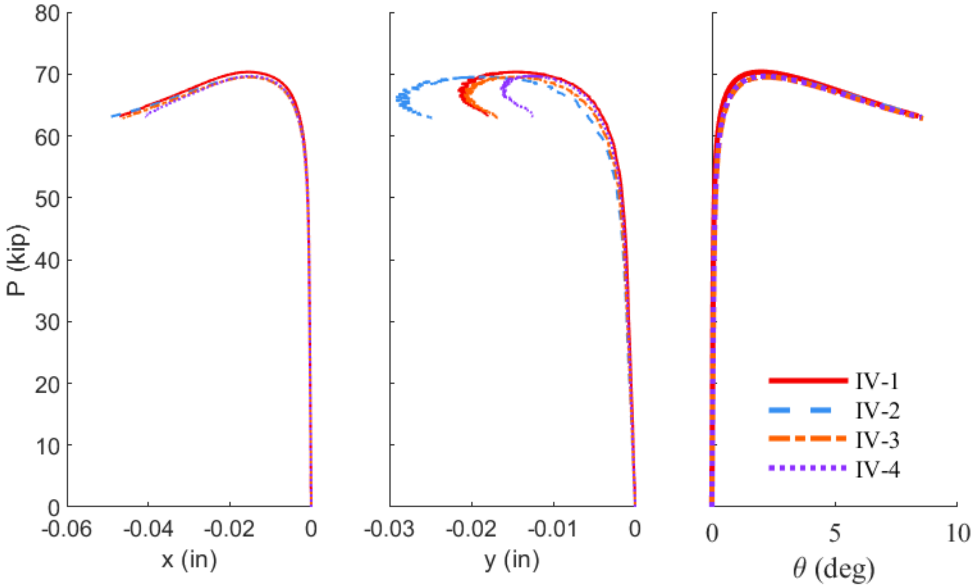

Figure B.2: Cross section displacement of S10-A1-1

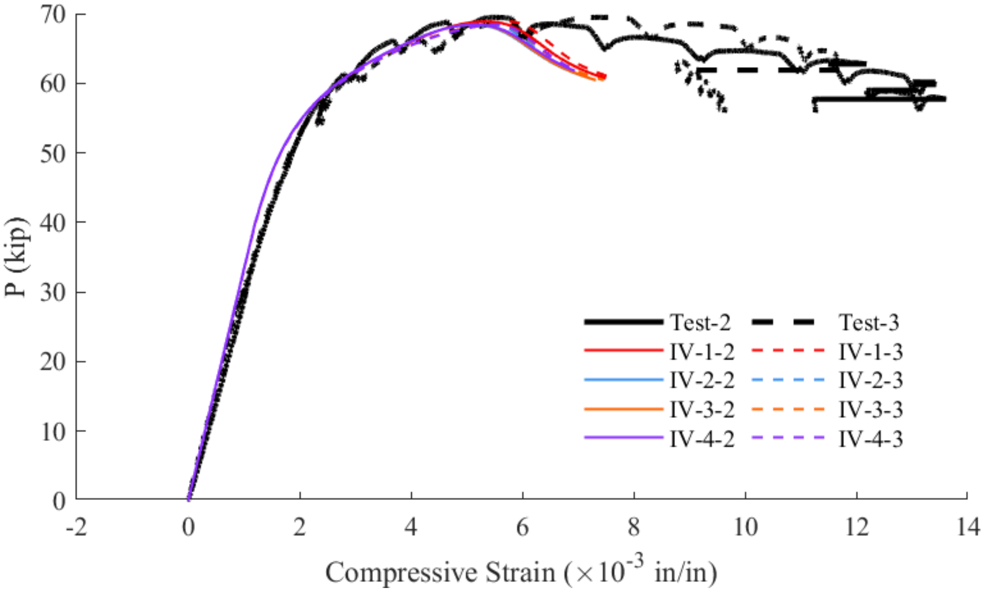

Figure B.3: Stress-strain response of S10-A2-1

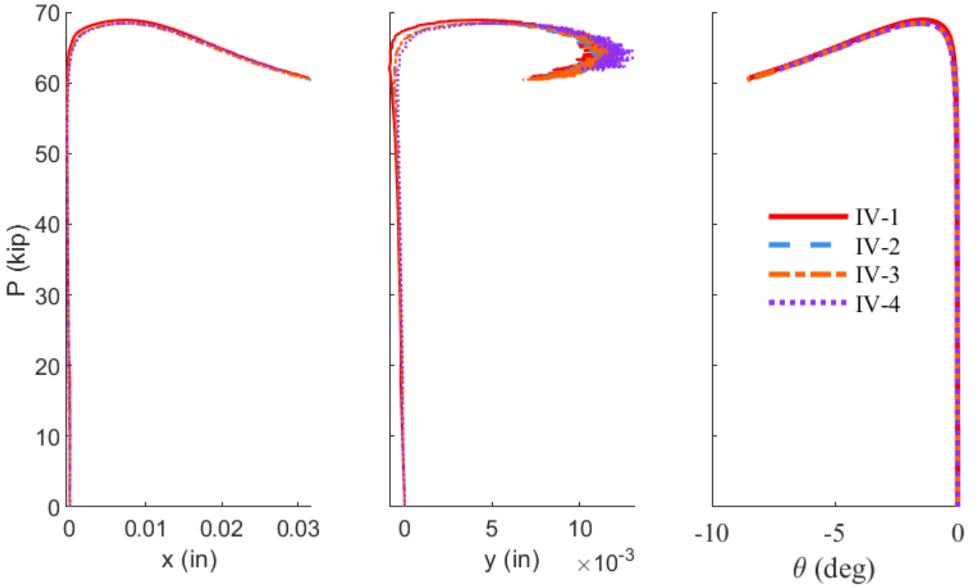

Figure B.4: Cross section displacement of S10-A2-1

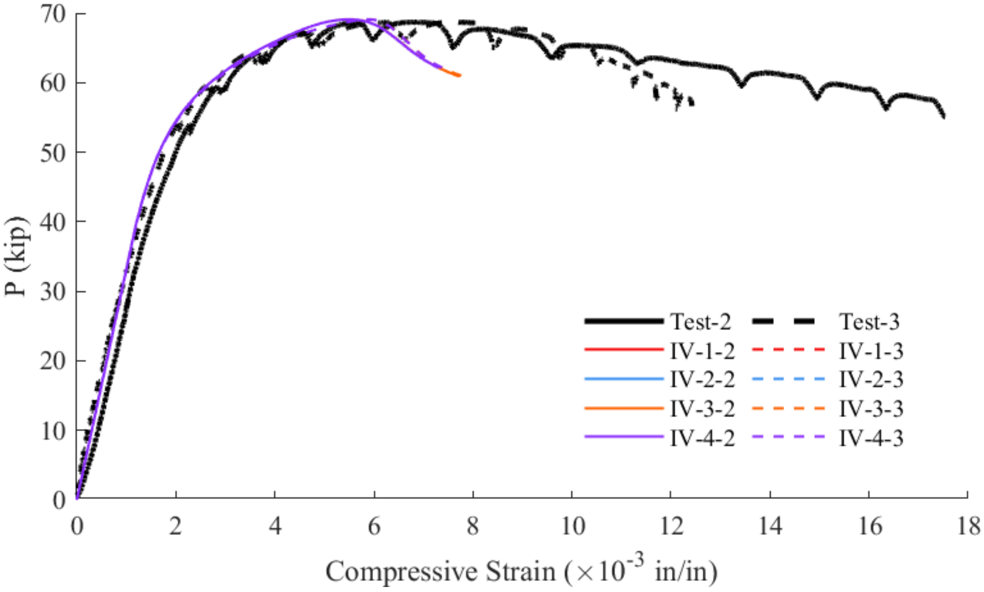

Figure B.5: Stress-strain response of S10-A2-2

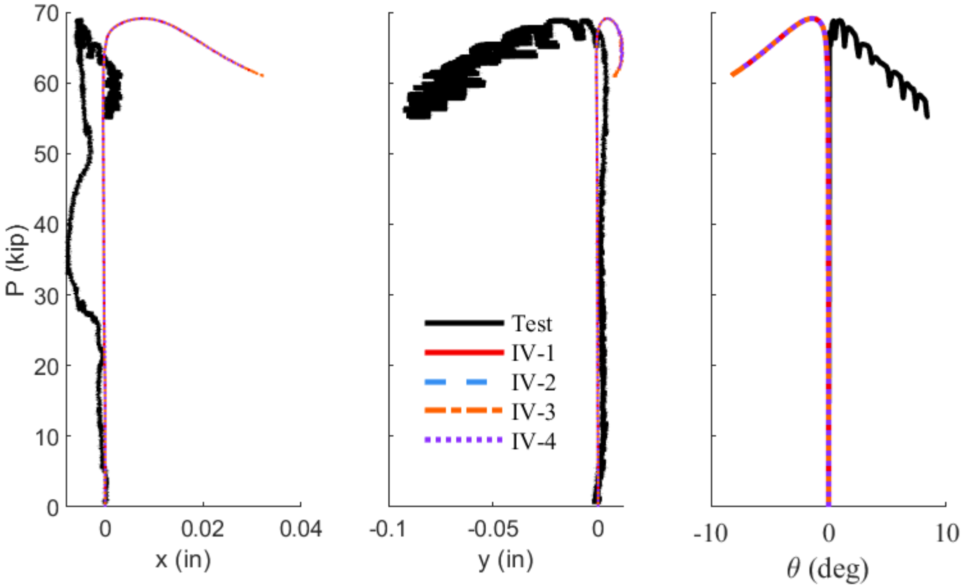

Figure B.6: Cross section displacement of S10-A2-2

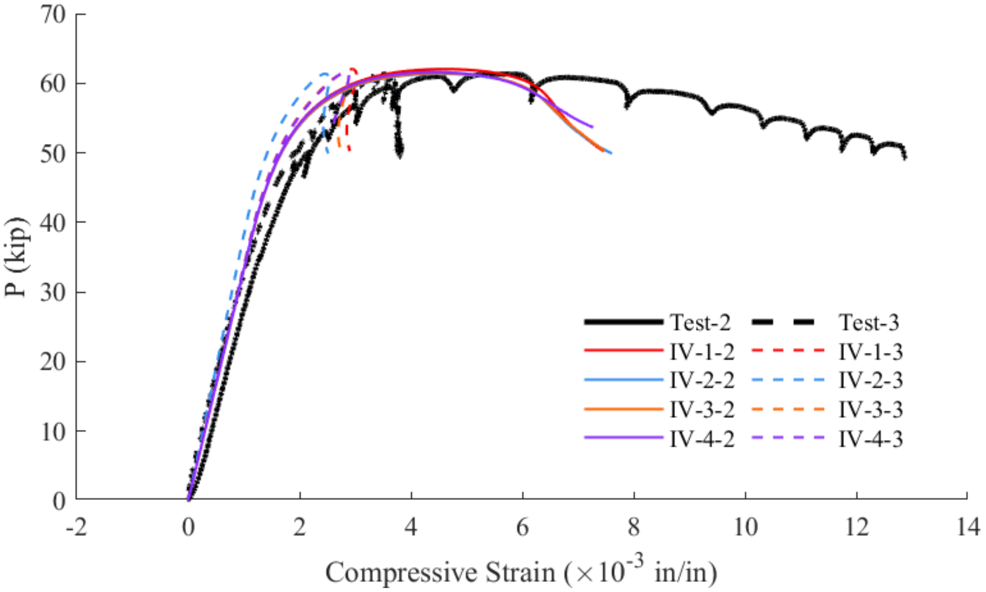

Figure B.7: Stress-strain response of S20-A1-1

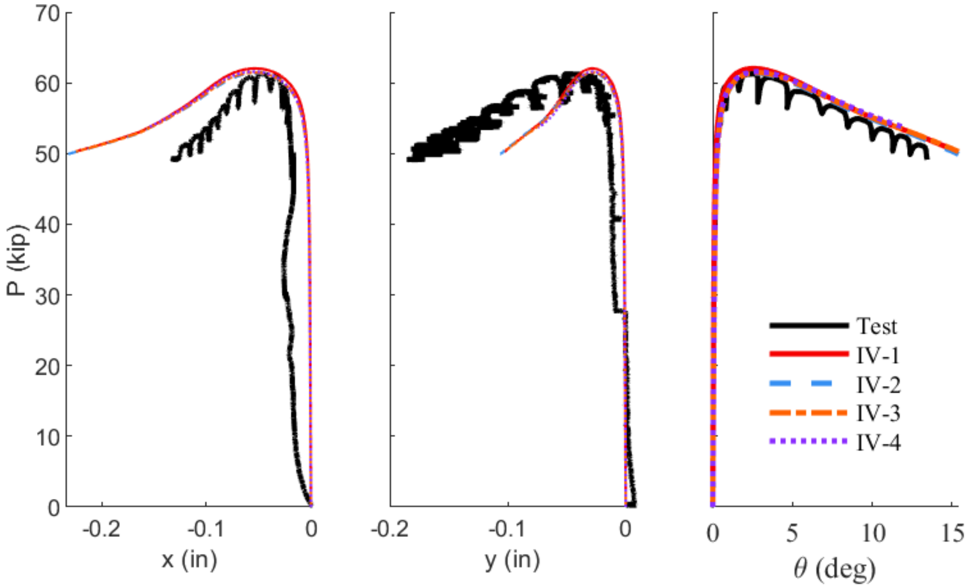

Figure B.8: Cross section displacement of S20-A1-1

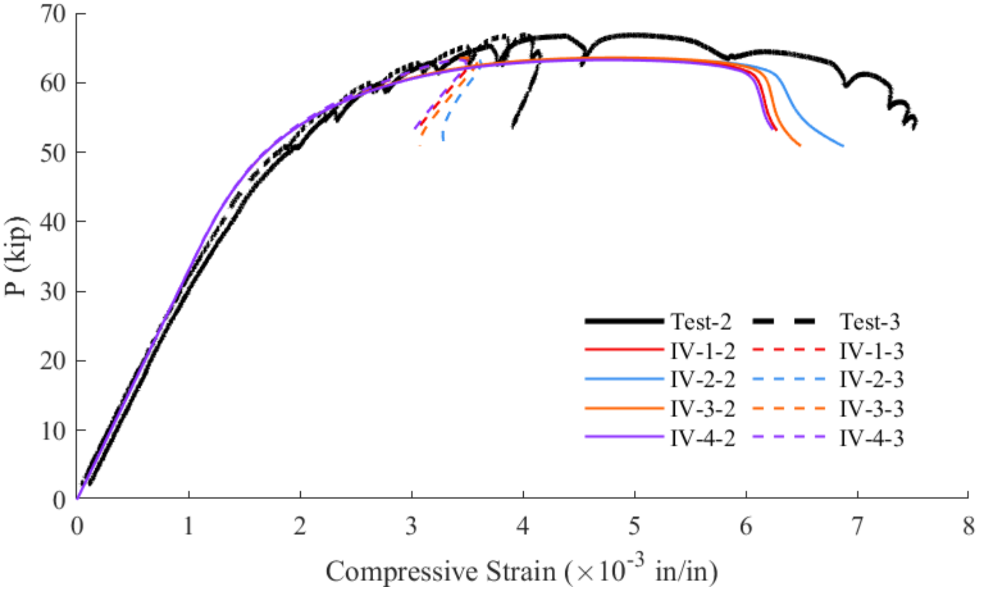

Figure B.9: Stress-strain response of S20-A2-1

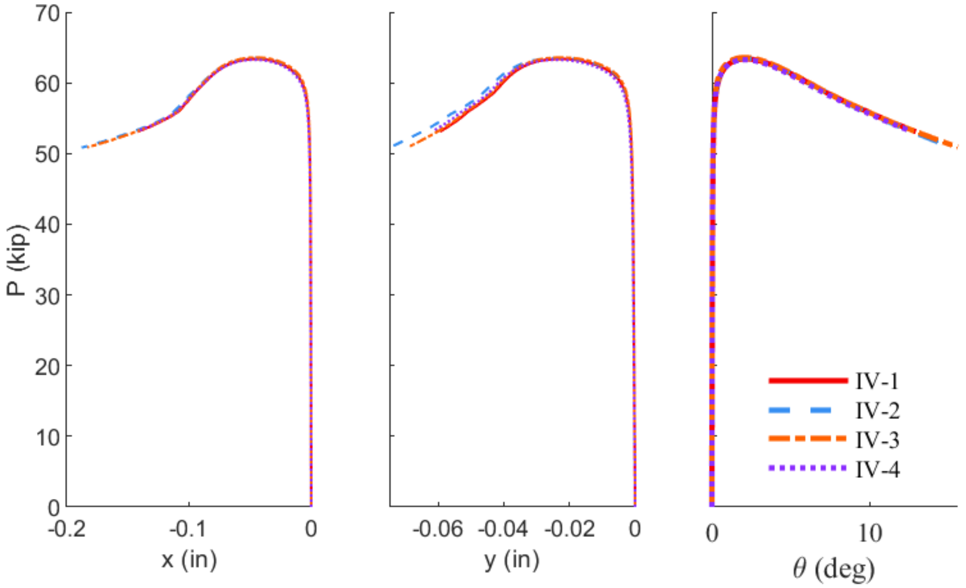

Figure B.10: Cross section displacement of S20-A2-1

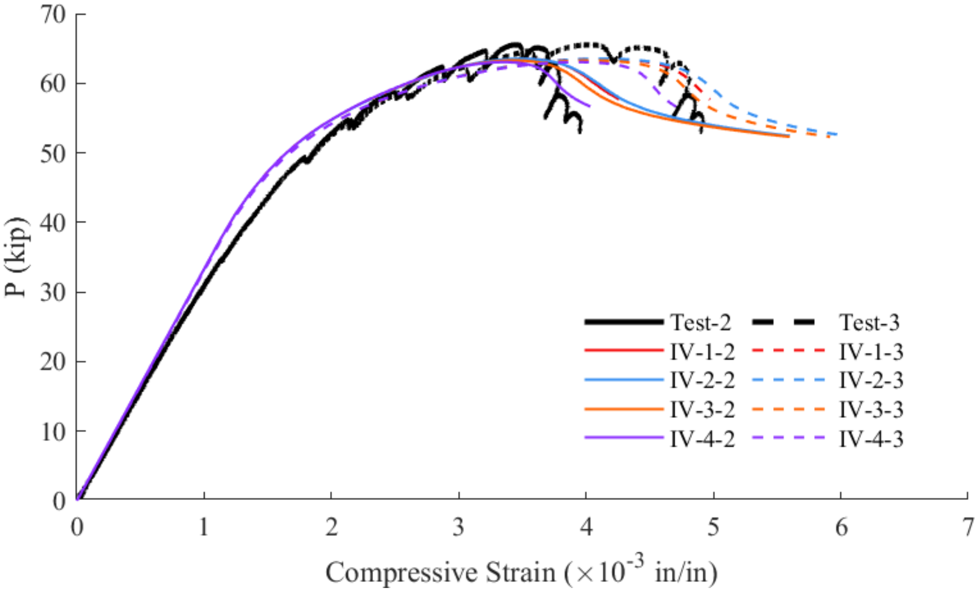

Figure B.11: Stress-strain response of S20-A2-2

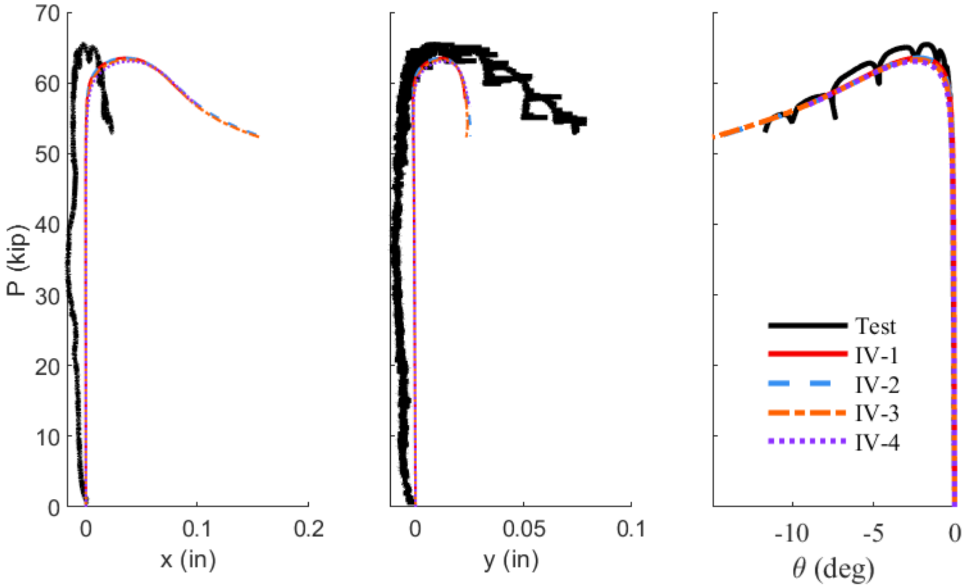

Figure B.12: Cross section displacement of S20-A2-2

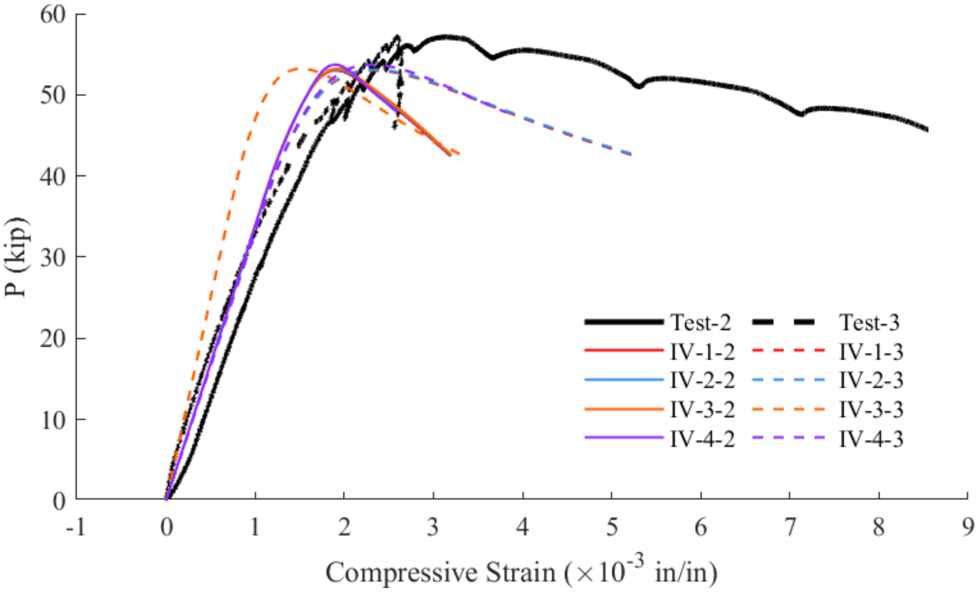

Figure B.13: Stress-strain response of S36-A1-1

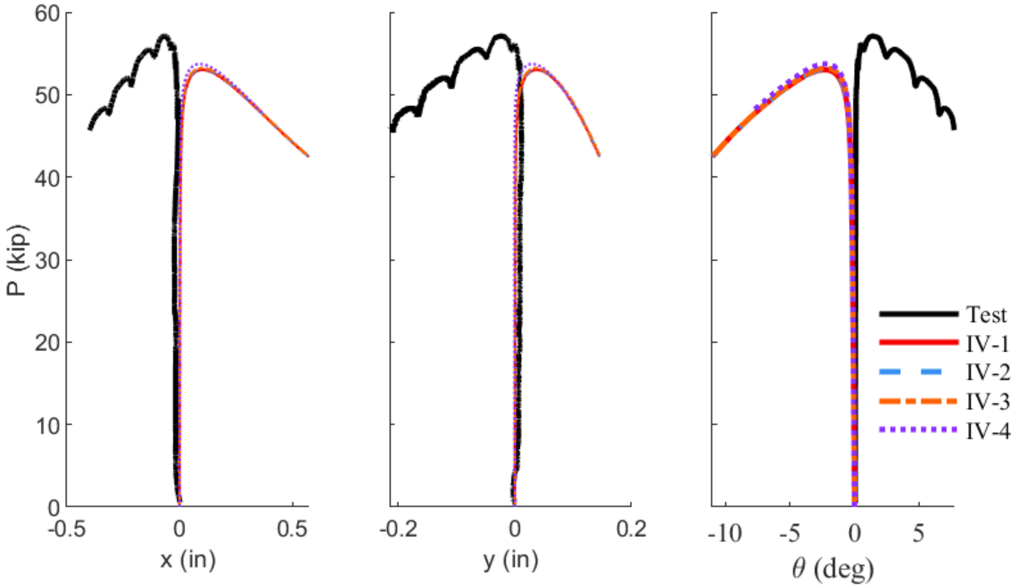

Figure B.14: Cross section displacement of S36-A1-1

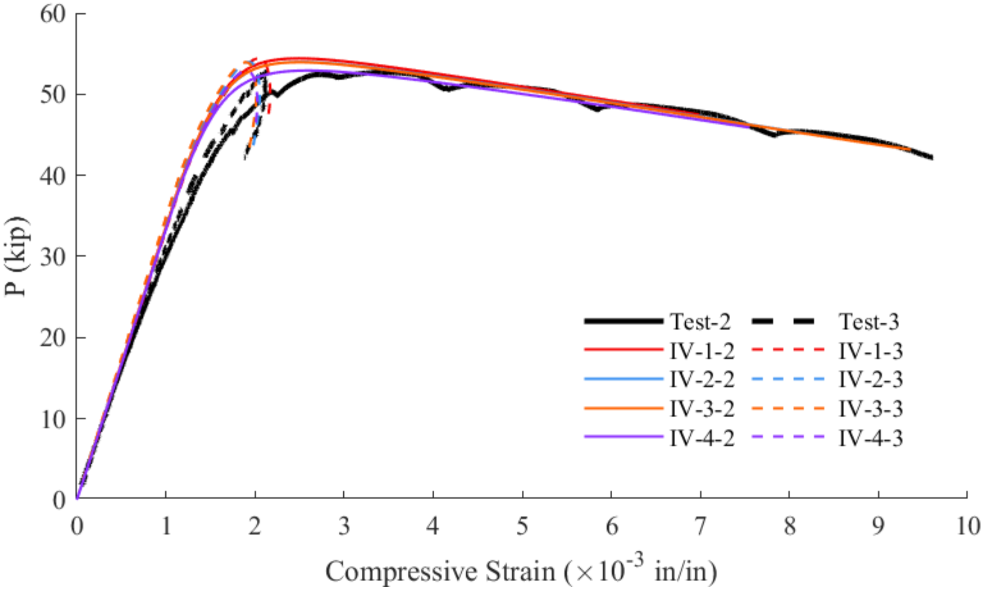

Figure B.15: Stress-strain response of S36-A1-2

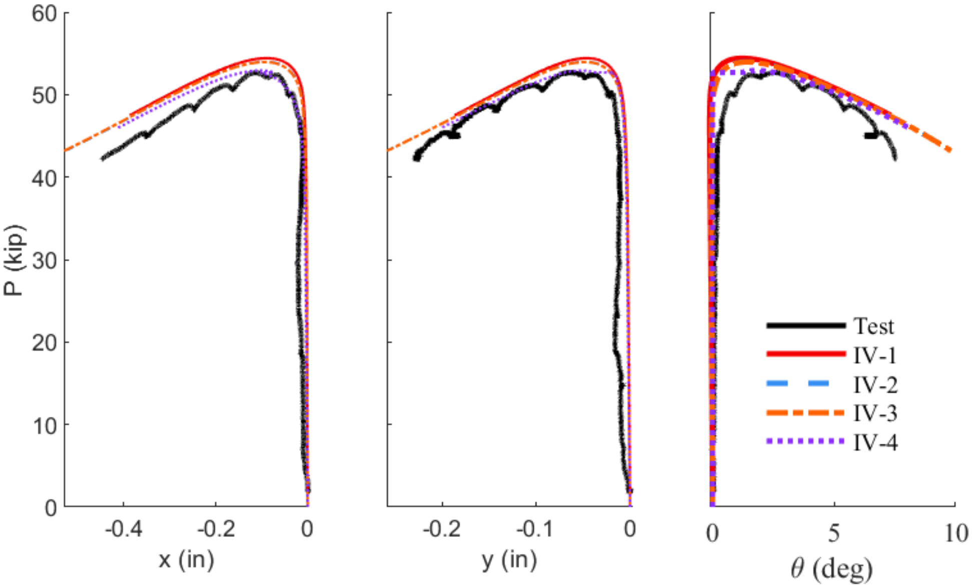

Figure B.16: Cross section displacement of S36-A1-2

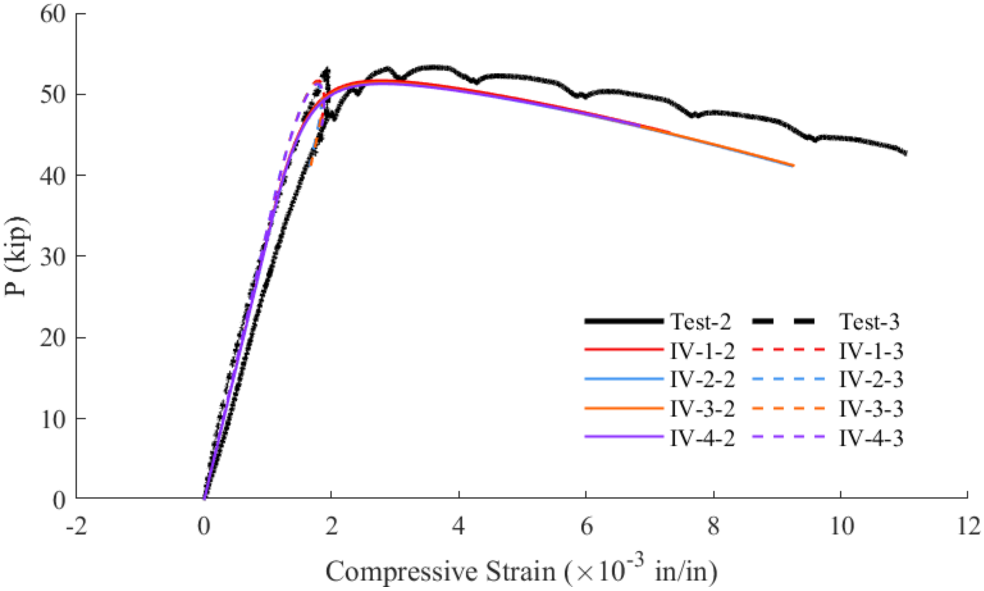

Figure B.17: Stress-strain response of S36-A2-1

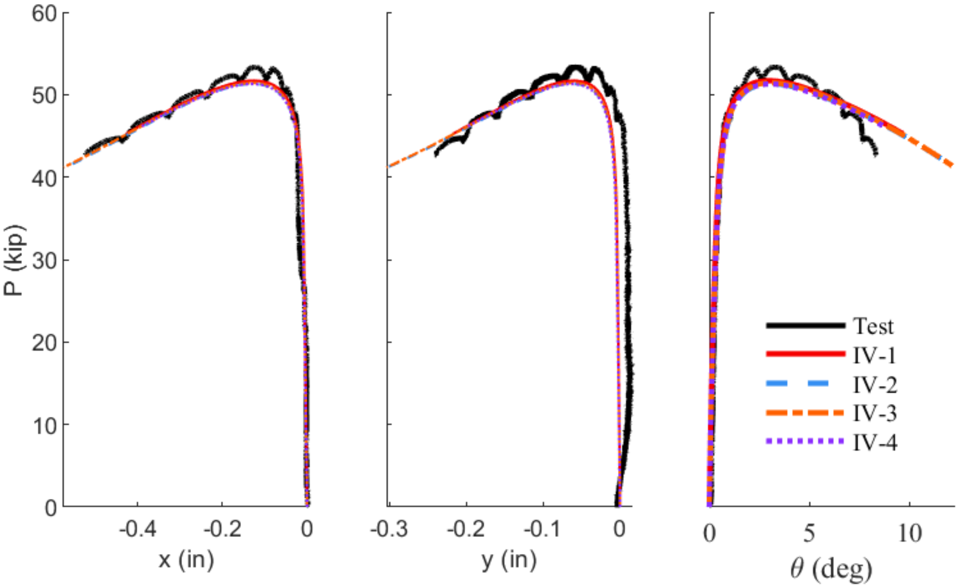

Figure B.18: Cross section displacement of S36-A2-1

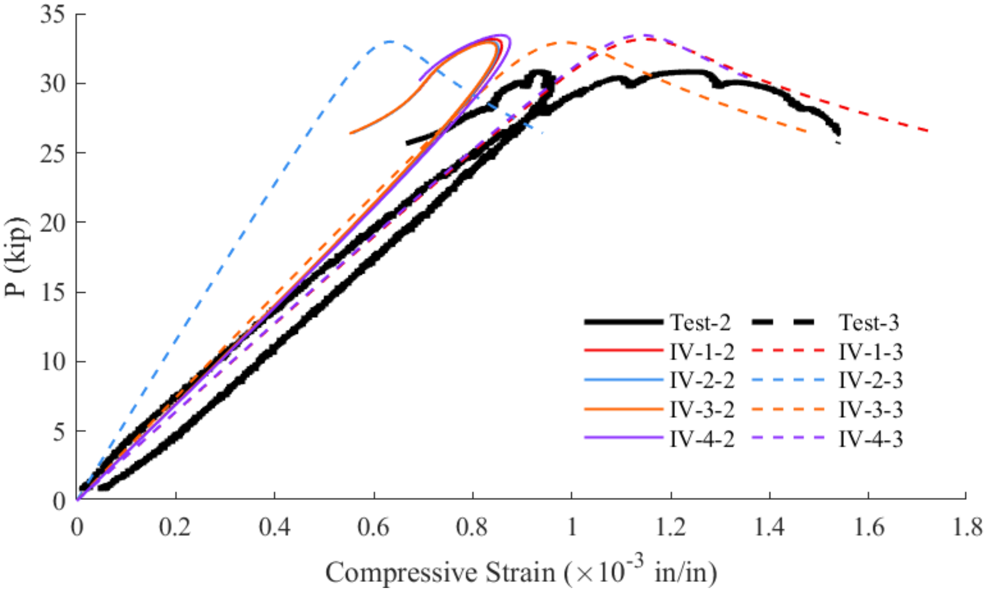

Figure B.19: Stress-strain response of S72-A5-1

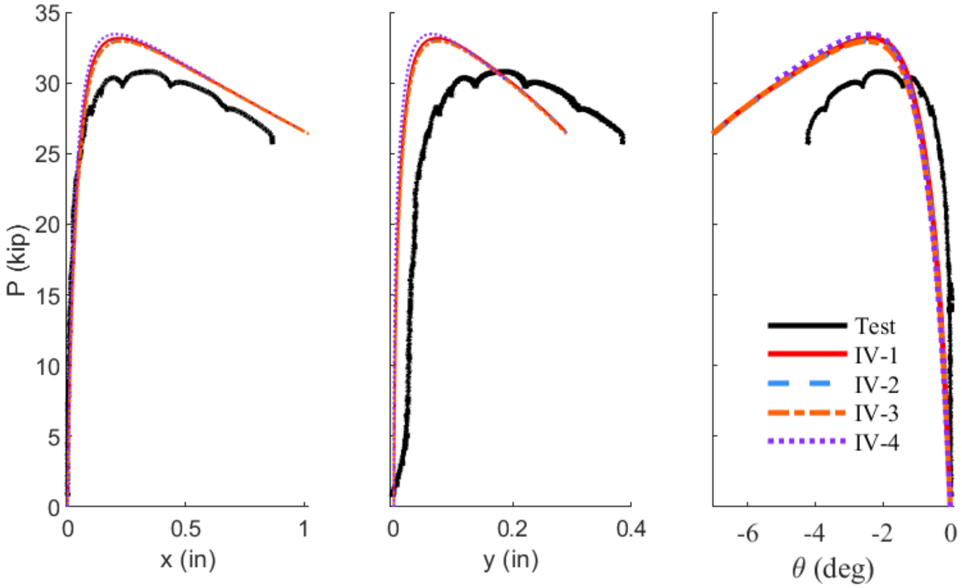

Figure B.20: Cross section displacement of S72-A5-1

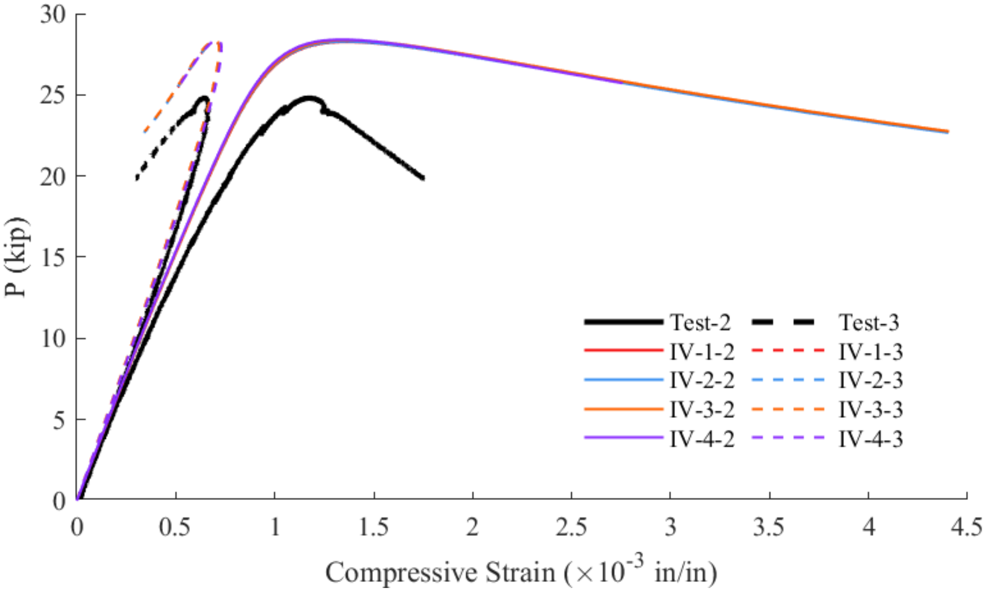

Figure B.21: Stress-strain response of S72-A5-2

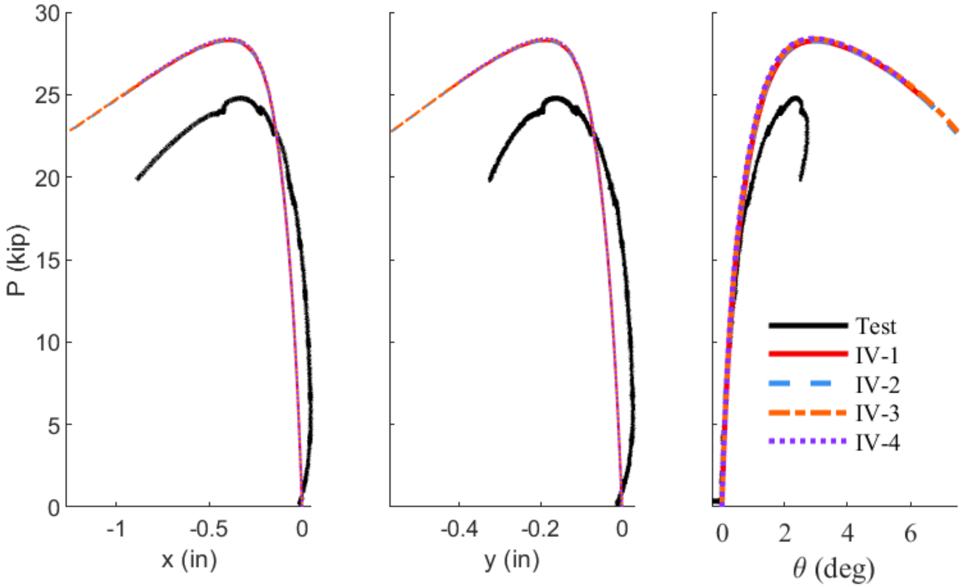

Figure B.22: Cross section displacement of S72-A5-2

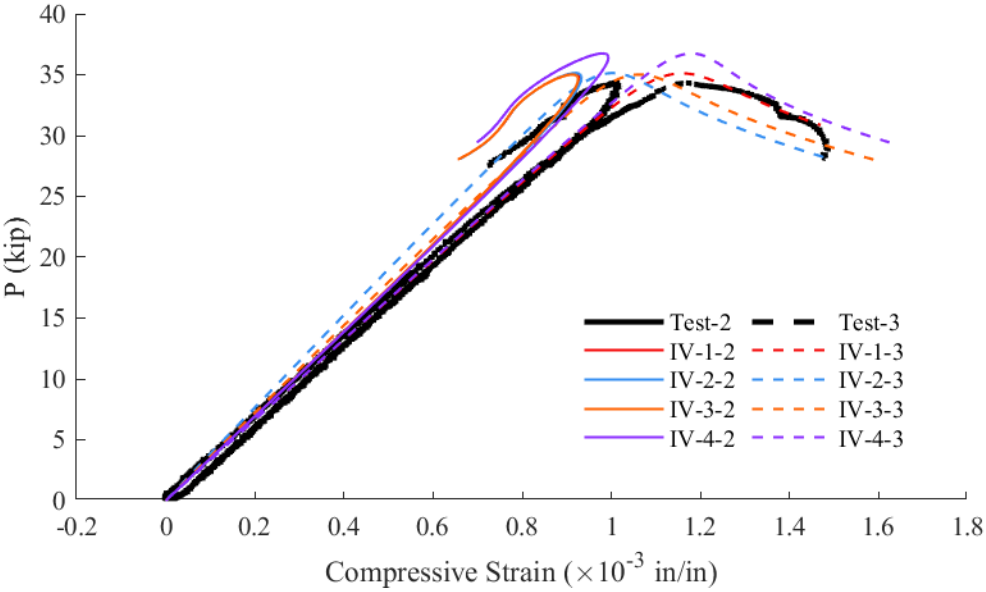

Figure B.23: Stress-strain response of S72-A6-1

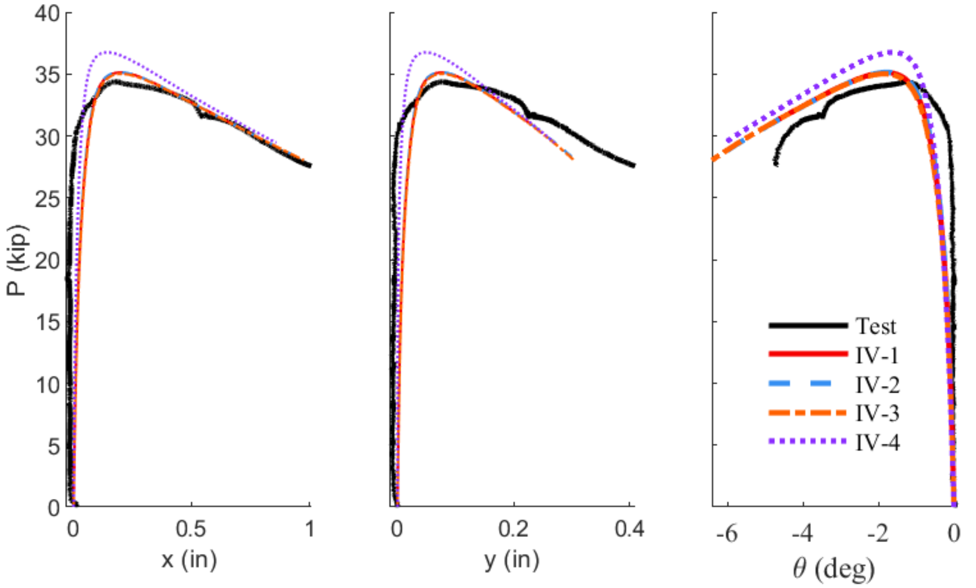

Figure B.24: Cross section displacement of S72-A6-1

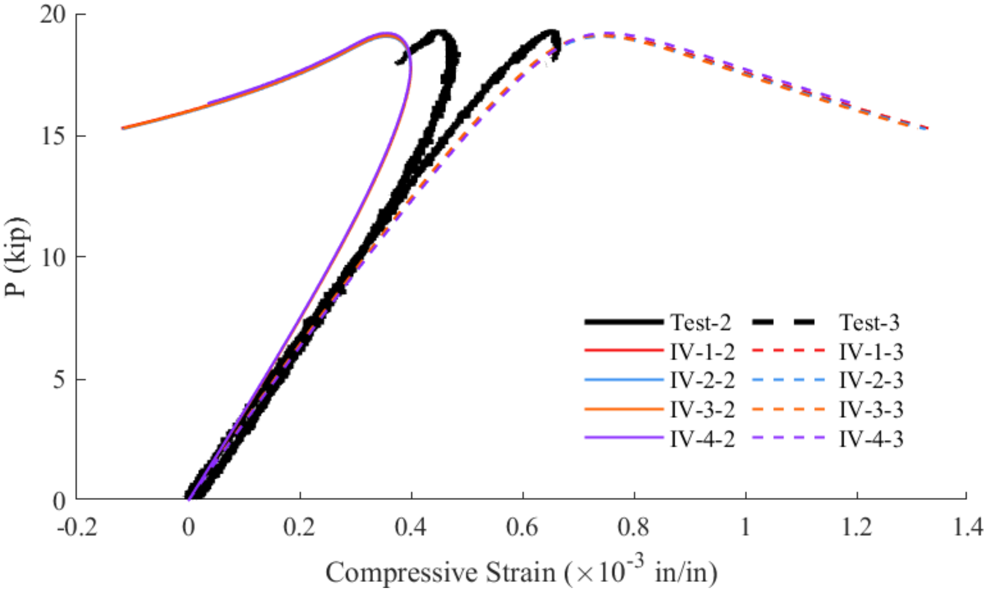

Figure B.25: Stress-strain response of S100-A3-1

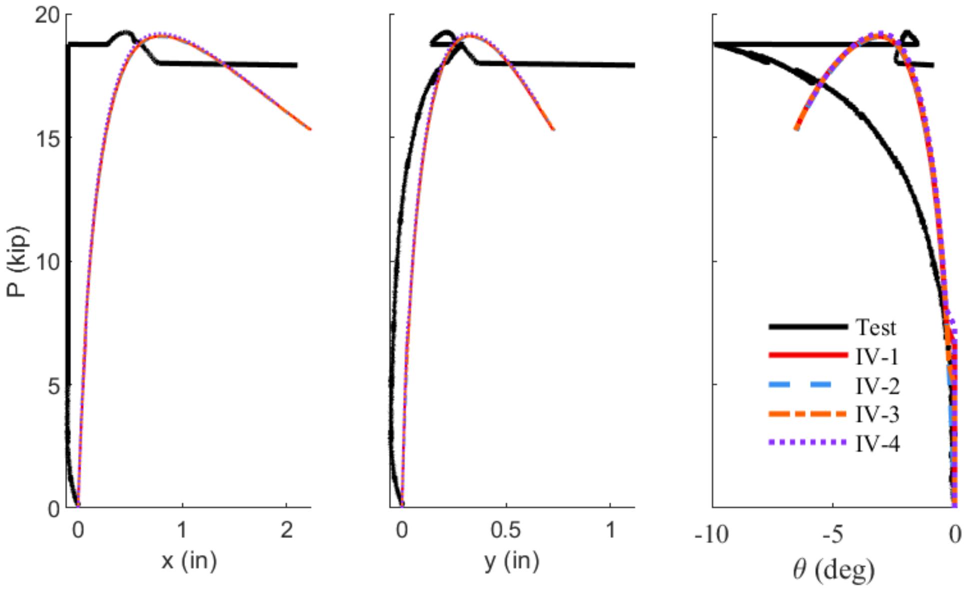

Figure B.26: Cross section displacement of S100-A3-1

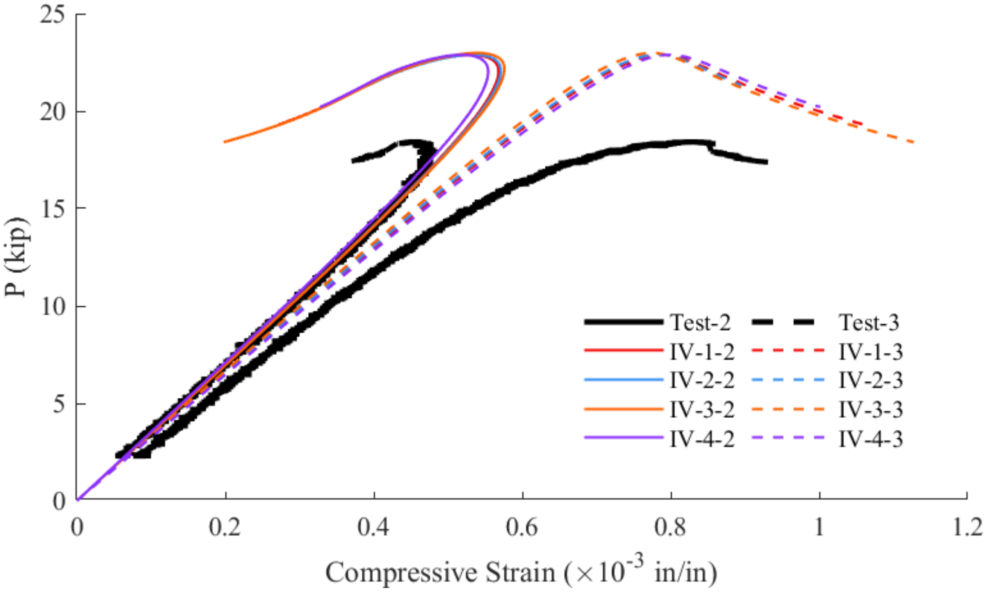

Figure B.27: Stress-strain response of S100-A4-1

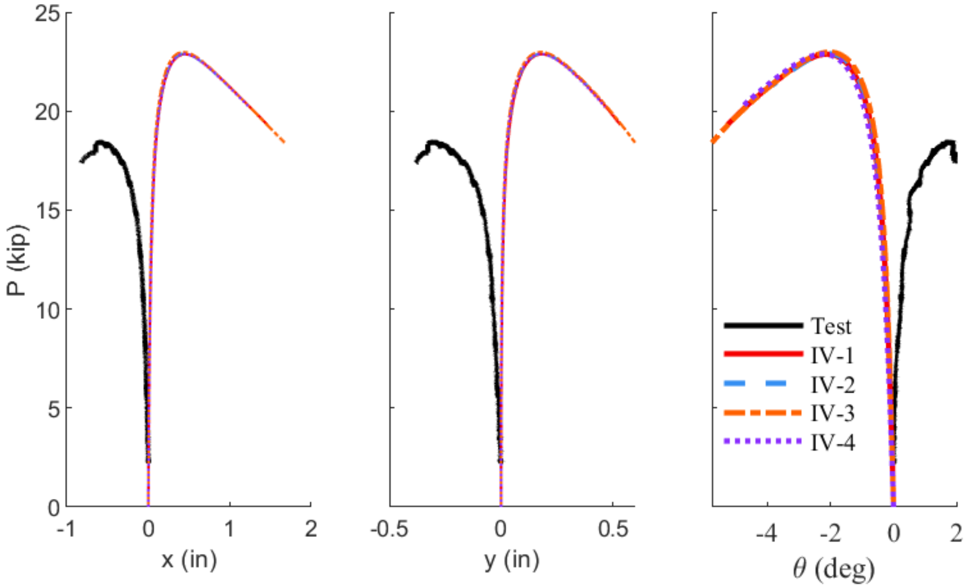

Figure B.28: Cross section displacement of S100-A4-1

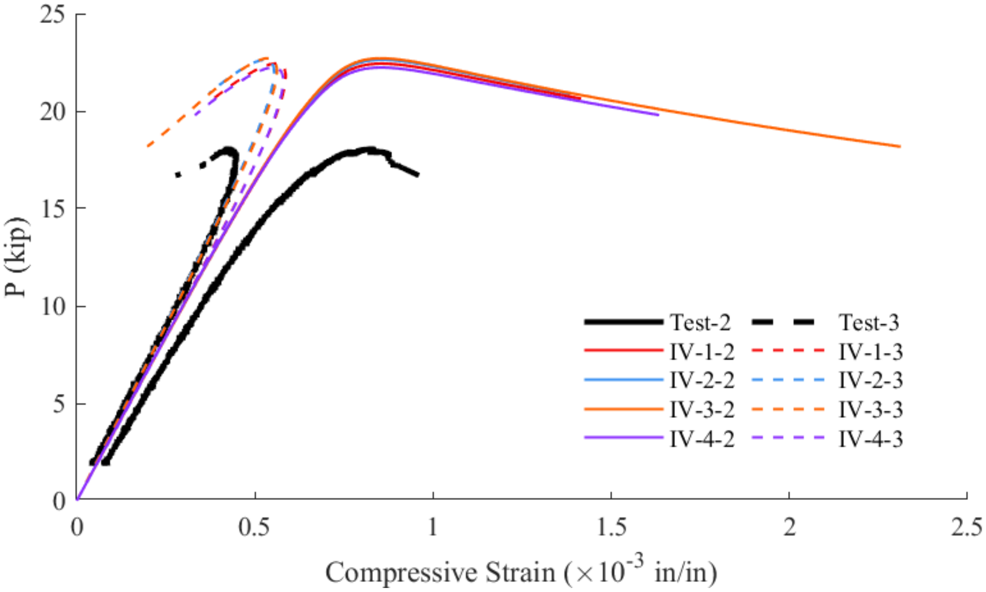

Figure B.29: Stress-strain response of S100-A4-2

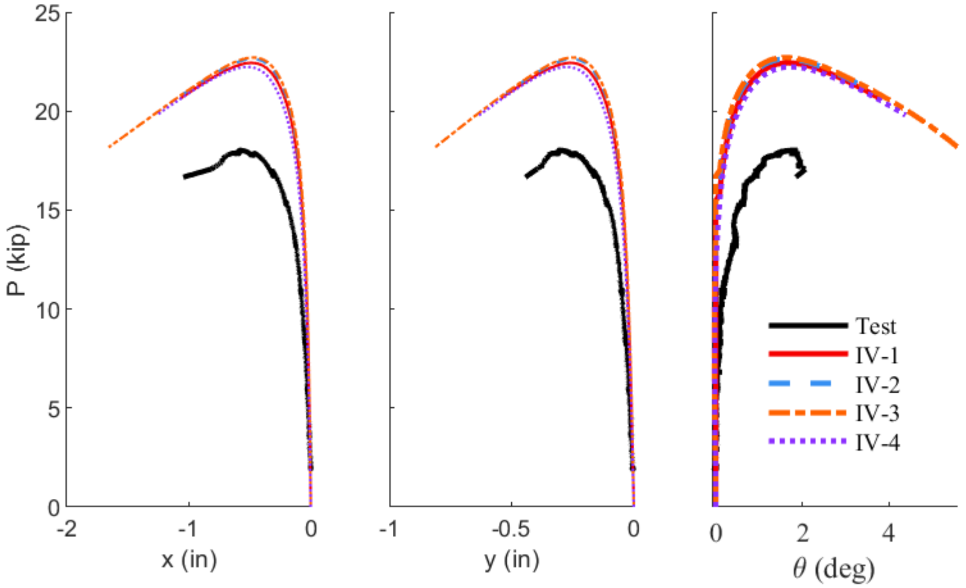

Figure B.30: Cross section displacement of S100-A4-2

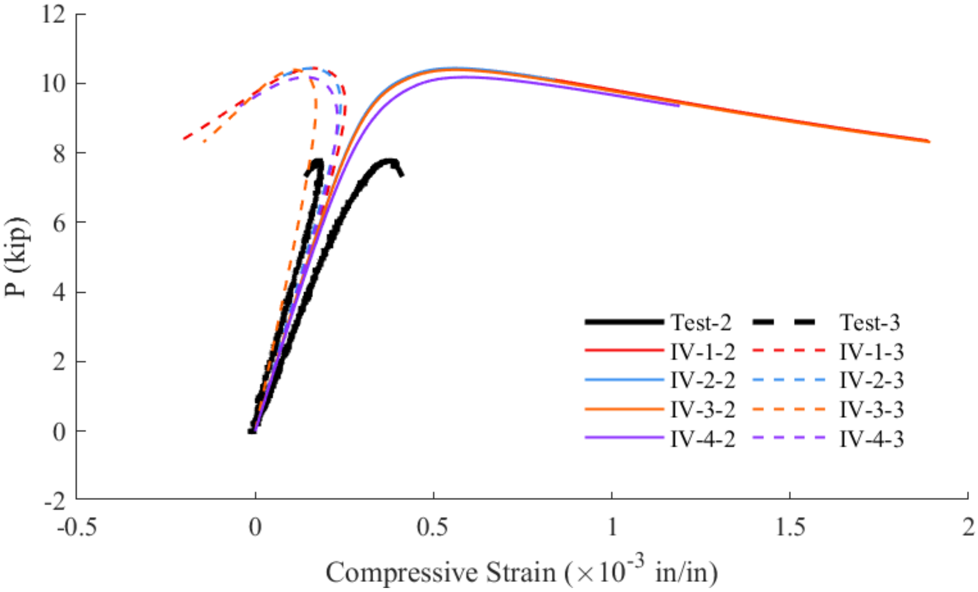

Figure B.31: Stress-strain response of S148-A1-1

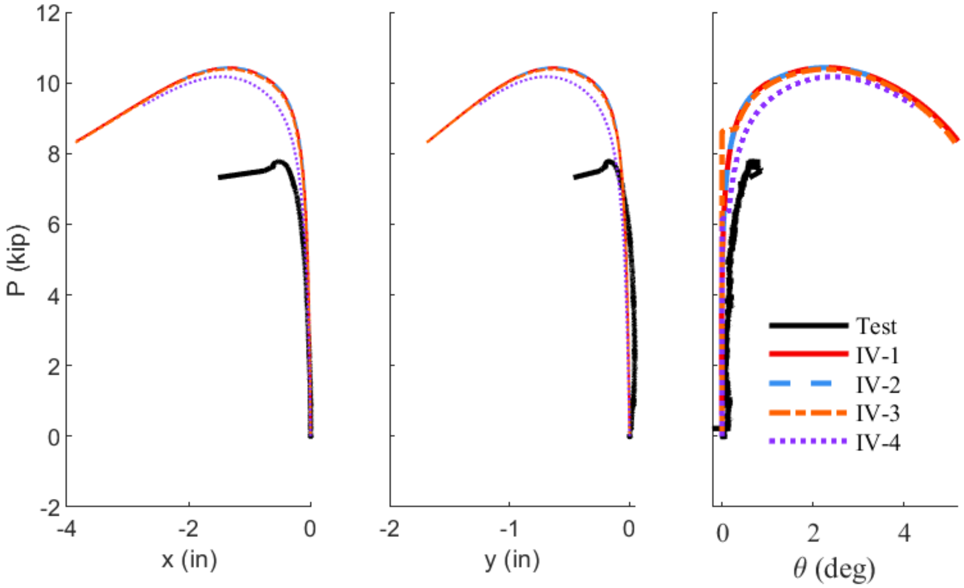

Figure B.32: Cross section displacement of S148-A1-1

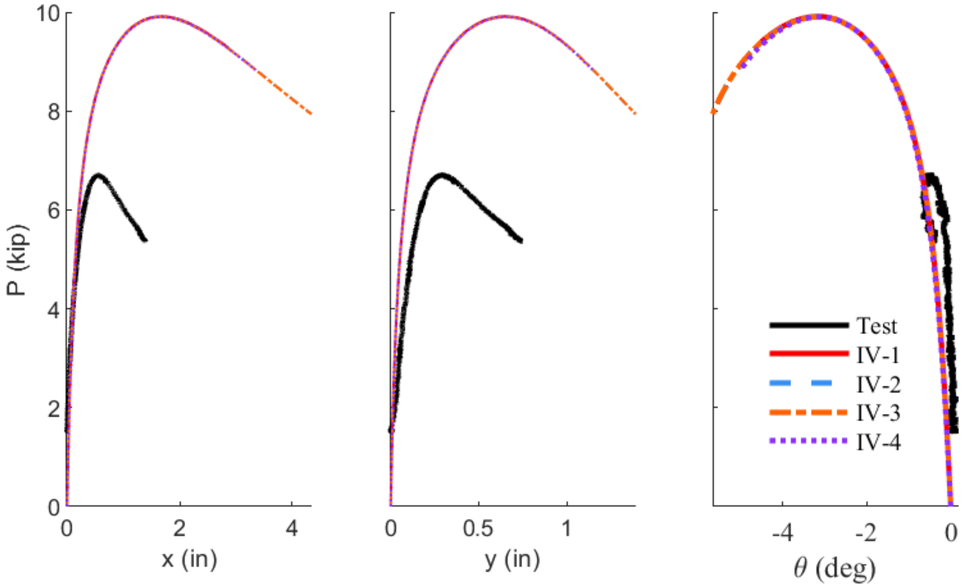

Figure B.33: Stress-strain response of S148-A2-1

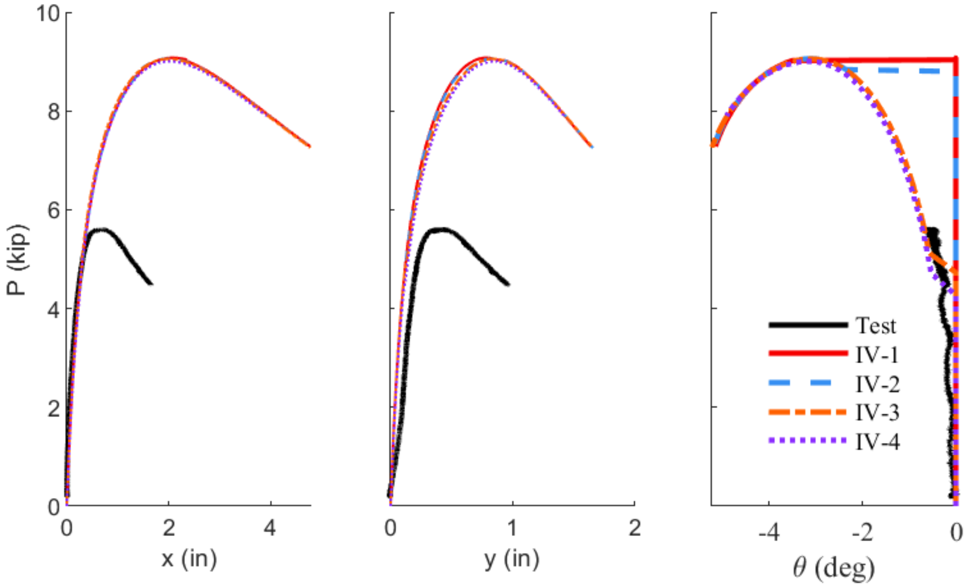

Figure B.34: Cross section displacement of S148-A2-1

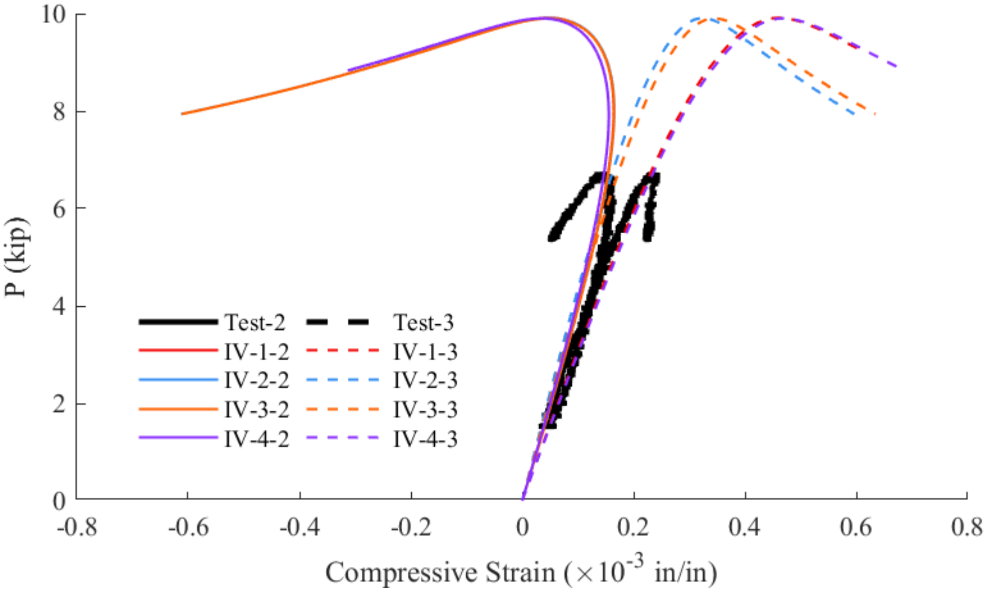

Figure B.35: Stress-strain response of S148-A3-1

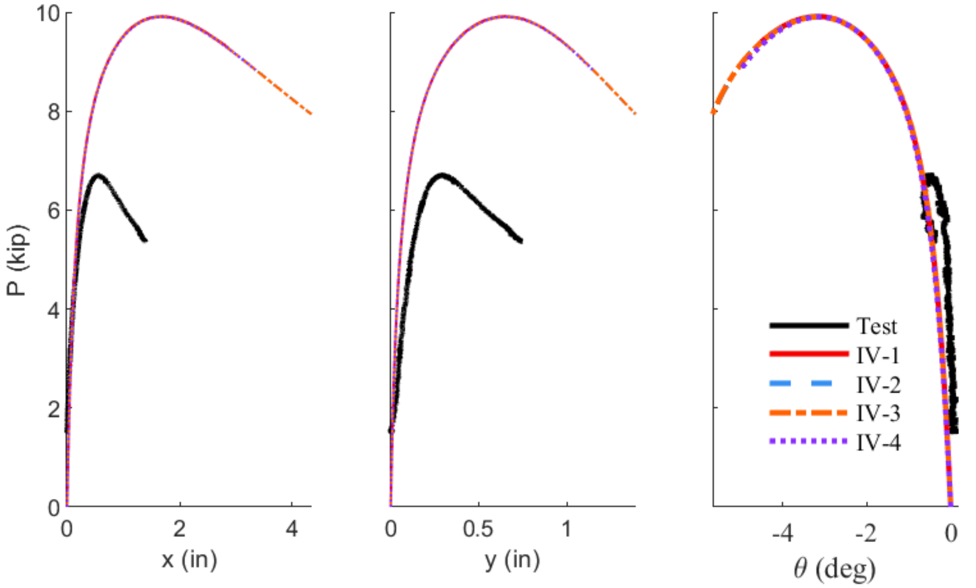

Figure B.36: Cross section displacement of S148-A3-1

C PARAMETRIC STUDY RESULTS

As described in Section 6.6, a parametric study of stainless steel unequal-leg angles subjected to concentric compression was completed. The following plots summarize the normalized buckling load versus the normalized slenderness ratio with the AISC 370 compression member design curves for reference. Separate plots are provided for the nominal and measured material properties.

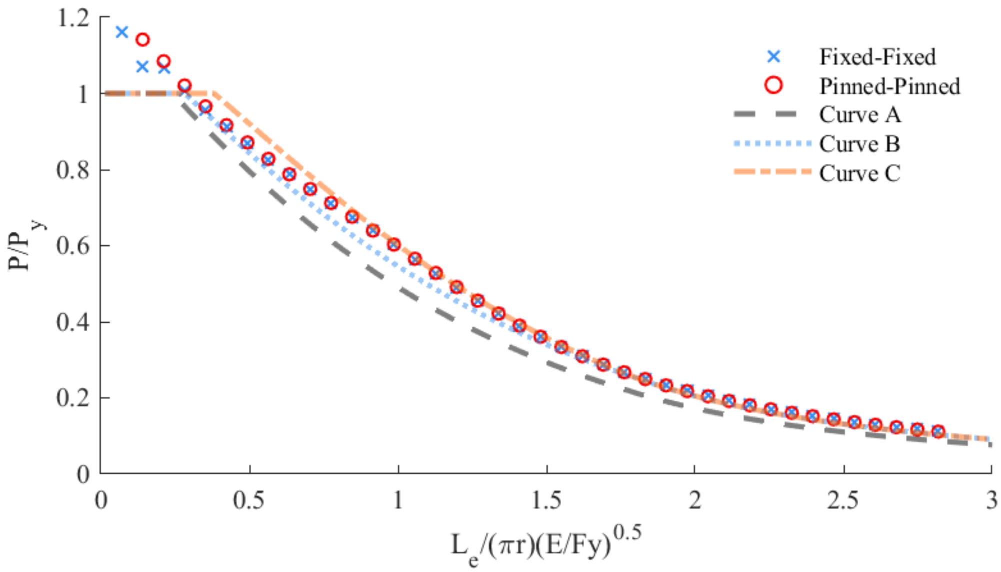

Figure C.1: Buckling behavior of L6"x5"x1/2" with measured material properties

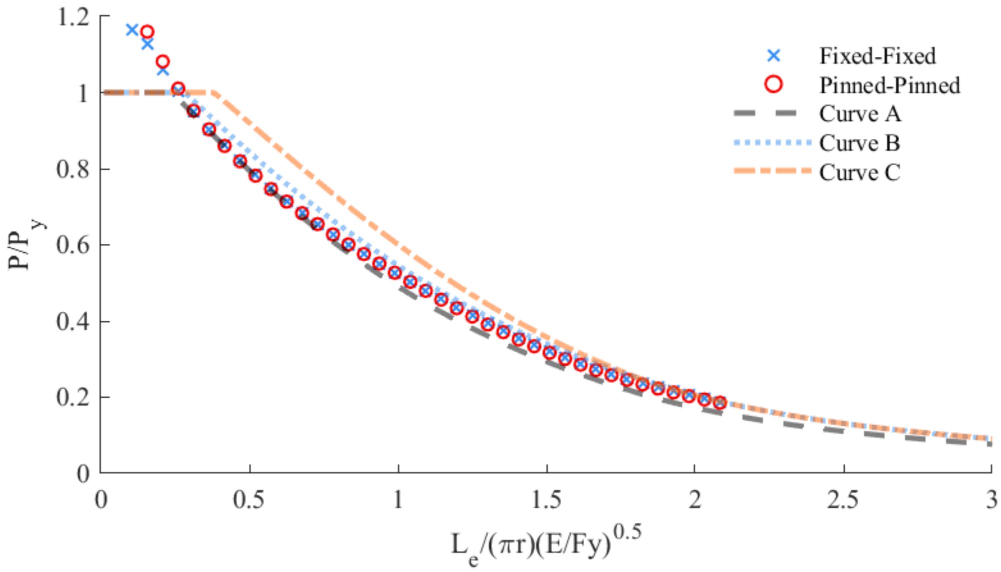

Figure C.2: Buckling behavior of L6"x5"x1/2" with nominal 304 material properties

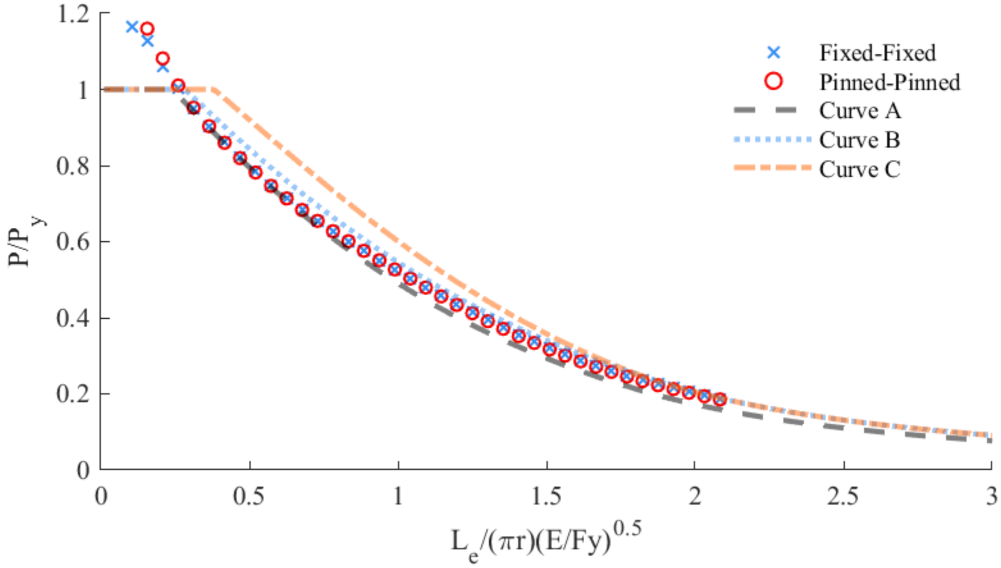

Figure C.3: Buckling behavior of L6"x5"x1/2" with nominal 304L material properties

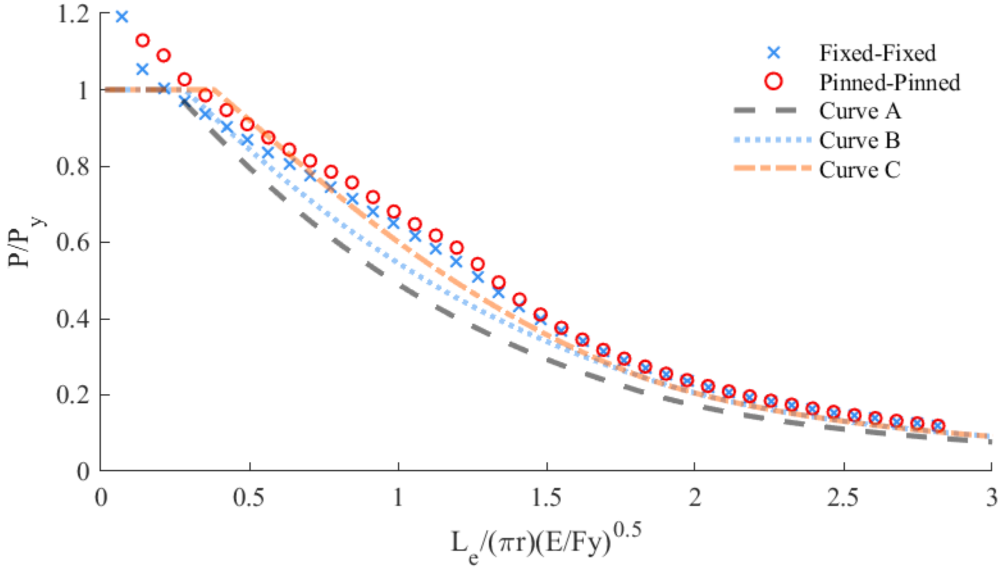

Figure C.4: Buckling behavior of L6"x4"x1/2" with measured material properties

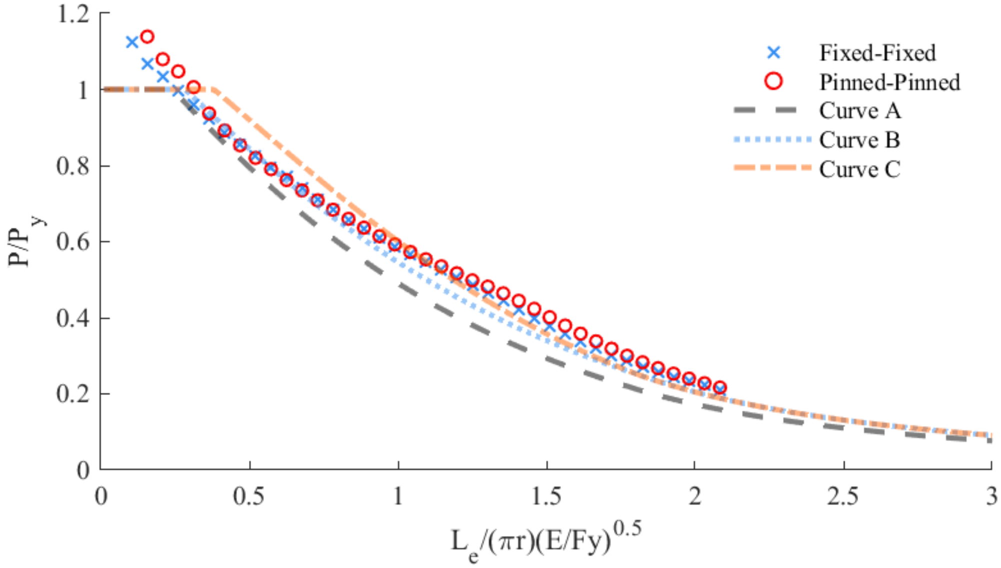

Figure C.5: Buckling behavior of L6"x4"x1/2" with nominal 304 material properties

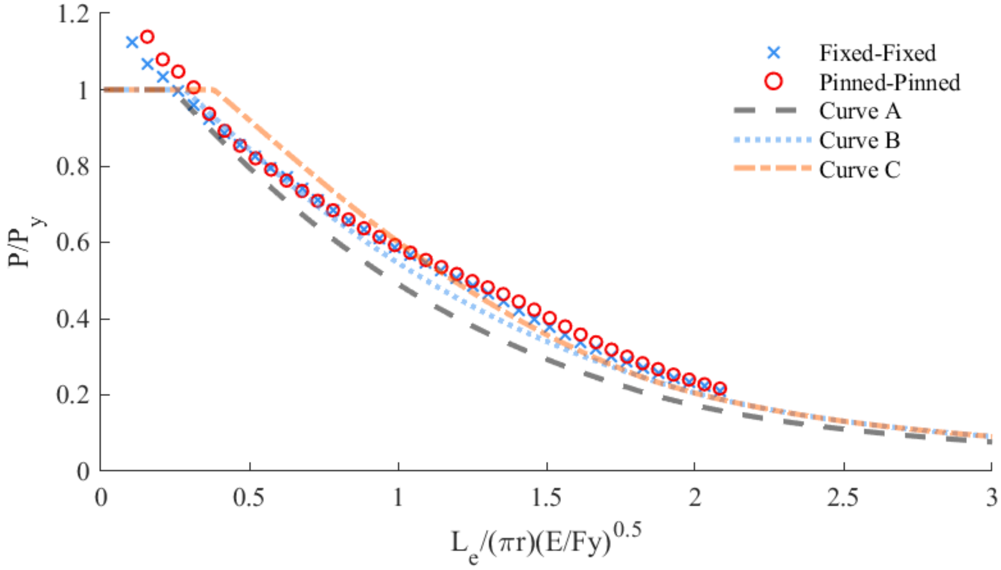

Figure C.6: Buckling behavior of L6"x4"x1/2" with nominal 304L material properties

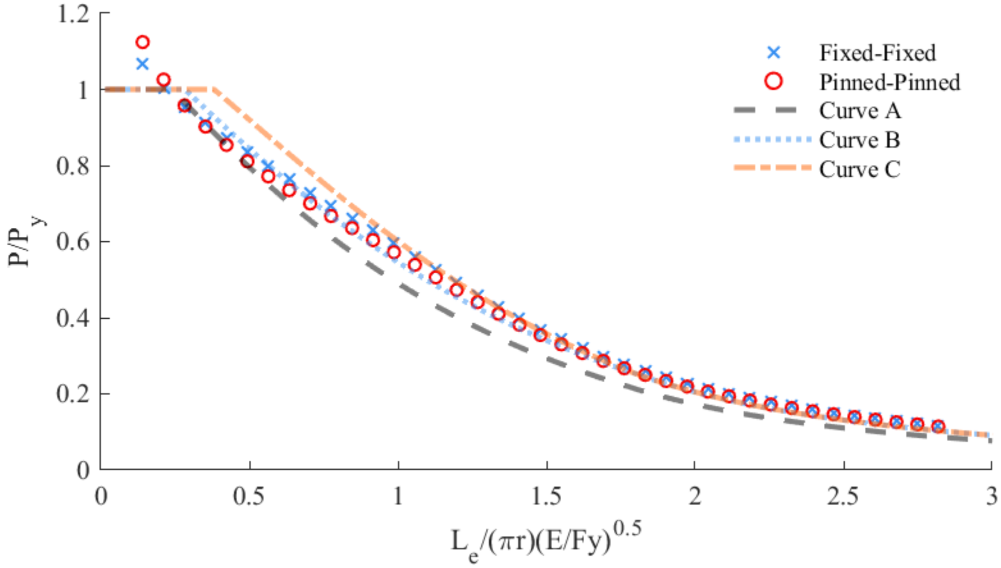

Figure C.7: Buckling behavior of L6"x3"x1/2" with measured material properties

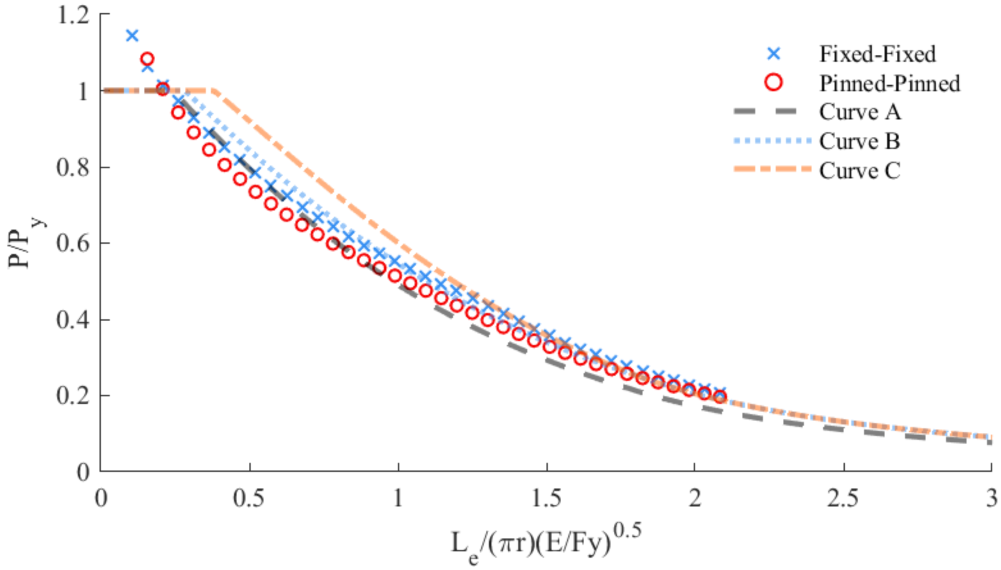

Figure C.8: Buckling behavior of L6"x3"x1/2" with nominal 304 material properties

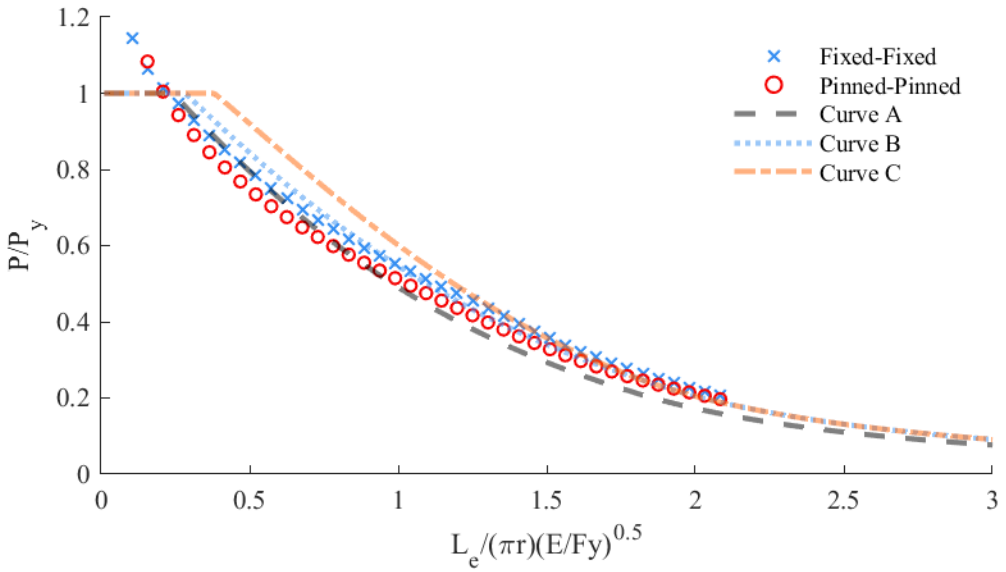

Figure C.9: Buckling behavior of L6"x3"x1/2" with nominal 304L material properties

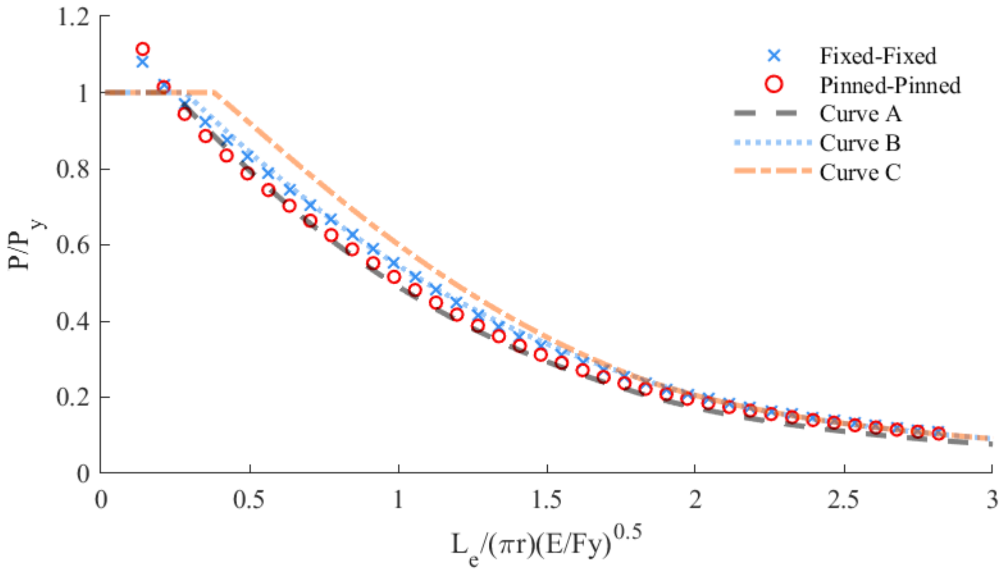

Figure C.10: Buckling behavior of L5"x3"x1/2" with measured material properties

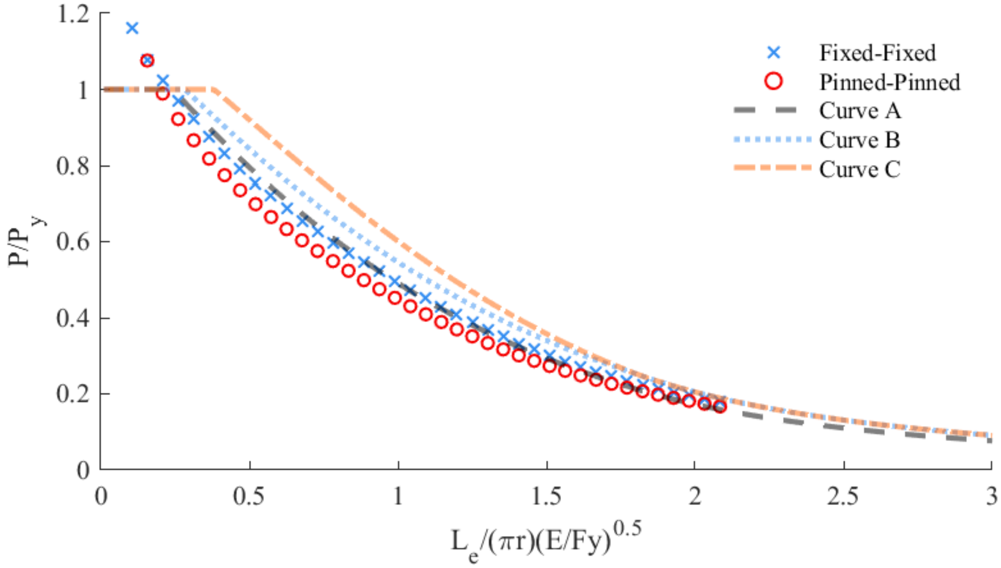

Figure C.11: Buckling behavior of L5"x3"x1/2" with nominal 304 material properties

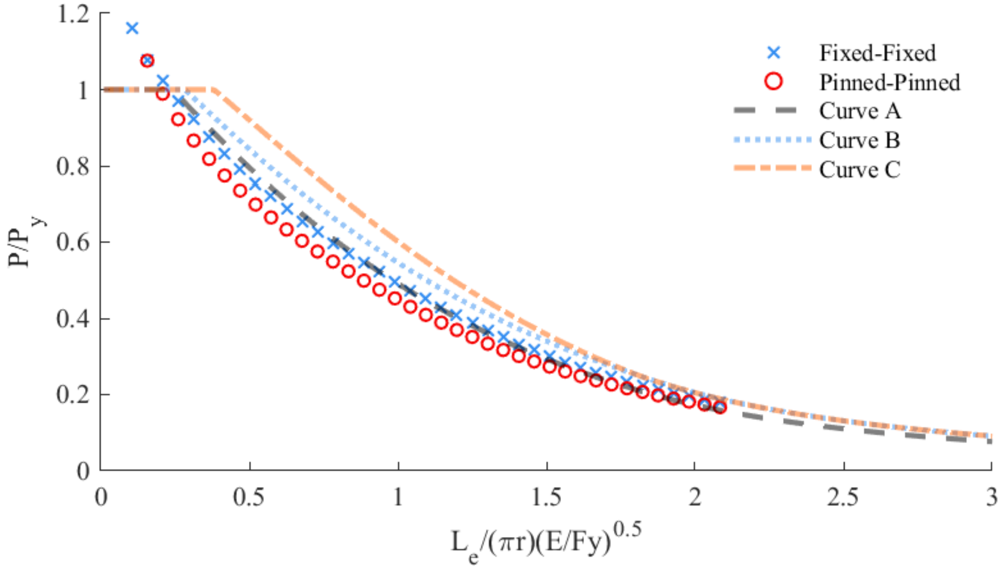

Figure C.12: Buckling behavior of L5"x3"x1/2" with nominal 304L material properties

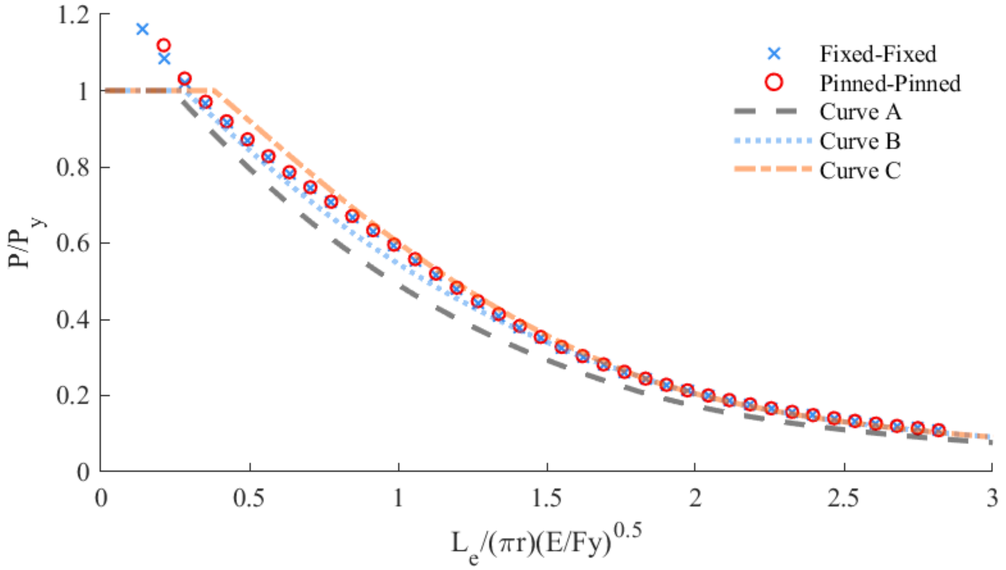

Figure C.13: Buckling behavior of L4"x3"x1/2" with measured material properties

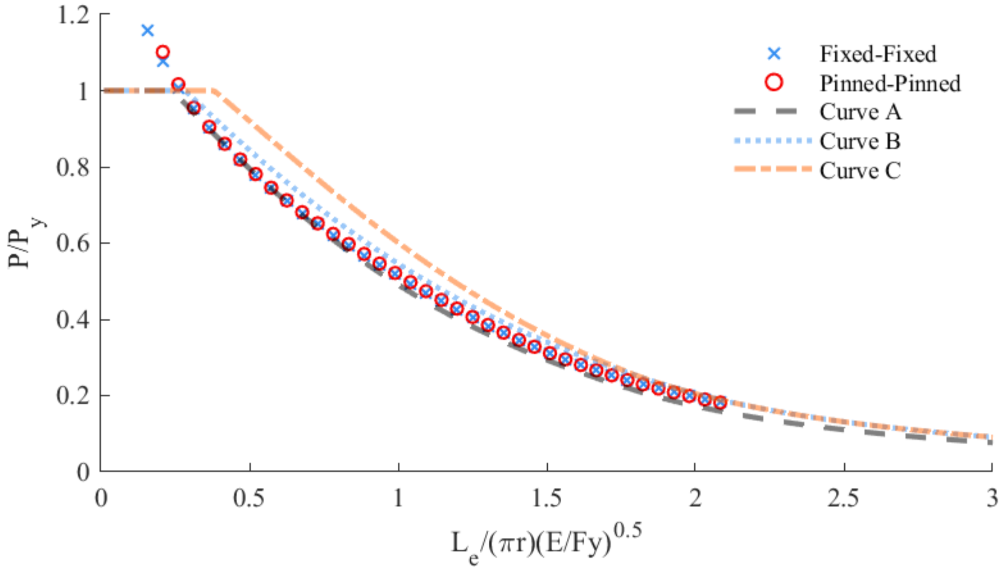

Figure C.14: Buckling behavior of L4"x3"x1/2" with nominal 304 material properties

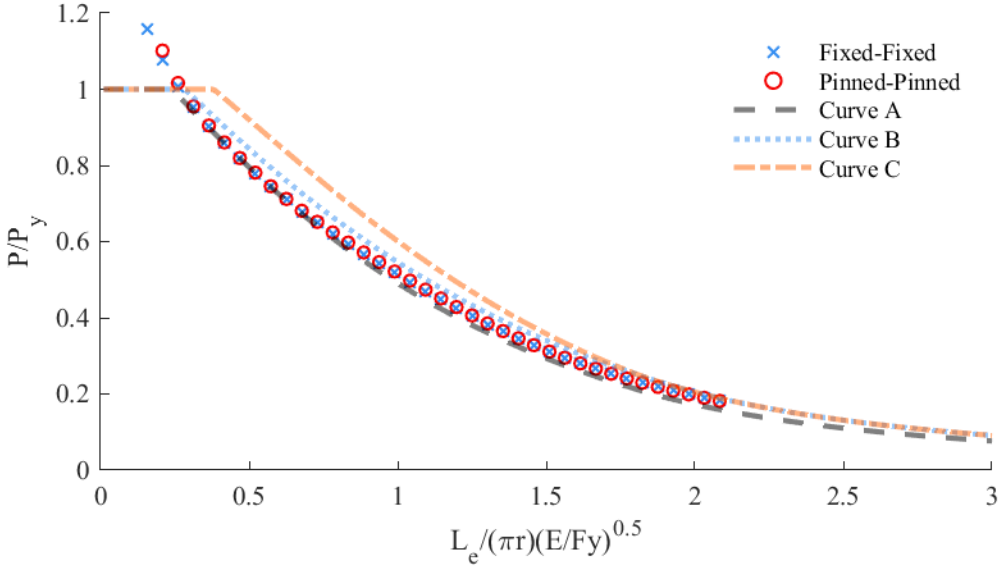

Figure C.15: Buckling behavior of L4"x3"x1/2" with nominal 304L material properties

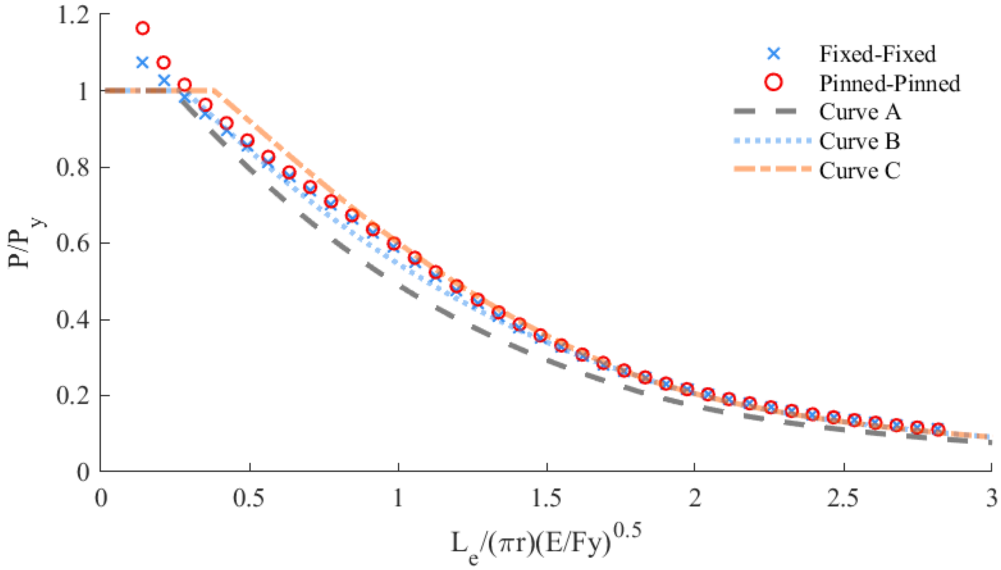

Figure C.16: Buckling behavior of L4"x3"x3/8" with measured material properties

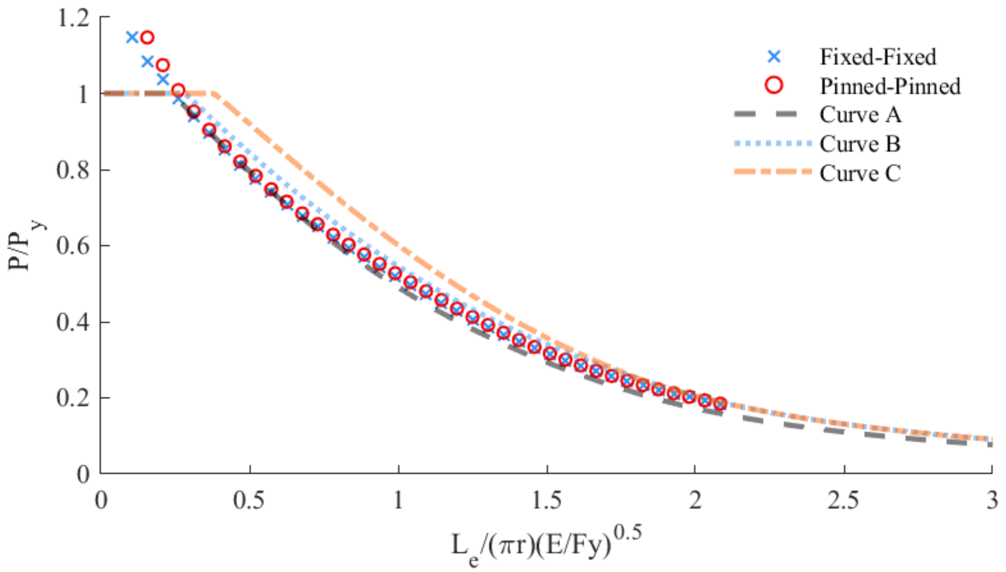

Figure C.17: Buckling behavior of L4"x3"x3/8" with nominal 304 material properties

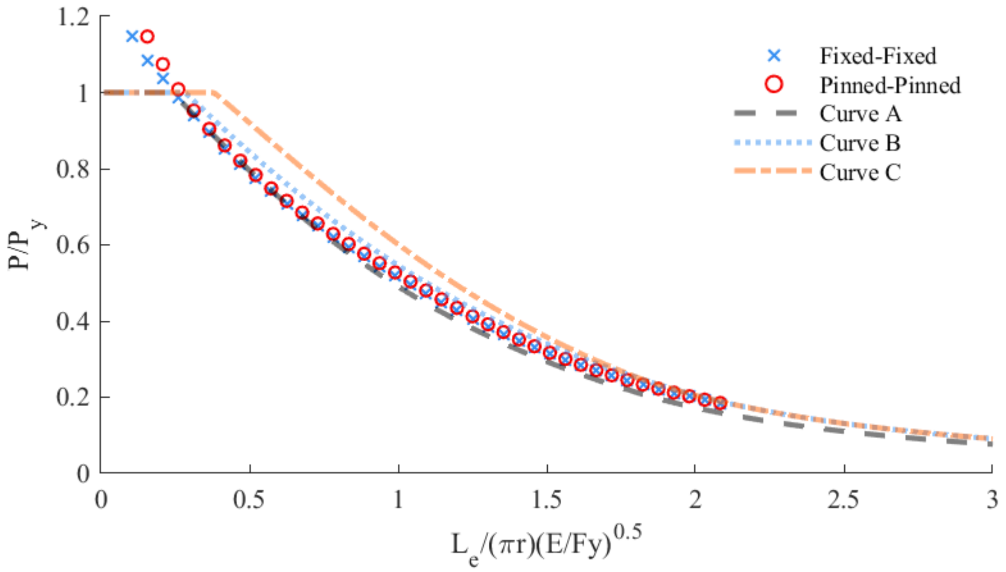

Figure C.18: Buckling behavior of L4"x3"x3/8" with nominal 304L material properties

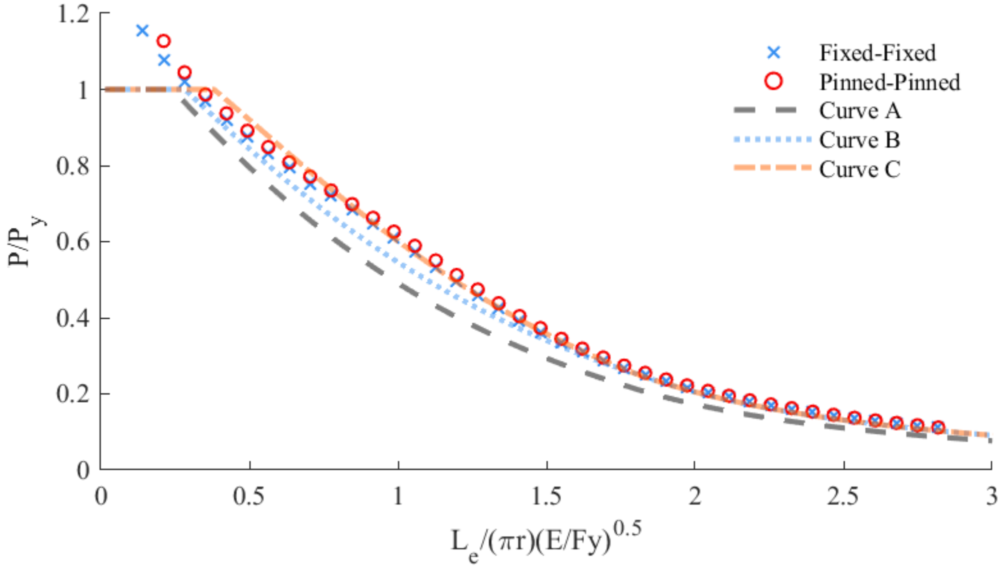

Figure C.19: Buckling behavior of L3"x2"x3/8" with measured material properties

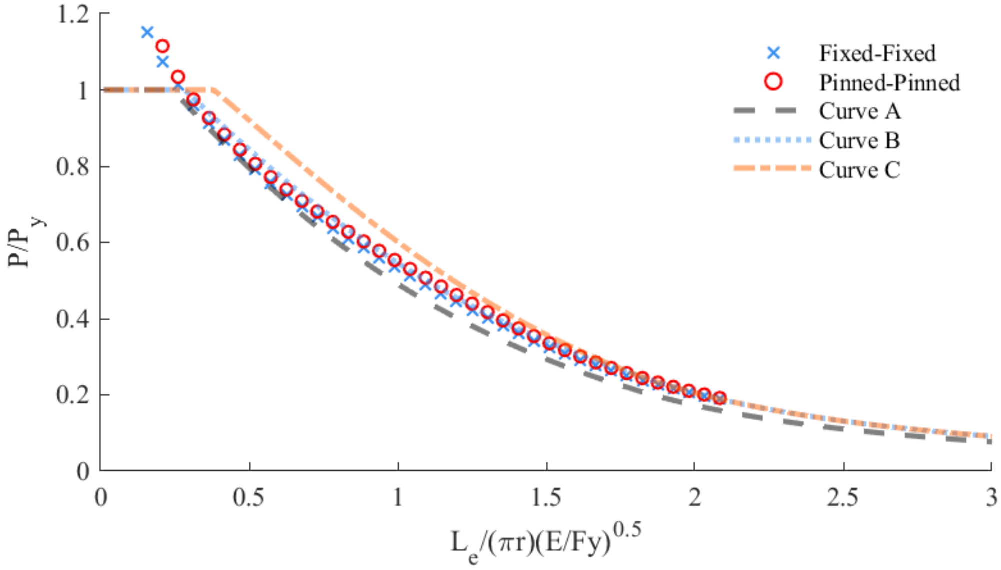

Figure C.20: Buckling behavior of L3"x2"x3/8" with nominal 304 material properties

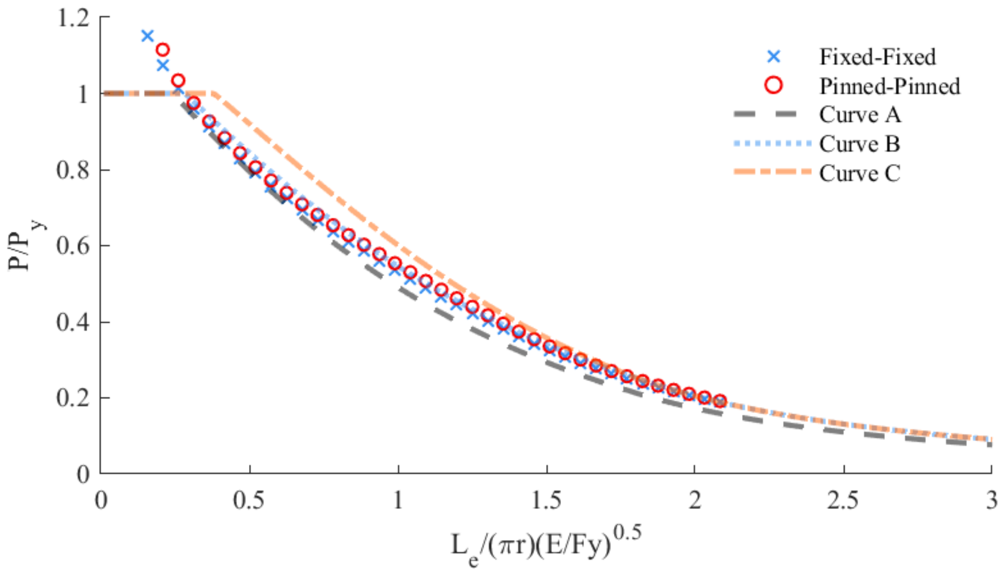

Figure C.21: Buckling behavior of L3"x2"x3/8" with nominal 304L material properties

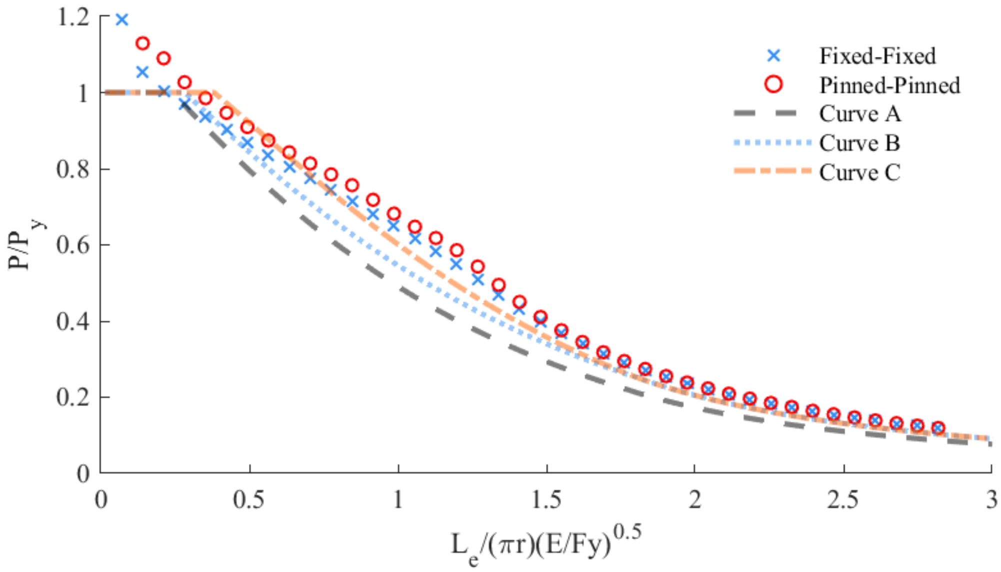

Figure C.22: Buckling behavior of L3"x2"x1/4" with measured material properties

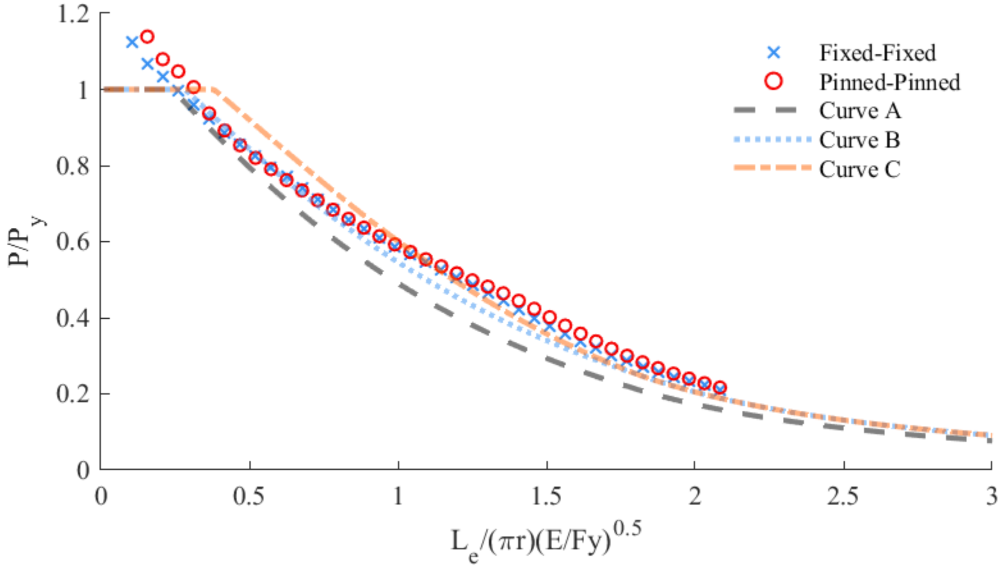

Figure C.23: Buckling behavior of L3"x2"x1/4" with nominal 304 material properties

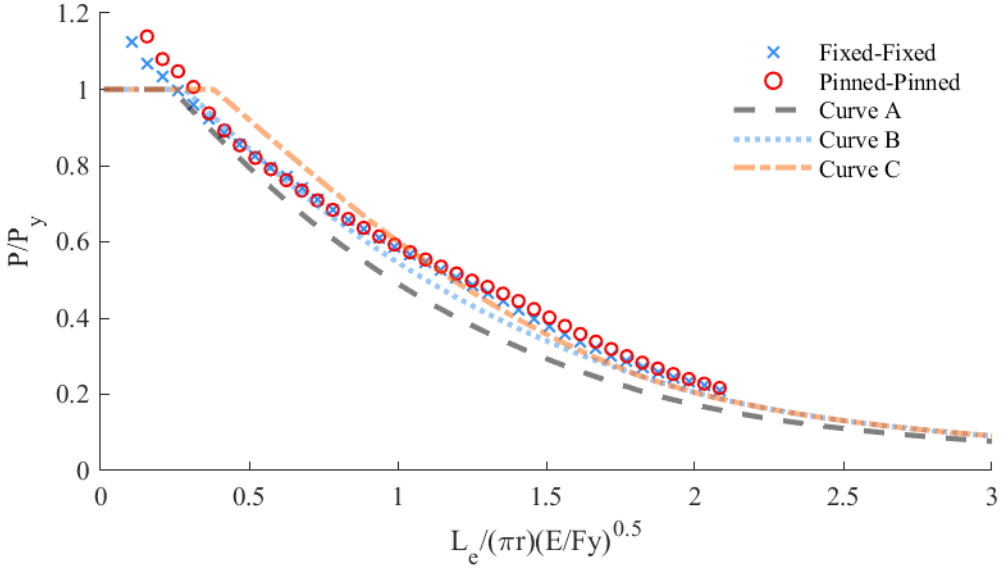

Figure C.24: Buckling behavior of L3"x2"x1/4" with nominal 304L material properties

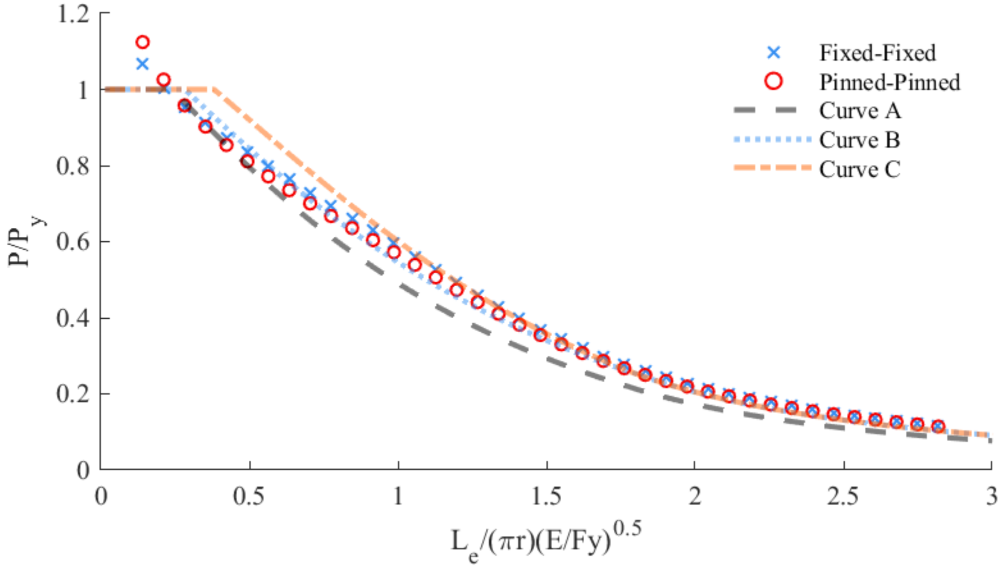

Figure C.25: Buckling behavior of L3"x1.5"x1/4" with measured material properties

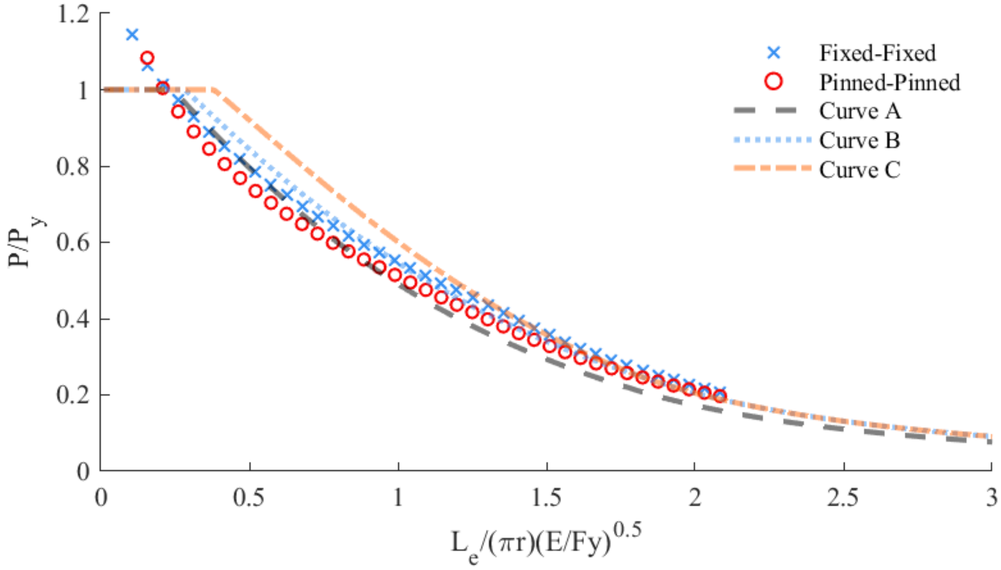

Figure C.26: Buckling behavior of L3"x1.5"x1/4" with nominal 304 material properties

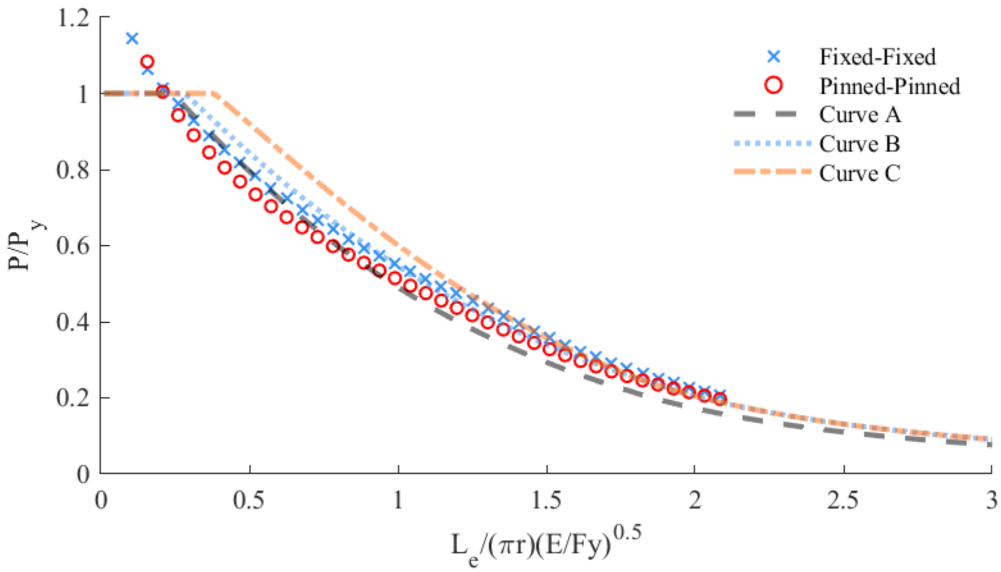

Figure C.27: Buckling behavior of L3"x1.5"x1/4" with nominal 304L material properties

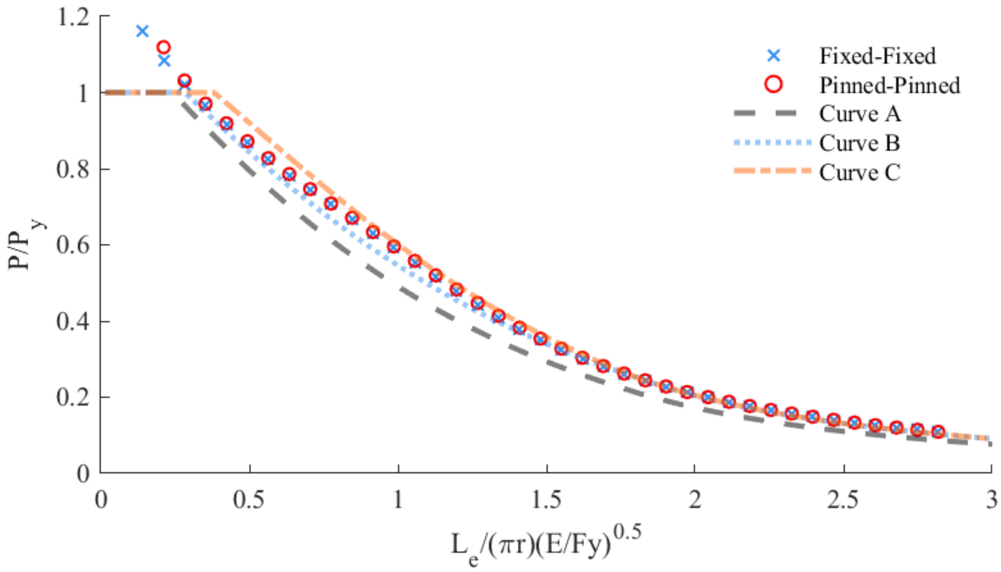

Figure C.28: Buckling behavior of L2"x1.5"x1/4" with measured material properties

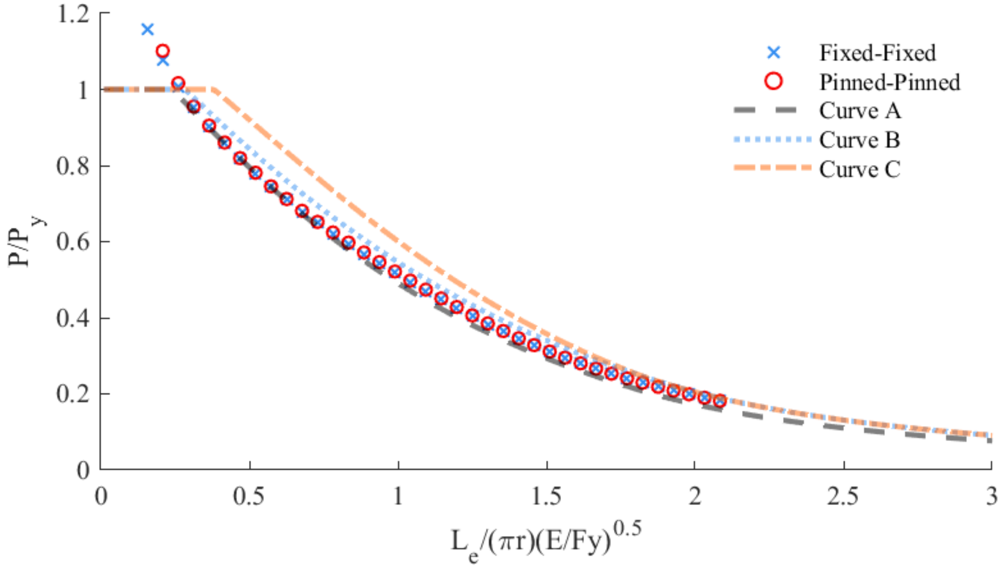

Figure C.29: Buckling behavior of L2"x1.5"x1/4" with nominal 304 material properties

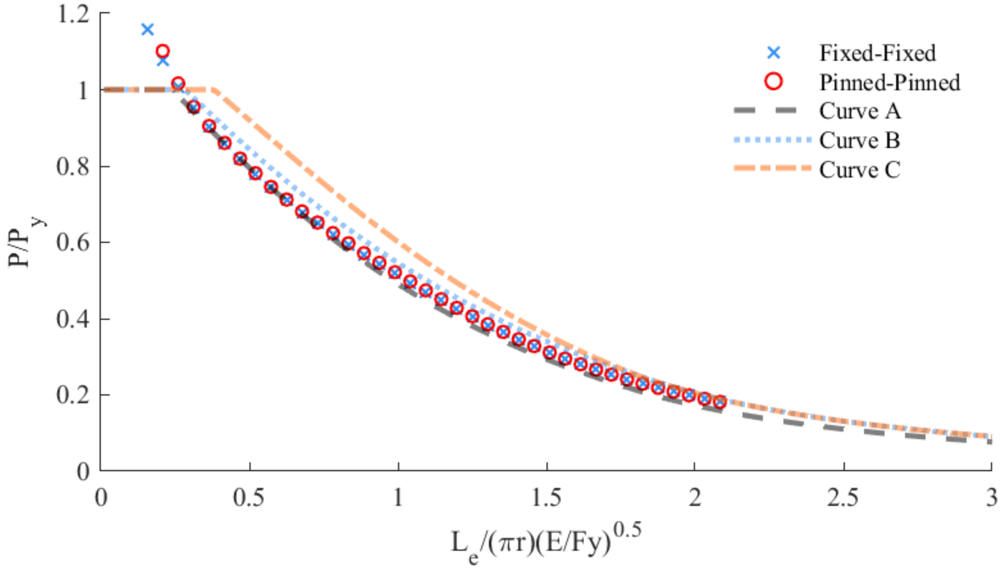

Figure C.30: Buckling behavior of L2"x1.5"x1/4" with nominal 304L material properties

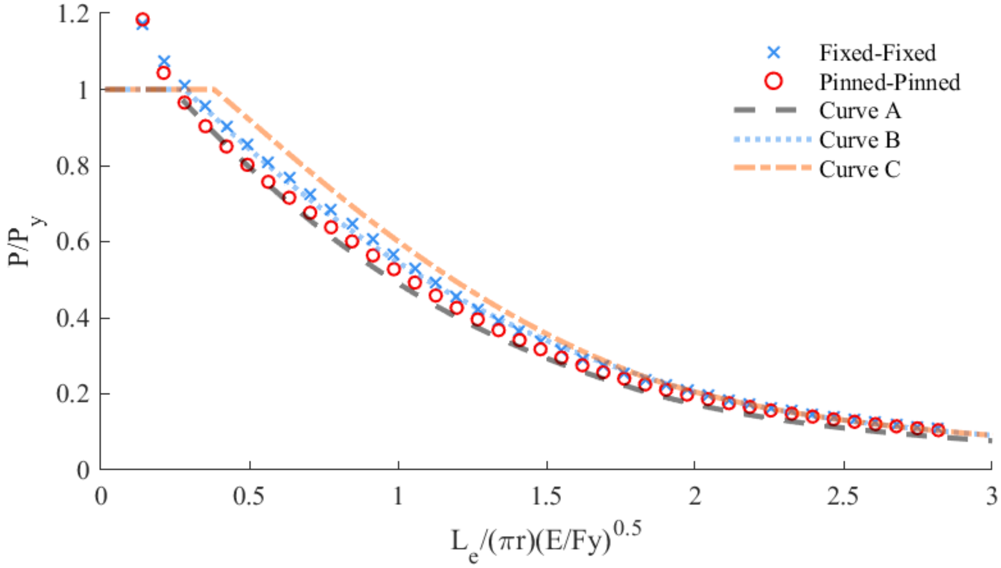

Figure C.31: Buckling behavior of L2"x1"x1/4" with measured material properties

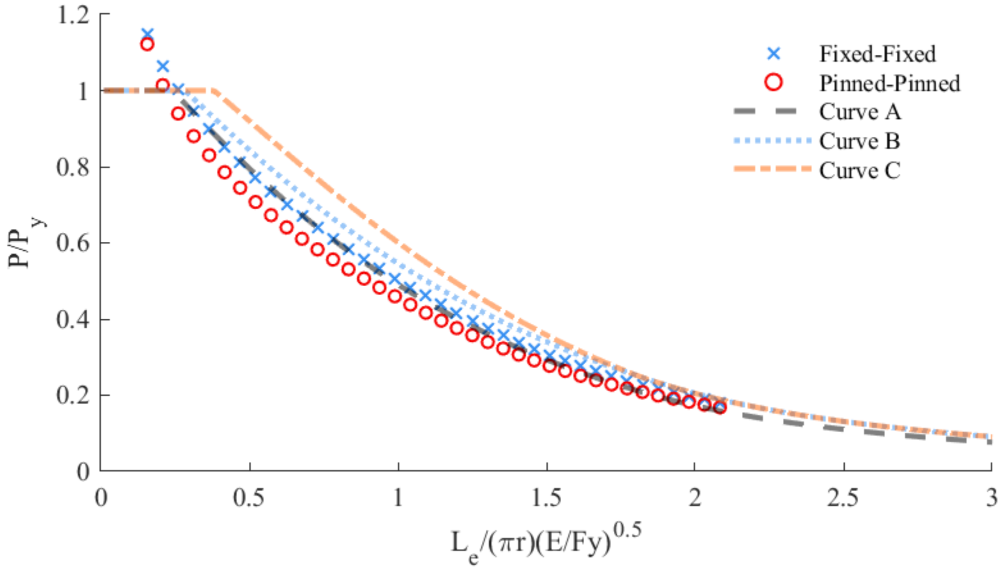

Figure C.32: Buckling behavior of L2"x1"x1/4" with nominal 304 material properties

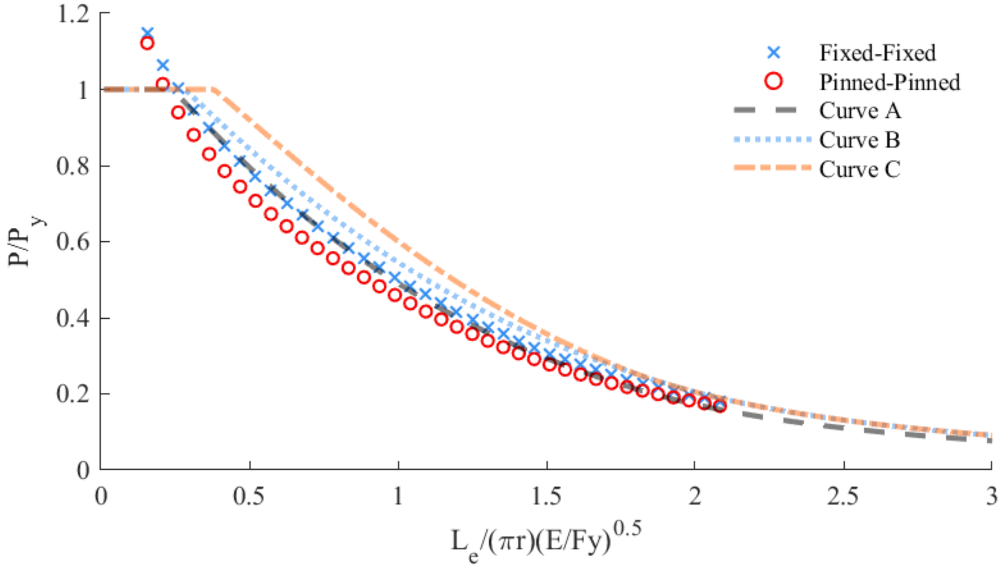

Figure C.33: Buckling behavior of L2"x1"x1/4" with nominal 304L material properties

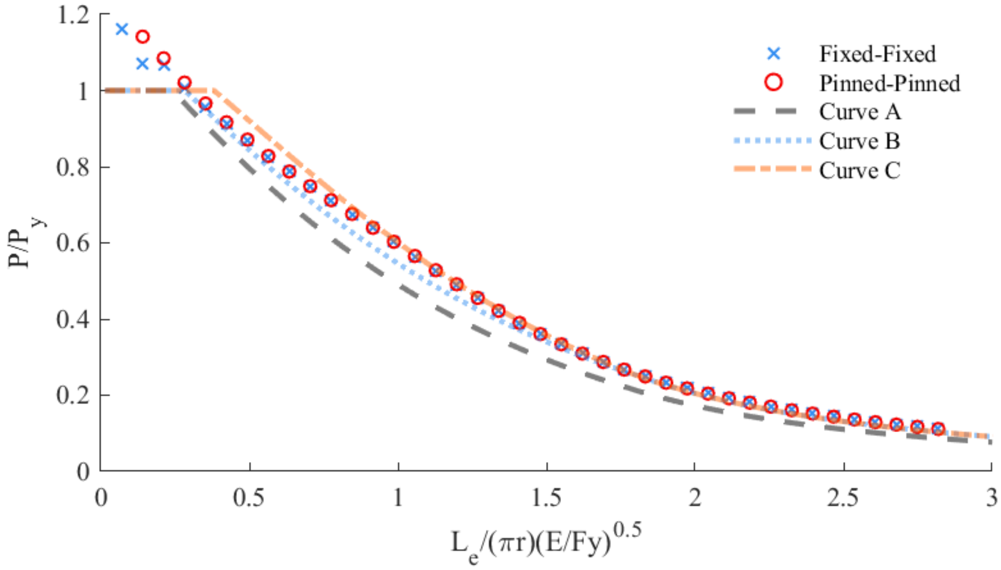

Figure C.34: Buckling behavior of L1.5"x1.25"x1/8" with measured material properties

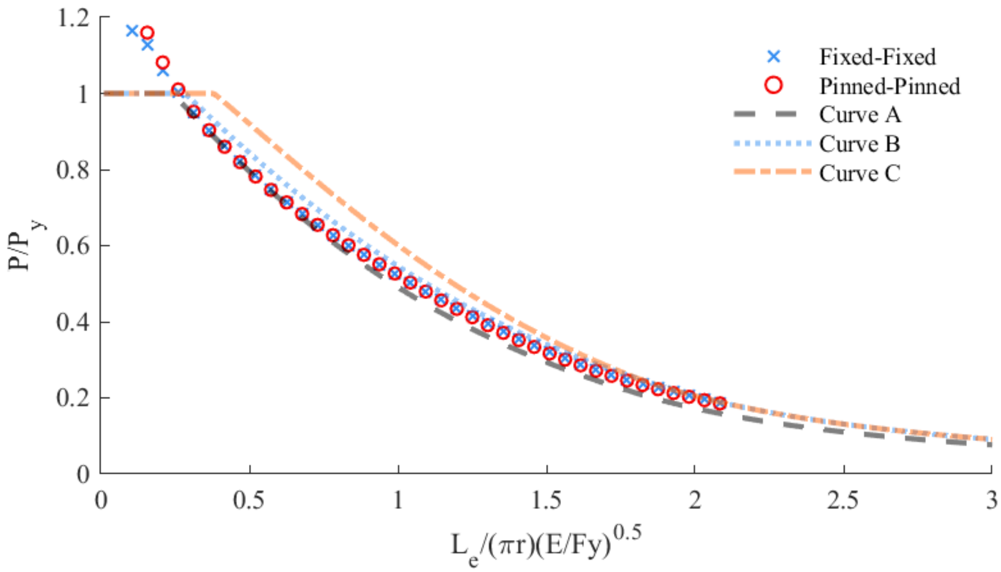

Figure C.35: Buckling behavior of L1.5"x1.25"x1/8" with nominal 304 material properties

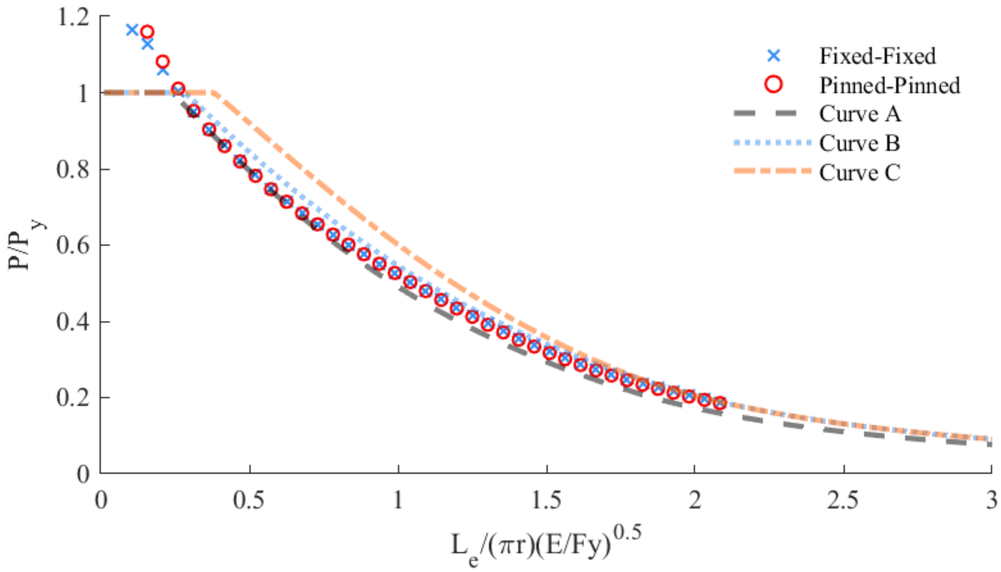

Figure C.36: Buckling behavior of L1.5"x1.25"x1/8" with nominal 304L material properties

D EDUCATIONAL STUDY ON VIRTUAL REALITY IN STEEL CLASSROOM

In addition to the main works of this dissertation, various educational experiences for the structural steel engineering classroom were developed in partnership with multiple individuals across the University of Wisconsin-Madison. This included work with virtual reality to view a construction site and investigate building plans and augmented reality to understand steel tension connections. The following is a summary of one activity that culminated in an educational study related to the use of virtual reality for a field trip.

Edward J. Sippel, and Hannah B. Blum, “Virtual Reality Field Trip of a Steel Building Under Construction," in *Proceedings of the 2022 ASEE Annual Conference*, 2022, p. 1-21.

Abstract

The objective of this study is to determine if a virtual reality field trip can provide a valuable educational experience to undergraduate students. The format of this virtual reality field trip was a tour of a steel-framed skyscraper under construction narrated by a lead structural engineer, who took the participants to eight stops around a typical floor and explained various steel framing concepts with illustrations. The tour was provided to the students using standalone virtual reality headsets in a classroom setting. The assessment method consisted of pre- and post-tour quizzes to quantify the comprehension improvement of specific structural steel framing concepts and to gauge the impact of the virtual reality tour on inspiring students’ interest in the subject. The assessment data was supplemented by additional post survey data on students’ opinions of the experience. It was found that students were excited to interact with the virtual site visit and left the experience with a better understanding of structural steel framing. Lessons learned from this experience are discussed along with student recommendations for improvements in the educational module.

D.1 Introduction

The field of structural engineering requires individuals to develop an understanding of how individual components of a structure work together to support loads from gravity, wind, snow, earthquakes, and other sources. In a structural steel design course, engineering students are introduced to the design of individual structural elements, such as tension members, beams, columns, and simple connections, which builds on students’ previous structural analysis knowledge. An important step in developing an understanding of structural steel framing design is merging the individual element design concepts with how various components are connected, constructed, and used in practice. Traditionally, the classroom experience has relied on photographs and diagrams to convey the information, which have improved due to new technologies [141]. A typical enhancement to the classroom experience is providing a physical field trip where students can combine the information they are learning in class with real world experience [142]. A visit to a construction site provides students with the opportunity to better visualize how the components of a steel framed-building interact and additional details and nuances not typically covered in the first structural steel design course. However, such a field trip is not always practical due to time limitations, financial considerations, or local availability among many logistical issues [142], [143]. While virtual reality (VR) is not a new technology [144], recent improvements have made it possible to readily implement VR field trips into the classroom allowing the instructor to bring the desired site visit to the students. For the field of structural engineering, a building site or other construction project would be a possibility. However, the possibilities are not limited to a single specialty and opportunities exist, for instance, to view a water and wastewater treatment plant or a brownfield restoration. This research investigated the use of VR via a head-mounted display (the Oculus Go) to provide a virtual field trip to undergraduate and graduate students. The findings focus on the impact to students in terms of the knowledge gained and students' perception to determine if the use of VR provided a valuable educational experience. This research does not compare VR field trips to in-person field trips as the VR field trip is intended to be used when a traditional field trip is not feasible.

D.2 Background

Physical field trips are incorporated throughout students' education as they provide meaningful, lasting learning and exposure to activities not available in the classroom. Falk and Dierking [145] interviewed middle school students through young adults and found most participants were able to remember details from a field trip taken during second or third grade. Even as adult, participants could recall who they were with and specific facts obtained on the trip. The benefits of a field trip are not limited to young children [142], [146]–[148]. For college students, field trips provide the opportunity to expose students to the breadth of an industry and what the profession looks like in practice, which can be difficult to present in an engaging manner in the classroom [146]. The experience can also be used to observe the classroom material in real-life applications [147]. Field trips can provide the opportunity to learn and apply new skills; however, this is not without risks [142], [148]. New field trip opportunities need to be adequately vetted to ensure the intended goals are addressed and students can safely participate. This time requirement is just one of the costs associated with attending a physical field trip that combines with other issues to limit students' opportunity to participate. Furthermore, most field trips are limited in the amount of personalized learning that can occur as students are commonly grouped to optimize resources.

VR is not a new concept with the first headset developed in 1968 [144]. The advancement of computing technologies has changed early aspirations in terms of use and availability [149] into current real world possibilities. Multiple reviews on VR in education [143], [150]–[152] have shown positive impacts in learning and training. Earlier applications were commonly found in the computer science field, but has since expanded into many fields. The use of VR allows for students to immerse themselves in historical events, investigate medical procedures without risking patient safety, and test training with realistic hazards. Many of the successful implementations of VR have used it as a precursor to further learning. For example, demonstrations of best maintenance practices [153] and virtual experimental work [154] allowed individuals to have additional training prior to completing the task in-person. Similarly, VR readily allows for gamification of the educational experience. In line with balsa bridge building competitions, the games posed in VR can provide an opening to discuss relevant classroom concepts [155]. VR technology has been implemented with students of all ages with many rapidly interacting with the virtual content [143]. Head-mounted displays (HMDs), such as the Oculus Rift, Oculus Go, Oculus Quest, HTC Vive, Samsung Gear, and HP Reverb, were found to be preferred as the headsets provided a greater level of immersion [152]. An additional benefit of the HMDs was that the student experience became more individualized. Students had greater control of the presentation allowing for them to adjust the speed and repeat components as necessary [151].

While the adoption of VR in civil engineering has been slower than some other fields, there has been growing interest to use VR to improve the architecture, engineering, and construction processes [156]. Unfamiliarity with the technology in terms of necessary resources and capabilities has made some individuals reluctant to fully invest [157]. There has been a growing understanding of the benefits in terms of time saving and improved communications among the contractor, engineers, architects, and owners, but without proof of cost saving and an experienced workforce the industry has been hesitant to adopt new practices. Despite the slower adoption of VR in the civil engineering industry, multiple successful implementations have occurred in the classroom. In the field of construction management, the combination of Building Information Modeling (BIM) and VR improved students understanding of scheduling and cost estimation [158]. By combining 4D technology available with BIM into VR, students were more readily able to identify scheduling conflicts than when presented in typical planning documentation [159]. The use of virtual reality allows students to see the mechanical systems and wall components in 3D without having to interpret the meaning from 2D paper drawings or having to wait for the opportunity to attend a construction site [160], [161]. In the field of structural engineering, de Almeida Mello and Almenara [162] used augmented reality to show students steel rebar within a concrete member which demonstrated the challenge of positioning rebar with a member at realistic scale. Hadigheh *et al.* [163] developed a VR application that allowed students to see bridges in need of rehabilitation from multiple orientations as part of a course project. Fogarty *et al.* [164] used 3D models of buckling columns to demonstrate the various failure modes that can occur within a steel member. A recurring theme of various VR implementations was providing students the ability to see something that was previously obscured or shown in a more abstract form, which gives students another way to learn the material.

D.3 Methodology

This study utilized a mixed-methods approach to access the educational value of the VR tour. Quantitative and qualitative data was gathered through the use of a quiz and survey taken pre- and post-tour. Before the virtual tour, students were presented with a survey of their background experience (App. D.11) and a quiz (App. D.12) consisting of nine multiple-choice questions about introductory structural steel framing concepts. The quiz questions were developed by the authors with feedback from the American Institute of Steel Construction (AISC) to cover general information related to steel construction that new engineers should know. Typically one question was created for each concept area presented in the tour. After the virtual tour, students were presented with the same quiz (App. D.12) and a follow-up survey (App. D.13). The post-tour survey included eighteen quantitative and five qualitative questions to assess students' perception of the experience.

The quiz results were evaluated using Welch's unequal variance t-tests to assess the statistical significance of the difference in mean values of the pre- and post-tour scores. In addition to assessing as a cohesive group, the students were divided into undergraduate (labeled 'undergrad') and graduate (labeled 'graduate') student groups to assess if there was a significantly different experience for the two groups using the virtual tour. The surveys were used to assess students perception of the virtual reality experience and to provide feedback on how to improve the experience. The two student groups' perception of the virtual tour was compared using Mann-Whitney U tests to see if there was a statistical

(a) (b)

Figure D.1: Students' view within headset of steel framing. (a) View from starting location (b) Example indicator to direct student's attention during presentation

difference in the median opinion. While using Welch's t-tests would have been an acceptable approach [165], [166], the Mann-Whitney U tests were selected based on the slightly better results noted when evaluating 5 option Likert scale data.

D.4 Virtual Tour Details

The virtual reality tour was developed in collaboration with AISC. Utilizing InstaVR [167], 360°, 8K photos of a high rise construction site were combined into an eight scene virtual reality experience that allowed users to view the steel framing of one entire typical floor as shown in Fig. D.1. Narration is provided by a lead structural engineer who worked on the building design. The students are led in a loop around the floor while being informed about the structural steel framing, specifically load path, composite metal deck floor system, column splices, beam connections, beam camber, and web penetrations. During the tour, students are able to control the playback of the video and are free to look in any direction with indicators provided to direct students when specific objects are discussed, as shown in Fig. D.1(b). For this project, students viewed the virtual tour on a Oculus Go HMD, which required approximately 25 minutes to complete.

D.5 Development

The first process of creating the virtual tour was to locate a site and obtain permission to record images. AISC located a building under construction and obtained permission from the building owner. Next, the authors borrowed a 360°, 8K resolution Insta360 Pro 2 camera from the University of Wisconsin-Madison's College of Engineering Makerspace to record the images at the construction site. A high quality camera with high resolution is important to produce images with adequate detail. After the images were post-processed using the

Insta360 Studio software, the authors collaborated with AISC's education committee to select which images to use, determine the features to include on the tour and in which order, and to write and edit the script for the narrator. AISC connected with the lead structural engineer of the building who volunteered to provide the narration and then AISC purchased a license of InstaVR [167] to create the tour application, which enabled them to add in notations, supplemental graphics such as floor plans or connection details, and voice clips to the images, and to link the images together in one application. The draft tour went through several revision rounds between the authors and AISC before being finalized. The authors wrote the quiz and survey questions and obtained feedback from AISC to create the final version.

The Makerspace at the College of Engineering has approximately 26 Oculus Go headsets, which were purchased through an Educational Innovation Small Grant program through University of Wisconsin-Madison's Provost office. The headsets are maintained by student staff at the Makerspace. A classroom in the Makerspace was setup for in-class virtual reality activities.

D.6 Participants

The majority of the students involved were enrolled in a steel design course at the University of Wisconsin - Madison. As part of a regularly scheduled class period, all enrolled students were required to participate in the virtual reality activity shown in Fig. D.2. However, each student was allowed to determine whether their results were included or excluded from this study. An incentive of a travel mug was provided to participating students to encourage a larger random sampling of the class. To further increase participation, the same incentive was extended to all graduate students in the Civil and Environmental Engineering department who had previously taken a steel design course.

This activity was first included in Spring 2021 in the advanced steel design course with all 6 enrolled graduate students participating in this study. In Fall 2021, the activity was completed in the introductory steel design course with 27 of the 36 students participating. This group consisted of 25 undergraduate students and 2 graduate students. All 9 who opted to not be included in this study were undergraduate students. Later in Fall 2021, the offer to all graduate students was extended resulting in 6 more participants. This additional data allowed for the comparison between the undergraduate and graduate student perspective.

Each group of students was provided the same background information for the activity as there was no specific classroom presentation addressing the concepts to be covered

Figure D.2: Students using virtual reality headsets in classroom space. Photo taken by the College of Engineering media staff.

on the tour. The students were informed of the general parameters of the tour including that it was a high rise steel building and that it covered the basics of steel framing, but not the specific topics. With the pre-tour survey and quiz, students were provided an additional instruction sheet on the basics of viewing the tour with the Oculus Go HMDs. A short summary of the key steps were repeated as students began using the VR headsets, but no additional description of the concepts was provided. The authors only provided troubleshooting aid while students viewed the tour, except in Spring 2021 when students were required to view the tour on their own due to health and safety concerns limiting contact.

D.7 Results

At the time of participation, the majority of undergraduate students were enrolled in their first structural design course. The majority had some confidence in their ability to evaluate individual elements of a structure, but not in their ability to design elements or understand how the structure works together in terms of load path. Most graduate students had completed concrete and steel design courses and were at least enrolled in their third structural design course. The graduate students did not have significantly more confidence in their analysis skills $(p > 0.21)$, but did have significantly more confidence in applying design concepts $(p <= 0.007)$. Despite the differences in educational experience, this virtual tour was the first opportunity for approximately 2/3 of each group to participate in a building tour focused on the structural framing.

Table D.1 summarizes the pre- and post-tour quiz results. Results from the t-tests in Table D.2 indicate that there was a statistically significant increase in the mean scores of

Table D.1: Descriptive statistics for quiz scores

Variable	Minimum	Maximum[1]	Median	Mean	Standard deviation
Pre-tour Undergrad	3	8	5	5.32	1.25
Post-tour Undergrad	5	9	8	7.16	1.52
Pre-tour Graduate	6	9	7	6.57	1.22
Post-tour Graduate	7	9	8	8.00	0.78
Pre-tour All	3	9	6	5.77	1.37
Post-tour All	5	9	8	7.46	1.35

[1] Scores are out of 9 possible points.

Table D.2: Comparison of means for virtual tour participants

Variable	Difference in mean score	t-Score	p-value
	Pre-Tour vs. Post-Tour		
Undergrad	1.84	4.68	<0.001
Graduate	1.43	3.68	0.001
All	1.69	5.49	<0.001
	Undergrad vs. Graduate		
Pre-tour	1.25	3.04	0.005
Post-tour	0.84	2.28	0.029

the structural steel quiz for students who participated in the virtual tour activity. This applied to both undergraduate and graduate students even though graduate students initially preformed statistically significantly better than the undergraduate students.

Table D.3 summarizes the pre- and post-tour quiz results with correct and incorrect responses labeled ‘Y’ and ‘N’, respectively. As students were not informed of their results between the quizzes or that it was to be the same quiz, those students who initially correctly answered and then incorrectly changed their response provide some insight in descriptions that might be misleading.

There was no statistically significant difference between the undergraduate and graduate students’ perception of the virtual tour as indicated by Table D.4. Both groups positively agreed that viewing the tour provided them a better understanding of the key concepts as shown in Fig. D.3. Confirmed through similar questions in Fig. D.4 and Fig. D.5, students viewed the virtual tour as a useful classroom activity. The virtual reality experience was appreciated over a traditional lecture; however, a majority of students would have preferred an actual field trip, which is in line with work by Seifan *et al.* [148]. This study did not focus on a comparison between a physical and a virtual field trip, only the educational value of the virtual field trip.

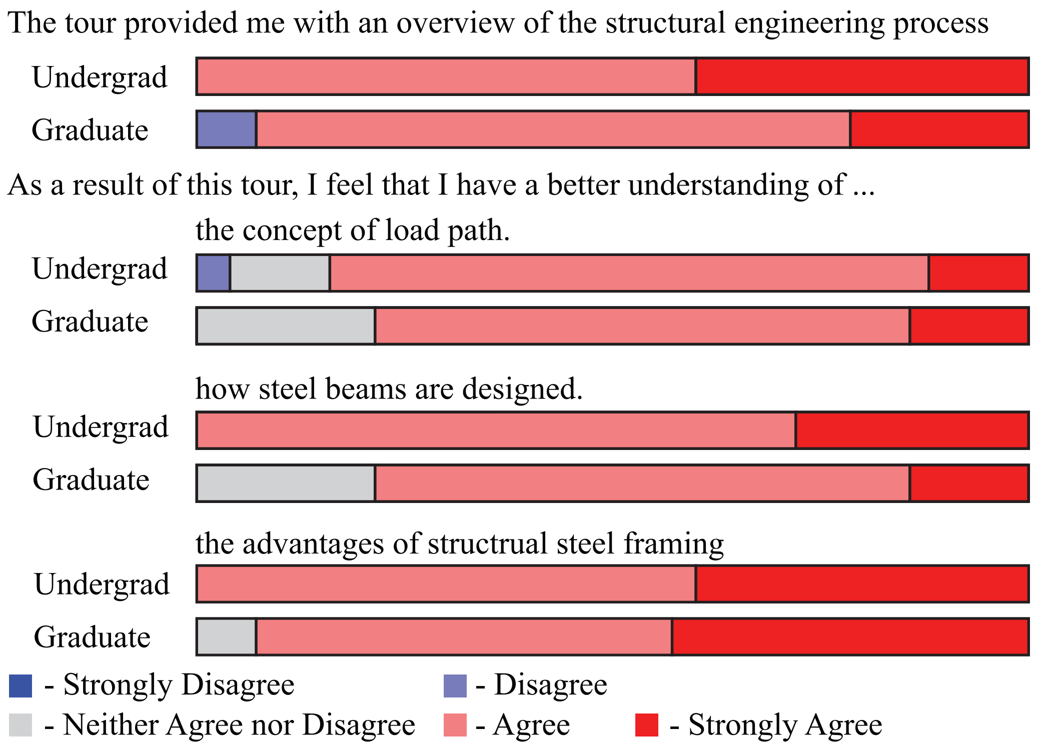

Figure D.3: Post survey results on understanding of general concepts

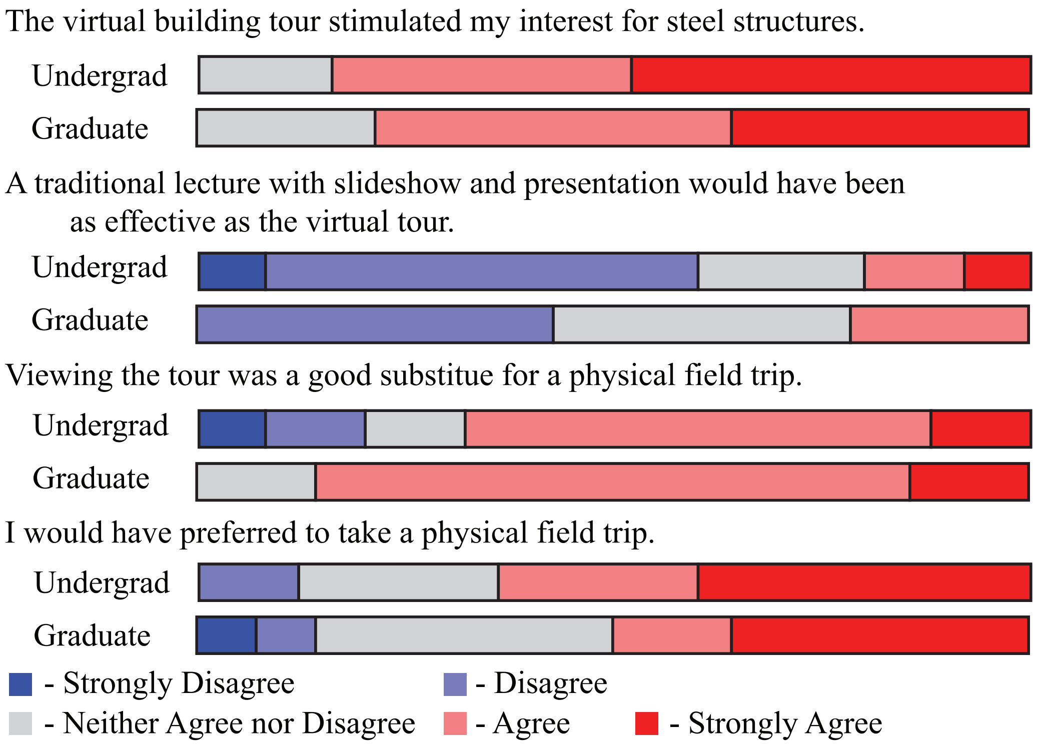

Figure D.4: Post survey results on alternative building tour presentations

Table D.3: Summary of individual question performance

			Post-Tour Response			
			Undergrad		Graduate	
			Y	N	Y	N
Pre-Tour Response	Q1	Y	64%	16%	100%	0%
		N	12%	8%	0%	0%
	Q2	Y	12%	12%	43%	0%
		N	36%	40%	14%	43%
	Q3	Y	84%	0%	93%	0%
		N	8%	8%	7%	0%
	Q4	Y	68%	8%	86%	0%
		N	16%	8%	7%	7%
	Q5	Y	24%	20%	50%	7%
		N	48%	8%	36%	7%
	Q6	Y	20%	8%	50%	7%
		N	60%	12%	36%	7%
	Q7	Y	68%	12%	57%	7%
		N	12%	8%	29%	7%
	Q8	Y	68%	4%	100%	0%
		N	20%	8%	0%	0%
	Q9	Y	44%	0%	50%	0%
		N	52%	4%	43%	7%

Table D.4: Summary of statistical significance in the difference between undergraduate and graduate student responses

Variable*	S2	S3	S4	S5	S6	S7	S8	S9	S10	S11
U-Score	540	503.5	551	502.5	523	472	465	519.5	461	482
p-value	0.243	0.957	0.096	1	0.542	0.396	0.256	0.552	0.211	0.499

* See Appendix C for question wording

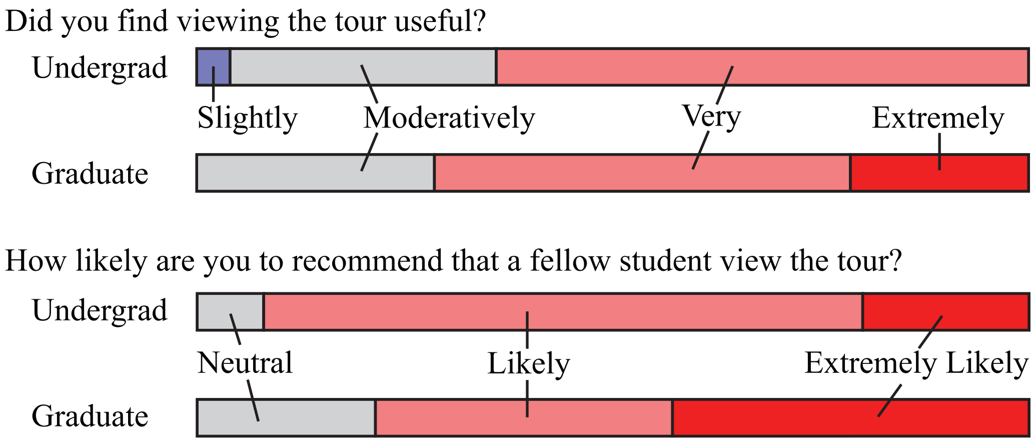

Figure D.5: Post survey results on usefulness of the experience

D.8 Discussion

Based on observations and post-tour feedback, it was found that students were excited to interact with the virtual site visit and left the experience with a better understanding of structural steel framing. The enthusiasm for the virtual tour built upon many students' general interest of trying virtual reality and provided an intriguing presentation to motivate future learning. Students appreciated having the guided narration while still having the ability to individually control their view in agreement with observations by Fogarty *et al.* [164] and Ragan *et al.* [168]. Students wished they had a bit more control through zooming or additional viewpoints to obtain closer views of discussed components, but only a minority expressed interest in a free-roaming experience. Overall, the discrete viewing locations were determined to be a good compromise giving students a continuous experience while not overwhelming them with the new technology.

The virtual tour introduced and expanded on multiple structural framing concepts to students. Based on the quiz scores, students' comprehension improved the most related to column splices and the least related to composite metal deck floor system. The primary challenge with metal decking was students were confusing the parallel and perpendicular directions. The presentation described the correct orientation and students agreed that it a good description; however, limited graphics were displayed to further clarify the directions for students. The column splice improvement was largely attributed to students being presented with a real structure. Students identified the description of column splices as one of the worst provided, but seeing the building showed students where columns are typically spliced, which differs from the simplifications that are made for analysis and design. The lowest rated descriptions were typically associated with difficult to see details. Overall, it was observed that students gained the most information where the narration was supplemented with near-by visuals that students could take their time to assess.

Despite the success of the virtual tour, various items were identified for possible improvement. The use of a commercial software [167] package allowed rapid development of the virtual tour, for those without previous developer experience, at the cost of a higher initial fee. However, this choice ultimately led to some limitations in the final project. For example, there was an issue with control options for the audio playback and scene rotation. When the audio was playing, two buttons on the controller either increased or decreased the audio playback speed. In all other instances, those same two buttons allowed the user to rotate either clockwise or counterclockwise 45° in the scene. Although users could physically turn their bodies to see all directions, some users preferred to use the controller to rotate and would occasionally press the buttons to rotate during the audio playback, resulting in an accidental speed change of the playback. These control difficulties did negatively affect students; however, it was not found to be a major factor unlike the complex control issues noted by Chen *et al.* [169] in their experiment. During development, it was desired to incorporate additional questions into the virtual tour to help students verify they understood key points of the narrations after selected scenes, which was even suggested by a few students as an improvement. However, the commercial software was not able to properly implement the quiz questions on the Oculus Go HMDs. Additionally, the commercial software had means to publish tour versions for alternative viewing platforms which was met with limited success during this project. An online web page with quiz questions was successfully implemented; however, at the time of writing that version is currently non-functioning. Other VR HMDs are theoretically supported, but another working application, specifically for the Oculus Quest headset, was never finalized due to nonexistent technical support by the commercial software despite the software claiming such technical support was available. This issue is exacerbated as the Oculus Go HMDs are no longer produced and thus new Oculus users would need to purchase the Quest 2 HMD. Currently, the most readily available version is distributed through YouTube, which has different limitations. For example, the narrations automatically begin after the completion of the previous video (scene) without the opportunity for students to view the structure at their own pace.

The virtual tour utilized multiple photographs as the backdrop for the presentation. A significant benefit was that students were presented with the actual structure and not a computer model. These photographs have the limitation that students were confined to a single location per image and could not get closer to features as desired to get a better view. Allowing students to have free movement around the structure would require a complete 3D model which would limit the realism of the setting. As noted by Kavanagh *et al.* [151], a significant issue with the VR environment is having the appropriate amount of realism. For this virtual field trip, it was determined that without realistic visuals students could miss the key information. Another negative factor that many students commented on was the background. For privacy, the building owner asked that the real skyline be obscured as the building could be identified based on the position of recognized landmarks. The result was a relatively bright, blank background which left students wishing they could see beyond the building and additional eye strain. While a detailed investigation of students' comfort was not completed similar to many other studies [151], the 20-25 minutes required to complete the virtual tour was pushing the limits of some students' preference. Finally, the students were intrigued by the various structural elements, but multiple students wished there would have been active construction occurring in the photos or a short video to allow them to see how structural elements are constructed and erected on site.

D.9 Conclusions

This mixed-methods study considers if the use of a virtual reality field trip can provide a valuable educational experience. A pre- and post-tour quiz was developed and implemented to quantify the comprehension improvement of specific structural steel framing concepts. Tests for statistical significance comparing the pre-tour and post-tour mean quiz scores of participants indicated that students on average increased their test scores suggesting improved understanding of the concepts. It was found that students had the most improvement in the comprehension of column splice and the least improvement in the comprehension of the composite metal deck floor system. Additional post survey data and interactions with students indicated that students were excited to interact with the virtual site visit and believed they benefited from the experience. A key factor for the positive outcomes was identified as the capability of the guided tour to direct students to important locations while allowing them to control the interaction with the tour elements.

D.10 Acknowledgements

This work was supported in part by an Educational Innovation Small Grant through the University of Wisconsin-Madison Provost's Office. Special thank you to the AISC Education Committee. Any opinions, findings, conclusions, and recommendations expressed in this paper are those of the authors and do not necessarily reflect the view of the sponsors or the other individuals mentioned here.

D.11 Background Assessment

Background Survey

Thank you for participating in this project. This first survey is to collect some general background information.

1. Current Year in College/University
    a) 1st Year
    b) 2nd Year
    c) 3rd Year
    d) 4th Year
    e) 5th+ Year
    f) Graduate student - 1st Year
    g) Graduate student - 2nd+ Year
2. Which of the following classes have you completed or are currently taken? (Options of “Completed", “Currently Enrolled", and “Not Taken")
    a) Structural Analysis 1
    b) Structural Analysis 2
    c) Introduction to Building Information Modeling
    d) First Semester Steel Design
    e) Second Semester Steel Design
    f) Design with Concrete
    g) Design with other Materials
3. Have you had any work experience related to civil engineering? If you select "other", please explain:
    a) None
    b) Internship
    c) Co-op position
    d) Full time job
    e) Other

4. If you have work experience, please indicate the general field(s) that your job responsibilities fell under?
    a) Construction Engineering and Management
    b) Environmental Science and Engineering
    c) Geotechnical Engineering
    d) Structural Engineering
    e) Transportation Engineering
    f) Water Resources Engineering
    g) Other
5. Have you been to a building tour of a steel building before where the structure was discussed and you could see the underlying structure either as exposed steel or during construction?
    a) No
    b) Yes, 1 or 2 times
    c) Yes, 3 or more times

Personal Assessment

For each of the following questions, please answer with how likely you think you would be able to complete the following tasks.

6. Analyze a truss to determine internal forces and displacements

    Definitely Not – Probably Not – Possibly – Probably – Definitely

7. Analyze a beam to determine internal forces and displacements

    Definitely Not – Probably Not – Possibly – Probably – Definitely

8. Analyze a frame to determine internal forces and displacements

    Definitely Not – Probably Not – Possibly – Probably – Definitely

9. Determine the load path for a given structure

    Definitely Not – Probably Not – Possibly – Probably – Definitely

10. Size a steel column for strength and serviceability for axial loading

    Definitely Not – Probably Not – Possibly – Probably – Definitely

11. Size a steel beam for strength and serviceability

    Definitely Not – Probably Not – Possibly – Probably – Definitely

D.12 Structural Steel Quiz

This [second/third] survey is to evaluate your general understanding of structural steel systems [/after the tour]. It is intended to be completed closed book without any external references.

1. Which of the following images illustrates a composite metal deck floor system?

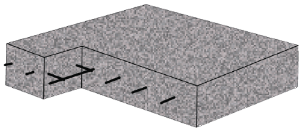

Option 1

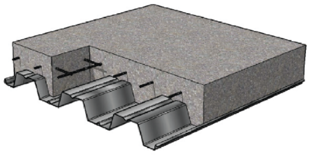

Option 2

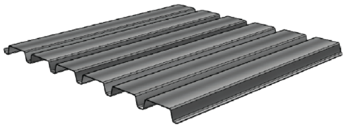

Option 3

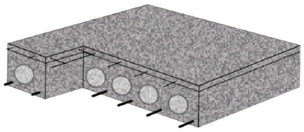

Option 4

   a) Option 1
   b) Option 2 ←
   c) Option 3
   d) Option 4

2. Which of the following statements is **CORRECT**?

   a) The metal deck spans in the direction perpendicular to the ribs.
   b) The metal deck spans in the direction parallel to the ribs. ←
   c) The metal deck spans in the shortest direction without consideration of the rib orientation.
   d) The metal deck spans in the longest direction without consideration of the rib orientation.
   e) The metal deck cannot support load by itself and requires concrete to support any load.

3. Based on the sketches provided, what is the tributary area of column B-3, the one in the red circle?

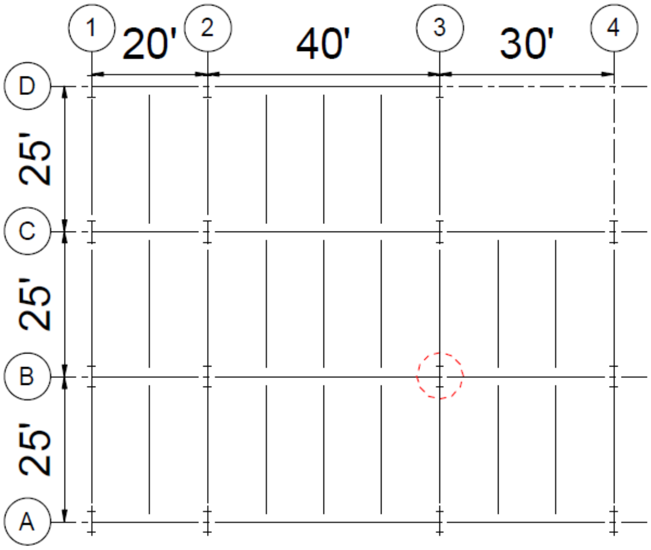

   a) 250 ft^2
   b) 750 ft^2
   c) 875 ft^2 ←
   d) 1000 ft^2
   e) 1750 ft^2

4. Why would a steel beam be cambered?

   a) Camber provides an initial downward deflection such that the applied loads do not cause more downwards deflection.
   b) Camber provides an initial upwards deflection that counteracts the deflection from applied loads. ←
   c) Camber provides an initial upwards deflection such that the beam can use arching action with applied loads.
   d) Camber provides an initial downward deflection to ensure that the poured concrete floor has adequate thickness.

5. With the loading indicated on the sketch, which location would likely be a preferred location for a web penetration in a steel beam?

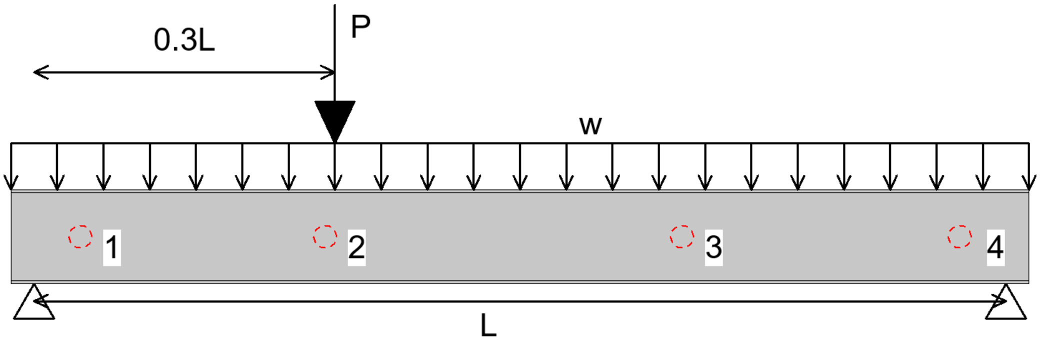

   a) 1
   b) 2
   c) 3 ←
   d) 4

6. Which statements is **FALSE** about steel columns?

   a) Column splices are commonly at locations that provide ease of construction.
   b) Some columns are designed to only carry vertical loads with another portion of the structure being relied upon to carry lateral loads.
   c) Column splices are commonly located at the same elevation as the floor slab to hide the connection. ←
   d) Column splices can utilize welded or bolted connections.
   e) Columns can be subjected to moments.

7. Which of the following is **FALSE** about steel connections?

   a) The design of connections can be done by the engineer of record or by another engineer through delegated design.
   b) Connections transfer load from one structural member to another and can often be a controlling component of the design.
   c) Connections must be either all-welded or all-bolted. ←
   d) Bolted connections can provide the opportunity for more adjustments in the field.

8. What is **NOT** a benefit of steel construction?
    a) Structural steel allows for rapid design, fabrication, and erection.
    b) Structural steel frames are readily adaptable for future alterations, such as renovations to provide new openings.
    c) The high strength of the material allows for the use of long spans and tall columns without large solid cross sections, which can allow wide open spaces.
    d) Steel material behavior is predictable making it possible to reliably calculate deflections and capacity.
    e) Steel is a fire rated material that never requires fireproofing. ←

9. Which of these statements accurately reflects the difference between the two steel beams based on the tags shown?

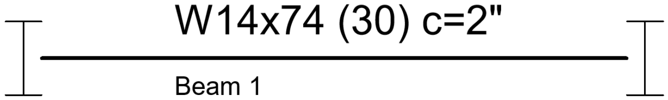

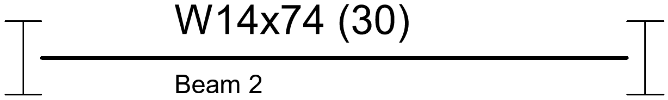

    a) Beam 1 has an extra 2″ cover plate attached to the bottom of the beam.
    b) Beam 1 is designed to act composite with the deck while Beam 2 is not.
    c) Beam 1 and Beam 2 are different grades of steel with different amounts of carbon required.
    d) Beam 1 is cambered to counteract the deflection due to the applied loads. ←
    e) Beam 2 is required to be shored during construction.

D.13 Building Tour - Experience Survey

This second follow-up survey is to learn about how your experience went.

1. In which format did you view the tour?
    a) Oculus Quest (Controllers have sticks)
    b) Oculus Go (Controller has clickpad)
    c) Web Browser
    d) YouTube Video

2. The tour provided me with an overview of structural engineering process.

Strongly Disagree – Disagree – Neither agree nor disagree – Agree – Strongly Agree

3. As a result of this tour, I feel that I have a better understanding of the concept of load path.

   Strongly Disagree – Disagree – Neither agree nor disagree – Agree – Strongly Agree

4. As a result of this tour, I feel that I have a better understanding of how steel beams are designed.

   Strongly Disagree – Disagree – Neither agree nor disagree – Agree – Strongly Agree

5. As a result of this tour, I feel that I have a better understanding of the advantages of structural steel framing.

   Strongly Disagree – Disagree – Neither agree nor disagree – Agree – Strongly Agree

6. The virtual building tour stimulated my interest for steel structures.

   Strongly Disagree – Disagree – Neither agree nor disagree – Agree – Strongly Agree

7. A traditional lecture with slideshow and presentation would have been as effective as the virtual tour.

   Strongly Disagree – Disagree – Neither agree nor disagree – Agree – Strongly Agree

8. Viewing the virtual tour was a good substitute for a physical field trip.

   Strongly Disagree – Disagree – Neither agree nor disagree – Agree – Strongly Agree

9. I would have preferred to take a physical field trip.

   Strongly Disagree – Disagree – Neither agree nor disagree – Agree – Strongly Agree

10. Did you find viewing the tour useful?

    Not at all Useful – Slightly Useful – Moderately Useful – Very Useful – Extremely Useful

11. How likely are you to recommend that a fellow student view the tour?

    Extremely Unlikely – Unlikely – Neutral – Likely – Extremely Likely

12. What did you like about the tour? (Free Response)
13. Was there anything you felt was missing from the tour? (Free Response)
14. Is there anything that you would improve in the tour? (Free Response)
15. Were there any challenges viewing the tour? (Free Response)
16. Is there anything else what you would like to tell us about your virtual reality experience?
    (Free Response)

Quality of Descriptions

Please rate the quality of the descriptions given during the tour of the following topics.

1. The description of the steel decking

   Poor – Fair – Good – Very Good – Excellent

2. The description of the composite beams

   Poor – Fair – Good – Very Good – Excellent

3. The description of beam-to-column connections.

   Poor – Fair – Good – Very Good – Excellent

4. The description of column splices

   Poor – Fair – Good – Very Good – Excellent

5. The description of beam camber

   Poor – Fair – Good – Very Good – Excellent

6. The description of tributary area

   Poor – Fair – Good – Very Good – Excellent

7. The description of web openings

   Poor – Fair – Good – Very Good – Excellent

8. The description of delegated design

   Poor – Fair – Good – Very Good – Excellent